ABSTRACT

Title of Document: CFD SIMULATIONS FOR SCALE UP OF WET MILLING IN HIGH SHEAR MIXERS

Meng Yang, Ph.D., 2011

Directed By: Professor Richard V. Calabrese, Department of Chemical & Biomolecular Engineering

Rotor-stator mixers are widely used in the chemical and pharmaceutical process industries. Up to now, however, few papers discuss the mean flow and turbulence fields generated by them and their influence on final product quality. In this work, CFD results at different scales are used to aid in the scale up of crystal wet milling processes. CFD simulations were performed to simulate different scale mixers. In addition, wet milling studies were conducted at the bench scale to complement the CFD results and predict wet milling performance in larger scale mixers.

The flow properties in a batch Silverson L4R rotor-stator mixer at 4000 and 6000 rpm were investigated. A hybrid technique was developed. The new method is computationally efficient compared with the standard sliding mesh method. Macro scale properties are predicted. The turbulent flow field and deformation rate field are compared and analyzed. After obtaining fully converged flow fields, one way coupled particle tracking calculations were performed using an efficient fast particle tracking

code. Particles trajectories were recorded, and analyzed. To validate the simulated flow field, particle image velocimetry (PIV) experiments were conducted.

CFD simulations of Silverson inline L4R (bench scale), 450LS (pilot scale) and 600LS (plant scale) mixers were conducted at constant tip speed to investigate the scale up effect. The macro scale properties werer predicted. The mean velocity, turbulent and deformation rate fields were investigated. The flow properties of the 450LS and 600LS mixers are quite similar, but they are significantly different from those of the L4R (bench scale) mixer. Therefore, it may be resonable to scale up from pilot scale to plant scale by the general accepted tip speed scale up criterion. However, considering tip speed alone may lead to a significant discrepancy between bench scale and larger scales.

Bench scale wet milling experiment were performed at 4000, 6000 and 8000 rpm using sucrose and mannitol in the Silverson L4R inline mixer. The crystal size decreases with rotation rate at both free pumping conditions and constant flow rate conditions. To investigate the effect of flow rate, wet milling of granulated sucrose in the Silverson L4R inline mixer with constant rotor tip speed were performed at different flow rates. It is found that the crystal size increases with the flow rate.

CFD SIMULATIONS FOR SCALE UP OF WET MILLING IN HIGH SHEAR MIXERS

By

Meng Yang

Dissertation submitted to the Faculty of the Graduate School of the
University of Maryland, College Park, in partial fulfillment
of the requirements for the degree of
Doctor of Philosophy
2011

Advisory Committee:
Professor Richard V. Calabrese, Chair
Professor Raymond A. Adomaitis
Professor James H. Duncan
Professor Sheryl Ehrman
Professor Chunsheng Wang

Acknowledgements

I would like to express my appreciation to my advisor Professor Calabrese for his steady support and patience. Without his support, this work would not have been possible. I am grateful to my colleagues, Karl Kevala, Marwan Charrouff, B.N. Murhty, Justin Walker and Paul Rueger for their help and suggestions. I wish to thank Dr. Xinan Liu for his guidance on PIV experiments.

Much appreciation is due to the members of my dissertation committee for taking time to critique my work. Many thanks to Professor Duncan and Professor Piomelli for their magnificent instruction on fluid dynamics.

Finally, I am indebted to my family for their encouragement and trust.

Table of Contents

Acknowledgements ii
List of Tables v
List of Figures vi
Chapter 1: Introduction 1
1.1. Motivation and purpose 1
1.2. Thesis Synopsis 4
Chapter 2: Literature Review 6
2.1 Review of Rotor-Stator Mixer Devices 6
2.2 Review of CFD for Rotor-Stator Mixer and Stirred Tank 9
2.3 Review of wet milling in rotor-stator mixers 20
Chapter 3: Computational Fluid Dynamics 22
3.1 Continuity and momentum equations 22
3.2 The k-ε model 25
3.3 Wall functions 27
3.3 The numerical scheme 32
3.4 Discretization methods 33
3.5 Frames of reference 36
3.6 Convergence criteria 39
Chapter 4: RANS Simulation of Silverson L4R Batch Rotor-Stator Mixer 41
4.1 Geometry and flow conditions 41
4.2 Grid generation and CFD model settings 43
4.3 Mesh independence tests 47
4.4 Time periodic solution 58
4.5 Hybrid RANS simulation technique 60
4.5.1 Define the periodic envelope 61
4.5.2 MRF simulations 74
4.5.3 Hybrid simulation 75
4.6 Results and discussion 80
4.6.1 Macro scale properties 80
4.6.2 The flow fields at 4000 and 6000 rpm 84
4.6.3 The turbulent fields at 4000 and 6000 rpm 100
4.6.4 The mean deformation fields at 4000 and 6000 rpm 111
4.6.5 Calculation of solid particles trajectories in Silverson L4R batch rotor-stator mixer 115
4.6.6 PIV validation of the flow field in Silverson L4R batch rotor-stator mixer 120
4.7 Summary 122
Chapter 5: RANS Simulation of Silverson Inline Rotor-Stator Mixer at Lab, Pilot and Plant Scale 127
5.1 Geometries and flow conditions 128
5.1.1 Geometry of Silverson L4R inline lab scale rotor-stator mixer 128

5.1.2 Geometry of Silverson 450LS inline pilot scale rotor-stator mixer..... 128
5.1.3 Geometry of Silverson 600LS inline plant scale rotor-stator mixer..... 130
5.1.4 Flow conditions..... 131
5.2 Grid generation..... 131
5.2.1 Grid generation procedure..... 132
5.2.2 Mesh of Silverson L4R, 450LS and 600LS..... 133
5.3 CFD model settings..... 141
5.4 Results and discussion..... 143
5.4.1 Macro scale properties..... 143
5.4.2 Flow fields of the Silverson inline L4R, 450LS and 600LS mixers..... 148
5.4.3 Turbulent flow field of the Silverson inline L4R, 450LS and 600LS mixers..... 186
5.4.4 The mean deformation rate field of the Silverson inline L4R, 450LS and 600LS mixers..... 209
5.4.5 Effect of flow rate at constant tip speed..... 217
5.5 Summary..... 226
Chapter 6: Wet Milling of Crystals in the Silverson L4R Inline Rotor-Stator Mixer 230
6.1 Equipment..... 230
6.2 Material..... 232
6.3 Image analysis..... 233
6.4 Wet milling experimental procedure..... 234
6.5 Image analysis procedure..... 235
6.6 Results and discussion..... 236
6.6.1 Pumping rate of the Silverson inline L4R rotor-stator mixer..... 236
6.6.2 Wet milling of Sucrose..... 238
6.6.3 Wet milling of mannitol..... 266
6.7 Summary..... 296
Chapter 7: Summary, Conclusions and Recommendations..... 298
7.1 Summary of RANS simulation of Silverson L4R batch rotor-stator mixer..... 298
7.1.1 Conclusions..... 299
7.2 Summary of RANS simulation of Silverson inline rotor-stator mixer at lab, pilot and plant scale..... 301
7.2.1 Conclusions..... 301
7.3 Summary of wet milling of crystals in Silverson L4R inline rotor-stator mixer..... 303
7.3.1 Conclusions..... 303
7.4 Recommendations..... 304
Glossary..... 306
REFERENCES..... 309

List of Tables

Table 4-1: Predicted power number at 4000 rpm for 1.6, 1.7, 4.2 and 5.6 million cell mesh.

Table 4-2: Predictions of distributions of turbulent energy dissipated in the tank at 4000 and 6000rpm.

Table 5-1: Shear frequency of the Silverson inline L4R, 450LS and 600LS mixers.

Table 5-2: Predicted flow rate and flow number of the Silverson inline L4R, 450LS and 600LS mixers.

Table 5-3: Predicted power properties of the Silverson inline L4R, 450LS and 600LS mixers.

Table 5-4: Predictions of distributions of turbulent energy dissipation in the Silverson inline L4R mixer at 4000 and 8000rpm.

Table 5-5: Predictions of distributions of turbulent energy dissipation in the Silverson inline 450LS mixer at 2100rpm.

Table 5-6: Predictions of distributions of turbulent energy dissipation in the Silverson inline 600LS mixer at 1575 rpm.

Table 5-7 Predictions of distributions of turbulent energy dissipation in the Silverson inline 450LS mixer with a flow rate of 1.2 L/s at 2100rpm.

Table 6-1 Particle size calculated at different number of particles at 8000 rpm

Table 6-2: Number of passes of sucrose crystals at specific times.

Table 6-3: SE and $\dot{\varepsilon}$ at different rotation rate (wet milling of sucrose).

Table 6-4: Number of passes of sucrose crystals at specific time.

Table 6-5: SE and $\dot{\varepsilon}$ at different rotation rate (wet milling of mannitol).

List of Figures

Figure 1-1: High shear mixers at bench, pilot and plant scale 3

Figure 4-1: Silverson Batch Rotor Stator Mixer 42

Figure 4-2: Silverson L4R batch rotor-stator mixer geometry. 43

Figure 4-3: Meshes for several parts of rotor stator mixer domain. 45

Figure 4-4: Rotating and fixed mesh on the mid-plane. 46

Figure 4-5: Magnified View of Rotating Mesh and Stationary Mesh. 48

Figure 4-6: Histgram of the skewness. 48

Figure 4-7: 3 meshes under investigation in mesh independence test. 49

Figure 4-8: The monitored mid-plane and slot 1. 49

Figure 4-9: Mesh independence test: 1.6 million and 1.7 million cells. 51

Figure 4-10: Mesh independence test: 1.7 million and 4.2 million cells. 52

Figure 4-11: The adapted regions (highlighted by red color). 53

Figure 4-12: 4.2 million cells mesh and the adapted mesh on the mid-plane. 53

Figure 4-13: Mesh independence test: 5.6 million and 4.2 million cells. 54

Figure 4-14: Monitored line in mesh independence test (highlighted by red color). . 55

Figure 4-15: Radial velocity change along the line in Figure 4-14 for 1.6 million cells, 1.7 million cells, 4.2 million cells and 5.6 million cells. 56

Figure 4-16: Experimental power number data for slotted stator head[9]. 57

Figure 4-17: Sliding mesh simulation of turbulent kinetic energy contours in the mid plane for a baffled Rushton Turbine stirred tank[27]. 58

Figure 4-18: Three monitored lines that indentified the envelope boundary in the x dimension direction. 62

Figure 4-19: The x coordinate in the computational domain..... 63
Figure 4-20: The velocity magnitudes change with time at different points on line 1 (mid-plane) in the x direction at 4000 rpm. 64
Figure 4-21: The velocity magnitudes change with time at different points on line 2 and 3 (mid-plane) in the x direction at 4000 rpm. 64
Figure 4-22: The velocity magnitudes change with time at different points on line 1 (mid-plane) in the x direction at 6000 rpm. 65
Figure 4-23: The velocity magnitudes change with time at different points on line 2 and 3 (mid-plane) in the x direction at 6000 rpm. 65
Figure 4-24: The velocity magnitudes change with time at different points on line 1 (mid-plane) in the x direction at 8000 rpm. 66
Figure 4-25: The velocity magnitudes change with time at different points on line 2 and 3 (mid-plane) in the x direction at 8000 rpm. 66
Figure 4-26: Three monitored lines that indentified the envelope boundary in the y direction. 67
Figure 4-27: The y coordinate in the computational domain..... 67
Figure 4-28: The velocity magnitudes change with time at different points on line 4 (mid-plane) in the y direction at 4000 rpm. 68
Figure 4-29: The velocity magnitudes change with time at different points on line 5 and 6 (mid-plane) in the y direction at 4000 rpm. 69
Figure 4-30: The velocity magnitudes change with time at different points on line 4 (mid-plane) in the y direction at 6000 rpm. 69

Figure 4-31: The velocity magnitudes change with time at different points on line 5 and 6 (mid-plane) in the y direction at 6000 rpm. 70
Figure 4-32: The velocity magnitudes change with time at different points on line 4 (mid-plane) in the y direction at 8000 rpm. 70
Figure 4-33: The velocity magnitudes change with time at different points on line 5 and 6 (mid-plane) in the y direction at 8000 rpm. 71
Figure 4-34: Three monitored lines that indentified the envelope boundary in the z direction. 71
Figure 4-35: The z coordinate in the computational domain. 72
Figure 4-36: The velocity magnitudes change with time at different points on line 7 and 8 (mid-plane) in the z direction at 4000 rpm..... 72
Figure 4-37: The velocity magnitudes change with time at different points on line 7 and 8 (mid-plane) in the z direction at 6000 rpm..... 73
Figure 4-38: The velocity magnitudes change with time at different points on line 7 and 8 (mid-plane) in the z direction at 8000 rpm..... 73
Figure 4-39: The hybrid time periodic envelope. 74
Figure 4-40: Steady and unsteady MRF residue at 4000 rpm. 76
Figure 4-41: Lines monitored in unsteady MRF simulation..... 76
Figure 4-42: The velocity magnitude change with time on the 3 lines..... 77
Figure 4-43: The monitored surfaces in the unsteady MRF solution. 77
Figure 4-44: The relative difference of velocity magnitudes, $\frac{|v_{8500} - v_{8572}|}{v_{8572}}$, on 3 surfaces at time step 8500 and 8572 for N = 4000 rpm. 78

Figure 4-45: The relative difference of velocity magnitudes, $\frac{|v_{8600} - v_{8672}|}{v_{8672}}$ 79

Figure 4-46: The monitored surfaces in the hybrid simulation..... 80

Figure 4-47: The relative difference of velocity magnitudes, $\frac{|v_{50} - v_{53}|}{v_{53}}$, on 3 surfaces for rotations 50 and 53 for N = 4000 rpm..... 81

Figure 4-48: The relative difference of velocity magnitudes, $\frac{|v_{55} - v_{58}|}{v_{53}}$, on 3 surfaces for rotation 55 and 58 for N = 6000 rpm. 82

Figure 4-49: The surfaces for the pumping capacity calculation..... 83

Figure 4-50: The coordinate on the mid-plane. 84

Figure 4-51: Normalized mean velocity magnitude snapshots on mid-plane inside the sliding mesh envelope (the rotor rotates in the anticlockwise direction)..... 86

Figure 4-52: Normalized mean velocity magnitude snapshots at plane y=0 inside the sliding mesh envelope..... 87

Figure 4-53: Normalized mean velocity magnitude vector plot on mid-plane outside the sliding mesh envelope..... 88

Figure 4-54: Normalized mean velocity magnitude vector plot at mid-plane outside the sliding mesh envelope by the pure sliding mesh and the hybrid method at 4000 rpm. 89

Figure 4-55: Normalized steady MRF mean velocity magnitude vector plots at mid-plane outside the envelope at two different rotor blade orientations for N = 6000 rpm. 90

Figure 4-56: Normalized mean velocity magnitude vector plot at mid-plane outside the sliding mesh envelope with different struts positon at 4000 rpm. 91
Figure 4-57: Three planes with different y coordinates outside the sliding mesh envelope. 92
Figure 4-58: Normalized mean velocity magnitude vector plots at plane y = 0 outside the sliding mesh envelope. 93
Figure 4-59: Normalized mean velocity magnitude snapshots at plane y = 30 (the rotor blade angle is same as Figure 4-51 (b)). 93
Figure 4-60: Normalized mean velocity magnitude snapshots at plane y = -30 (the rotor blade angle is same as Figure 4-51 (b)). 94
Figure 4-61: Normalized mean velocity magnitude vector plots at plane z = -15 mm 94
Figure 4-62: Normalized mean velocity magnitude vector plots at plane z = -180mm 95
Figure 4-63: Velocity vectors normalized by the rotor tip speed around the stator slot at various blade positions (4000 rpm). The rotor rotates in the anti-clockwise direction. 96
Figure 4-64: Velocity vectors normalized by the rotor tip speed around the stator slot at various blade positions (6000 rpm). The rotor rotates in the anti-clockwise direction. 97
Figure 4-65: Normalized angularly averaged radial velocity profiles along line 1 99
Figure 4-66: Normalized angularly averaged tangential velocity profiles along line 1 100

Figure 4-67: Normalized TKE snapshots on mid-plane inside the sliding mesh envelope. The rotor rotates in the anti-clockwise direction. 102
Figure 4-68: Normalized TKE contours at mid-plane outside the sliding mesh envelope. 103
Figure 4-69: Normalized TKE around the stator slot at various blade positions..... 104
Figure 4-70: Normalized TKE around the stator slot at various blade positions..... 105
Figure 4-71: Normalized TDR snapshots on mid-plane inside the sliding mesh envelope. The rotor rotates in the anti-clockwise direction. 106
Figure 4-72: Normalized TDR contours at mid-plane outside the sliding mesh envelope. 107
Figure 4-73: Normalized TDR around the stator slot at various blade positions 108
Figure 4-74: Normalized TDR around the stator slot at various blade positions 109
Figure 4-75: Definition of regions in the rotor stator mixer for turbulent dissipation rate comparison. 110
Figure 4-76: Normalized shear rate contours on mid-plane inside the sliding mesh envelope. The rotor rotates in the anti-clockwise direction. 111
Figure 4-77: Normalized mean shear rate contours at mid-plane outside the sliding mesh envelope. 112
Figure 4-78: Normalized mean shear rate around the stator slot at various blade positions (4000 rpm). The rotor rotates in the anti-clockwise direction. 113
Figure 4-79: Normalized mean shear rate around the stator slot at various blade positions (6000 rpm). The rotor rotates in the anti-clockwise direction. 114
Figure 4-80: Particle tracking at 4000 rpm colored by mean shear rate. 117

Figure 4-81: Particle tracking at 6000 rpm colored by mean shear rate. 118
Figure 4-82: The regions focused on in PIV experiments superimposed on the CFD results. 121
Figure 4-83: Vector fields of RANS simulation and PIV in region 1. 123
Figure 4-84: Vector fields of RANS simulation and PIV in region 2. 124
Figure 4-85: Vector fields of RANS simulation and PIV in region 3. 125
Figure 5-1: Silverson Inline Lab Scale L4R Rotor Stator Mixer. 128
Figure 5-2: Silverson L4R batch rotor-stator mixer geometry. 129
Figure 5-3: Silverson Inline Pilot Scale 450LS Rotor Stator Mixer. 129
Figure 5-4: Silverson L4R batch rotor-stator mixer geometry. 130
Figure 5-5: Rotating and fixed mesh on the mid-plane of Silverson inline L4R mixer. 134
Figure 5-6: Mesh of Silverson inline L4R mixer. 135
Figure 5-7: Rotating and fixed mesh on the mid-plane of Silverson inline 450LS mixer. 136
Figure 5-8: Mesh of Silverson inline 450LS mixer. 137
Figure 5-9: Rotating and fixed mesh on the mid-plane of Silverson inline 600LS mixer. 138
Figure 5-10: Mesh of Silverson inline 450LS mixer. 139
Figure 5-11: Histgram of the skewness of Silverson L4R mixer. 140
Figure 5-12: Histgram of the skewness of Silverson 450LS mixer. 140
Figure 5-13 Histgram of the skewness of Silverson 600LS mixer. 141
Figure 5-14: Experimental flow rate of Silverson inline L4R rotor-stator mixer. 145

Figure 5-15: Experimental power number data of Silverson inline L4R rotor-stator mixer[9]. 146
Figure 5-16: The coordinate on the mid-plane of Silverson inline rotor-stator mixers. The tangential coordinate of Line 1 is from -8.1˚to 0˚ in the L4R mixer, from-2.4˚ to 0˚ in the 450LS mixer and from -1.8˚ to 0˚ in the 600LS mixer..... 149
Figure 5-17: Normalized velocity magnitude snapshots on mid-plane of Silverson inline L4R mixer at 4000 and 8000 rpm. 150
Figure 5-18: Normalized velocity magnitude snapshots at plane y = 0 in Silverson inline L4R rotor-stator mixer. 152
Figure 5-19: The z coordinate in the Silverson inline L4R rotor-stator mixer. 153
Figure 5-20: Normalized velocity magnitude vector plots at plane z = 23 mm 154
Figure 5-21: Normalized velocity magnitude vector plots at plane z = -9 mm 155
Figure 5-22: The monitored stator slot 1 on the mid-plane of Silverson inline L4R rotor-stator mixer 156
Figure 5-23: Position of the rotor blades relative to stator slot 1..... 156
Figure 5-24: Velocity vectors normalized by the rotor tip speed around the stator slot at various blade positions (4000 rpm)..... 157
Figure 5-25: Normalized velocity vectors normalized around the stator slot at various blade positions (8000 rpm). 158
Figure 5-26: Normalized angularly averaged radial velocity profiles along line 1 .. 159
Figure 5-27: Normalized angularly averaged tangential velocity profiles along line 1 160

Figure 5-28: Radial velocity profiles along line 1 (Figure 5-16) at 4000 rpm in the Silverson L4R inline mixer. The downstream edge of the stator tooth is at θ = 0º and upstream edge is at θ = -8º. 161
Figure 5-29: Radial velocity profiles along line 1 (Figure 5-16) at 8000 rpm in Silverson L4R inline mixer. The downstream edge of the stator tooth is at θ = 0º and upstream edge is at θ = -8º. 162
Figure 5-30: Line 2 monitored in the simulation. 163
Figure 5-31: Axial profiles of the Normalized angularly averaged radial and tangential velocity component along line 2 (Figure 5-30) at 4000 and 8000 rpm.... 164
Figure 5-32: Normalized velocity magnitude snapshots on mid-plane of the Silverson inline 450LS mixer at 2100 rpm. 165
Figure 5-33: Normalized velocity magnitude snapshots at plane y=0 in the Silverson inline 450LS rotor-stator mixer. 165
Figure 5-34: The z coordinate in Silverson inline 450LS rotor-stator mixer. 166
Figure 5-35: Normalized velocity magnitude vector plots at plane z = -34 mm 167
Figure 5-36: Normalized velocity magnitude vector plots at plane z = 62 mm 168
Figure 5-37: Position of the rotor blades relative to stator slot 1 in the 450LS mixer. 169
Figure 5-38: Normalized velocity vectors normalized around the stator slot at various blade positions (2100 rpm) in the 450LS mixer. 170
Figure 5-39: Normalized angularly averaged radial velocity profiles along line 1 .. 172
Figure 5-40: Normalized angularly averaged tangential velocity profiles along line 1 173

Figure 5-41: Normalized radial velocity profiles along line 1 (Figure 5-16) at 2100 rpm in Silverson inline 450LS mixer. The downstream edge of the stator slot is at θ = 0º and the upstream edge is at θ = -2.4º. 174
Figure 5-42: Line 2 monitored in the simulation. 175
Figure 5-43: Axial profiles of the normalized angularly averaged radial and tangential velocity component along line 2 (Figure 5-42) at 2100 rpm 176
Figure 5-44: Normalized velocity magnitude snapshots on mid-plane of Silverson inline 600LS mixer at 1575 rpm. 177
Figure 5-45: Normalized mean velocity vector snapshots at plane y = 0 in the Silverson inline 600LS rotor-stator mixer. 178
Figure 5-46: The z coordinate in Silverson inline 600LS rotor-stator mixer. 178
Figure 5-47: Normalized mean velocity vector plots at plane z = -37 mm 179
Figure 5-48: Normalized velocity magnitude vector plots at plane z = 55 mm 180
Figure 5-49: Position of the rotor blades relative to stator slot 1 in the 600LS mixer. 181
Figure 5-50: Normalized velocity vectors normalized around the stator slot at various blade positions (1575 rpm) in the 600LS mixer. 182
Figure 5-51: Normalized angularly averaged radial velocity profiles along line 1 (Figure 5-16) at 1575 rpm in the Silverson inline 600LS mixer. The downstream edge of the stator slot is at θ = 0º and the upstream edge is at θ = -1.8º. 183
Figure 5-52: Normalized angularly averaged radial mean velocity profiles along line 1 (Figure 5-25) at 1575 rpm in Silverson inline 600LS mixer. The downstream edge of the stator slot is at θ = 0º and the upstream edge is at θ = -1.8º. 184

Figure 5-53: Normalized radial mean velocity profiles along line 1 (Figure 5-16) at 1575 rpm in Silverson inline 600LS mixer. The downstream edge of the stator slot is at θ = 0º and the upstream edge is at θ = -1.8º. 185
Figure 5-54: Line 2 monitored in the simulation. 186
Figure 5-55: Axial profiles of the normalized angularly averaged mean radial and tangential velocity components along line 2 (Figure 5-54) at 1575 rpm 187
Figure 5-56: Normalized TKE contours at 4000 and 8000 rpm on the mid-plane of the Silverson inline L4R rotor-stator mixer. 189
Figure 5-57: Normalized TKE around the stator slot at various blade positions..... 191
Figure 5-58: Normalized TKE around the stator slot at various blade positions..... 192
Figure 5-59: Axial profiles of the normalized angularly averaged TKE along line 2 (Figure 5-30) at 4000 and 8000 rpm in the Silverson L4R inline mixer. 193
Figure 5-60: Normalized TDR contours at 4000 and 8000 rpm on the mid-plane of the Silverson inline L4R rotor-stator mixer. 194
Figure 5-61: Normalized TDR around the stator slot at various blade positions 195
Figure 5-62: Normalized TDR around the stator slot at various blade positions 196
Figure 5-63: Normalized TKE contours at 2100 rpm on the mid-plane of the Silverson inline 450LS rotor-stator mixer. 197
Figure 5-64: Normalized TKE around the stator slot at various blade positions..... 198
Figure 5-65: Axial profiles of the normalized angularly averaged TKE along line 2 (Figure 5-42) at 2100 rpm in the Silverson 450LS inline mixer..... 199
Figure 5-66: Normalized TDR contours at 2100 rpm on the mid-plane of the Silverson inline 450LS rotor-stator mixer. 200

Figure 5-67: Normalized TDR around the stator slot at various blade positions 201
Figure 5-68: Normalized TKE contours at 1575 rpm on the mid-plane of the Silverson inline 600LS rotor-stator mixer. 203
Figure 5-69: Normalized TKE around the stator slot at various blade positions..... 204
Figure 5-70: Axial profiles of the normalized angularly averaged TKE along line 2 (Figure 5-54) at 1575 rpm in the Silverson 600LS inline mixer..... 205
Figure 5-71: Normalized TDR contours at 1575 rpm on the mid-plane of the Silverson inline 600LS rotor-stator mixer. 206
Figure 5-72: Normalized TDR around the stator slot at various blade positions 207
Figure 5-73: Normalized mean deformation rate contours at 4000 and 8000 rpm on the mid-plane of the Silverson inline L4R rotor-stator mixer..... 210
Figure 5-74: Normalized mean deformation rate around the stator slot at various blade positions at 4000 rpm in the Silverson inline L4R mixer. 211
Figure 5-75: Normalized mean deformation rate around the stator slot at various blade positions at 8000 rpm in the Silverson inline L4R mixer. 212
Figure 5-76: Normalized mean deformation rate contours at 2100 rpm on the mid-plane of the Silverson inline 450LS rotor-stator mixer. 213
Figure 5-77: Normalized mean deformation rate around the stator slot at various blade positions at 2100 rpm in the Silverson inline 450LS mixer..... 214
Figure 5-78: : Normalized mean deformation rate contours at 1575 rpm on the mid-plane of the Silverson inline 600LS rotor-stator mixer. 215
Figure 5-79: Normalized mean deformation rate around the stator slot at various blade positionsat 1575 rpm in the Silverson inline 600LS mixer..... 216

Figure 5-80: Normalized mean velocity magnitude snapshots on the mid-plane of the Silverson inline 450LS mixer at 2100 rpm with a flow rate of 1.2 L/s. 218
Figure 5-81: Normalized mean velocity magnitude snapshots at plane y = 0 in the Silverson inline 450LS rotor-stator mixer with a flow rate of 1.2 L/s..... 218
Figure 5-82: Normalized mean velocity vectors near the stator slot at various blade positions (2100 rpm) with a flow rate of 1.2 L/s. 219
Figure 5-83: Normalized TKE contours at 2100 rpm with a flow rate of 1.2 L/s on the mid-plane of Silverson inline 450LS rotor-stator mixer. 220
Figure 5-84: Normalized TKE around the stator slot at various blade positions..... 222
Figure 5-85: Normalized TDR contours at 2100 rpm with a flow rate of 1.2 L/s on the mid-plane of the Silverson inline 450LS rotor-stator mixer. 223
Figure 5-86: Normalized TDR near the stator slot at various blade positions..... 225
Figure 5-87: Normalized mean deformation rate field around the stator slot at various blade positions at 2100 rpm with a flow rate of 1.2 L/s 226
Figure 5-88: Normalized mean deformation rate near the stator slot at various blade positions at 2100 rpm with a flow rate of 1.2 L/s in the Silverson inline 450LS mixer. 227
Figure 6-1: The wet milling process experiment set up..... 231
Figure 6-2: Microscope camera arrangement[9]. 233
Figure 6-3: The flow rate measurement experiment set up 236
Figure 6-4: Flow rate in Silverson inline L4R mixer..... 237
Figure 6-5: Initial sucrose crystals before wet milling experiments. 239

Figure 6-6: Granulated sucrose crystals removed at different times at 4000 rpm in the Silverson inline L4R rotor-stator mixer. 240
Figure 6-7: Granulated sucrose crystal removed at different times at 6000 rpm in Silverson inline L4R rotor-stator mixer. 241
Figure 6-8: Granulated sucrose crystals removed at different times at 8000 rpm in the Silverson inline L4R rotor-stator mixer. 242
Figure 6-9: Granulated sucrose crystal size reduction with time at 4000, 6000 and 8000 rpm in Silverson inline L4R rotor-stator mixer. 243
Figure 6-10: The normalized PSD of initial granulated sucrose..... 244
Figure 6-11: The PDF of granulated sucrose at 4000 rpm..... 246
Figure 6-12: The PDF of granulated sucrose at 6000 rpm..... 248
Figure 6-13: The normalized PSD of granulated sucrose at 8000 rpm..... 250
Figure 6-14: Raw sucrose crystals removed at different times at 4000 rpm in the Silverson inline L4R rotor-stator mixer. 251
Figure 6-15: Raw sucrose crystals removed at different times at 6000 rpm in the Silverson inline L4R rotor-stator mixer. 252
Figure 6-16: Granulated sucrose crystals removed at different times at 6000 rpm in the Silverson inline L4R rotor-stator mixer. 253
Figure 6-17: Raw sucrose crystal size reduction with time at 4000, 6000 and 8000 rpm in Silverson inline L4R rotor-stator mixer. 254
Figure 6-18: The PDF of initial raw sucrose 255
Figure 6-19: The PDF of raw sucrose at 4000 rpm. 258
Figure 6-20: The PDF of raw sucrose at 6000 rpm. 260

Figure 6-21: The PDF of raw sucrose at 8000 rpm. 262
Figure 6-22: Granulated sucrose crystals removed at different times at 5.3 L/min, 8000 rpm in the Silverson inline L4R rotor-stator mixer. 263
Figure 6-23: Granulated sucrose crystals removed at different times at 3.8 L/min, 8000 rpm in the Silverson inline L4R rotor-stator mixer. 264
Figure 6-24: Granulated sucrose crystal size reduction with time at 6.8, 5.3 and 3.8 L/min in Silverson inline L4R rotor-stator mixer (8000 rpm). 265
Figure 6-25: Initial mannitol crystals size before wet milling experiments 266
Figure 6-26: Plate shaped mannitol crystals removed at different times at 4000 rpm in the Silverson inline L4R rotor-stator mixer. 267
Figure 6-27: Plate shaped mannitol crystals removed at different times at 6000 rpm in the Silverson inline L4R rotor-stator mixer. 268
Figure 6-28: Plate shaped mannitol crystals removed at different times at 8000 rpm in the Silverson inline L4R rotor-stator mixer. 269
Figure 6-29: Plate shaped mannitol crystal size reduction with time at 4000, 6000 and 8000 rpm in the Silverson inline L4R rotor-stator mixer. 3rd dimension is 1/4 of the width. 271
Figure 6-30: Plate shaped mannitol crystal size reduction with time at 4000, 6000 and 8000 rpm in the Silverson inline L4R rotor-stator mixer. 3rd dimension is the width. 271
Figure 6-31: The PDF of initial plate shaped mannitol (3rd dimension is the width). 272

Figure 6-32: The PDF of plate shaped mannitol at 4000 rpm (3rd dimension is the width). 274
Figure 6-33: The PDF of plate shaped mannitol at 6000 rpm (3rd dimension is the width). 276
Figure 6-34: The PDF of plate shaped mannitol at 8000 rpm (3rd dimension is the width). 278
Figure 6-35: The PDF of initial plate shaped mannitol (3rd dimension is 1/4 of the width). 279
Figure 6-36: The PDF of plate shaped mannitol at 4000 rpm (3rd dimension is 1/4 of the width). 281
Figure 6-37: The PDF of plate shaped mannitol at 6000 rpm (3rd dimension is 1/4 of the width). 283
Figure 6-38: The PDF of plate shaped mannitol at 4000 rpm (3rd dimension is 1/4 of the width). 285
Figure 6-39: Needle shaped mannitol crystals removed at different times at 4000 rpm in the Silverson inline L4R rotor-stator mixer. 286
Figure 6-40: Needle shaped mannitol crystals removed at different times at 6000 rpm in the Silverson inline L4R rotor-stator mixer. 287
Figure 6-41: Needle shaped mannitol crystals removed at different times at 8000 rpm in the Silverson inline L4R rotor-stator mixer. 288
Figure 6-42: Needle shape mannitol crystal size reduction with time at 4000, 6000 and 8000 rpm in Silverson inline L4R rotor-stator mixer 289
Figure 6-43: The PDF of initial needle shaped mannitol. 289

Figure 6-44: The PDF of needle mannitol at 4000 rpm. 291

Figure 6-45: The PDF of needle mannitol at 6000 rpm. 293

Figure 6-46: The PDF of needle mannitol at 8000 rpm. 295

Chapter 1: Introduction

1.1. Motivation and purpose

Rotor-stator mixers are widely used in many industries to perform high demanding mixing operations. In these mixers, a large amount of the power is dissipated in a small volume close to the mixing head. Because of their power dissipation characteristics, rotor-stator mixers are widely applied for wet milling of crystals, dispersion, emulsification, particle breakage, and so on[1] (Calabrese 2001). Despite widespread use of high shear rotor-stator mixers in chemical process industries, there is a noticeable lack of the fundamental knowledge on how to design or assess rotor-stator mixers[2]. There are few papers on the turbulent flow field generated by rotor-stator mixer and how this flow field influences process scale-up and product quality.

With the rapid development of computer and computation technology, computational fluid dynamics plays a more and more important role in chemical process design and evaluation. Computational fluid dynamics has been applied to simulate both laminar and turbulent flows in stirred tanks, and has shown promise in providing rational design decisions for stirred vessels in the chemical industries. As is the case with stirred tanks, it is desirable by CFD simulation to predict the macro properties, such as power number and flow number, and the effect of operating condition, such as rotation rate, fluid properties and rotor-stator geometry on the properties of flow field and the wet milling, mixing, reaction, and other processes occurring in rotor-stator mixers. If accurate CFD simulation can be performed, it may be used as a relatively

inexpensive tool, saving the significant time and cost involved in trial and error experiments in at least the initial step of process design and scale up. With the significant increase of computational resources recently, it is now affordable to perform accurate CFD simulations of high shear rotor-stator mixers.

The purpose of this research is to use CFD to provide guidance for scale up of crystal wet milling processes in high shear rotor stator mixers. Because the scale up process is very complicated, only certain aspects of this process will be investigated in this research. The basic criteria for scale up of high shear mixers is that the particles should experience an equal number of "high shear evants" in different scale mixers. Hence we will simulate the flow field of high shear mixers at 3 different scales and investigate the different conditions inside these mixers.

Currently, batch and inline mixers are used at laboratory scale and inline mixers are applied at pilot and plant scale as shown in Figure 1. First of all, the performance of a batch mixer will be discussed in the CFD simulation at bench scale. Then velocity fields and deformation fields of 3 inline mixers (Silverson L4R, 450LS and 600LS) will also be investigated. The simulation results at different scales will be compared and discussed, and then will be used to provide insight to the scale up process of Silverson rotor-stator mixers.

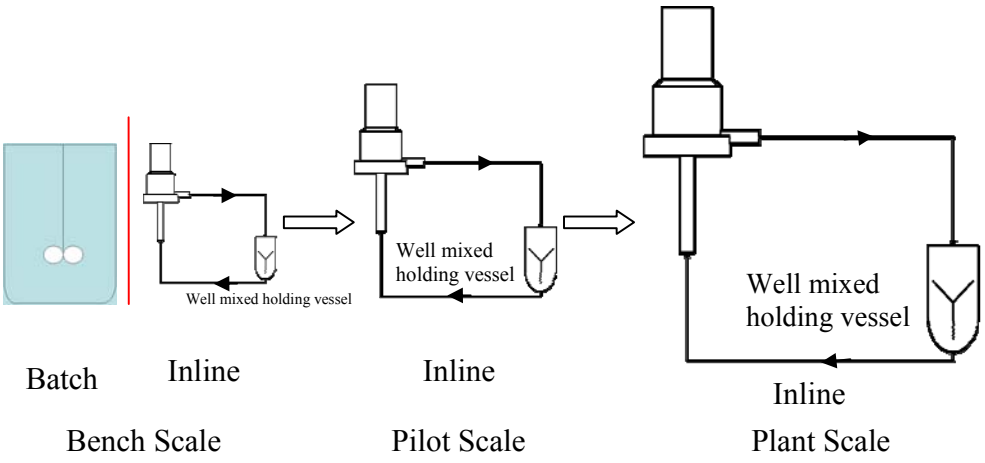

Figure 1-1: High shear mixers at bench, pilot and plant scale

In the pharmaceutical industries, high shear wet milling involving high shear rotor-stator mixers to reduce and control crystal size has advantages over the typical dry milling process. When an active pharmaceutical ingredient (API) is highly potent, dry milling methods, such as jet milling and mechanical milling, are not desirable due to the generation of finer crystals and the health risks to operators. Wet milling is also preferred as it accommodates higher yields and lower equipment costs compared with dry milling. In addition, large amounts of heat are generated during the dry milling process, which can affect the crystal morphology. In this research, bench scale wet milling studies will also be conducted and used to predict milling performance of high shear mixers at larger scales.

1.2. Thesis Synopsis

Thus far, a general picture of this research has been portrayed. The remainder topics covered in this dissertation are outline below:

- Chapter 2 presents a literature review of high shear rotor stator mixers, both experimental and numerical. Since stirred vessels are very similar to rotor-stator mixers, recent developments on stirred tank are also summarized.
- Chapter 3 describes the fundamental CFD theoretical equations and turbulence models along with wall functions used to arrive at a fluid flow solution. In addition, numerical schemes, frame of reference and convergence criteria are discussed.
- Chapter 4 covers the simulation of Silverson L4R batch rotor-stator mixer. It includes the mesh generation preprocess, mesh independence tests, the details of a novel hybrid technique and the analysis of the flow field.
- Chapter 5 covers the simulation of Silverson inline L4R (bench scale), 450LS (pilot scale) and 600LS (plant scale) mixers. The mesh used in the simulations is discussed. The flow fields in these 3 scales mixers are compared and discussed.
- Chapter 6 deals with the wet milling experiments in a Silverson L4R inline bench scale mixer. Selected crystals, solvent, experimental technique and results are discussed.
- Chapter 7 concludes with a summary of the main findings in this research. It is found that beside constant nominal shear rate, scale up of high shear mixers

may require an equal flow rate per slot and power per slot as well.

Recommendations for future research are addressed in this chapter.

Chapter 2: Literature Review

2.1 Review of Rotor-Stator Mixer Devices

Rotor-stator mixers have been extensively used in pharmaceutical, chemical, petrochemical, food and cosmetic industries because of their high-intensity and high-shear features. They are employed in many applications including homogenization, dispersion, emulsification, grinding, dissolving, chemical reaction, cell disruption and coagulation. They are mainly used in the production of latexes, adhesives, personal care and cleaning products, dispersions and micro dispersions of chemicals, and agricultural pesticide formulations[2]. A rotor-stator mixer can be used in either batch or inline operation. In the batch operation, a rotor-stator mixer is used as the mixing head in a closed tank system. In the inline operation, an input stream is continuously fed into the mixer and an output stream is pumped out of the mixer.

The typical feature of rotor-stator mixers is a high speed rotor close to a stationary stator. Generally the gap between the rotor and stator, known as shear gap, is from 100 to 3000 μm[3] and the typical rotor rotation rate is from 1000 to 10000 rpm. They are also called high shear mixers because the local energy dissipation rate and shear rate in these mixers are much higher than in a traditional stirred tank. The shear rate in these mixers range from 20000 to 100000 s^{-1} [2].

The rotor rotating at high speed accelerates the fluid tangentially in the rotor region. While fluid elements enter the gap between the rotor and stator, they experience a

very high shear which is orders of magnitude greater than in the traditional turbine stirred tank, and then they impinge onto the stator wall. Very intense localized turbulence, very high shear in the shear gap and the impingement on the stator wall are believed to be the reason that rotor-stator mixers are very efficient wet milling devices.

The emulsion droplet sizes in Hurrell type high shear mixers were investigated by J. T. Davies[4]. He concluded that drop break-up results from the turbulent fluctuation and shear is not responsible for droplet break-up when the viscosity ratio μ_d / μ_c was larger than 3.5[5] in Hurrell mill.

K. J. Myers et al.[6] discussed the use of high-shear mixers in mixing processes and they reported that there are three important shears; planar shear, elongation shear and the shear in the smallest eddies of turbulent flow, in mixing operations. The planar shear is generated in the narrow gap between the rotor and stator, and responsible for droplet and agglomerate break-up. The elongation shear occurs when the fluid is accelerated. It is very effective for droplet and agglomerate break-up when the viscosities for the mixing fluids differ significantly[5]. However, it is hard to estimate its magnitude in high shear mixers. The shear in the smallest eddies of turbulent flow only matters when the droplet size goes is of the order of the Kolmogorov scale.

Francis[7] investigated droplet break-up in a Ross ME 100 LC rotor-stator mixer with a slotted stator head and found that stator geometry is more significant than the gap

width between the rotor and stator in affecting the drop size distribution. When the gap width is doubled, the drop size is changed little. Phongikaroon[8] studied drop break-up in a Ross ME 100 LC rotor-stator mixer and Silverson L4R batch rotor-stator mixer with disintegrating and slotted stator head, and drew the conclusion that there are two breakage mechanisms for the drop break-up i.e., drop interaction with inertial subrange eddies and sub-Kolmogorov scale stresses.

Padron[9] measured the power number inside the Ross ME-100LC the Silverson LR4 and the Greerco XLR rotor-stator mixers and found the relation between power number and Reynolds number in these high shear mixers is similar to that in a stirred tank. In the laminar region, power number is inversely proportional to Reynolds number. In fully developed turbulent regime, it is almost constant. Also, he found that in turbulent regime, the power number is affected by the stator geometry, but the effect of the gap width between the rotor and stator is little.

Mortensen et al[10] investigated the flow field in a full scale, custom built, bottom-mounted, TPS rotor-stator mixer with water as the working fluid, by shaft torque and angularly resolved two dimensional PIV measurements. Measurements were performed at two rotor speeds, i.e., 333 and 1433 rpm, which corresponded to Reynolds numbers 2×10^5 and 8.5×10^5. They found that the flow filed is highly three dimensional. Both instantaneous and mean field were elucidated. High speed jets originating from stator slots are found. Circulation loops are formed in stator slots,

which make the bulk fluid back into the stator slots and further into the rotor region. The turbulent and deformation rate field were also discussed.

To the author's knowledge, despite the extensive application of rotor-stator mixers, scientific publications on these mixers are very scarce and the flow pattern, power data and other fundamental information is hardly found. There is a significant lack of knowledge on how to design and predict the performance of such mixers.

2.2 Review of CFD for Rotor-Stator Mixer and Stirred Tank

The first publication the author found involving CFD simulation of rotor-stator mixer is the work done by LeClaire[11]. He simulated the laminar flow field of a KADY Mill Model 4C rotor-stator mixer. It is two dimensional simulation and the working fluid is 5,000-cps liquid, with a specific gravity of 1.3, which is similar to a light paint. The tip speed of the rotor is 50 m/s. The boundary condition at the inlet of the rotor is pressure boundary condition and the gage pressure is 9 psi. LeClaire did not report the details about the simulation such as the geometry of the mixer, the mesh, boundary conditions, flow model being used and the reference frame. He reported that the high tip speed and the small clearance between rotor and stator resulted in significantly high shear rate. He showed that immediately after the rotor pass by a stator slot, part of the fluid exiting the rotor slot goes opposite to the direction of the rotor rotation.

Epee-Bounya[12] simulated an IKA rotor-stator mixer using commercial CFD software FLUENT. He performed this two dimensional simulation using a sliding mesh

reference frame. The rotor speed was 3000 rpm and the volumetric pumping rate was about 20 gallon per minute. The clearance between rotor and stator is 4 mm and the working fluid is water. In the simulation, the standard k-ε turbulence model, the RNG k-ε turbulence model and RSM model are applied and compared. The standard wall function is selected. He found that the results predicted by standard k-ε model are very similar to those predicted by the RNG model and RSM model. He also found than the fluid in the volute rotates opposite to the direction of rotor rotation. Epee-Bounya's work laid a solid foundation for the simulation of rotor-stator mixers by the sliding mesh method and the results are physically realistic.

Two dimensional CFD simulations of IKA in-line rotor-stator mixer were carried out by Kevala, etal[13]. Both a wide shear gap (4 mm) and standard shear gap (0.5 mm) IKA type inline rotor-stator mixer were investigated. The rotor speeds were 50 and 30 rps and the inlet flow rates were 78.8 and 45.4 gpm. The working fluid was water. The simulation was performed using commercial CFD software FLUENT and sliding mesh methods. The standard k-ε turbulence model was applied. Standard wall functions were used in the cells adjacent to walls in order to decrease the required computation time. In the case of standard shear gap, while the fluid impinged on the leading edge of stator teeth, jets are generated from the stator slots and part of fluid is circulated and re-entrained into stator slots. From the simulation results, Kevala also found that the shear in the gap was not a simple shear, but a turbulent shear flow. In the case of enlarged shear gap, the impingement of fluid on the leading edge of stator teeth is much weaker than in the standard gap, which leads to a much lower turbulent

kinetic energy. Therefore, although the shear in the gap does not contribute significantly to the dispersion process, a narrow gap will improve the mixing and dispersion process efficiency. He also conducted fixed frame LDA experiments to validate the simulation results. He found that CFD simulation results compared favorably with LDA results. However, The LDA data showed stronger jets and re-entrainment flows than predicted by CFD simulations.

Pacek et al[14] investigated the flow field inside a Silverson 4 LRT batch rotor-stator mixer at different rotor speeds. In this study, a fully three dimensional CFD simulation was employed using the sliding mesh method. The mixing head was placed in the center of the unbaffled mixing vessel and the clearance between rotor and stator was 0.175 mm. The rotor speed ranged from 2000 to 4000 rpm. The stator was a standard disintegrating head. The simulation was performed using commercial CFD software FLUENT. Unsteady solver is applied and QUICK discretization scheme and enhanced wall function were used in the simulation. Standard k-ε model was selected as the turbulence model. Based on the simulation, they investigated the flow pattern and turbulence energy dissipation rate distribution in the rotor-stator mixer. They calculated the power number and compared it with the experimental value. They ran the simulation for up to 20 revolutions, but they did not show if the whole flow field, especially far away from the mixing head in the bulk of the tank, reached convergence after 20 revolutions. In another work done by Pacek et al[15], they investigated the effect of stator geometry on the flow pattern and turbulence energy dissipation rate distribution in the rotor-stator mixer. They found that for different

shape and size of the holes in the stator, the flow pattern in the hole is very similar. They also found reversal of the flow in the bulk relative to the rotor rotation direction, which is consistent with previous findings. They ran the simulation up to 100 revolutions, but they still did not show if the whole flow field reached convergence. To date, the author knows only few publications involving CFD simulations of rotor-stator mixers. For the stirred tank, however, the literature on CFD applications is much more intensive. Both laminar flow and turbulent flow, steady state and transient phenomenon, two and three dimensional studies are all covered. Since stirred vessels are similar to rotor-stator mixers, the simulation of stirred tank is instructive to that of rotor-stator mixers.

Even though the flow field is highly transient in baffled stirred tank reactors, the earliest study on applying CFD in these mixers attempted to simulate the fixed frame flow by modeling the baffles as a momentum sink or pressure-induced drag and then solving the steady state equations. In the work of Harvey and Greaves[16], they simulated the turbulent flow field in a baffled, 6-blade impeller stirred tank using the k-ε turbulence model. The simulation was two dimensional. During the simulation, the impeller blades were treated as a "black box". The time averaged velocities in the outflow of the impeller were prescribed using velocity data from experiments and then the CFD solver calculated the flow in the rest of the tank. But there were no experimental data for the turbulence variable k and ε. They just selected arbitrary values for these quantities. The simulation results were qualitatively similar to the experimental results.

Sheng et al[17] simulated the flow field in a cylindrical stirred tank with baffles and validated their simulation results by Particle Image Velocimetry (PIV) experimental data. A 45° pitched turbine (PBT) axial impeller was used. The diameter and height of the stirred tank were 0.292 and 0.311 m respectively. The working fluid is water and the impeller was operated at 60 rpm resulting in a Reynolds number of 9200 based on the impeller diameter and tip velocity. In the CFD simulation, a body fitted curvilinear (BFC) cylindrical coordinate system was adopted and the simulations were performed in a fixed frame without considering the moving impeller blades. The effect of blades was accounted for by prescribing the boundary conditions just a little below the impeller using experimental data. The k-ε RNG turbulence model and more computational intensive RSM model were both used. The simulations were performed using commercial CFD software package FLUENT. In the work of Sheng, they studied the effect of impeller boundary conditions on the simulation results. The results revealed that the boundary condition settings have significant effect on the final prediction of the flow field. They also suggested that the widely accepted scale up rules, such as scaling by the impeller tip speed, may not be enough for predicting correct flow field. With correct boundary conditions, they can predict the mean velocity pattern pretty well. However, there were large deviations found between the simulations and experiments in high shear region, trailing vortex sweeping region and low Reynolds number swirling flow region. The k-ε RNG model can qualitatively predict the turbulence field. The simulations are satisfactory in the impeller region while in the flow discharge region, the turbulence field is under-predicted. The

authors also compared the results of the k-ε RNG model and RSM model. They found that the mean velocity fields predicted by the k-ε RNG model and RSM model are almost the same. The turbulence fields are under-predicted by both the k-ε RNG model and RSM model.

To this author's knowledge, the first publication about fully time dependent three-dimensional simulations of a baffled stirred tank was performed by Luo et al[18]. The flow field in a tank with four baffles attached to the vessel wall and a six blade pitched impeller was investigated. The standard k-ε model was used for turbulence model closure. In this work, the sliding mesh method was first applied to simulate a stirred tank. The whole flow field was divided into two separate zones which were stationary relative to their respective frames of reference. One zone was cylindrical expanding from the bottom of the vessel to the top and rotating with the impeller. The impeller was encompassed in this zone and the diameter of this zone is a little bit larger than that of the impeller. Another zone was the rest of the domain and was stationary. During the simulation, as the impeller and the inner mesh rotated incrementally, the momentum fluxes were interpolated across the interface between the inner and outer mesh. They ran the simulation up to 7 revolutions. The unsteady results from the simulations were averaged over time and compared to experimental LDA data from the literature. They found that the radial profile of axial velocity and circumferential velocity from the unsteady simulations compared well with the experimental data. But when they compared their results with steady state simulation results, there were large discrepancies. This indicates that for the investigation of

highly transient system, a fully unsteady simulation is preferred over a steady state simulation.

An assessment of CFD using the sliding mesh technique and validation by experimental LDA data was reported by Ng et al[19]. The flow field in a Rushton turbine mixer with four baffles attached to the mixer wall was investigated. The vessel was standard configuration cylinder with diameter 100 mm and the diameter of the Rushton turbine impeller was 33 mm. It was operated at 2165 rpm, resulting in the Reynolds number as 40,000 and a tip speed as 3.77 m/s. The working fluid was water. The three dimensional simulations were performed using commercial CFD code STAR-CD. Turbulence was modeled using the standard k-ε model and logarithmic wall functions were applied. Sliding mesh was used to account for the relative motion between the moving part and stationary part. Unstructured grids were used in the simulation in order to model complex geometries. Four grids with different densities, 46016, 102296, 138632, and 239468 cells, were generated for the simulations and determination of grid dependence. A Self-Filtered Central differencing scheme was employed in the simulations, which was a blended scheme involving a combination of second-order differencing and a first-order upwind differencing scheme and can remove any non-physical extremes automatically. A final periodic steady state was reached with twenty simulated revolutions. The authors observed that in the bulk of the tank, far away from the impeller, all four grids yielded essentially identical predictions, while close the impeller blades, in the region where steep gradients of velocity and turbulent energy existed near the impeller

blades, the coarse mesh showed poor performance. They concluded that grids near the impeller surfaces have to be fine enough to capture the steep gradient changes in this region. As with other work using similar turbulence models, excellent agreement was obtained when the mean velocity flow fields of the simulations were compared with those of experiments. Similar structures were observed for turbulent kinetic energy (TKE) contours, but the predicted TKE was underpredicted on the average by 50%.

In the work of Ng, seven possible sources for the discrepancies between CFD and LDA turbulent kinetic energy values were summarized: three from the LDA experimental method and four from the CFD turbulence model. The four more likely reasons for discrepancies in turbulent kinetic energy caused by CFD modeling were grid size, time step size, wall region treatment and the turbulence model. Ng observed that except for the coarsest mesh, grid refinements did not result in a significant improvement of the predicted velocities. It may be expected that if a denser mesh is used, slightly higher turbulence may be produced. However much more computation resources and time may be required. They suggested that more than a million cells might be necessary to produce CFD results close the measured data. Ng also found that when the time step size was decreased from 5° to 1°, the prediction of TKE was not improved significantly. The deviation could also stem from the turbulence model employed. The k-ε model assumes that the turbulent flow is isotropic. However, they found that in the periodic region the turbulence is anisotropic based on the three turbulent velocity component measurements. Therefore, the standard k-ε model may not be the appropriate turbulence model for all regions of flow, especially close to the

impeller blades. However, far away from the impeller, the isotropic assumption of the standard k-ε model seemed to hold well and was vindicated by the good agreement with the LDA data.

The last contributor to the possible error in CFD modeling is the simulation of flow close to the wall regions. The effects of wall boundaries are modeled using the wall function, which basically is an empirical relation. This relation requires that the distance of the first node adjacent to the wall be within the log-law region of the turbulent boundary layer so that the dimensionless quantity y+ is in the range 30-500. However, it is quite difficult to determine that y+ is within this range until a solution has been obtained. It is also difficult to ensure that this criterion is satisfied at all time steps in the simulations. Ng concluded that the sliding mesh conjunction with the standard k-ε model predicted the mean flow field accurately everywhere within the mixer, but the levels of turbulent kinetic energy near the blade tip were severely underpredicted.

Wei et al[20] investigated the flow field in a semibatch crystallizer and the effect of flow field on the precipitation process. The semibatch vessel was cylindrical of laboratory scale with diameter of 120 mm and had four vertical baffles. The fluid was agitated by a six blade Rushton turbine. Three impeller speeds, 150, 300 and 600 rpm were investigated, which corresponded to Reynolds numbers of 6,250, 12,500 and 25,000 respectively. This crystallizer was modeled by FLUENT. The three dimensional simulation was performed using the sliding mesh method in conjunction

with the k-ε RNG method. The whole domain was discretized by unstructured hexahedral cells. In the sliding mesh methods, the flow field was divided into two parts. The two cells rotated relative to each other during the simulations. The effects of impeller speed and feed location were discussed. The author observed that the effect of impeller speed on the final crystal size distribution (CSD) was very complicated. It was an interplay among three mechanisms, i.e., reaction, crystallization and mixing. They found that there was a critical value of the impeller speed. At this critical speed, the mean crystal size was a minimum. The author also found that the feed position influenced the crystal size significantly. Poor mixing at the feed position led to bigger particle size and wider range of crystal size.

Most recently, a new turbulence modeling method, Large Eddy Simulation (LES) has drawn a lot of attention. This model attempts to directly resolve large turbulent structures occurring in a flow and models those that are smaller than the computational grid size using a subgrid scale model. But LES requires an extremely fine mesh and much more computation resources. Derksen et al[21] is one of the earliest people applying LES to a stirred tank driven by a six-blade Rushton turbine. The mixer was operated at Reynolds number 29,000. The Navier-Stokes equations were discretized by a lattice-Boltzmann scheme and a force field technique for representing the action of the impeller on the fluid. A conventional Smagorinsky model with a Smagorinsky constant as 0.12 was used for the subgrid-scale modelling. The LES simulation results were compared to experimental data. Both the radial and axial mean velocities agreed well with the experimental data. The mean tangential

velocities were overpredicted by as much as 15% by the simulation. Unlike most of the Reynolds Average Navier-Stokes (RANS) simulations, the turbulent kinetic energy (TKE) was well predicted by the LES simulations. The vortex core paths were also predicted correctly. Since the kinetic energy was simulated accurately, the authors were confident about the simulated turbulent energy dissipation rate results. They investigated the distribution of turbulent energy dissipation rate in the mixer and found it was very inhomogeneously distributed throughout the mixing tank.

Murthy et al[22] assessed the standard k-ε and Reynolds Stress Model (RSM-RANS) turbulence models, and a LES model in a baffled stirred tank agitated by several different impellers. The tank was cylindrical with 4 baffles attached to the wall. Five impellers, disc turbine (DT), a variety of pitched blade down flow turbine impellers varying in blade angle (Standard PBTD60, 45 and 30) and hydrofoil (HF) impeller, were investigated. The impeller rotation speed was 4.5 rps resulting in Reynolds number as 45,000 and the working fluid was water. The simulations were performed using commercial CFD software package FLUENT. Hexahedral cells were used. The computational mesh was composed of 575,000 cells for the standard k-ε and RSM model. In the case of LES, 1,275,567 cells were used to satisfy the LES requirement. During the calculation, the second order implicit method was used for time discretization in all turbulence models. The second order central bounded difference scheme was used for spatial discretization in the case of LES and the second order upwind scheme for the standard k-ε and RSM model. They compared the simulation results to experimental data throughout the vessel and found that the LES model

performs well for predicting both the velocity field and turbulence field. Whereas, the standard k-ε model and RSM under estimate the turbulence kinetic energy significantly, especially in the region close to the impeller. RSM is able to capture all the mean flow characteristics correctly. But the standard k-ε model performs poorly to simulate the flow involving the strong swirl.

2.3 Review of wet milling in rotor-stator mixers

Although rotor-stator mixers are wide used in industry, publications on the wet milling process in these mixers are very scarce. To the author's knowledge, only two papers are found.

Lee et al[23] investigated milling of several APIs in a rotor-stator mixer. A lab scale rotor-stator wet mill was used and the rotor rotation speed ranged from 3,500 – 14,000 rpm. The solvent used was isopropyl acetate at 120-180 g/l. The solid APIs were milled under various conditions using recycle mode. Slurry samples were collected periodically to measure the particle size distribution (PSD) during milling and low angle laser light scattering was used to characterize the particle shape of the crystals. They found two regimes existing for the wet milling process. One is mass fracture regime, where particle size reduction is very sensitive to milling conditions such as tip speed and shear frequency. Another is attrition regime where particle size decreases very slowly and the milling rate is relatively insensitive to the milling conditions. They observed that the wet mill performance is relatively independent of slurrey concentration, shear gap width between the rotor and stator and flow rate when using the natural pumping of the mill. They also found that the profile of

particle size dependence on shear frequency is reproducible when wet mills at different scales are compared and suggested that the shear frequency was a practical and critical scale-up parameter. However, they did not illustrate the kind of rotor stator mixer they used and which APIs were under investigation.

Kamahara et al[24] investigated the generation of find particles in rotor-stator mixers during crystallization. They developed a semibatch crystallization process coupled with a high speed rotor-stator mixer. A recycle mode was employed. The tip speed of the rotor was 21.4 m/s. The particle size reduction during the operation was monitored by FBRM. They observed that the feed to recycle flow rate has no effect on the particle size. In their scale up studies, the rotor tip speed was selected as the scale up parameter and kept constant during scale up. They found that the particle size in the pilot scale process is identical to that in the laboratory scale. Whereas, the authors did not show which kind of rotor stator mixers they used and what crystals were selected.

Chapter 3: Computational Fluid Dynamics

The application of computers to fluid dynamics has led to the emergence of Computational Fluid Dynamics (CFD). With the significant increase of computational resources year by year, CFD plays a more and more important role in predicting the fluid flow under various situations. It has become an important tool in the chemical, pharmaceutical and other industries to assess process design, optimization, and scale-up. It reduces the attendant cost and contribute to our understanding of the major problem of scale-up. Problems in computational fluid dynamics are solved by generation of a structured or unstructured body-fitted grid around the modeled geometries. This grid is used to discretize the governing equations in space. The equations are then assembled into a non-linear system which is usually solved by iterative linearized numerical methods. This chapter will cover the governing equations, its solution and the turbulence models.

3.1 Continuity and momentum equations

For all flows, conservation equations for mass and momentum are solved to obtain the velocity field. The continuity equation prescribes the conservation of mass and can be written as follows

$$\frac{\partial \rho}{\partial t} + \nabla \bullet (\rho \vec{v}) = 0 \qquad (3.1.1)$$

where ρ is the density, ∇ is the divergence operator and $\vec{v}$ is the fluid velocity vector. For incompressible flow, the continuity equation reduces to

$$\nabla \bullet \vec{v} = 0 \qquad (3.1.2)$$

Conservation of momentum in an inertial (non-accelerating) reference frame is described by

$$\frac{\partial}{\partial t}(\rho\vec{v}) + \nabla\bullet(\rho\vec{v}\vec{v}) = -\nabla p + \nabla\bullet(\bar{\bar{\tau}}) + \rho\vec{g} \tag{3.1.3}$$

where p is pressure, $\bar{\bar{\tau}}$ is the stress tensor and $\rho\vec{g}$ is the gravitational body force. For Newtonian fluid, $\bar{\bar{\tau}}$ is given by Newton's law of viscosity as:

$$\bar{\bar{\tau}} = 2\mu\bar{\bar{S}} - \frac{2}{3}\mu\bar{\bar{\delta}}\nabla\bullet\vec{v} \tag{3.1.4}$$

where $\bar{\bar{S}}$ is the rate-of-strain tensor, $\bar{\bar{\delta}}$ is the identity tensor and μ is the viscosity of the fluid. $\bar{\bar{S}}$ is defined as the follows

$$\bar{\bar{S}} = \frac{1}{2}(\nabla\vec{v} + \nabla\vec{v}^{T}) \tag{3.1.5}$$

For the incompressible Newtonian flow, equation 3.1.3 reduces to

$$\rho\frac{\partial}{\partial t}(\vec{v}) + \rho\nabla\bullet(\vec{v}\vec{v}) = -\nabla p + \nabla^{2}\vec{v} + \rho\vec{g} \tag{3.1.6}$$

Ideally, any incompressible Newtonian flow can be solved directly by equation 3.1.2 and 3.1.6 and these equations are commonly known as Navier-Stokes equations. However, currently because of the limitation of computational resources, this method is only applied to low Reynolds number. The need to solve turbulent flows in engineering problems has led to the concept of time averaging these equations first and then solving the resulting system of equations for mean quantities, which was presented by Reynolds in 1895.

Reynolds Averaged Navier Stokes (RANS) equations are obtained by decomposing the instantaneous (exact) flow variables into the mean and fluctuating components. The decompositions of velocity and pressure are shown as the follows

$$U_i = \bar{U}_i + u_i \tag{3.1.7}$$

$$P = \bar{P} + p \tag{3.1.8}$$

where $\bar{U}_i$ and u_i are the mean and fluctuating component (i=1, 2, 3) respectively. Substituting these equations into the Navier-Stokes equations and averaging them gives the following results in index notation,

$$\frac{\partial U_i}{\partial x_i} = 0 \tag{3.1.9}$$

$$\rho\left(\frac{\partial \bar{U}_i}{\partial t} + \bar{U}_j \frac{\partial \bar{U}_i}{\partial x_j}\right) = -\frac{\partial \bar{P}}{\partial x_i} + \mu \nabla^2 \bar{U}_i - \rho \frac{\partial (\overline{u_i u_j})}{\partial x_j} \tag{3.1.10}$$

Equation 3.1.9 and 3.1.10 are called as Reynolds Averaged Navier Stokes (RANS) equations. Except for the last term, they are of the same form as the Navier-Stokes equations. The last term $-\rho\overline{u_i u_j}$ is referred as the Reynolds stress tensor and it generates an additional unknown that need to be specified in order for the system of equations to be fully closed. It represents the transfer of momentum due to turbulent fluctuations.

3.2 The k-ε model

Applying the Reynolds-averaged method to turbulence modeling requires that the Reynolds stresses be appropriately modeled. A most common method employs the Boussinesq hypothesis. One of the most significant contributions to turbulence modeling was made in 1877 by Boussinesq[25]. The Boussinesq hypothesis assumes that the turbulent stress is related linearly to the mean rate of strain, as in a laminar flow. The proportionality factor is the eddy viscosity. Unlike the molecular viscosity μ, the eddy viscosity does not represent any physical characteristic of the fluid. It is a function of the local flow conditions and is also strongly affected by flow history effects. Based on this hypothesis, equation 3.1.10 becomes

$$\rho(\frac{\partial \bar{U}_i}{\partial t} + \bar{U}_j \frac{\partial \bar{U}_i}{\partial x_j}) = -\frac{\partial \bar{P}}{\partial x_i} + (\mu + \mu_t)\nabla^2 \bar{U}_i \qquad (3.2.1)$$

The k-ε turbulence model is the most widely used two-equation eddy viscosity model. It is based on the solution of equations for the turbulent kinetic energy and the turbulent dissipation rate. Turbulent kinetic energy and its rate of dissipation are obtained from the solution to the following equations

$$\rho(\frac{\partial k}{\partial t} + \bar{U}_i \frac{\partial k}{\partial x_i}) = \frac{\partial}{\partial x_i}[(\mu + \frac{\mu_t}{\sigma_k})\frac{\partial k}{\partial x_i}] + G_k - \rho\varepsilon \qquad (3.2.2)$$

$$\rho(\frac{\partial \varepsilon}{\partial t} + \bar{U}_i \frac{\partial \varepsilon}{\partial x_i}) = \frac{\partial}{\partial x_i}[(\mu + \frac{\mu_t}{\sigma_\varepsilon})\frac{\partial \varepsilon}{\alpha x_i}] + C_{1\varepsilon}\frac{\varepsilon}{k}(G_k) - C_{2\varepsilon}\rho\frac{\varepsilon^2}{k} \qquad (3.2.3)$$

The first term on the right hand side of equation 3.2.2 is the transport of turbulent kinetic energy *k*. The second term, G_k, represents the generation of turbulence kinetic energy by mean velocity gradient and is given as follows

$$G_k = -\rho\overline{u_i u_j}\frac{\partial \bar{U}_j}{\partial x_i} \tag{3.2.4}$$

The third term is the dissipation rate of turbulent kinetic energy. The turbulent viscosity, μ_t, is computed from *k* and ε

$$\mu_t = \rho C_\mu \frac{k^2}{\varepsilon} \tag{3.2.5}$$

The model constant $C_{1\varepsilon}$, $C_{2\varepsilon}$, C_μ, σ_k and σ_ε are determined from experiments with air and water. They have the following values and have been found to work well for a wide range of flows.

$C_{1\varepsilon} = 1.44,\ C_{2\varepsilon} = 1.92,\ C_\mu = 0.09,\ \sigma_k = 1.0,\ \sigma_\varepsilon = 1.3$

The two equations and Reynolds Averaged Navier Stokes equations form a closed system of equations which can be used to calculate a flow field solution for the whole computational domain.

In this study, the FLUENT CFD code is used to simulate the flow. In FLUENT, there are three k-ε models available, i.e., standard, RNG and realizable k-ε model. Compared with the standard k-ε model, the RNG model is similar in form, but has several advantages: the RNG model improves the accuracy for rapidly strained flows; it enhances accuracy for swirling flows; the RNG theory provides an analytical method for turbulent Prandtl numbers; The RNG theory provides a formula accounting for low-Reynolds-number effects. The realizable k-ε model was developed recently and differs from the other k-ε model in two important ways: it has

a new formulation for the turbulent viscosity; and a new transport equation for the energy dissipation rate, ε, has been developed from an exact equation for the transport of the mean-square vorticity fluctuation. The term "realizable" means that the model satisfies certain mathematical constraints on the Reynolds stresses, which is consistent with the physics of turbulent flows. Neither the standard k-ε model nor the RNG k-ε model is realizable. An immediate benefit of the realizable k-ε model is that it can predict the spreading rate of both planar and round jets more accurately. It is also likely to provide superior performance for flows involving rotation, boundary layers under strong adverse pressure gradients, separation, and recirculation. In this work, the realizable k-ε model is applied in all of the simulations.

3.3 Wall functions

Turbulent flows are significantly affected by the presence of walls. Generally, the mean velocity field is affected by the no-slip condition that has to be satisfied at the wall. On the other hand, the turbulence is also affected by the presence of the wall in other ways. Very close to the wall, viscous damping reduces the tangential velocity fluctuations, while kinematic blocking reduces the normal fluctuations. Toward the outer part of the near-wall region, however, the turbulence is rapidly augmented by the production of turbulence kinetic energy due to the large gradients in mean velocity.

The near-wall treatment in the modeling significantly impacts the numerical solutions, since walls are the main source of mean vorticity and turbulence. In

addition, it is in the near-wall region that the variables have large gradients, and the momentum and other scalar transports change rapidly. Therefore, accurate representation of the flow in the near-wall region is very important to successfully predict wall-bounded turbulent flows.

A large number of experiments have shown that the wall region can be divided into three layers: a viscous sublayer, a buffer sublayer and a logarithmic sublayer or turbulent sublayer. In the viscous sublayer, the flow is laminar, and the (molecular) viscosity dominates. The mean velocity in the viscous layer depends linearly on the distance from the wall. In the turbulent layer, turbulence controls the flow and the mean velocity is characterized by a logarithmic law. In the buffer sublayer, both viscosity and turbulence affect the dynamics.

Wall functions are a set of semi-empirical relations used to predict the mean velocity and turbulence quantities close to the wall in turbulent flow. These relations define a boundary condition for the numerical solution of the closure equations at the first mesh point away from the wall. Standard wall functions and non-equilibrium wall functions are two widely used methods.

Standard wall function

In FLUENT, the value of a dimensionless wall unit y* is used to determine which wall function is selected. The definition of y* is given as follows

$$y^* = \frac{\rho C_\mu^{1/4} k_P^{1/2} y_p}{\mu} \tag{3.2.6}$$

where k_P is the turbulence kinetic energy at point P and y_P is the distance from point P to the wall.

In the viscous layer, y* < 11.225 and the dimensionless mean velocity is given by

$$U^* = y^* \tag{3.2.7}$$

where U^* is defined by

$$U^* = \frac{U_P C_\mu^{1/4} k_P^{1/2}}{\tau_w / \rho} \tag{3.2.8}$$

Where U_P is the mean velocity at point P and τ_w is the shear stress on the wall. When y* > 11.225, the law of wall for the mean velocity is given by

$$U^* = \frac{1}{k} \ln(Ey^*) \tag{3.2.9}$$

where k is the von Karman constant and it is 0.4187, and E is an empirical constant and is 9.793.

For turbulence properties, the value of k for the cells adjacent to the wall is obtained by integrating the kinetic equation all the way to the wall. The boundary condition for k imposed at the wall is

$$\frac{\partial k}{\partial n} = 0 \tag{3.2.10}$$

where n is unit vector normal to the wall. The local equilibrium hypothesis is applied in the wall-adjacent cells. Based on this assumption, the production of k and its dissipation rate ε are equal in these wall-adjacent cells. The production of k is computed by

$$G_k = \tau_w \frac{\partial U}{\partial y} = \tau_w \frac{\tau_w}{k\rho C_\mu^{1/4} k_P^{1/2} y_P} \tag{3.2.11}$$

and ε is calculated by

$$\varepsilon = \frac{C_\mu^{3/4} k_P^{3/2}}{k y_P} \tag{3.2.12}$$

The standard wall function is the default option in FLUENT. It has been widely used in many wall bounded flows and the results are satisfatory. But when the simulated situation departs far from the ideal conditions defined by the hypotheses, the standard wall function does not perform well. Especially when the flow close to the wall is subject to severe pressure gradients and the flow is in a significant non-equilibrium state, the results of the prediction are likely to be compromised. The non-equilibrium wall function provides another option to improve the results in such situations.

Non-equilibrium wall function

In addition to the standard wall function, the non-equilibrium wall function includes two major components: Launder and Spalding's log law is used when the mean velocity is sensitive to pressure gradient effects; and a two layer based concept is applied to calculate the budget of *k* in the wall-adjacent control volumes.

The log law for the mean velocity sensitive to pressure gradients is

$$\tilde{U} C_\mu^{1/4} \frac{k^{1/2}}{\tau_w / \rho} = \frac{1}{k} \ln(E \rho \frac{C_\mu^{1/4} k^{1/2} y}{\mu}) \tag{3.2.13}$$

where $\tilde{U}$ is defined by

$$\tilde{U} = U - \frac{1}{2}\frac{dp}{dx}[\frac{y_v}{\rho k\sqrt{k}}\ln(\frac{y}{y_v}) + \frac{y - y_v}{\rho k\sqrt{k}} + \frac{y_v^2}{\mu}] \tag{3.2.14}$$

y_v is the thickness of the viscous layer and is given by

$$y_v = \frac{\mu y_v^*}{\rho C_\mu^{1/4} k_P^{1/2}} \tag{3.2.15}$$

where y_v^* = 11.225. The cells adjacent to the wall consist of a viscous sublayer and a fully turbulent layer based on the two-layer concept. The assumptions for turbulence quantities are:

$$\tau_t = \begin{cases} 0, & y < y_v \\ \tau_w, & y > y_v \end{cases} \quad \mathrm{k} = \begin{cases} \left(\frac{y}{y_v}\right)^2 k_P, & y < y_v \\ k_P, & y > y_v \end{cases} \quad \varepsilon = \begin{cases} \frac{2\upsilon k}{y^2}, & y < y_v \\ \frac{k^{3/2}}{C_l^* y}, & y > y_v \end{cases} \tag{3.2.16}$$

where $C_l^* = kC_\mu^{-3/4}$. Using these profiles, the averaged production of k, $\overline{G}_k$ and the averaged dissipation rate $\overline{\varepsilon}$ can be computed by

$$\overline{G}_k = \frac{1}{y_n}\int_0^{y_n} \tau_t \frac{\partial U}{\partial y} dy = \frac{1}{k y_n}\frac{\tau_w^2}{\rho C_\mu^{1/4} k_P^{1/2}}\ln(\frac{y_n}{y_v}) \tag{3.2.17}$$

$$\overline{\varepsilon} = \frac{1}{y_n}\int_0^{y_n} \varepsilon dy = \frac{1}{y_n}[\frac{2\upsilon}{y_v} + \frac{k_P^{\frac{1}{2}}}{C_l^*}\ln(\frac{y_n}{y_v})]k_P \tag{3.2.18}$$

where y_n is the height of the cell.

Because the non-equilibrium wall functions can partly account for the effects of pressure gradients and departure from equilibrium, they are recommended for use in complicated flows involving separation, reattachment, and impingement where the

mean flow and turbulence are subjected to severe pressure gradients and change rapidly. In this work, non-equilibrium wall functions are applied in all simulations.

3.3 The numerical scheme

FLUENT applies the governing partial differential equations to the conservation of mass, momentum, energy and turbulence quantities such as turbulent kinetic energy, turbulent dissipation rate, etc. using a finite volume method. A segregated algorithm is used to solve the governing equations and the individual equations for various variables, such as velocity, pressure, turbulent kinetic energy and turbulent dissipation rate, are solved one after another. During this process, each governing equation is decoupled or segregated from each other, hence its name.

The finite volume technique consists of the following:

- Division of the whole computational domain into discrete control volumes.
- Integration of the governing equations on the control volumes to generate algebraic equation for the discrete variables.
- Solution of the discretized equations.

In the first step, the momentum equations are solved sequentially with current value of unknowns to create an updated value for the velocity field. If the continuity equation is not satisfied by the new velocity field, a Poisson-type pressure correction equation is solved to fulfill the continuity equation requirement. Equations for additional scalars, such as turbulent kinetic energy and turbulent dissipation rate, are

solved using the current values of the solution variables. A convergence check with a specified convergence criterion is performed at the end of the loop.

3.4 Discretization methods

The governing equations are integrated over each control volume using finite volume method and a series of discrete algebraic equations that express the conservation law on the control volumes are created. The discrete equations can be solved numerically.

Discretization of the governing equations can be illustrated by considering the unsteady conservation law of a scalar quantity ϕ in a control volume V:

$$\int_V \frac{\partial(\rho\phi)}{\partial t} dV + \oint \rho\phi\vec{U} \bullet d\vec{A} = \oint \Gamma_\phi \nabla\phi \bullet d\vec{A} + \int_V S_\phi dV \qquad (3.4.1)$$

where $\vec{U}$ is a velocity vector, $\vec{A}$ is a surface area vector, Γ_ϕ is the diffusion coefficient of ϕ and S_ϕ is the source of ϕ per unit volume. In the discrete domain, the integrals are represented by summations over the control volume and the above equation is discretized as follows:

$$\frac{\partial(\rho\phi)}{\partial t} V + \sum_f^N \rho_f \vec{U}_f \phi_f \bullet \vec{A}_f = \sum_f^N \Gamma_\phi \nabla\phi_f \bullet \vec{A}_f + S_\phi V \qquad (3.4.2)$$

where N is the number of faces enclosing a cell, ϕ_f is the convective quantity through face f, $\vec{A}_f$ is the area of face f and $\nabla\phi_f$ is the gradient of ϕ at face f. When the face value ϕ_f is evaluated, different discretization schemes can be selected since ϕ_f is only

stored at the center of the cell. In this work, first-order upwind and second-order upwind scheme are used.

When first-order accuracy is desired, it is assumed that the cell center value of any field variable represents a cell average value and hold for the entire cell. The face quantities are the same as the cell quantities. Therefore, the face value ϕ_f is equal to the cell center value of ϕ in the upstream cell (upwind cell). In the second-order scheme, the ϕ_f value at the face is computed using a truncated Taylor series expansion about the cell center and is given as follows:

$$\phi_f = \phi + \nabla\phi \bullet \vec{d} \tag{3.4.3}$$

where $\phi$and $\nabla\phi$ are the cell center value of the scalar and its gradient in the upstream cell, and $\vec{d}$ is the displacement vector from the upstream cell center to the face centroid. The scalar gradient, $\nabla\phi$, is computed from the discrete form of the divergence theorem as:

$$\nabla\phi = \frac{1}{V}\sum_f \tilde{\phi}_f \vec{A}_f \tag{3.4.4}$$

where ϕ_f is the value of ϕ computed from the arithmetic average of the values at the neighboring cell centers.

For transient simulations, such as in this work, the governing equations need to be discretitzed in both space and time. In the temporal discretization process, every term

in the governing equations is integrated over a time step Δt. A general expression for the time evolution of a variable ϕ is defined by:

$$\frac{\partial \phi}{\partial t} = F(\phi) \tag{3.4.5}$$

where F represents any discretization in space. Then the first-order temporal discretization is given by:

$$\frac{\phi^{n+1} - \phi^n}{\Delta t} = F(\phi) \tag{3.4.6}$$

and the second-order discretization is given by:

$$\frac{3\phi^{n+1} - 4\phi^n + \phi^{n-1}}{2\Delta t} = F(\phi) \tag{3.4.7}$$

where *n* is the value at current time step *t*, *n+1* is the value at next time step $t + \Delta t$ and *n-1* is the value at previous time step $t - \Delta t$. If ϕ on the right hand side of equation (3.4.6) is replaced with ϕ^{n+1}:

$$\frac{\phi^{n+1} - \phi^n}{\Delta t} = F(\phi^{n+1}) \tag{3.4.8}$$

then this equation is called as implicit integration. ϕ^{n+1} can be calculated by:

$$\phi^{n+1} = \phi^n + \Delta t F(\phi^{n+1}) \tag{3.4.9}$$

This implicit equation can be solved iteratively at every time step before moving to the next time step. The advantage of the fully implicit scheme is that it is unconditionally stable with respect to time step size.

The discretization method outlined above can be generalized and applied to discretize the continuity, momentum and turbulence equations. As mentioned before, the

governing equations are solved sequentially, so there has to be a relationship between the pressure and velocity to satisfy the continuity law. This relationship is called pressure-velocity coupling or pressure correction. Semi-Implicit Method for Pressure-Linked Equations (SIMPLE), SIMPLEC (SIMPLE-Consistent) and Pressure-Implicit with Splitting of Operators (PISO) schemes are three widely used pressure-velocity coupling algorithms. PISO pressure-velocity coupling scheme is one of the SIMPLE family of algorithms and is based on the higher degree of the relation between the corrections for pressure and velocity. Compared with SIMPLE and SIMPLEC algorithms, PISO is more efficient for transient simulations. The PISO algorithm takes more CPU time per solver iteration, but it can significantly decrease the number of iterations required for convergence, especially for transient problems.

3.5 Frames of reference

FLUENT solves the governing equations of fluid flow, by default, in a stationary (or inertial) reference frame. However, there are many problems where it is advantageous to solve the equations in a moving (or non-inertial) reference frame. These problems typically involve moving parts (such as rotating blades, impellers, and similar types of moving surfaces), and it is the flow around these moving parts that is of interest. Currently there are three widely applied methods, single rotating reference frame (SRF), multiple reference frame (MRF) and the sliding mesh method.

In the SRF method, the equations of fluid motion are solved in a frame of reference stationary relative to the rotor or impeller. The tank wall or stator then moves with

respect to this reference frame. The SRF method can be used in turbo-machinery and mixing tanks without baffles or where the stationary surfaces do not interact with the rotating part. In these cases, the solution of the resulting steady state equations will in principle yield a satisfactory solution. SRF is sometimes valid if the interaction between the stationary and moving walls is weak. For the class of problem where the rotating and non-rotating parts interaction is significant, the SRF method cannot render the problem steady by choosing a reference that rotates. Then two techniques are usually employed: multiple reference frame (MRF) and sliding mesh.

The multiple reference frame method (MRF) yields a satisfactory solution under the same conditions as the SRF method. In MRF, the fluid domain is divided into two or more regions. It is a steady-state approximation in which individual cell zones move at different rotational or translational speeds. The flow in each moving cell zone is solved using the moving reference frame equations. In the regions including rotating walls, the equations of motion are written and solved for a rotating frame of reference. In regions including stationary walls, the equations are written in a stationary frame of reference. At the interfaces between different cell zones, a local reference frame transformation is performed to enable flow variables in one zone to be used to calculate fluxes at the boundary of the adjacent zone. Although the MRF method is an approximation, it can provide a reasonable simulation of the flow for many applications in which the rotor-stator interaction is relatively weak. In some mixing tanks, for example, since the impeller-baffle interactions are relatively weak, large-scale transient effects are not present and the MRF model can be used. Another

potential use of the MRF model is to provide a flow field that can be used as an initial condition for a transient sliding mesh calculation. This eliminates the need for a startup computation. The MRF model should not be used, however, if it is necessary to actually simulate the transients that may occur in strong rotor-stator interactions. Then, the sliding mesh model should be employed.

When a time-accurate solution for rotor-stator interaction (rather than a angularly-averaged solution) is desired, the sliding mesh model is employed to compute the unsteady flow field. It is the most accurate and computationally intensive method. Sliding mesh simulations are fully transient. In this method, the computational domain is divided into two or more zones. Each cell zone is bounded by at least one interface zone where it meets the opposing cell zone. The interface zones of adjacent cell zones are associated with one another to form a grid interface pair. During the calculation, the cell zones move (i.e., rotate or translate) with respect to one another along the grid interface in discrete steps. At the end of each time step, the mesh attached to moving walls slides with the wall. In doing so, the interface pair between the stationary and moving mesh is broken and reformed. The interface itself must thus consist of non-conformal cells. Fluxes across the interface are computed by interpolation.

3.6 Convergence criteria

At the end of each solver iteration, the total residual for each of the conserved variables is computed and stored, thus recording the convergence history. The discretized governing equation of a scalar quantity ϕ is given by:

$$a_P \phi_P = \sum_{nb} a_{nb} \phi_{nb} + b \tag{3.6.1}$$

where a_P is the center coefficient, a_{nb} are the coefficient for the neighboring cells of cell *P* and *b* is the source term. The residual computed by FLUENT is the imbalance in Equation (3.6.1) summed over all the computational cells. This is called the "unscaled" residual and is defined as:

$$R^{\phi} = \sum_{All\ cells} \left| \sum_{nb} (a_{nb} \phi_{nb}) + b - a_P \phi_P \right| \tag{3.6.2}$$

Actually it is hard to judge convergence by evaluating the residuals defined by the above equation. The "scaled" residual is another option in FLUENT and it can be written as:

$$R^{\phi} = \frac{\sum_{All\ cells} \left| \sum_{nb} (a_{nb} \phi_{nb}) + b - a_P \phi_P \right|}{\sum_{All\ \text{cells}} \left| a_P \phi_P \right|} \tag{3.6.3}$$

The residual for the continuity equation is defined as:

$$R^{c} = \frac{\sum_{All\ \text{cells}} \left| Rate\ of\ mass\ \text{creation in cell P} \right|}{\sum_{All\ \text{cells}} \left| Rate\ of\ mass\ \text{creation iteration 5} \right|} \tag{3.6.4}$$

The denominator denotes the largest absolute value of the continuity residual in the first five iterations.

In this work, the convergence criterion is that all residuals are required to reach a value smaller than 10^{-6} before proceeding to the next time step.

Chapter 4: RANS Simulation of Silverson L4R Batch Rotor-Stator Mixer

This chapter contains the results of CFD simulations and validation of the flow field in Silverson batch rotor-stator mixer at 4000 and 6000 rpm. A mesh independence test was performed first to determine the suitable mesh size for the simulation. Then a hybrid technique is developed and discussed, which is believed to give a realistic converged flow field in reasonable time. Macroscopic properties are predicted based on the simulation results. The mean velocity field, turbulent field and deformation field are also predicted and discussed.

Solid particles are introduced into the simulated flow field in the batch rotor-stator mixer. The particle trajectories and shear history are predicted using a fast particle tracking model.

To validate the flow pattern in the mixer, PIV experiments were conducted on several vertical planes at 4000 rpm.

4.1 Geometry and flow conditions

The batch high shear mixer, Silverson L4R, investigated is shown as Figure 4-1 and several aspects of the simulated geometry are shown as Figure 4-2. The volume of the tank is 2 liters and the rotor is a 4 blade impeller of diameter 28.12 mm. The gap between the rotor and stator, where the highest shear rate exists, is 0.2 mm. The

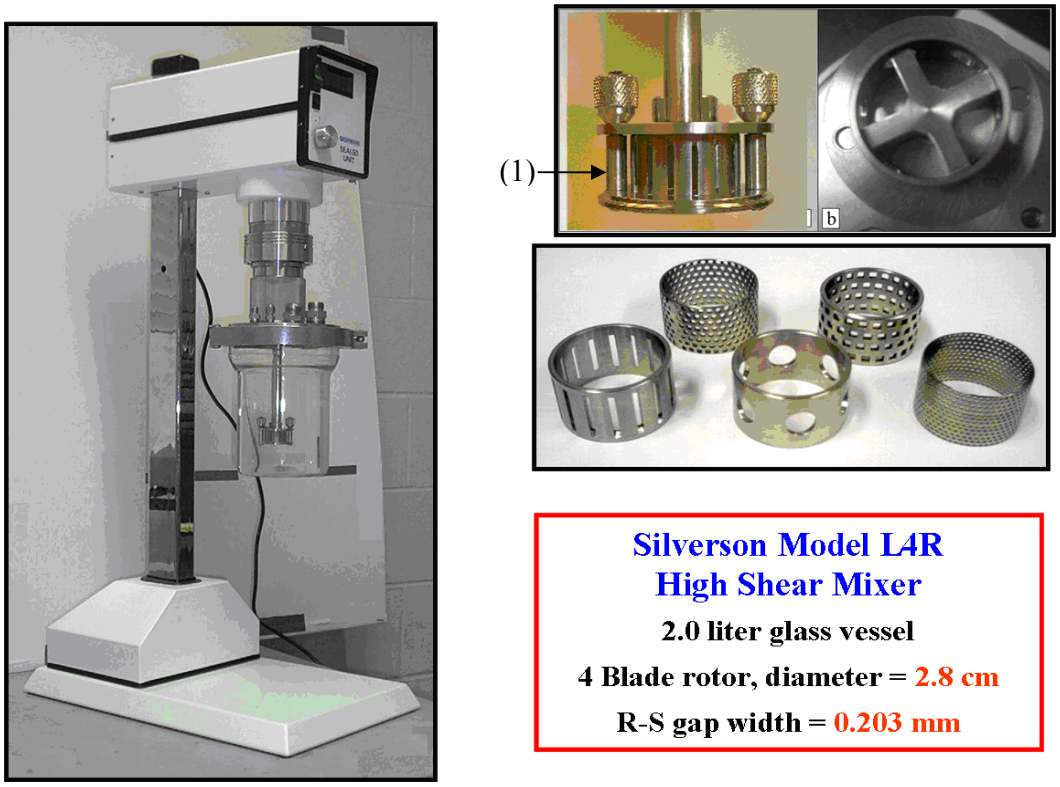

Figure 4-1: Silverson Batch Rotor Stator Mixer
(1) Vertical screws connecting the top and bottom plate to hold the stator.

slotted stator head (16 slots) was used in this study. Three struts (see Figure 4-2) connect the mill head to the top of the tank. The rotor rotates anticlockwise from the top view and the rotation speed can be varied from 4000 rpm to 8000 rpm. A Cartesian coordinate system is used to describe the geometry. The working fluid is water and its density and viscosity is 998.2 kg/m^3 and 0.0010 Pa·s, respectively. The z-axis coincides with the vertical axis of the shaft. The origin of the coordinate system is located at the top of the domain (vessel lid) and the positive z direction is upward.

4.2 Grid generation and CFD model settings

In order to perform a realistic CFD simulation, a good quality grid needs to be created. Grid generation is one of the most important and time consuming steps of

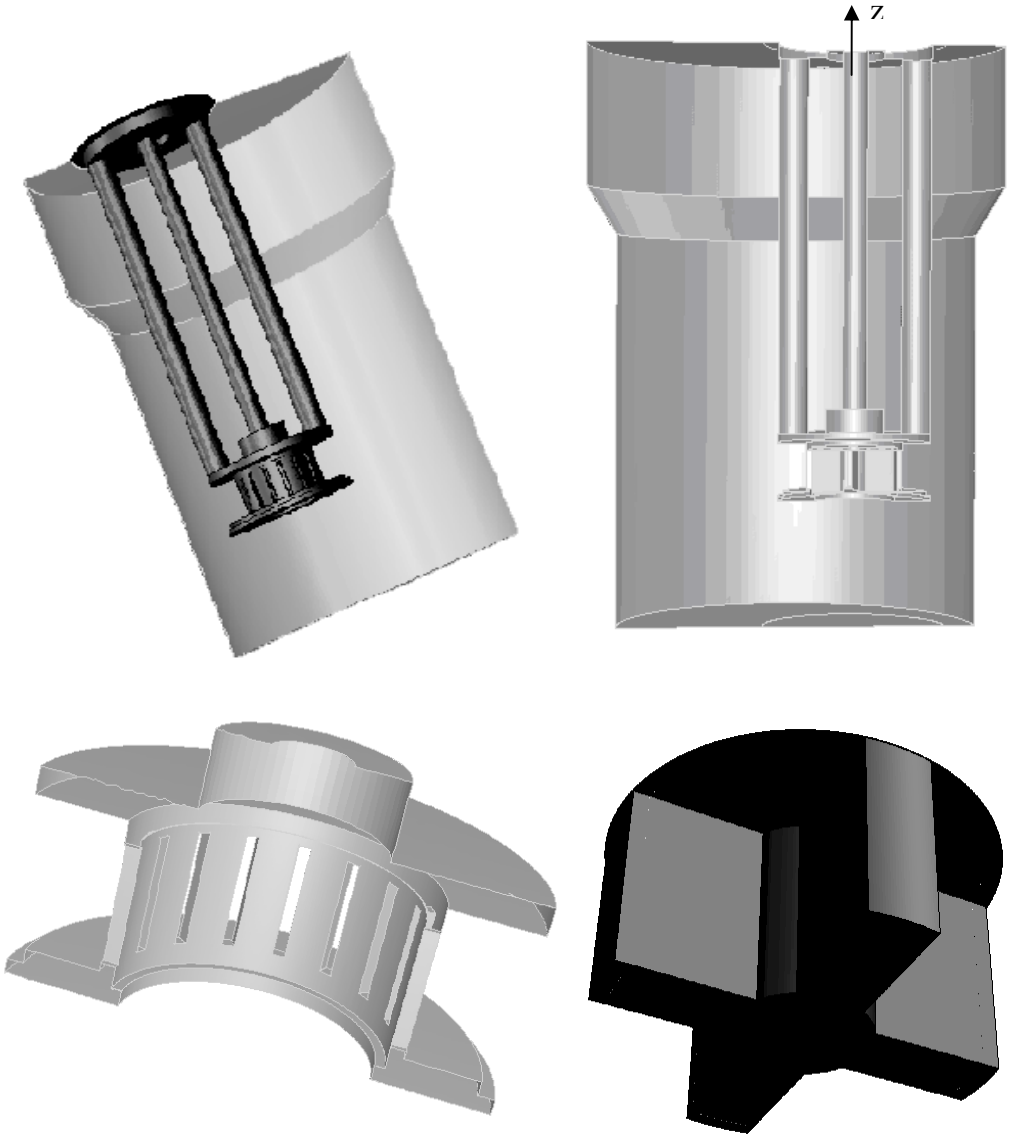

Figure 4-2: Silverson L4R batch rotor-stator mixer geometry.

any practical CFD simulation. The quality of the mesh determines the overall quality of the CFD analysis; therefore, caution must be taken when meshing the computation

domain. The grid generation for the Silverson L4R batch rotor-stator mixer is very challenging because of the complexity of the mixer geometry. The mixing head is off center so that any symmetry or periodic boundary cannot be used to simplify the mesh. A fully three dimensional mesh for the entire mixer has to be created. GAMBIT (mesh generation software) preprocessing is used to generate the hexahedral elements over the entire computation domain. Some mesh details are shown in Figure 4-3 and the meshes on the mid-plane of the mixing head are shown in Figure 4-4 and Figure 4-5. The interface is highlighted by a magenta color. The interface divides the whole domain into a stationary zone and a rotating zone. The high grid density within the rotor zone is evident. Figure 4-5 is a detailed view of the mesh close to the small tolerance between the rotor and stator. This tolerance is the smallest geometry scale in the rotor-stator mixer and the flow field here changes rapidly. Therefore, fine mesh is required in this region to capture the characteristic of the flow field.

The quality of the mesh is a very important aspect of any CFD simulation because the grid determines the stability of the numerical solution. One of the most important properties to evaluate the quality of the mesh is the skewness of the grid. A grid with Skewness smaller then 0.97 is considered to be acceptable. The skewness of the mesh in this work is shown as Figure 4-6. From this figure, it can be found that the quality of the generated grid is satisfactory.

In this work, all the simulations have been carried out using the commercially available software package FLUENT 6.3 at 4000 and 6000 rpm. The discretized form of the governing equations for each cell is obtained such that the conservation

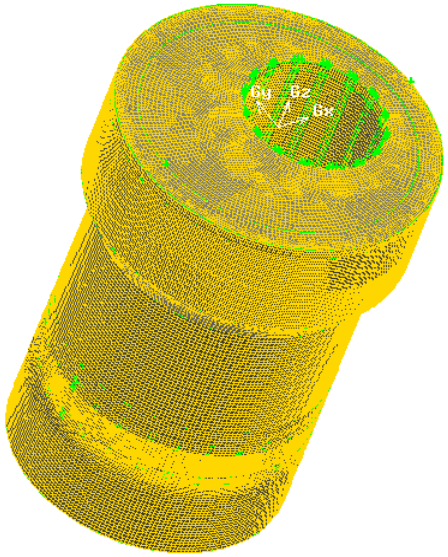

Mesh on outside walls

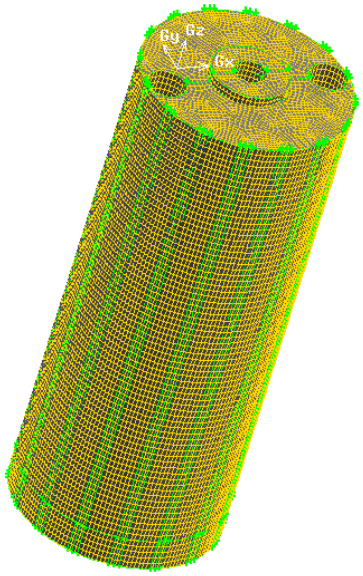

Mesh above the mixing head

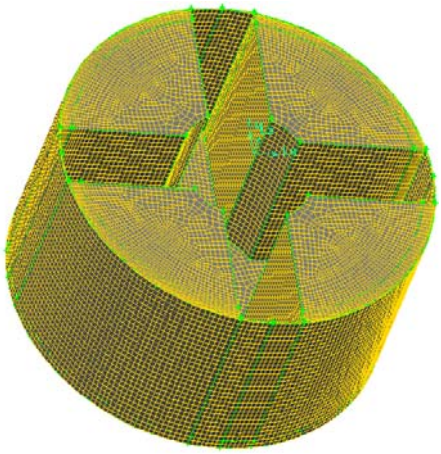

Mesh in the rotating zone

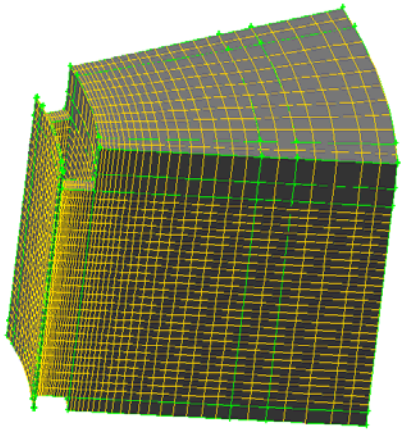

Mesh in one stator sector

Figure 4-3: Meshes for several parts of rotor stator mixer domain.

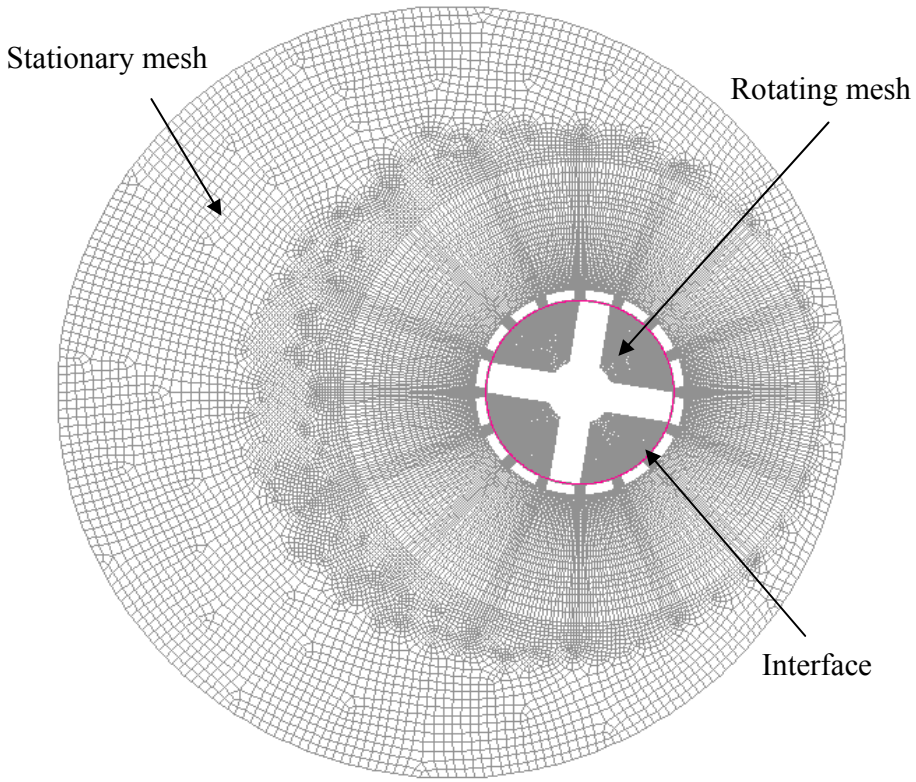

Figure 4-4: Rotating and fixed mesh on the mid-plane.

principles are satisfied on each cell. The second-order implicit scheme is used for time discretization in all the turbulence models. The major advantage of this kind of implicit time advancement method is that the time step size is not limited by stability reasons, i.e. CFL condition. This means that, contrary to explicit schemes, stability is ensured for any value of the time step size. In this way a small number of iterations are required to complete the simulation, which leads to a significant reduction in computation time. Further, the second-order upwind difference scheme was used for spatial discretization. All the discretized equations were solved in a segregated solver with the PISO algorithm. PISO involves one predictor step and two corrector steps

and may be considered as an extension of SIMPLE. PISO is a pressure–velocity coupling procedure developed originally for the non-iterative computation of unsteady compressible flows. Therefore, PISO has better performance in unsteady simulations than SIMPLE series algorithms. To improve the efficiency of this calculation, the PISO algorithm includes two additional corrections :neighbor correction and skewness correction.

FLUENT scales the residual using a scaling factor representative of the flow rate of variable throughout the domain. Standard model constants have been used for all the turbulence models. Realizable k-ε model is used to model the turbulence. The non-equilibrium wall functions are applied for the wall treatment because of the capability to partly account for the effects of pressure gradients and departure from equilibrium.

4.3 Mesh independence tests

In order to resolve the flow field, especially in the high shear region, an appropriate mesh cell number for the whole computation domain should be determined first. A mesh independence study is necessary to determine the appropriate mesh size for the whole geometry to completely resolve the average flow field. Therefore, three different mesh size are considered, i.e. 1.6, 1.7 and 4.2 million cells respectively (shown in Figure 4-7). In 1.7 million mesh, the mesh size in radial direction is decreased by twice relative to 1.6 million mesh.). In 4.2 million mesh, the mesh size in radial and tangential direction is decreased by twice relative to 1.6 million mesh In

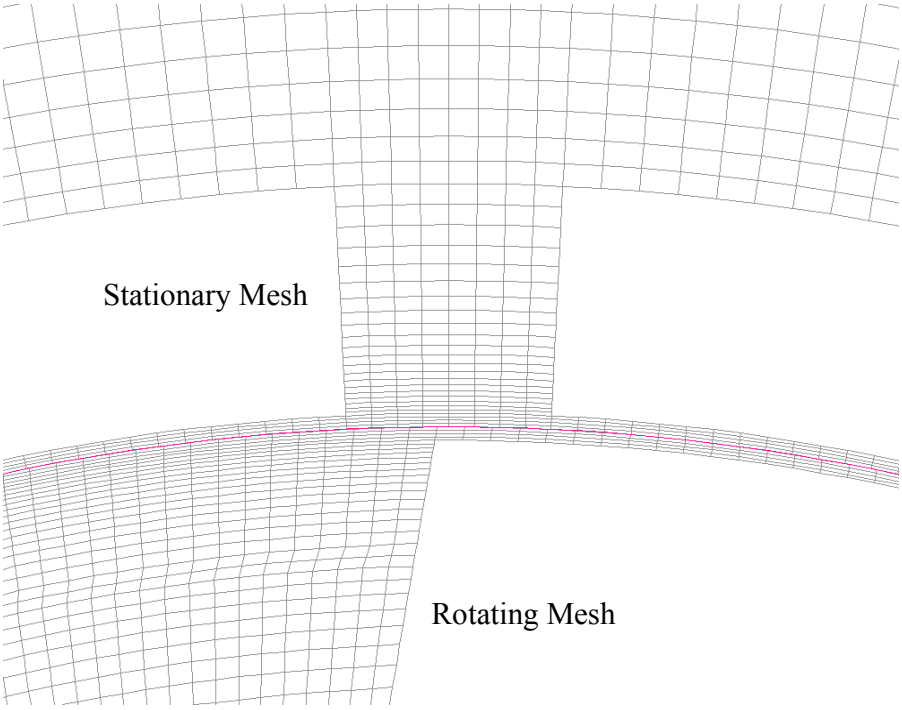

Figure 4-5: Magnified View of Rotating Mesh and Stationary Mesh.

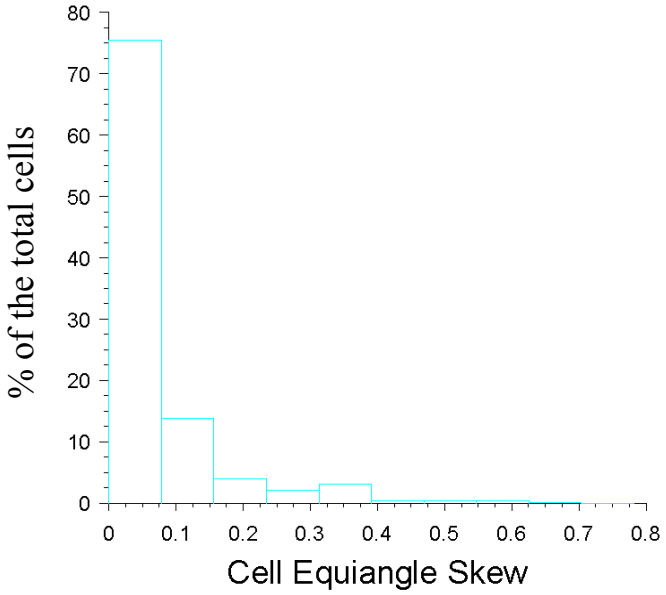

Figure 4-6: Histgram of the skewness.

Since a high shear region exists in the mid-plane, the results on this plane are compared (shown in Figure 4-8) using the sliding mesh after 2 revolution at 4000 rpm

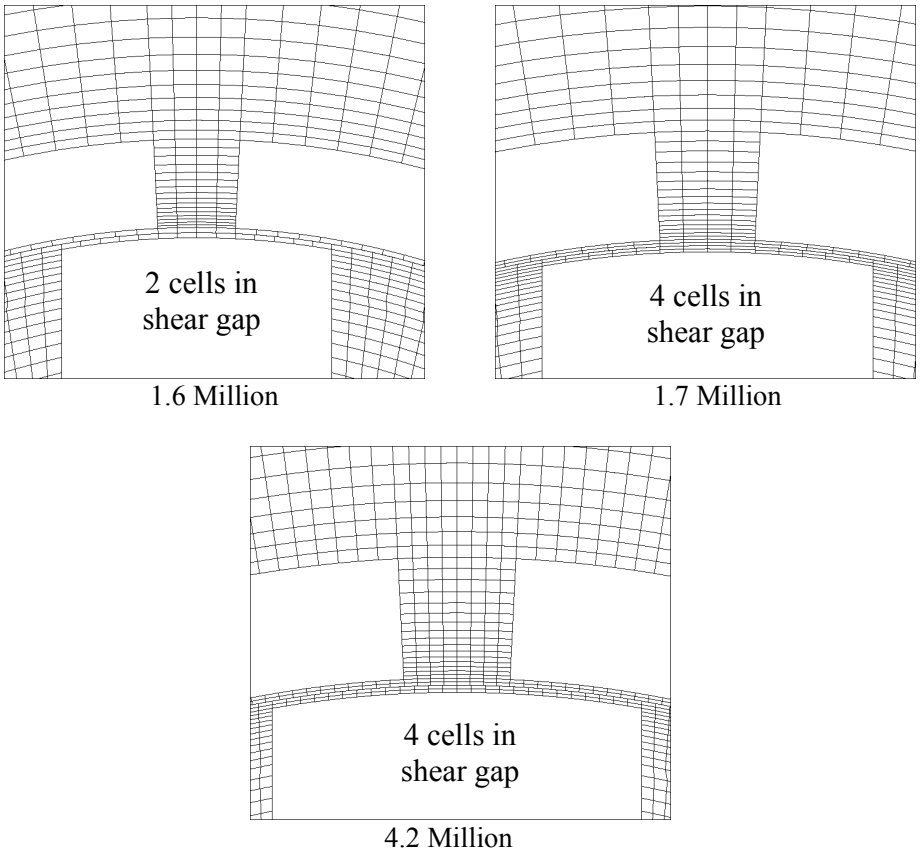

Figure 4-7: 3 meshes under investigation in mesh independence test.

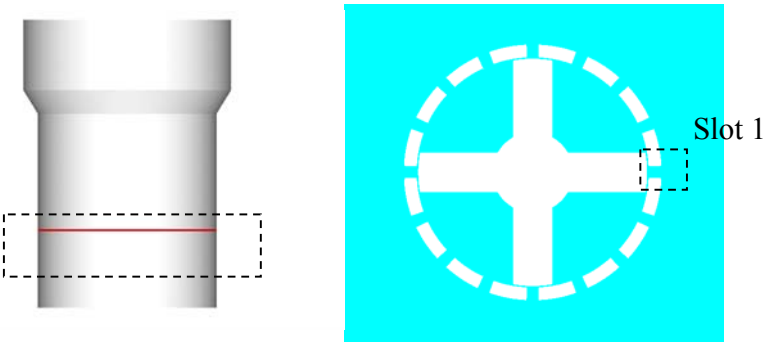

Figure 4-8: The monitored mid-plane and slot 1.

when slot 1 is fully closed, partially closed and fully open by the rotor blade. Velocity magnitude and turbulent kinetic energy are selected as the variables under investigation and are compared after two revolutions. The results are shown as the contours in Figure 4-9 and Figure 4-10.

From these contours, it is concluded that there is a significant change in the flow field with the increase of the mesh size from 1.6 to 4.2 million cells. Therefore 1.6 and 1.7 million cells mesh are not enough to perform the simulation. To determine whether 4.2 million mesh volumes are adequate, the adaptation function of Fluent is used to increase cells locally especially in the rotor zone and stator slots, which results in 5.6 million cells mesh. The adapted regions are highlighted by red color and shown in Figure 4-11. In addition, the adapted mesh on the mid-plane (shown in Figure 4-8) is shown in Figure 4-12. The comparison of velocity magnitude and turbulent kinetic energy between the 5.6 million mesh results and the 4.2 million mesh results are shown in Figure 4-13. These figures show that differences in the mean flow field and turbulent field between these two meshes are not significant.

The radial velocity along the line shown in Figure 4-14 (highlighted by red color) for different cell number meshes is given in Figure 4-15. From Figure 4-15, it can be found that there is big difference between 1.6 or 1.7 and 5.6 million cells. However, the difference between 4.2 and 5.6 million cells is very small so that it can be concluded that a 4.2 million cell mesh is enough to perform the simulations.

1.6m vs 1.7m 2 Revolutions
Stator slot 1 fully closed by rotor blade

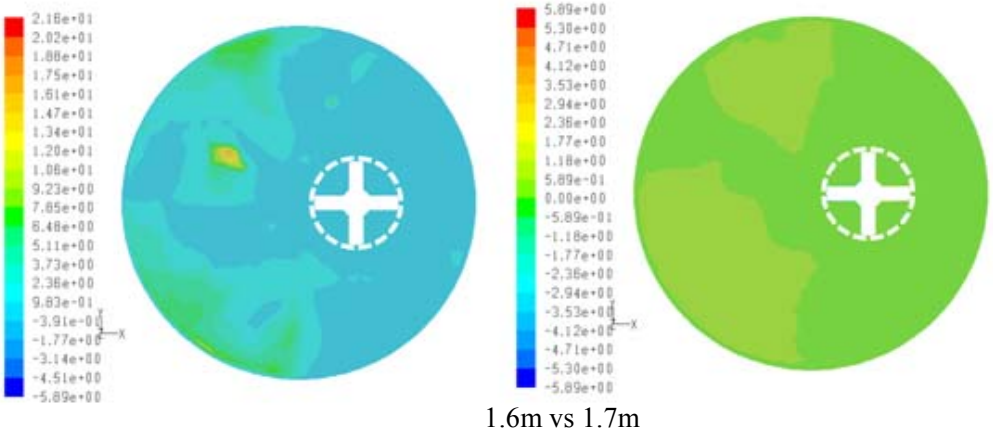

1.6m vs 1.7m
Stator slot 1 partially closed by rotor blade

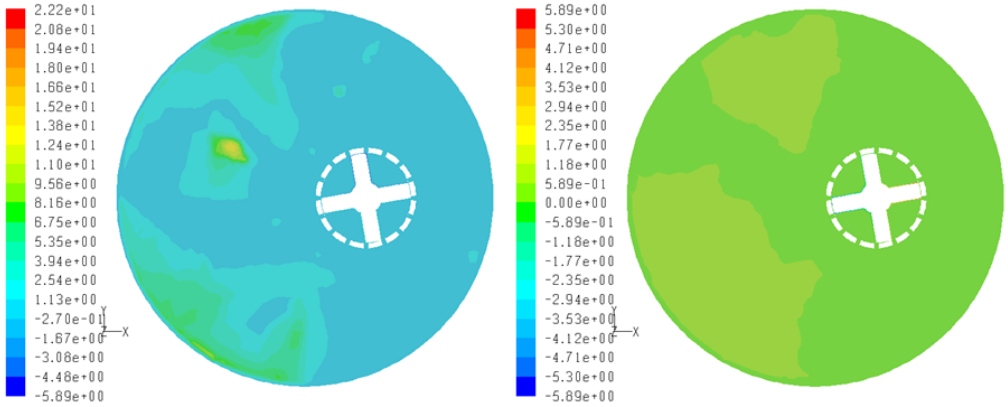

1.6m vs 1.7m
Stator slot 1 fully open

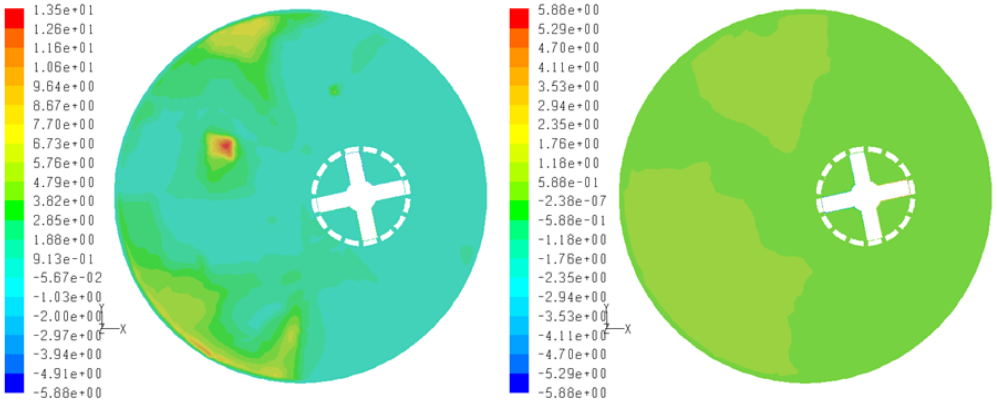

Relative difference in velocity magnitude
$(v_{1.7}-v_{1.6})/v_{1.7}\cdot 100$

Relative difference in turbulent kinetic energy
$(k_{1.7}-k_{1.6})/k_{1.7}\cdot 100$

Figure 4-9: Mesh independence test: 1.6 million and 1.7 million cells.

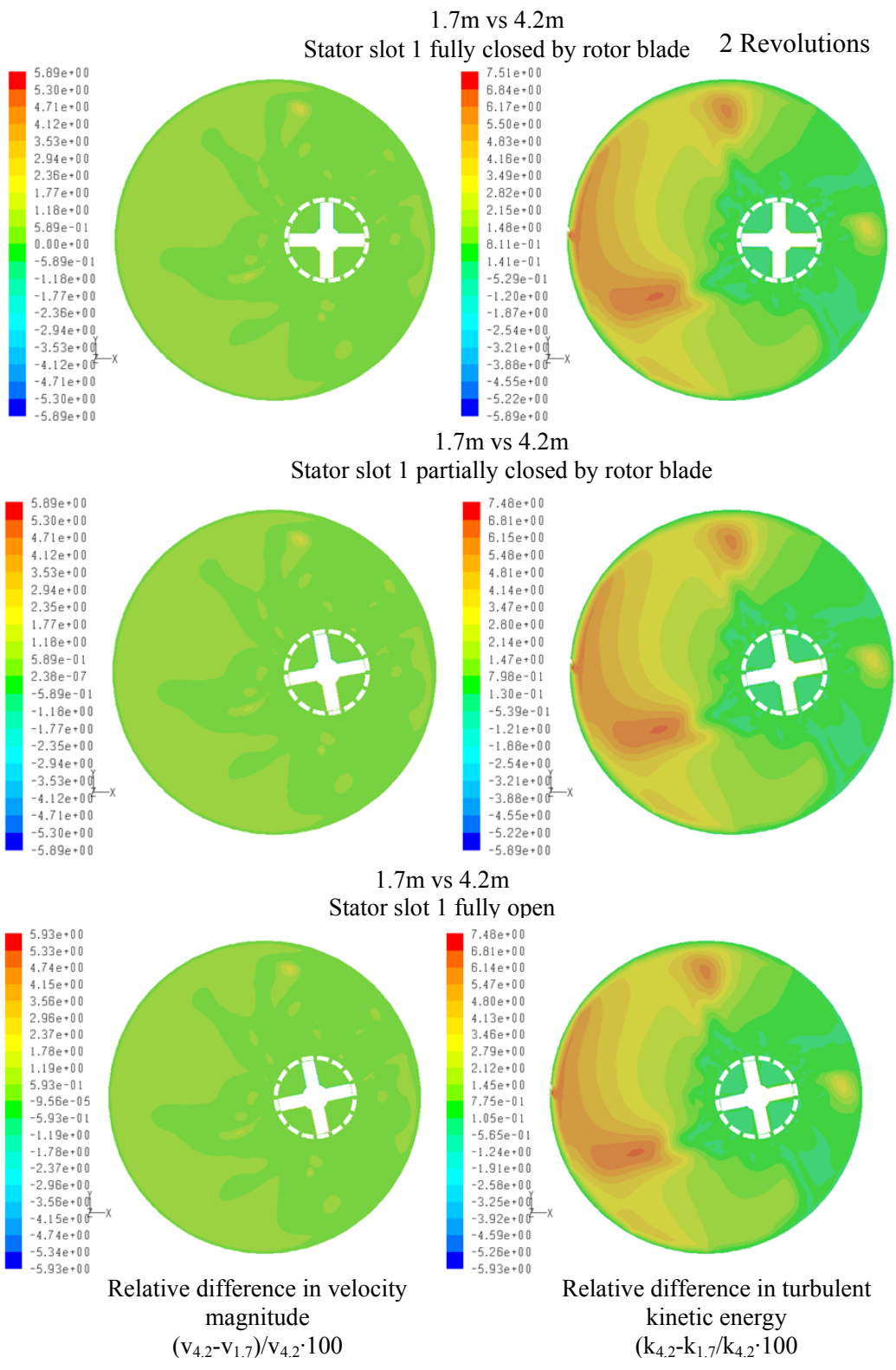

Figure 4-10: Mesh independence test: 1.7 million and 4.2 million cells.

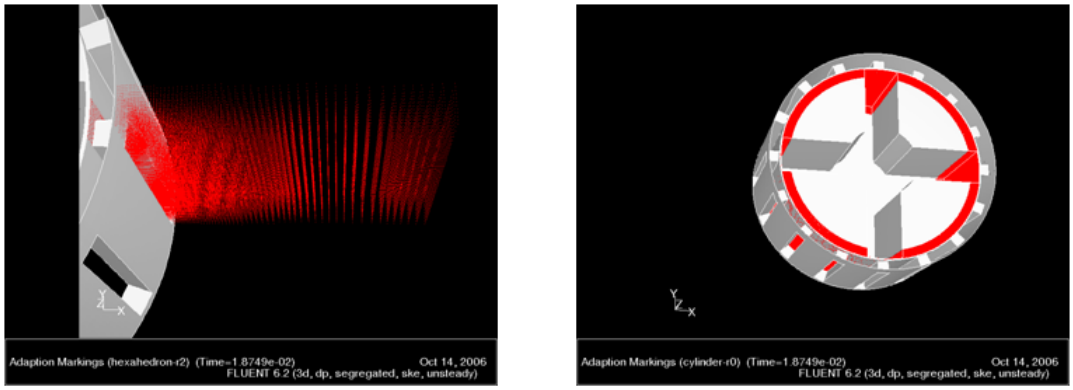

Figure 4-11: The adapted regions (highlighted by red color).

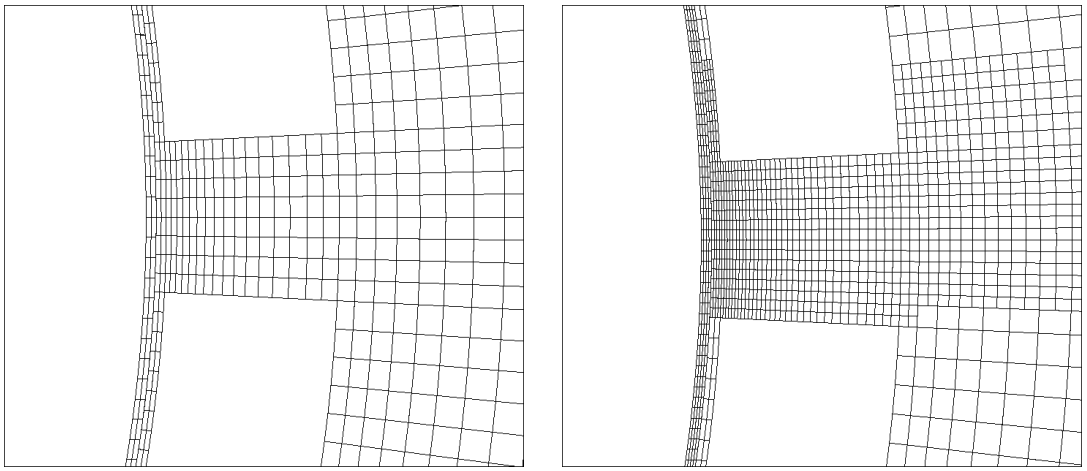

4.2 Million 5.6 Million

Figure 4-12: 4.2 million cells mesh and the adapted mesh on the mid-plane.

The macro scale properties, power and power number, are also compared between mesh with different cell number. The power, P, is calculated from[26] for the 1.6, 1.7, 4.6 and 5.6 million mesh:

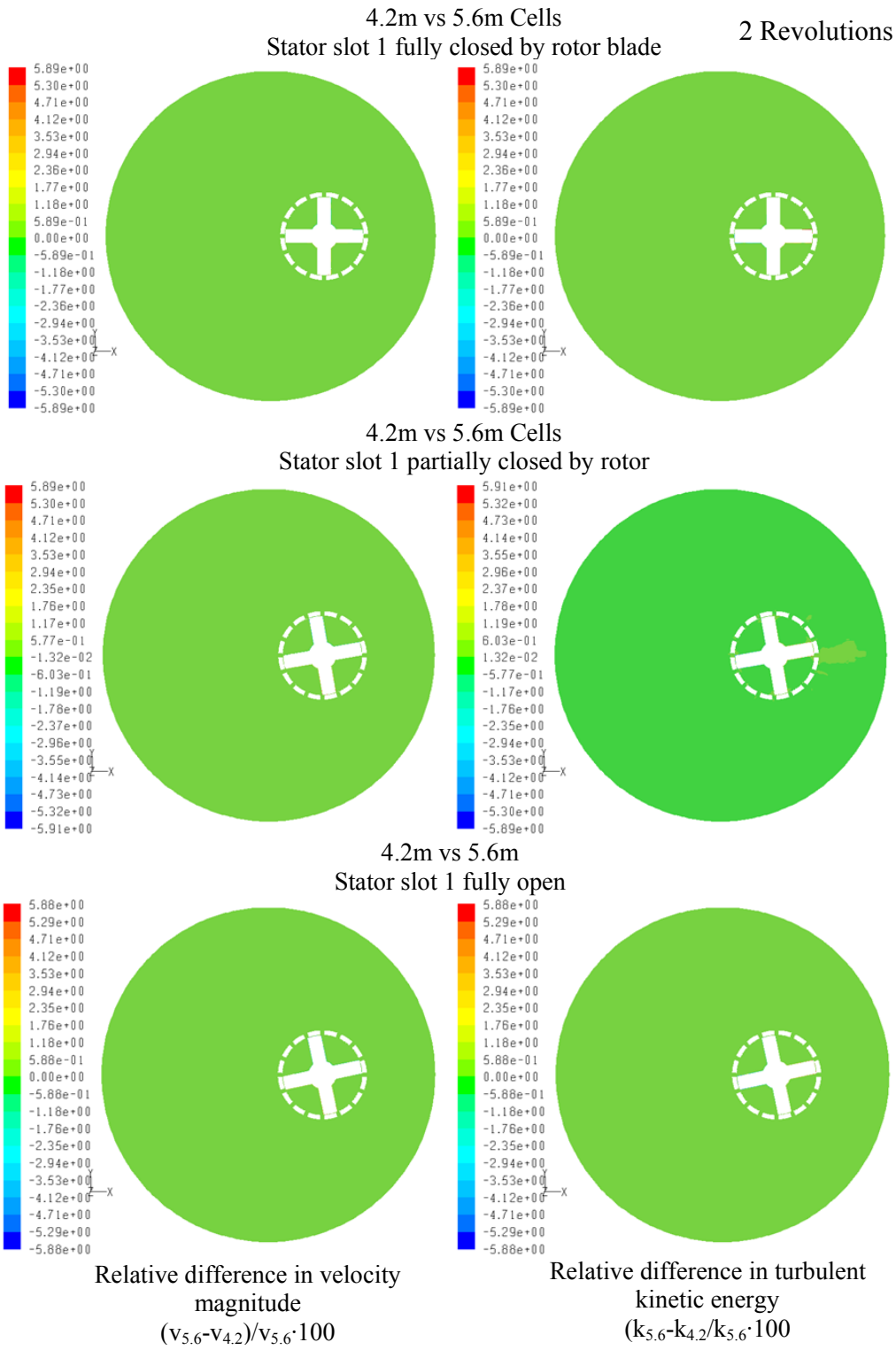

Figure 4-13: Mesh independence test: 5.6 million and 4.2 million cells.

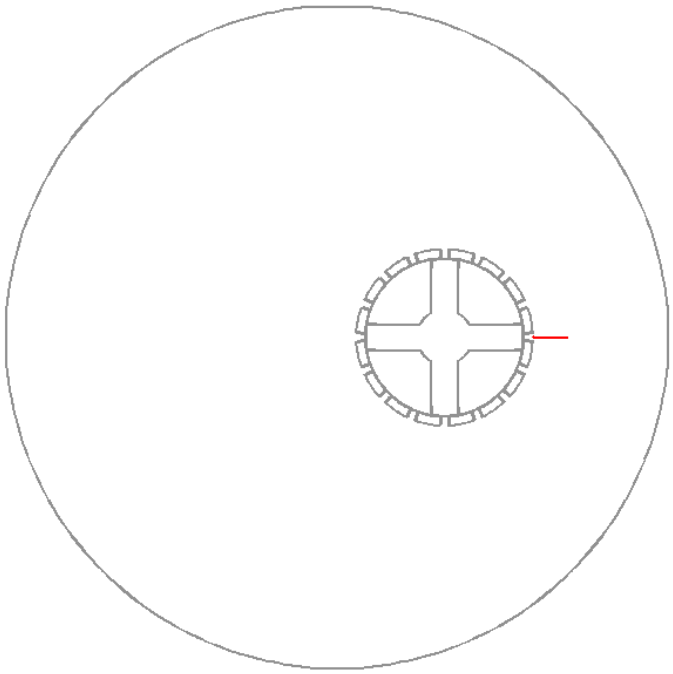

Figure 4-14: Monitored line in mesh independence test (highlighted by red color).

$$P = T \bullet \omega \tag{4.3.1}$$

where T is the torque exerted on the rotor from the center of rotation, ω is angular velocity of the rotor. The power number is defined by the relationship:

$$N_p = \frac{P}{N^3 D^5 \rho} \tag{4.3.2}$$

where P is power, D is the rotor diameter (0.02812m), and ρ is fluid density (998.2kg/m^3). The power numbers are shown as Table 4-1.

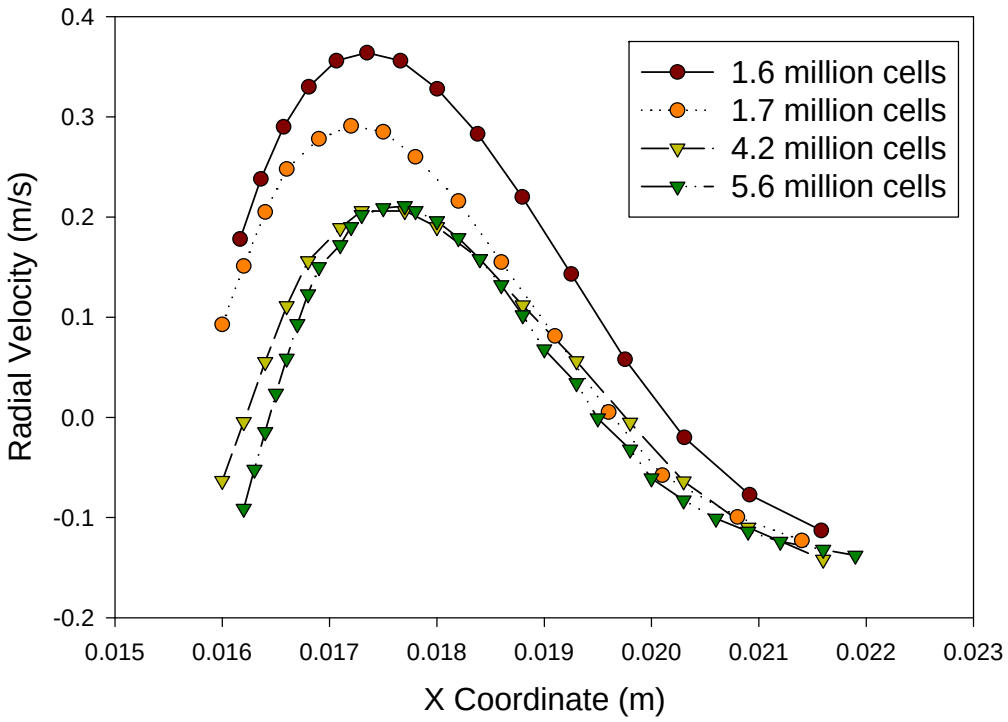

Figure 4-15: Radial velocity change along the line in Figure 4-14 for 1.6 million cells, 1.7 million cells, 4.2 million cells and 5.6 million cells.

Table 4-1: Predicted power number at 4000 rpm for 1.6, 1.7, 4.2 and 5.6 million cell mesh.

Cell number (million)	1.6	1.7	4.2	5.6
Power number	1.7	1.6	2.1	2.1

The power numbers for the slotted stator head obtained from experiments[9] are shown in Figure 4-16. The Reynolds Number, Re calculated by $\mathrm{Re} = \frac{D^2 N}{\nu}$, is 52463 at 4000 rpm and 78400 at 6000 rpm, and in this work, the slotted stator head is used.

Therefore, from Figure 4-16, the measured power number is 2.1 at 4000 rpm. It is

found that the CFD results for the 4.2 million and 5.6 million cell meshes are very close to the experimental data.

From the mesh independence test results of the velocity magnitude, turbulent kinetic energy (TKE) and power number, it can be concluded that in most parts of the domain, the simulated flow field and turbulence field are almost the same for 4.2 and 5.6 million cell meshes. Hence 4.2 million hexahedral cells are enough to capture the characteristic of the flow field in a Silverson L4R batch Rotor-Stator. In this work, to capture the flow details in the high shear gap between the rotor and stator, the cells spanning the gap are increased to 8 layers from 4 layers in the 4.2 million cell mesh.

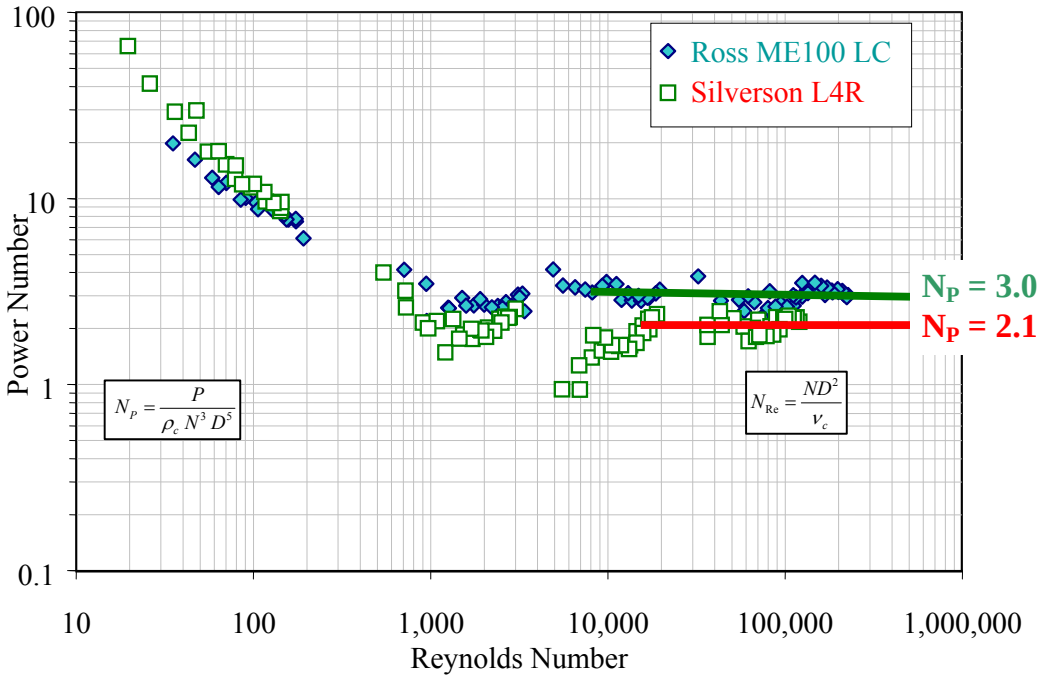

Figure 4-16: Experimental power number data for slotted stator head[9].

This gives a total cell number of 4.6 million. This mesh is used for the simulations that follow.

4.4 Time periodic solution

From the geometry character of the batch rotor stator mixer, it can be concluded that after long enough time, the flow field will exhibit time periodic behavior. The time periodic behavior is illustrated in Figure 4-17[27], which is in a Rushton Turbine stirred tank. From Figure 4-17, it can be seen that because the Rushton Turbine impeller has 6 blades and the tank wall with baffles is 90º symmetric, the flow field is time periodic and the period is the time that the impeller takes to rotate 60°. Furthermore, close to the mixing head, the repeatable time periodic behavior is significant. For the region far from the mixing head, however, the flow field almost cannot feel the effect of the impeller, so it is almost steady.

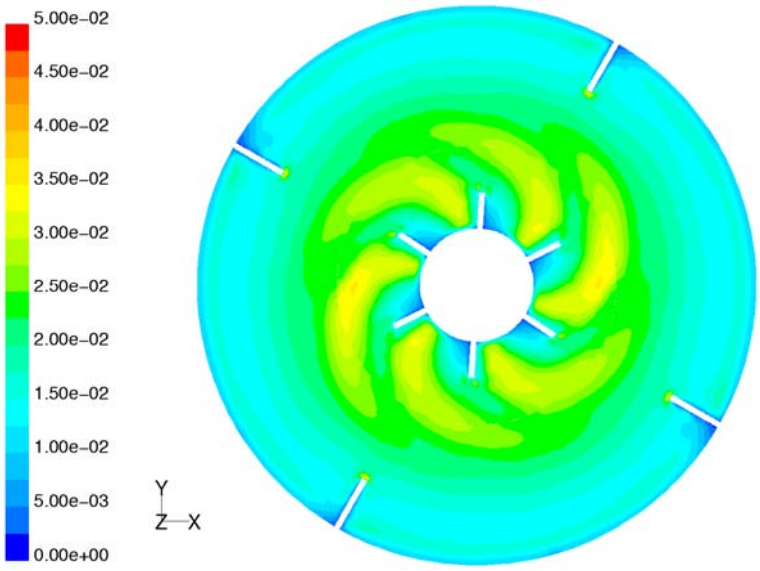

Figure 4-17: Sliding mesh simulation of turbulent kinetic energy contours in the mid plane for a baffled Rushton Turbine stirred tank[27].

The time periodic behavior can be described by the following equation:

$$f(\theta, r, z, \omega t) = f(\theta, r, z, \omega t + period) \tag{4.4.1}$$

where f is any flow property, such as velocity and TKE, θ is angular coordinate, r is radial coordinate, z is axial coordinate, ω is angular velocity and t is time. In the Silverson mixer, there are four blades on the rotor, so the flow near the mixing head repeats itself every 90º rotor rotation. Therefore, the period in this study is 90º of rotor revolution.

During the simulation, however, it is found that the flow field takes unaffordablely long computation time to become converged using the pure sliding mesh method. It is observed that even after 30 revolutions, the regions, away from the rotor, are still far from steady state.

This can be explained by the pumping capacity. At 4000 rpm, the pumping capacity is about 0.7 liter/s while the mixer volume is about 2 liters. As a result, it takes 3 seconds to pass the whole volume once through the mixing head, i.e., 200 revolutions (1 revolution takes one week of computational time), which is unaffordable for our current computational resources. Therefore, it is not ok to parametrically simulate the flow in the batch mixer by a pure sliding mesh method. A hybrid technique, which can reduce the computation time but still keep the important features of the flow field, is required.

4.5 Hybrid RANS simulation technique

To address the above problem, a hybrid RANS simulation technique is developed. The sliding mesh model accounts for the relative motion of stationary and rotating components. However, time periodic motion is confined to the region near the mixing head. Outside this region, the flow is almost steady in time. It is also found that close to the mill head, the flow field converges rapidly using the sliding mesh method. Throughout the mixing vessel, the hybrid technique applies the sliding mesh method to the region where the interaction between stator walls and the rotating fluid is significant and uses the MRF method in the region where the time periodicity is negligible.

Yianneskis et al.[28] used Laser Doppler Anemometry (LDA) to measure the flows in vessels stirred by a Rushton turbine. They suggested dividing the flow into two different regions: the impeller region where the periodic behavior is significant and it is necessary to use time-resolved measurement to describe the flow, and the bulk flow where 360º ensemble averaged techniques are appropriate. In other LDA experiments done by Lee and Yianneskis[29], they also indentified the two regions: periodic region and non-periodic region. They suggested that outside the periodic region, the flow can be treated as steady and a steady CFD simulation may be adequate to describe the flow. In a word, these findings are consistent with our proposed hybrid RANS simulation technique.

.

The procedure for the hybrid technique simulations is defined as the followings:

- Define an envelope around the mill head where the flow field is time periodic (outside this envelope the effect of rotor-stator interactions is negligible and the flow is non-periodic or steady);
- Perform a very well converged MRF simulation for the entire vessel;
- Apply the results of the MRF solution on the surfaces of the time periodic envelope as the boundary conditions for a sliding mesh simulation inside the envelope;
- Perform a sliding mesh simulation inside the envelope until a time periodic solution is obtained.

The MRF simulation results are then used outside of the envelope while the sliding mesh simulation results are applied inside the envelope. During the envelope definition process, a coarse mesh, about 2 million cells, is used and the time step size corresponds to 2° rotor revolution. In the hybrid simulation, a 4.6 million cell mesh are used and the time step size in the time periodic region corresponds to 0.5° of rotor revolution.

4.5.1 Define the periodic envelope

The following protocol is used to define the periodic and non periodic behavior: in one period, if the difference between the maximum and minimum value is less than 1% of the average value, it is non-periodic. Otherwise it is periodic.

To define the time periodic envelope, the velocity magnitude change with time in the x, y, and z direction are monitored using the full sliding mesh simulation. The largest radial jet ought to be close to the rotor, so three lines in the y = 0 plane shown in Figure 4-18 are monitored to set the x direction boundary of the envelope. The x coordinate used in the simulation is shown in Figures 4-19.

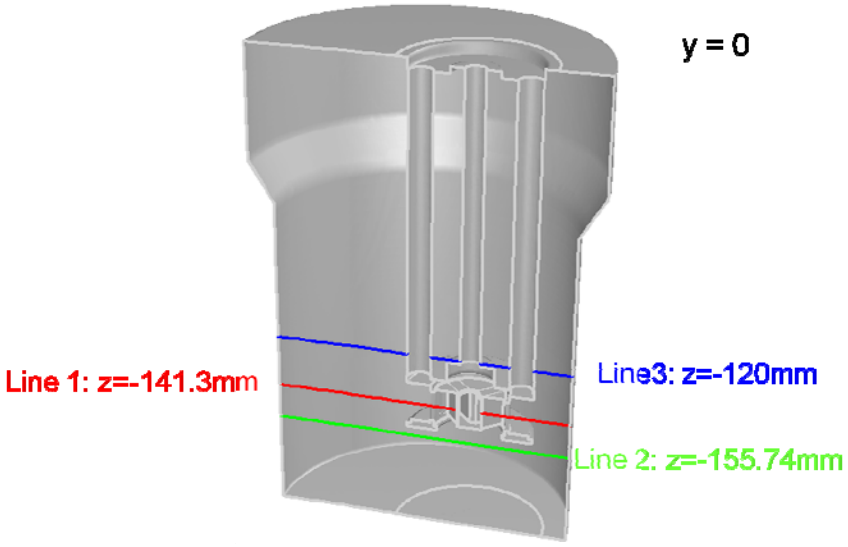

Figure 4-18: Three monitored lines that indentified the envelope boundary in the x dimension direction.

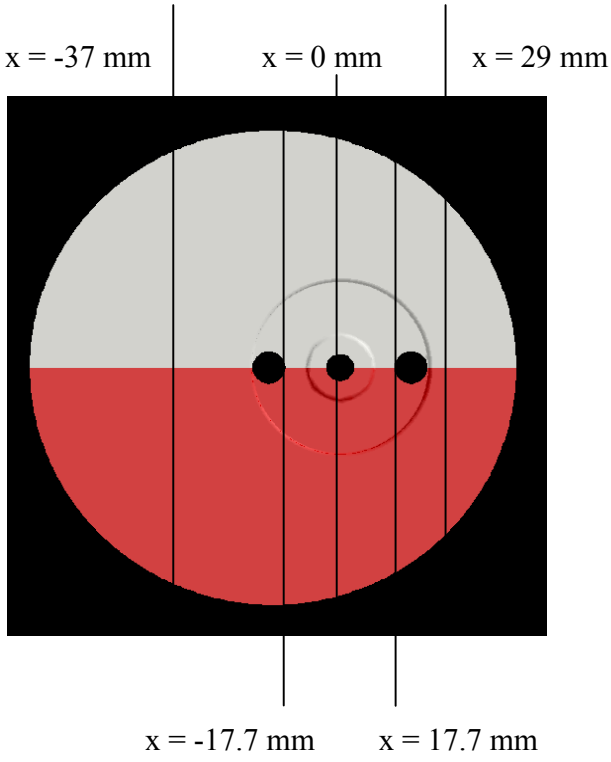

Figure 4-19: The x coordinate in the computational domain.

The velocity magnitude variations with time at different x coordinates on the three lines at 4000 rpm, 6000 rpm and 8000 rpm are shown in Figures 4-20 and 4-21, Figures 4-22 and 4-23 and Figures 4-24 and 4-25 respectively. From these figures, it can be found that when the x coordinate is inside the range from -0.035 m to 0.035 m, the time periodic behavior is significant; otherwise, outside the range the flow field does not exhibit strong time periodic behavior.

Three lines in the x = 0 plane shown in Figure 4-26 are monitored to set the y direction boundary of the envelope. The y coordinate used in the simulation is shown in Figures 4-27.

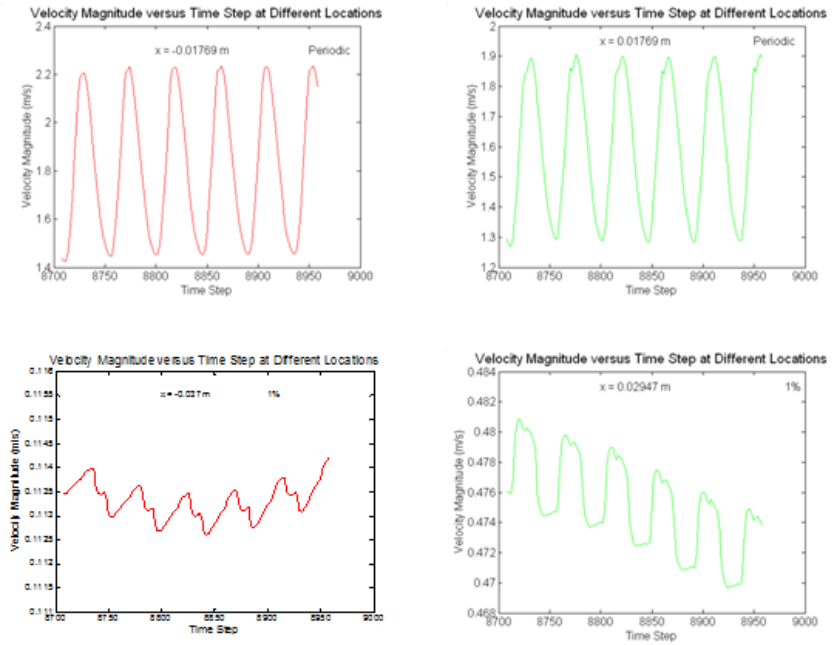

Figure 4-20: The velocity magnitudes change with time at different points on line 1 (mid-plane) in the x direction at 4000 rpm.

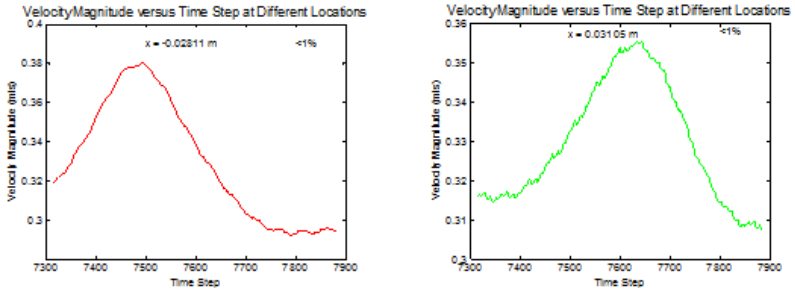

Line 2

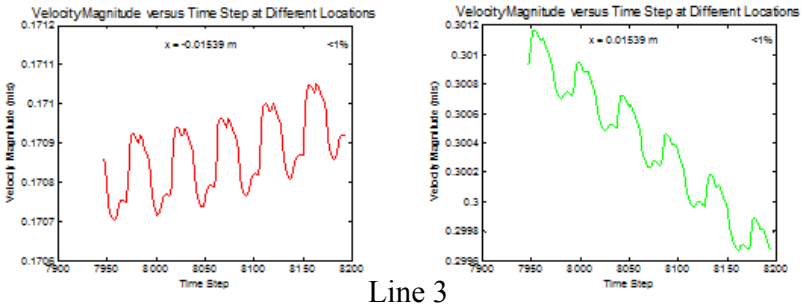

Line 3

Figure 4-21: The velocity magnitudes change with time at different points on line 2 and 3 (mid-plane) in the x direction at 4000 rpm.

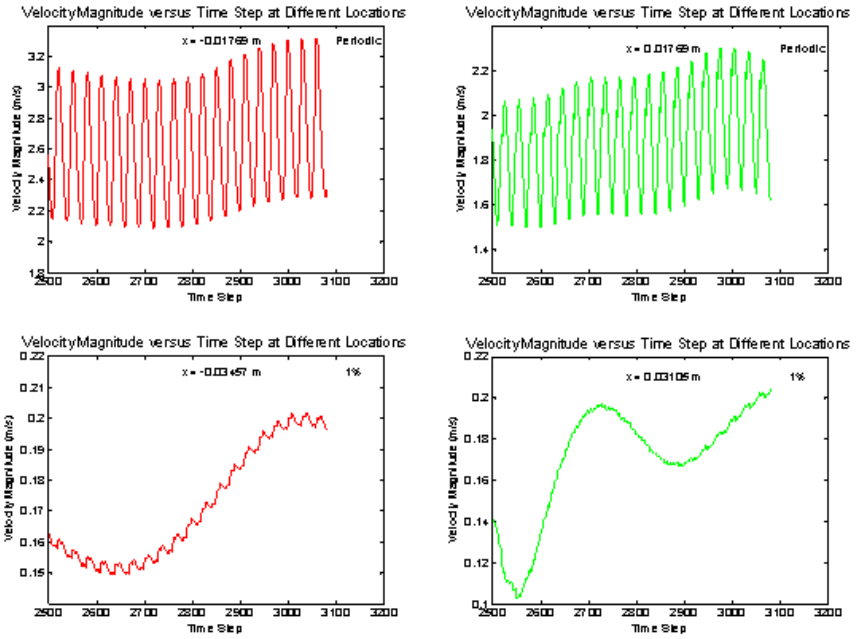

Figure 4-22: The velocity magnitudes change with time at different points on line 1 (mid-plane) in the x direction at 6000 rpm.

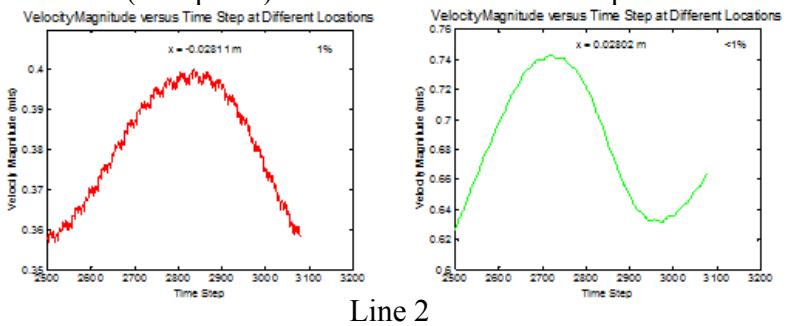

Line 2

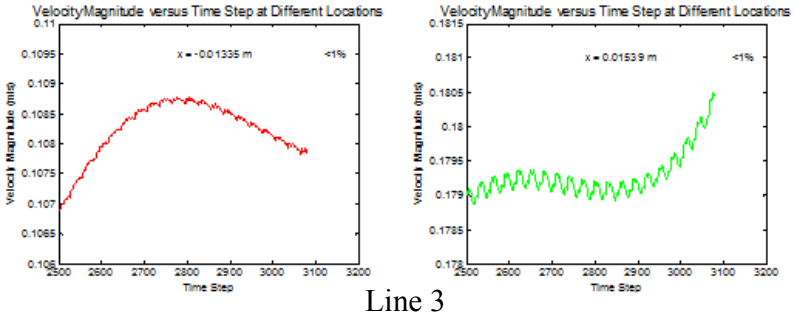

Line 3

Figure 4-23: The velocity magnitudes change with time at different points on line 2 and 3 (mid-plane) in the x direction at 6000 rpm.

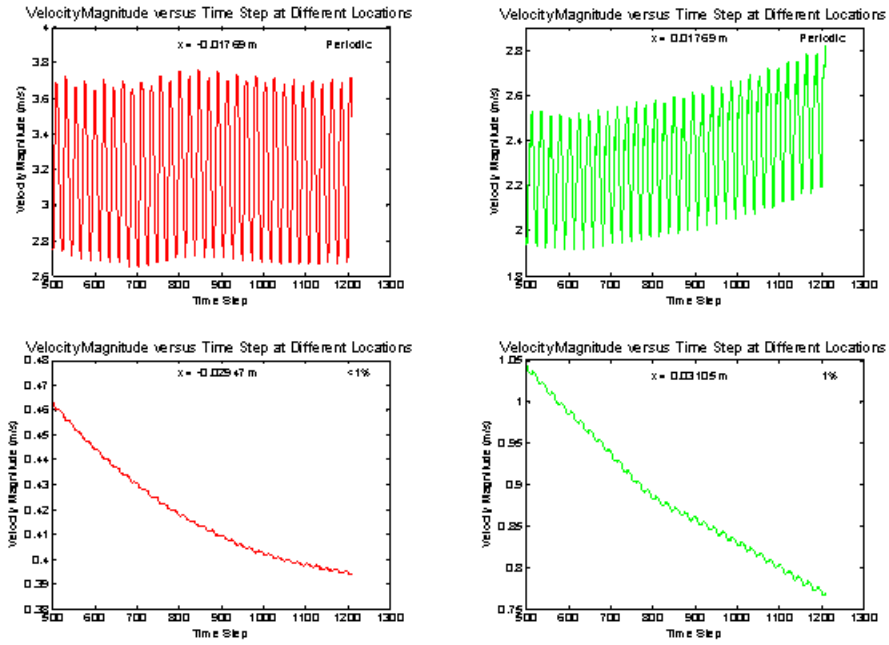

Figure 4-24: The velocity magnitudes change with time at different points on line 1 (mid-plane) in the x direction at 8000 rpm.

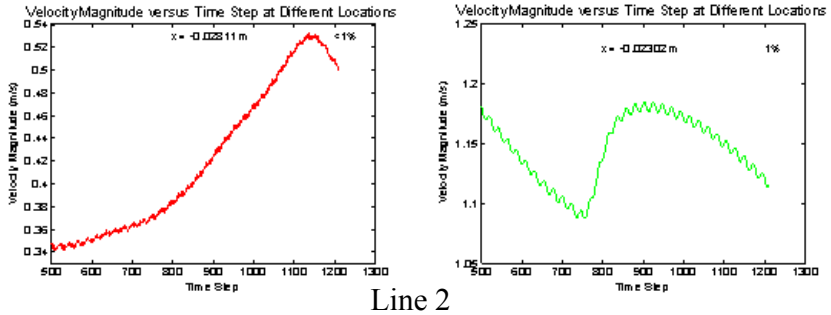

Line 2

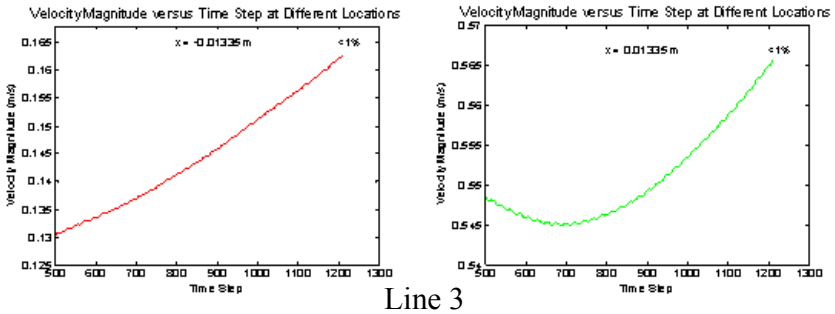

Line 3

Figure 4-25: The velocity magnitudes change with time at different points on line 2 and 3 (mid-plane) in the x direction at 8000 rpm.

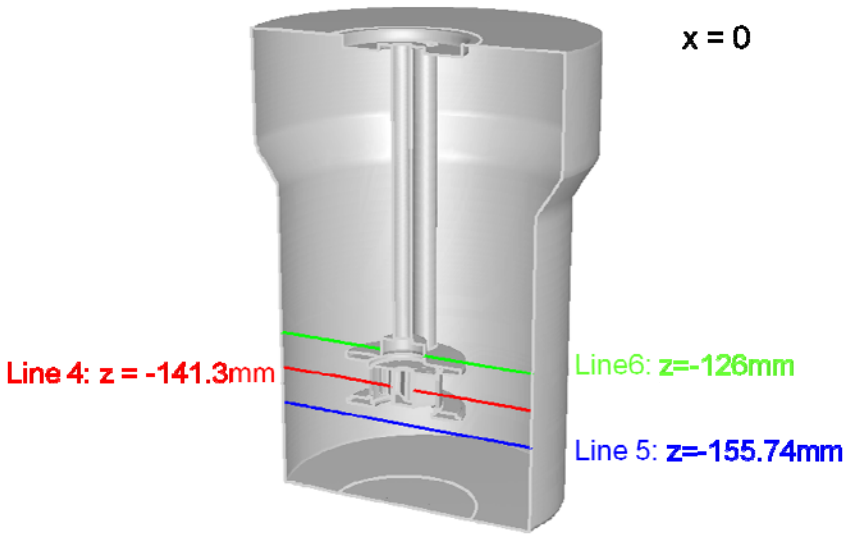

Figure 4-26: Three monitored lines that indentified the envelope boundary in the y direction.

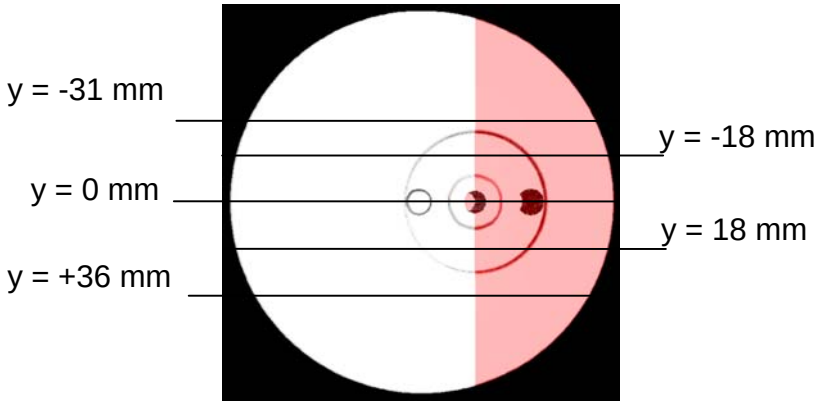

Figure 4-27: The y coordinate in the computational domain.

The velocity magnitude variations with time at different y coordinates on the three lines at 4000 rpm, 6000 rpm and 8000 rpm are shown in Figures 4-28 and 4-29, Figures 4-30 and 4-31 and Figures 4-32 and 4-33, respectively. From these figures, it can be found that when the y coordinate is inside the range from -0.035 m to 0.035 m,

the time periodic behavior is significant; otherwise, outside the range the flow field does not exhibit strong time periodic behavior.

Two lines in Figure 4-34 are monitored to set the z direction boundary of the envelope. The z coordinate used in the simulation is shown in Figures 4-35. Figures 4-36 to 4-38 show the velocity magnitude change with time at different z coordinates at 4000 rpm, 6000 rpm and 8000 rpm, respectively. From these figures, it can be found that when the z coordinate is outside the range -0.1579 m to -0.127 m, the flow field does not exhibit significant time periodic behavior.

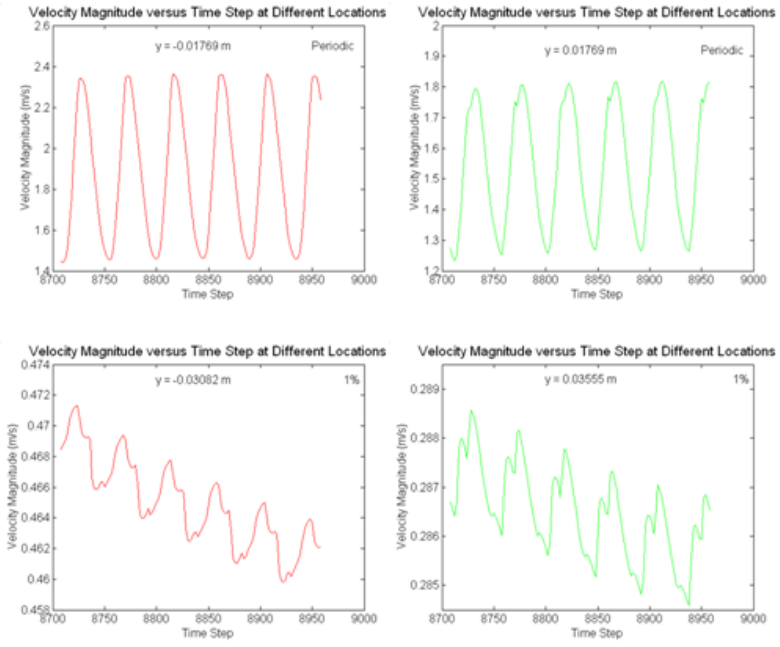

Figure 4-28: The velocity magnitudes change with time at different points on line 4 (mid-plane) in the y direction at 4000 rpm.

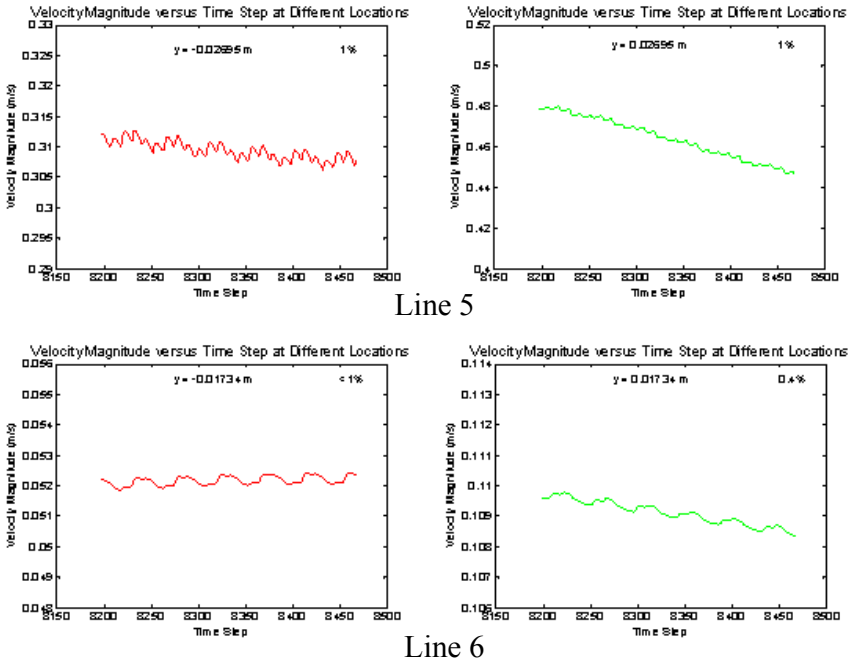

Figure 4-29: The velocity magnitudes change with time at different points on line 5 and 6 (mid-plane) in the y direction at 4000 rpm.

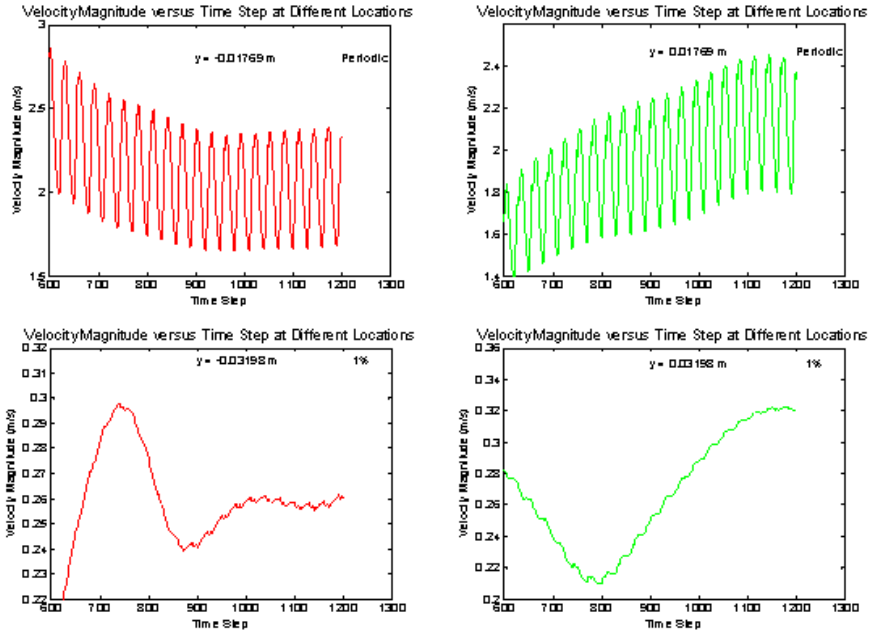

Figure 4-30: The velocity magnitudes change with time at different points on line 4 (mid-plane) in the y direction at 6000 rpm.

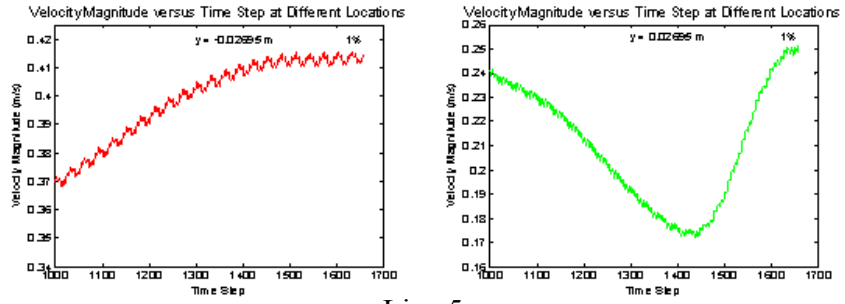

Line 5

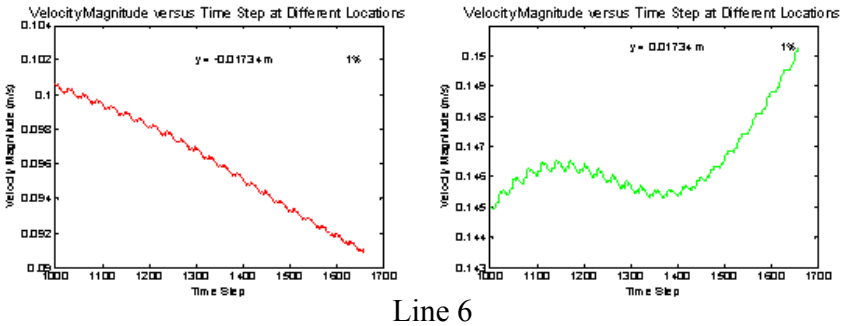

Line 6

Figure 4-31: The velocity magnitudes change with time at different points on line 5 and 6 (mid-plane) in the y direction at 6000 rpm.

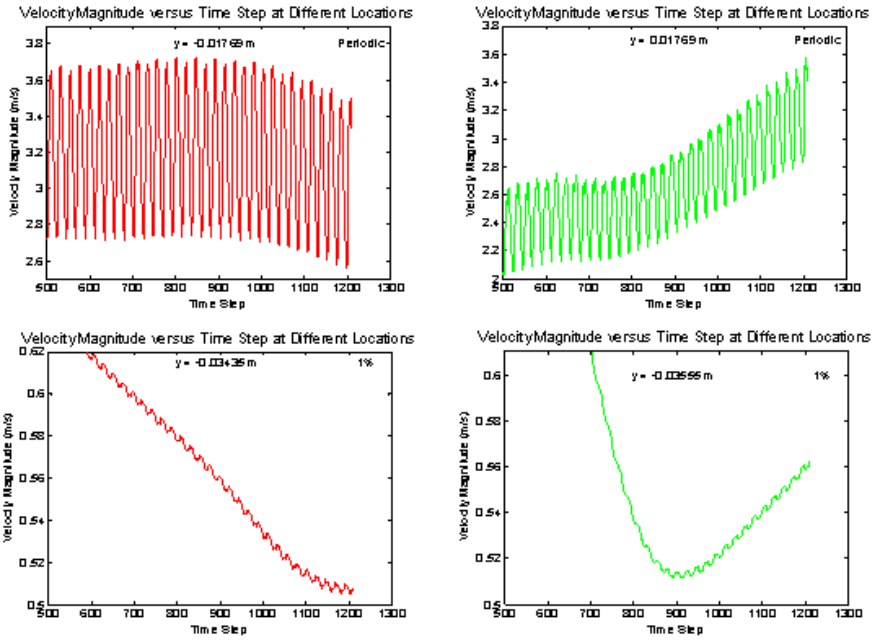

Figure 4-32: The velocity magnitudes change with time at different points on line 4 (mid-plane) in the y direction at 8000 rpm.

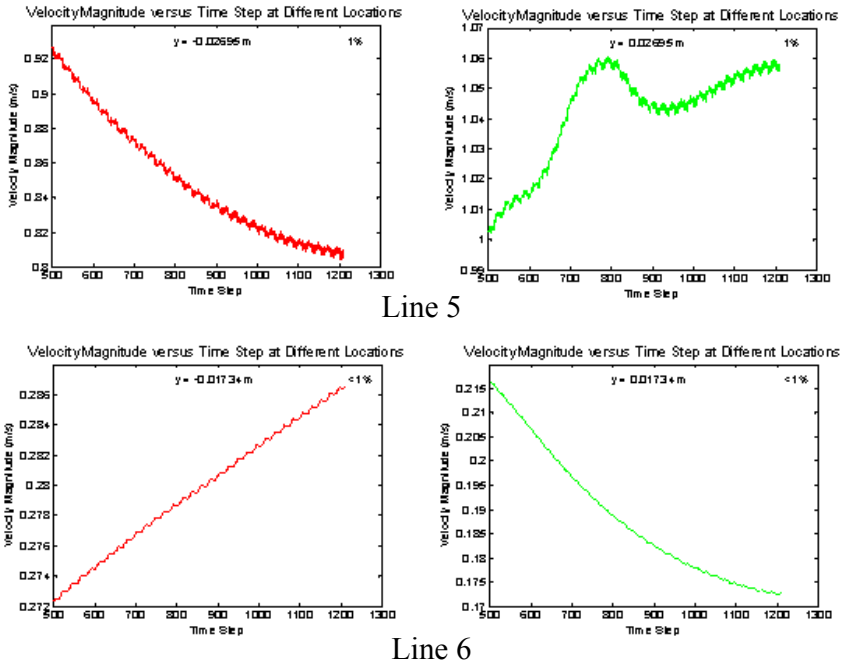

Figure 4-33: The velocity magnitudes change with time at different points on line 5 and 6 (mid-plane) in the y direction at 8000 rpm.

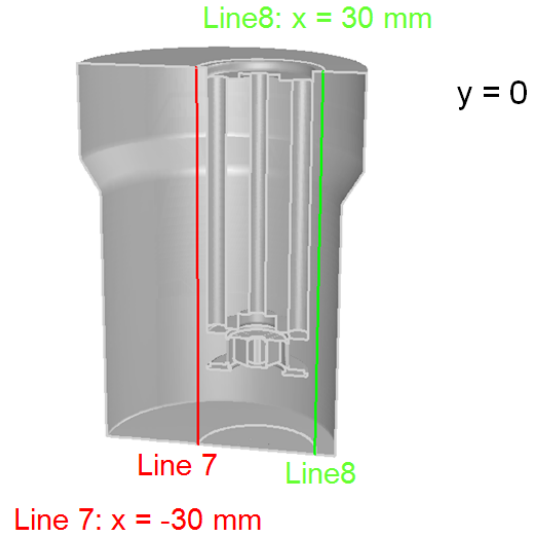

Figure 4-34: Three monitored lines that indentified the envelope boundary in the z direction.

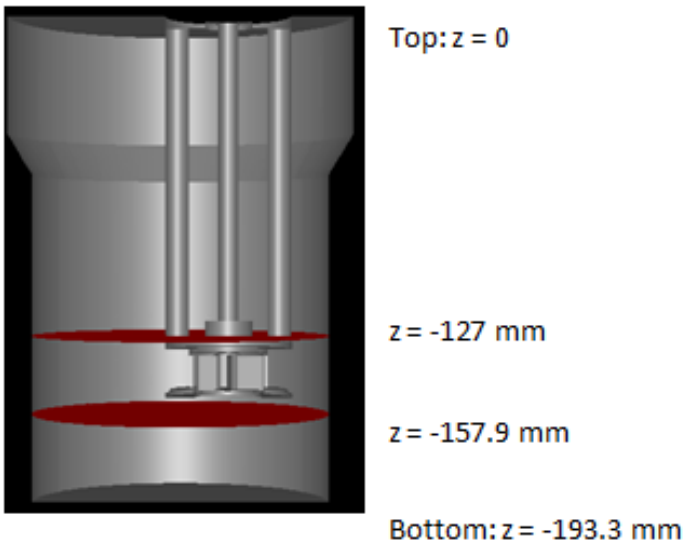

Figure 4-35: The z coordinate in the computational domain.

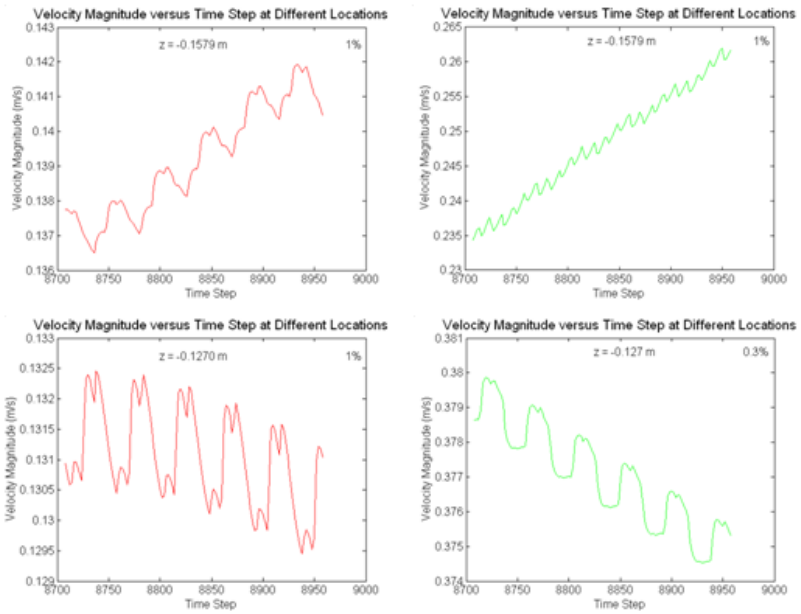

x = -0.03 m
Line 7

x = 0.03 m
Line 8

Figure 4-36: The velocity magnitudes change with time at different points on line 7 and 8 (mid-plane) in the z direction at 4000 rpm.

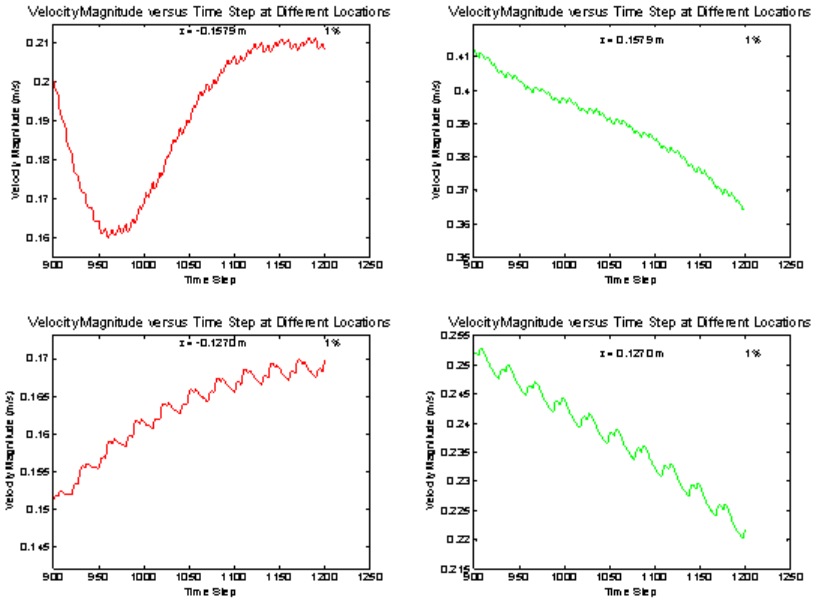

x = -0.03 m
Line 7

x = 0.03 m
Line 8

Figure 4-37: The velocity magnitudes change with time at different points on line 7 and 8 (mid-plane) in the z direction at 6000 rpm.

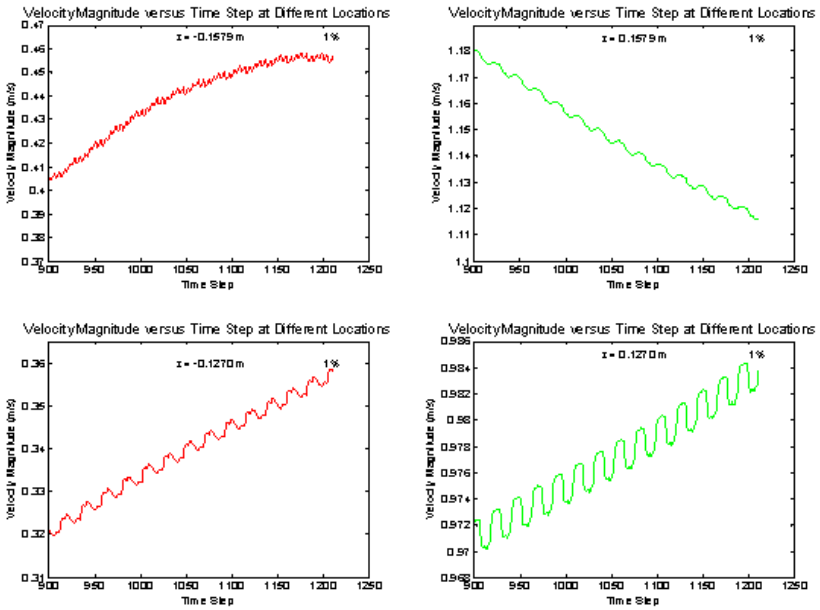

x = -0.03 m

x = 0.03 m

Figure 4-38: The velocity magnitudes change with time at different points on line 7 and 8 (mid-plane) in the z direction at 8000 rpm.

In summary, from these figures the time periodic envelope can be defined as a cylinder with a radius of 0.037 m and with axial dimensions from -0.1579 m to -0.127 m centered on the mill head. Inside this cylinder, the flow is periodic and the sliding mesh method is applied; outside the cylinder, the flow is steady and MRF method is used. The envelope is shown as Figure 4-39 and highlighted by the red color.

4.5.2 MRF simulations

The MRF simulation is performed for the entire vessel. Both steady and unsteady MRF simulations were investigated and their residue at 4000 rpm are shown as Figure 4-40. From Figure 4-40, the residue of the unsteady MRF can reach 1e-09, which is more accurate than that of steady MRF. Therefore, the unsteady solver is used to perform MRF simulations. The convergence criterion for the unsteady MRF simulation is 1e-6 and the "time step size" is 2.083e-4 second, which is the largest time step size that does not lead to divergence..

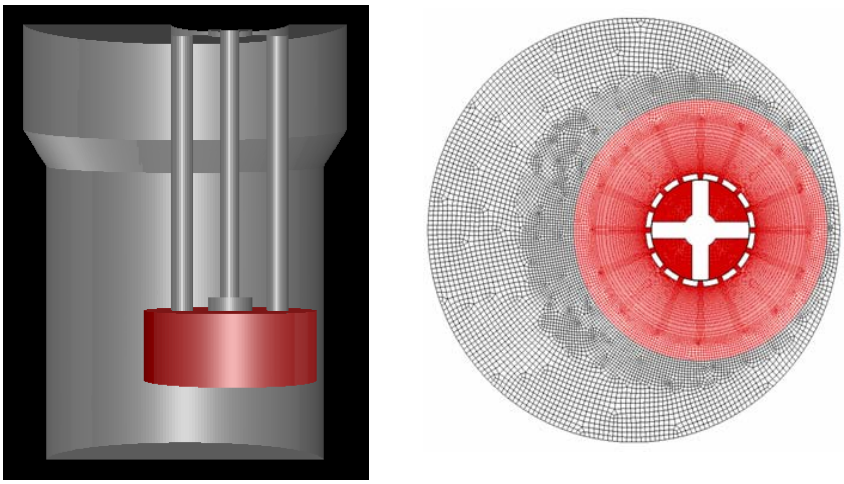

Figure 4-39: The hybrid time periodic envelope.

In MRF model, it is supposed that the rotor does not move, so the flow field properties should be independent of time. The velocity magnitudes on 3 lines in Figure 4-41 are monitored and the results are shown in Figure 4-42 at 4000 rpm. The changes of profiles of these lines with time are monitored and highlighted using different colors. It can be found that on line 1 in the mid-plane, the velocity magnitude does not change significantly with time; on line 2 and 3, however, the velocity magnitudes change dramatically with time. At 4000 rpm, the results on 3 surfaces shown as Figure 4-43 (z = -5 mm, z = -141.3 mm and z = -190 mm) at time steps 8500 and 8572 are compared and the relative difference are shown in Figure 4-44. When the average relative deviation of the flow field at different time steps is smaller than 5%, the flow field is considered to be converged. From Figure 4-44, the differences for the two time steps are very small, and the converged MRF solution is reached. The converged results for 6000 rpm on these 3 surfaces at time steps 8600 and 8672 are compared and the relative differences are shown in Figure 4-45.

4.5.3 Hybrid simulation

The MRF solution on the envelope is applied as the boundary conditions for sliding mesh simulation inside the envelope shown in Figure 4-39 while the MRF solution of

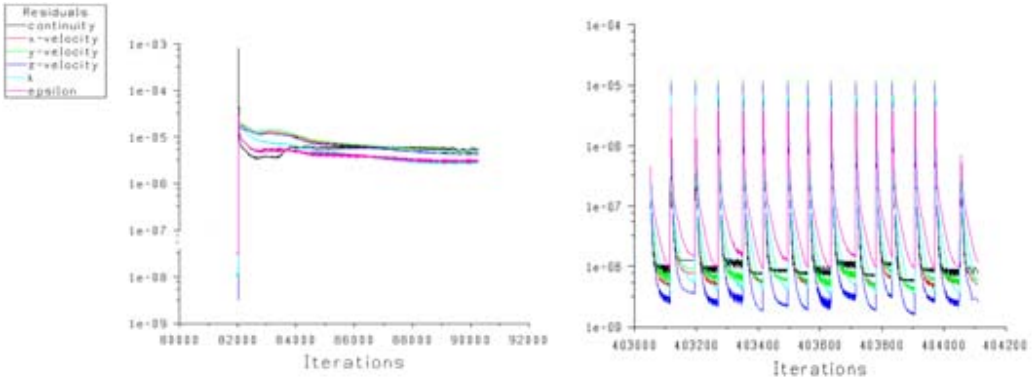

Figure 4-40: Steady and unsteady MRF residue at 4000 rpm.

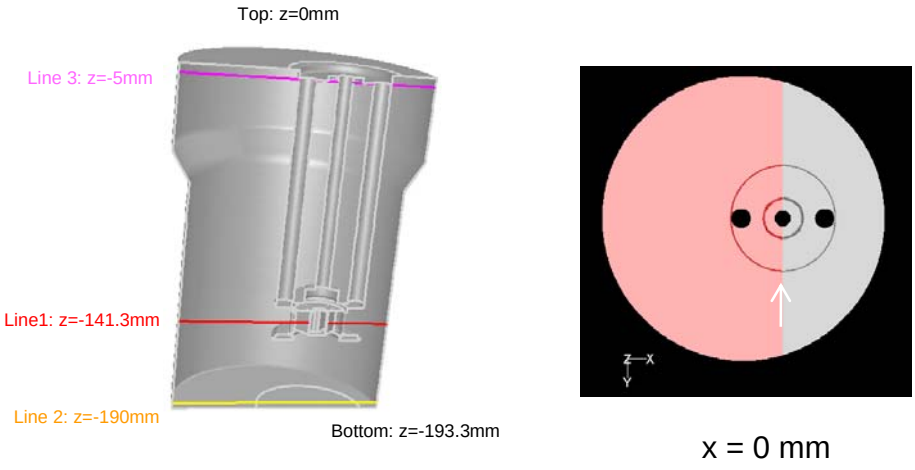

Figure 4-41: Lines monitored in unsteady MRF simulation.

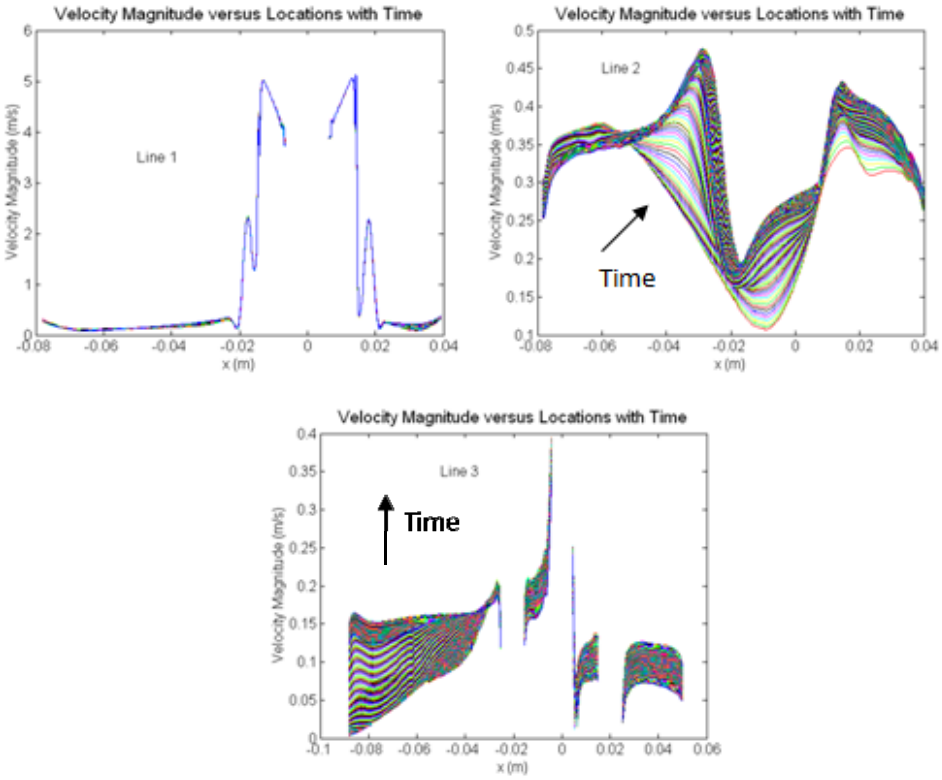

Figure 4-42: The velocity magnitude change with time on the 3 lines.

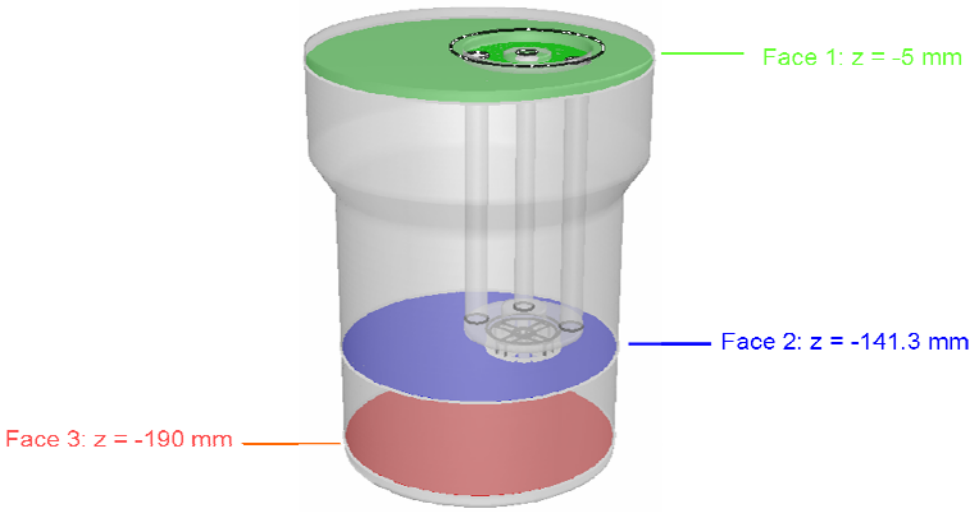

Figure 4-43: The monitored surfaces in the unsteady MRF solution.

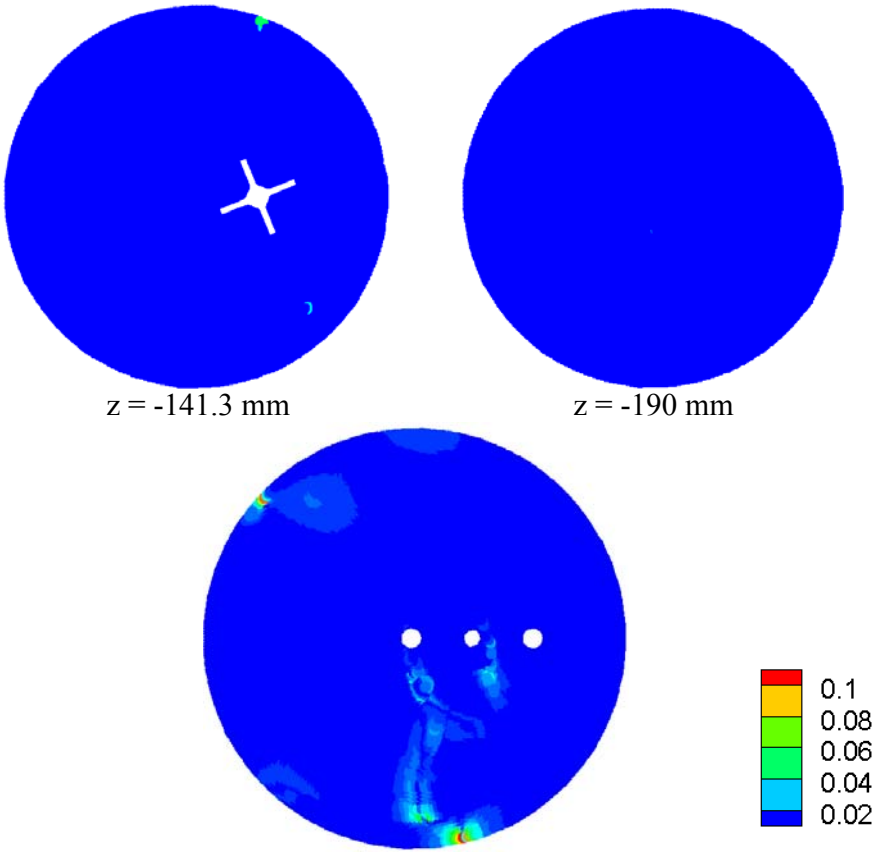

Figure 4-44: The relative difference of velocity magnitudes, $\frac{|v_{8500} - v_{8572}|}{v_{8572}}$, on 3 surfaces at time step 8500 and 8572 for N = 4000 rpm.
The average relative deviation: face z = -141.3 mm, 0.05%; face z = -190 mm, 0.06%; face z = -5 mm, 0.2%.

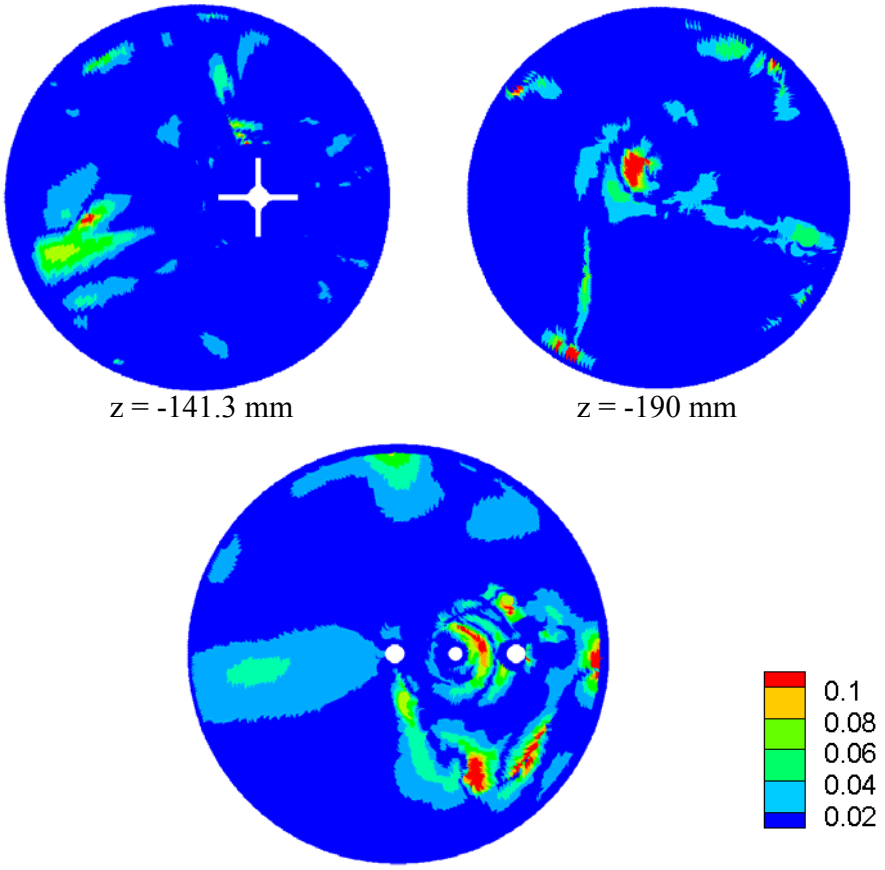

Figure 4-45: The relative difference of velocity magnitudes, $\frac{|v_{8600} - v_{8672}|}{v_{8672}}$ on 3 surfaces at time steps 8600 and 8672 for N = 6000 rpm. The average relative deviation: face z = -141.3 mm, 0.98%; face z = -190 mm, 1.09%; face z = -5 mm, 1.99%.

the region outside the envelope is kept unchanged. Then sliding mesh simulation is performed inside the envelope until a time periodic solution is obtained. The results at 4000 rpm on 3 surfaces shown in Figure 4-46 (z = -135 mm, z = -141.3 mm and z = -158 mm) at the 50th revolution and 53rd revolution are compared and the relative differences are shown in Figure 4-47. When the average relative deviation of the flow field at different revolutions is smaller than 5%, the flow field is considered to be

converged. From Figure 4-47, the difference between two time steps is very small, so a converged time periodic flow field is obtained. The results for 6000 rpm are shown in Figure 4-48.

Figure 4-46: The monitored surfaces in the hybrid simulation.

4.6 Results and discussion

4.6.1 Macro scale properties

Based on the hybrid simulation results, macro scale properties of the Silverson L4R batch rotor-stator mixer, namely pumping and power, are investigated.

Pumping capacity, Q_v, is calculated by equation (4.6.1)

$$Q_v = \frac{\int |\vec{v} \cdot \hat{n}| dS}{2} \tag{4.6.1}$$

where $\vec{v}$ is the mean velocity vector, S is the surfaces covering the rotor-stator, $\hat{n}$ is the unit normal vector of surfaces S. This pumping capacity means the flow rate of the fluid going out the domain enclosed by surfaces S. The closed surfaces used to calculate pumping capacity are shown in Figure 4-49. This equation is developed

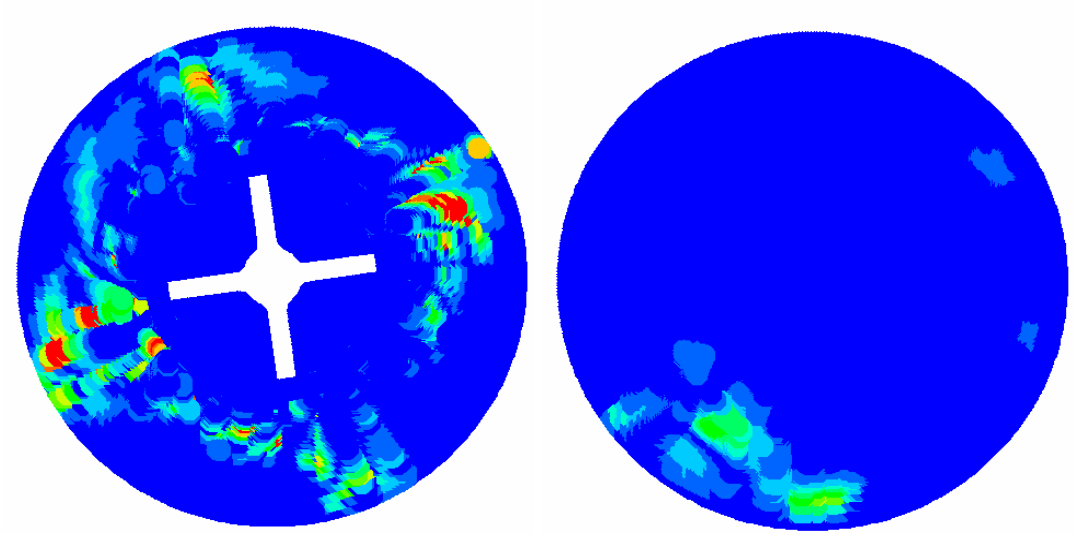

z = -141.3 mm

z = -158 mm

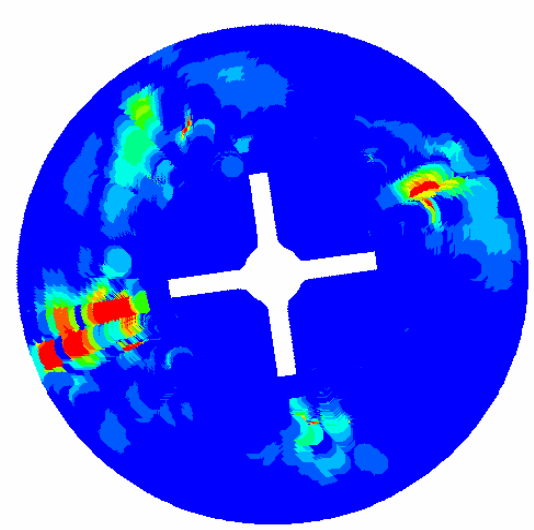

z = -135 mm

Figure 4-47: The relative difference of velocity magnitudes, $\frac{|v_{50} - v_{53}|}{v_{53}}$, on 3 surfaces for rotations 50 and 53 for N = 4000 rpm.
The average relative deviation: face z = -141.3 mm, 0.47%; face z = -158 mm, 0.28%; face z = -135 mm, 0.5%.

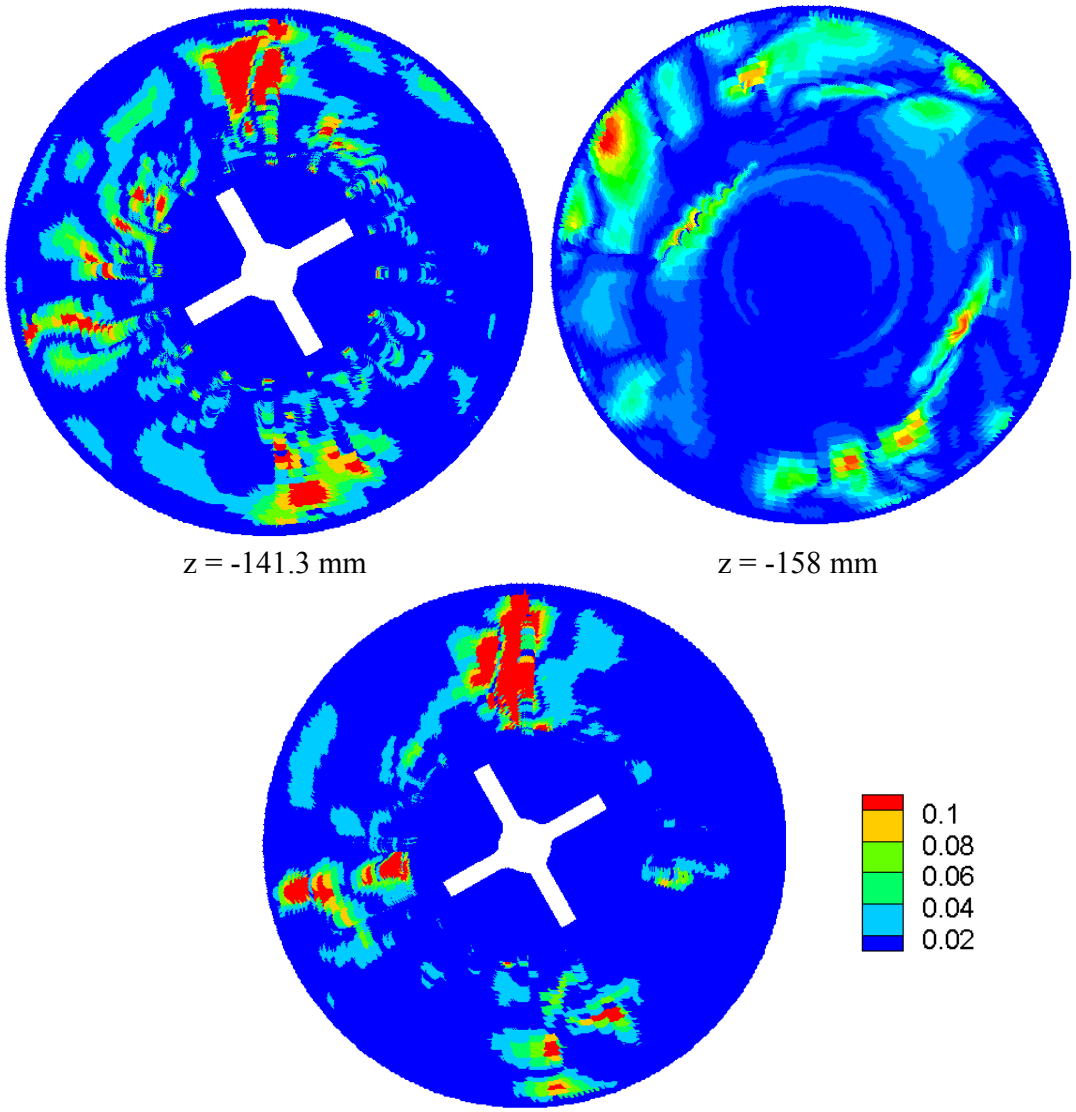

Figure 4-48: The relative difference of velocity magnitudes, $\frac{|v_{55} - v_{58}|}{v_{53}}$, on 3 surfaces for rotation 55 and 58 for N = 6000 rpm.
The average relative deviation: face z = -141.3 mm, 1.18%; face z = -158 mm, 0.68%; face z = -135 mm, 0.91%.

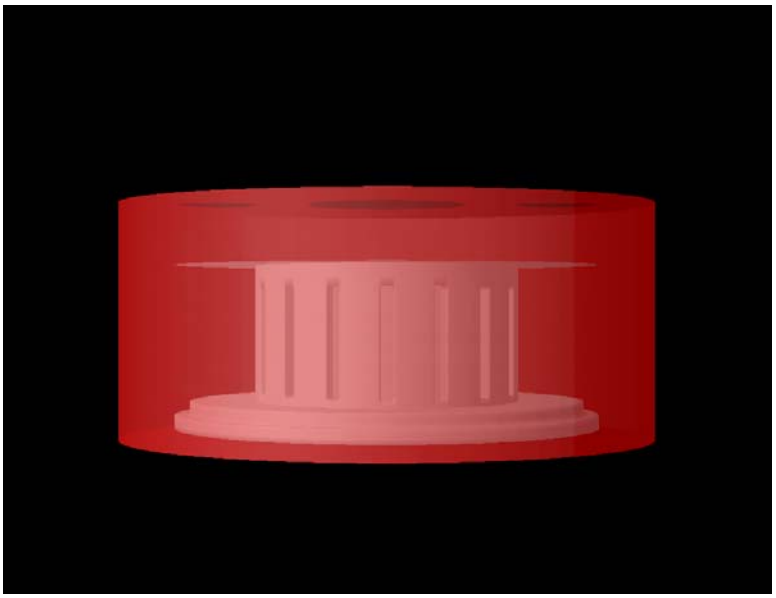

Figure 4-49: The surfaces for the pumping capacity calculation.

based on mass balance. For the volume enclosed by these surface, the radial coordinate these surfaces, the radial coordinate is from 0 to 30 mm and the z coordinate is from -153 mm to -125 mm.

The computed average pumping capacities are 0.7 liter/s at 4000 rpm and 1.25 liter/s at 6000 rpm. The pumping number can be calculated by equation (5), where Q_v is the pumping capacity, N is the rotor speed and D is the rotor diameter. The pumping numbers are 0.50 at 4000 rpm and 0.57 at 6000 rpm. These are comparable to typical pumping numbers for turbine stirred tanks.

$$N_Q = \frac{Q_v}{ND^3} \tag{4.6.2}$$

Power and power number at 4000 and 6000 rpm are calculated by equation (4.3.1) and (4.3.2). The power number at 4000 and 6000 rpm are 2.1 and 2.1 respectively, which compare favorably with our experimental results (Figure 4-14).

4.6.2 The flow fields at 4000 and 6000 rpm

The coordinate used in the simulation is shown in Figure 50. θ is the tangential coordinate. ϕ is the angle between the center line of the rotor blade and $\theta = 0$. The rotor rotates in anticlockwise direction. Line 1 is in the middle of stator slot 1.

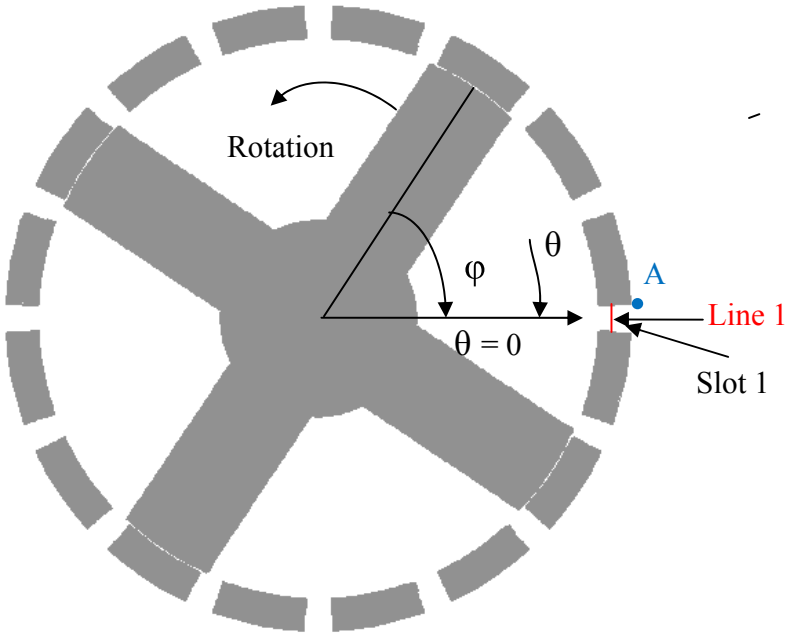

Figure 4-50: The coordinate on the mid-plane.
The tangential coordinate of Line 1 is from -2.8˚to 2.8˚.

The flow fields on the mid-plane inside the sliding mesh envelope at 4000 and 6000 rpm are shown in Figure 4-51. The flow fields are normalized by the tip speed (5.889 m/s at 4000 rpm and 8.834 m/s at 6000 rpm). From the vector plots, it is found that the flow pattern of 4000 rpm is very similar to that of 6000 rpm. Close to each stator

slot, a strong jet exists in both cases. Meanwhile fluid close to the stator slot outlets is sucked into the stator slot due to low pressure behind the blade, and further enters the rotor region. Therefore in the region near every stator outlet, vortices are generated. Another interesting phenomenon in these vector plots is that the rotor rotates in anti-clockwise direction while the fluid that leaves the stator and furthermore enters the bulk of the tank tends to move in the clockwise direction, which is opposite to the rotation direction of rotor.

The flow fields on plane y=0 (see Figure 4-27) inside the sliding mesh envelope at 4000 and 6000 rpm are shown in Figure 4-52, where the rotor blade orientations are the same as Figure 4-51. From the vector plots, it is found that the flow pattern at 4000 rpm is very similar to that of 6000 rpm. The fluid enters the rotor zone from the bottom and top of the mill head, and is pumped rapidly out of the stator from the side. Therefore vortices between the rotor blades are generated in the vertical plane.

The flow fields, normalized with tip speed, on the mid-plane (z = -141.3 mm) outside the sliding mesh envelope at 4000 and 6000 rpm are shown in Figure 4-53. The flow

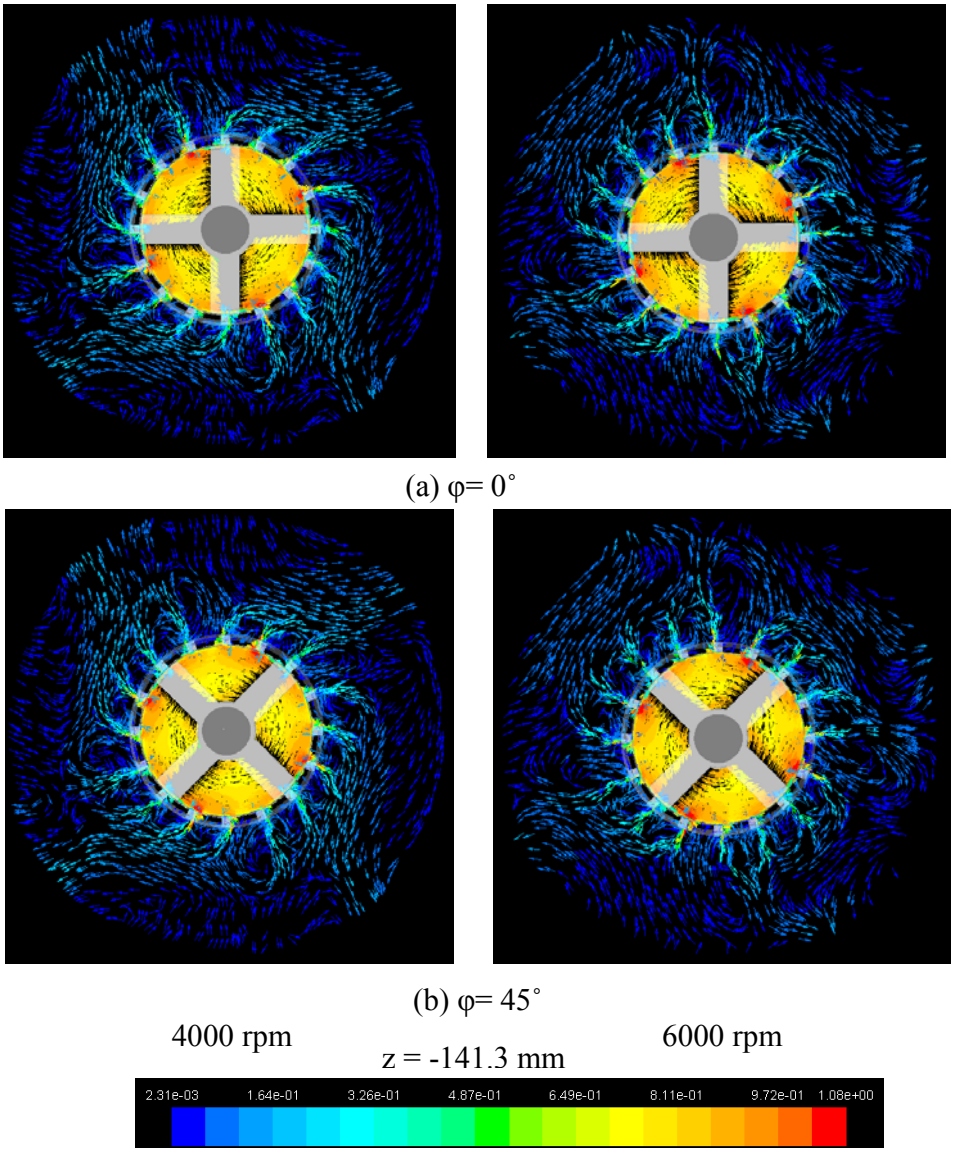

Figure 4-51: Normalized mean velocity magnitude snapshots on mid-plane inside the sliding mesh envelope (the rotor rotates in the anticlockwise direction).

pattern at 4000 rpm is quite similar to that at 6000. There are several vortices close to the tank wall for both rotation rates and the positions of these vortices are very close.

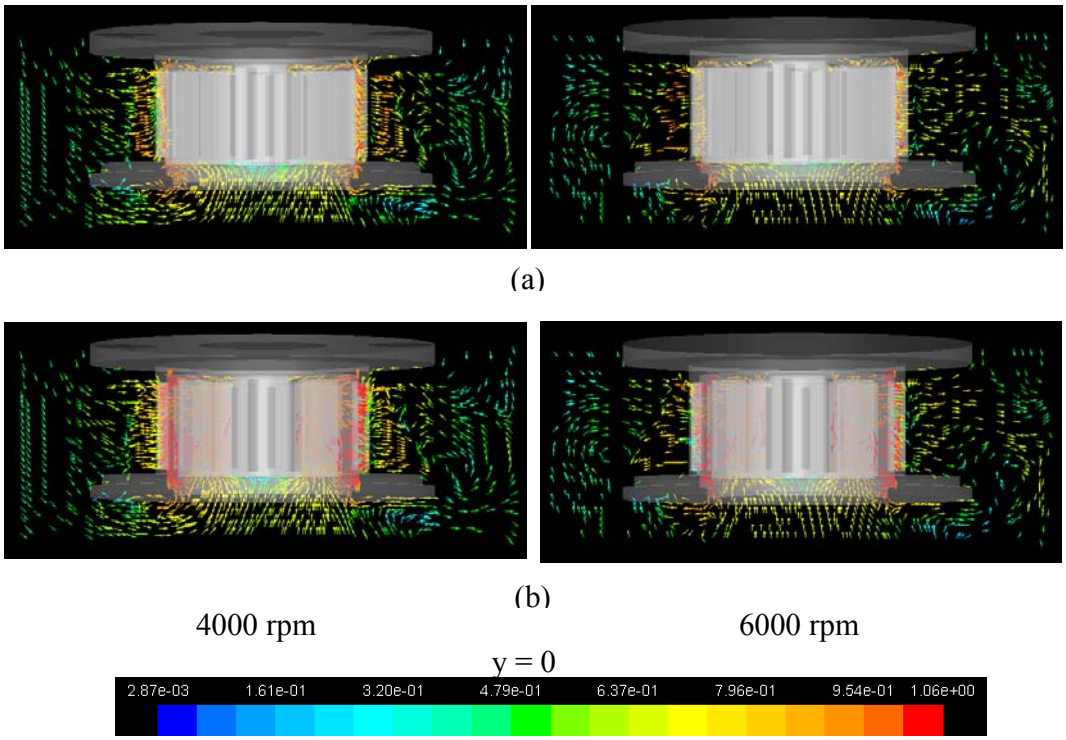

Figure 4-52: Normalized mean velocity magnitude snapshots at plane y=0 inside the sliding mesh envelope.

In the hybrid simulation, this flow field outside the periodic envelope is independent of rotor position and will not change during the simulation. Outside the envelope, four significant jets are found and an interesting finding is that these jets do not change orientation with rotor rotation based on the hybrid simulation concept. It appears that every four adjacent time periodic jets from the stator slots form one of these steady outside jets. Although with the rotor rotation, every time periodic jet from the stator slots change correspondingly, the comprehensive effect of these jets does not change with time (rotor position).

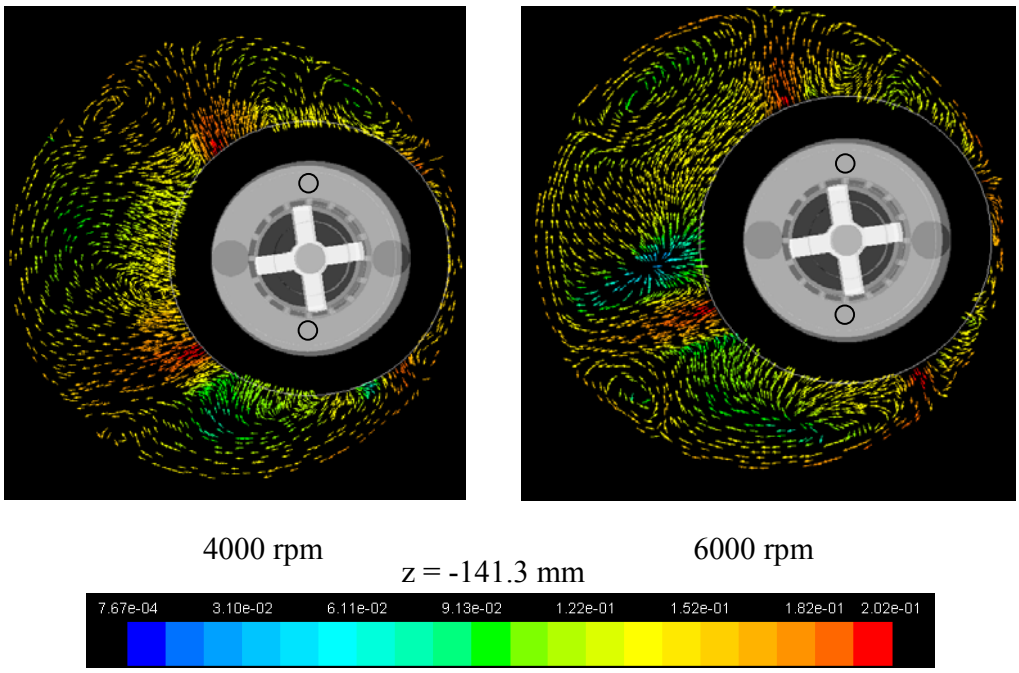

Figure 4-53: Normalized mean velocity magnitude vector plot on mid-plane outside the sliding mesh envelope.

It could be postulated that the four steady jets of Figure 4-53 are not real but instead an artifact of the rotor orientation in the MRF used to start the sliding mesh simulation. To rule out this possibility, these hybrid simulation results are compared with those for the full sliding mesh simulation. Figure 4-54 shows the flow field outside the sliding mesh envelope at 4000 rpm by the pure sliding mesh method after 50 revolutions. On the mid-plane, the flow field converges faster than in regions far from the mixing head. It is found that the normalized flow field on this plane by the pure sliding mesh method is very similar to that by hybrid technique, which serves to confirm that our hybrid simulation is accurate.

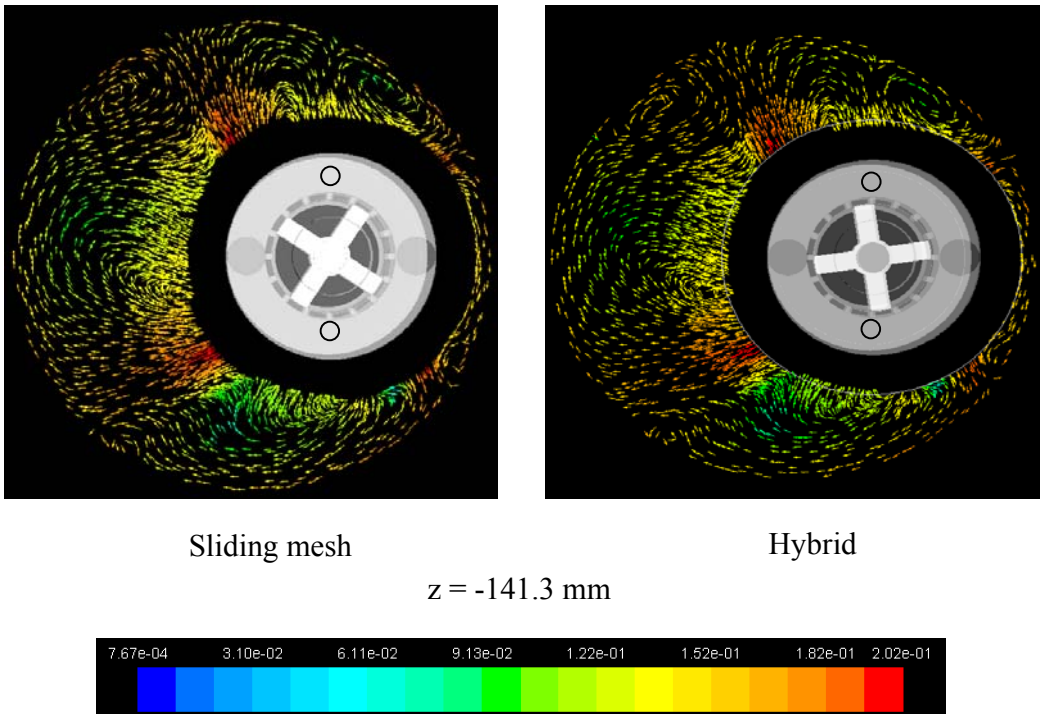

Figure 4-54: Normalized mean velocity magnitude vector plot at mid-plane outside the sliding mesh envelope by the pure sliding mesh and the hybrid method at 4000 rpm.

To further confirm that the existence of the 4 steady merged jets, two 6000 rpm steady MRF simulations starting with different rotor orientations were also performed. The vector plots for these MRF simulations are shown as Figure 4-55. It is found from Figure 4-55 that the four steady jet orientations do not change significantly. It is not surprising that there are some velocity differences here, since the steady MRF solver is not so accurate. These simulations were only performed to further confirm the existence of the steady jets.

To investigate how these merged jest are generated, two MRF simulations with different struts (these struts screw the top plate and bottom plate of the mill head

together) were performed and the normalized mean velocity field out of the time periodic envelope at 4000 rpm is shown in Figure 4-56.

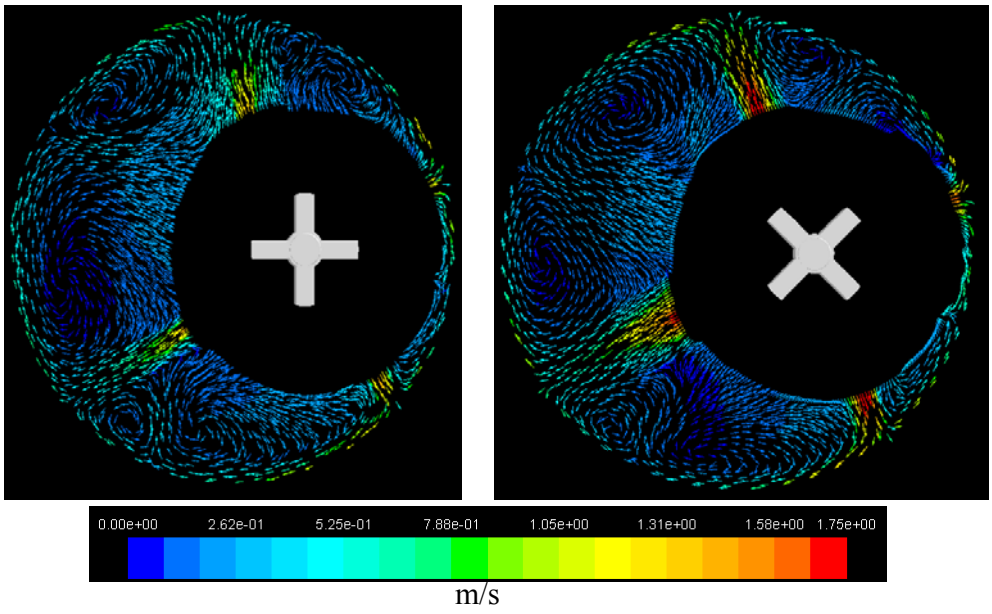

Figure 4-55: Normalized steady MRF mean velocity magnitude vector plots at mid-plane outside the envelope at two different rotor blade orientations for N = 6000 rpm.

From Figure 4-56, it is found that with different vertical screws (see Figure 4-1) position, the positions of the merged jets also change. Therefore, the vertical screws have significant effects on the merged jets. The generation of these jets could be the result of the struts.

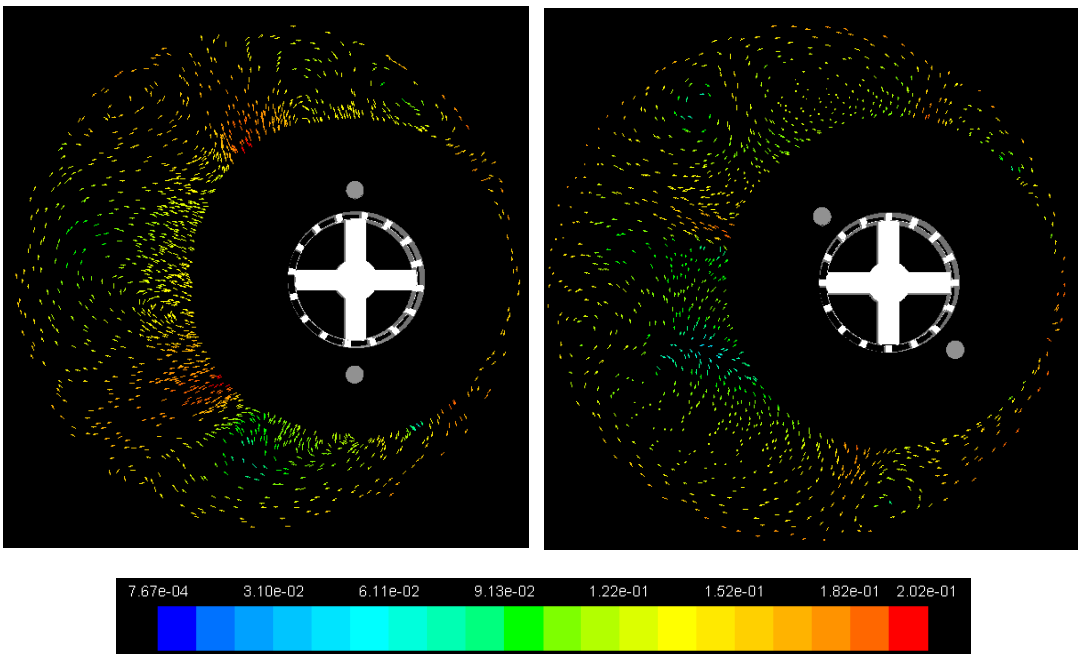

Figure 4-56: Normalized mean velocity magnitude vector plot at mid-plane outside the sliding mesh envelope with different struts positon at 4000 rpm.

The mean flow fields at different y coordinates shown in Figure 4-57 are given in Figures 4-58, 4-59 and 4-60. In Figure 4-58, there are two vortices around the corner near the tank bottom for 4000 and 6000 rpm. The vortex structures at 4000 rpm are similar to those at 6000 rpm in Figures 4-59 and 4-60. The differences between 4000 and 6000 rpm probably result from the stronger jets at 6000 rpm. It is also found that even though, plane y = -30 and 30 are symmetric about y = 0, the mean flow filed of these two planes are not symmetric. This is because the mixing head is placed off the

center of tank. During the rotor rotation, the downstream and upstream environment of these two planes are different.

The flow fields at different z coordinate are shown in Figure 4-61 and 4-62 respectively. Plane z = -15 mm is close to the tank top while plane z = -180 mm is close to the tank bottom (see Figure 4-35). From these flow fields plots it can be concluded that in Silverson L4R batch rotor-stator mixer, the flow field is very complicated and highly three dimensional.

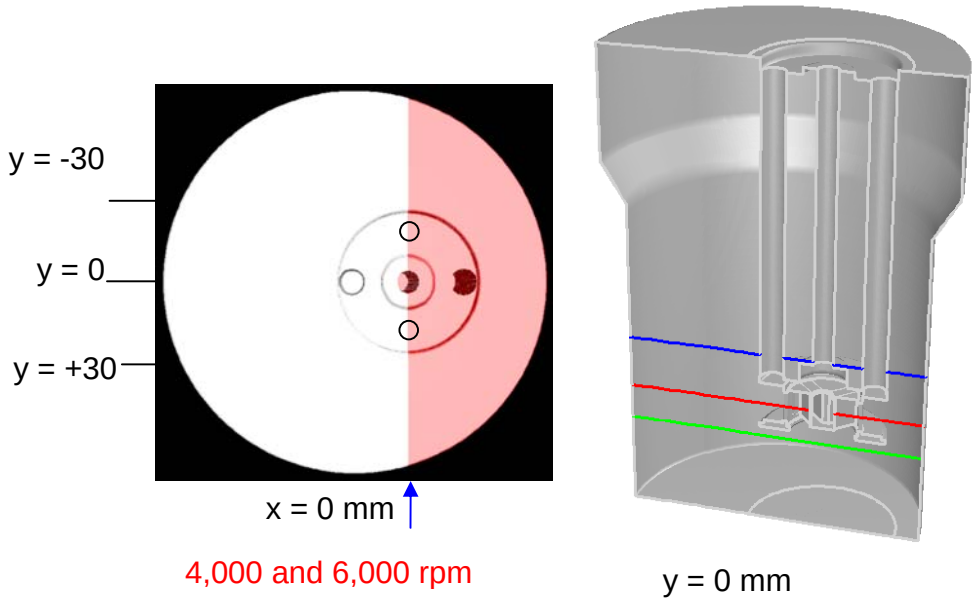

Figure 4-57: Three planes with different y coordinates outside the sliding mesh envelope.

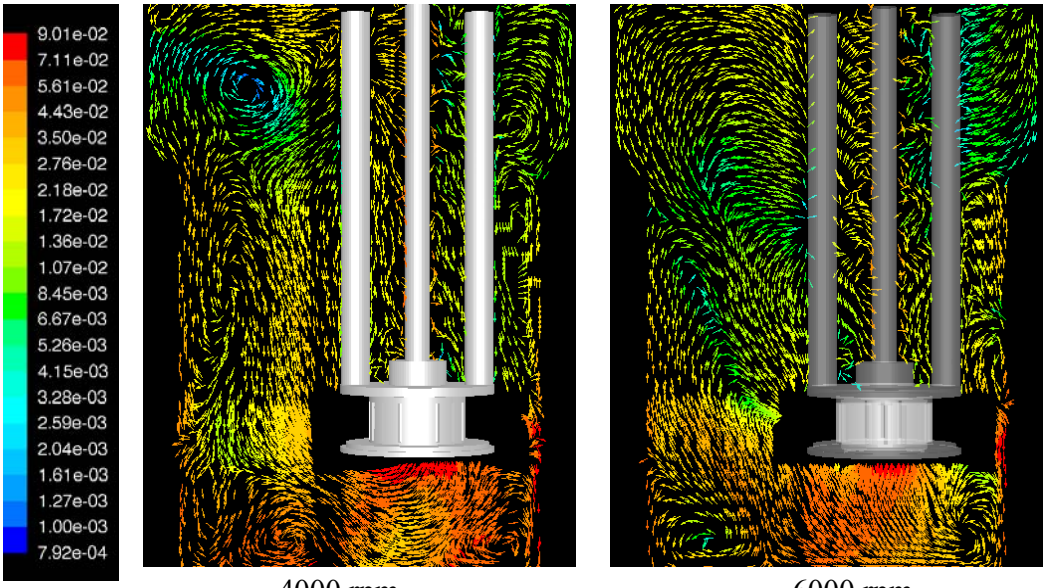

4000 rpm 6000 rpm

Figure 4-58: Normalized mean velocity magnitude vector plots at plane y = 0 outside the sliding mesh envelope.

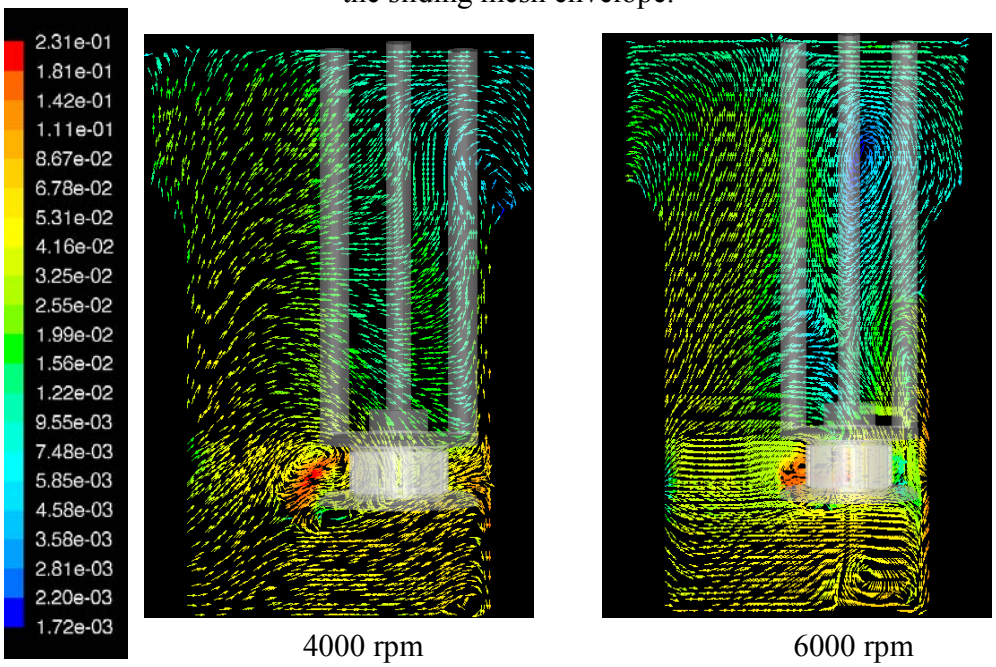

4000 rpm 6000 rpm

Figure 4-59: Normalized mean velocity magnitude snapshots at plane y = 30 (the rotor blade angle is same as Figure 4-51 (b)).

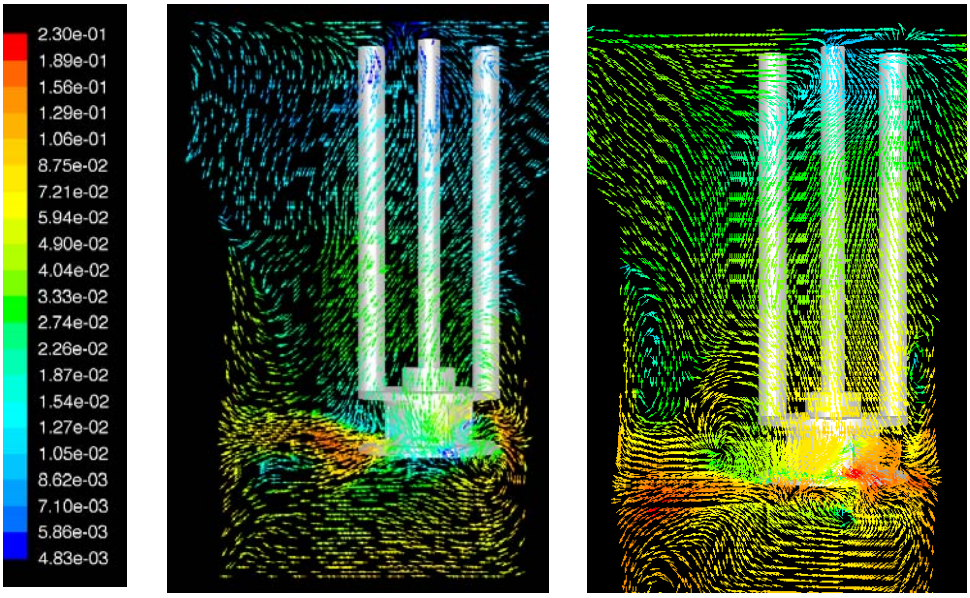

Figure 4-60: Normalized mean velocity magnitude snapshots at plane y = -30 (the rotor blade angle is same as Figure 4-51 (b)).

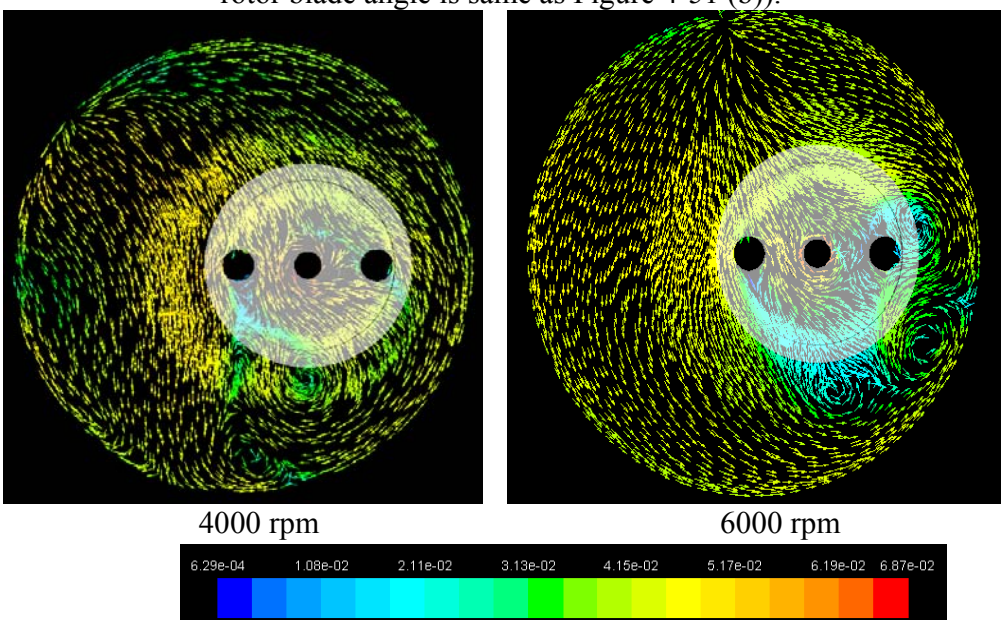

Figure 4-61: Normalized mean velocity magnitude vector plots at plane z = -15 mm (close to the tank top).

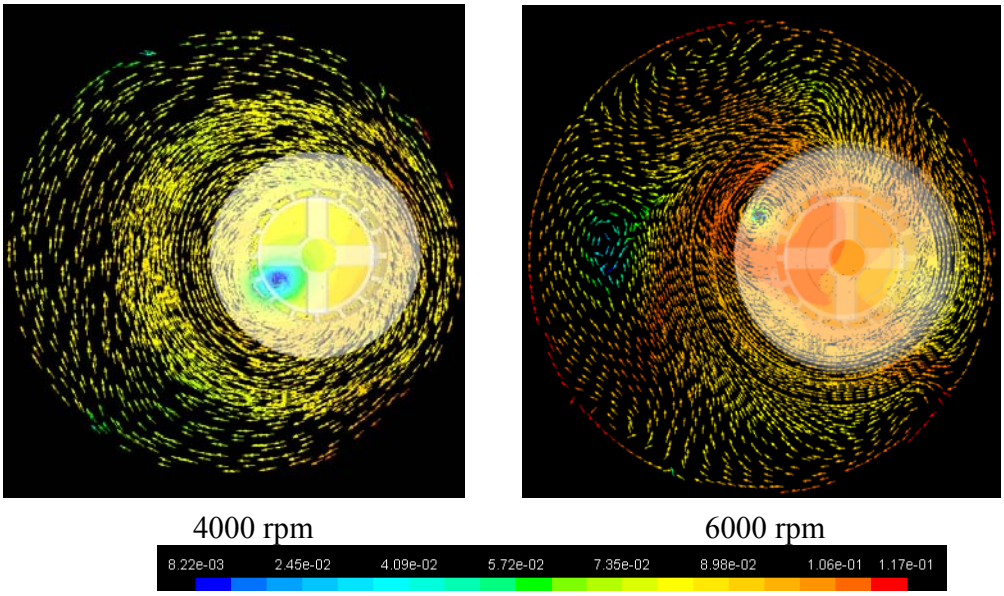

Figure 4-62: Normalized mean velocity magnitude vector plots at plane z = -180mm (close to the tank bottom).

The flow patterns normalized by the rotor tip speed close to the stator slot 1 on the mid-plane (in Figure 4-8) at 4000 and 6000 rpm are shown in Figure 4-63 and 4-64.

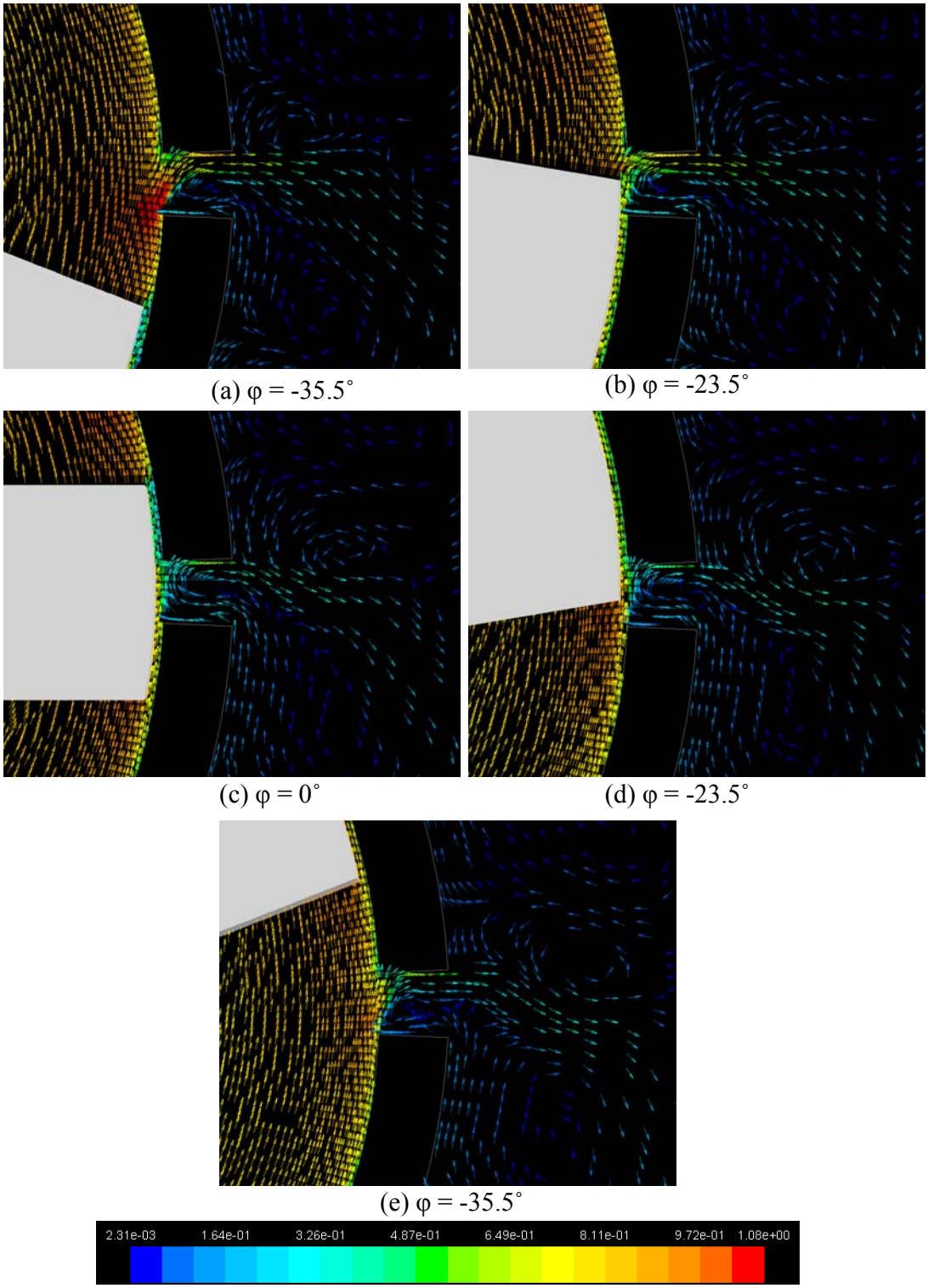

(a) φ = -35.5˚ (b) φ = -23.5˚

(c) φ = 0˚ (d) φ = -23.5˚

(e) φ = -35.5˚

Figure 4-63: Velocity vectors normalized by the rotor tip speed around the stator slot at various blade positions (4000 rpm). The rotor rotates in the anti-clockwise direction.

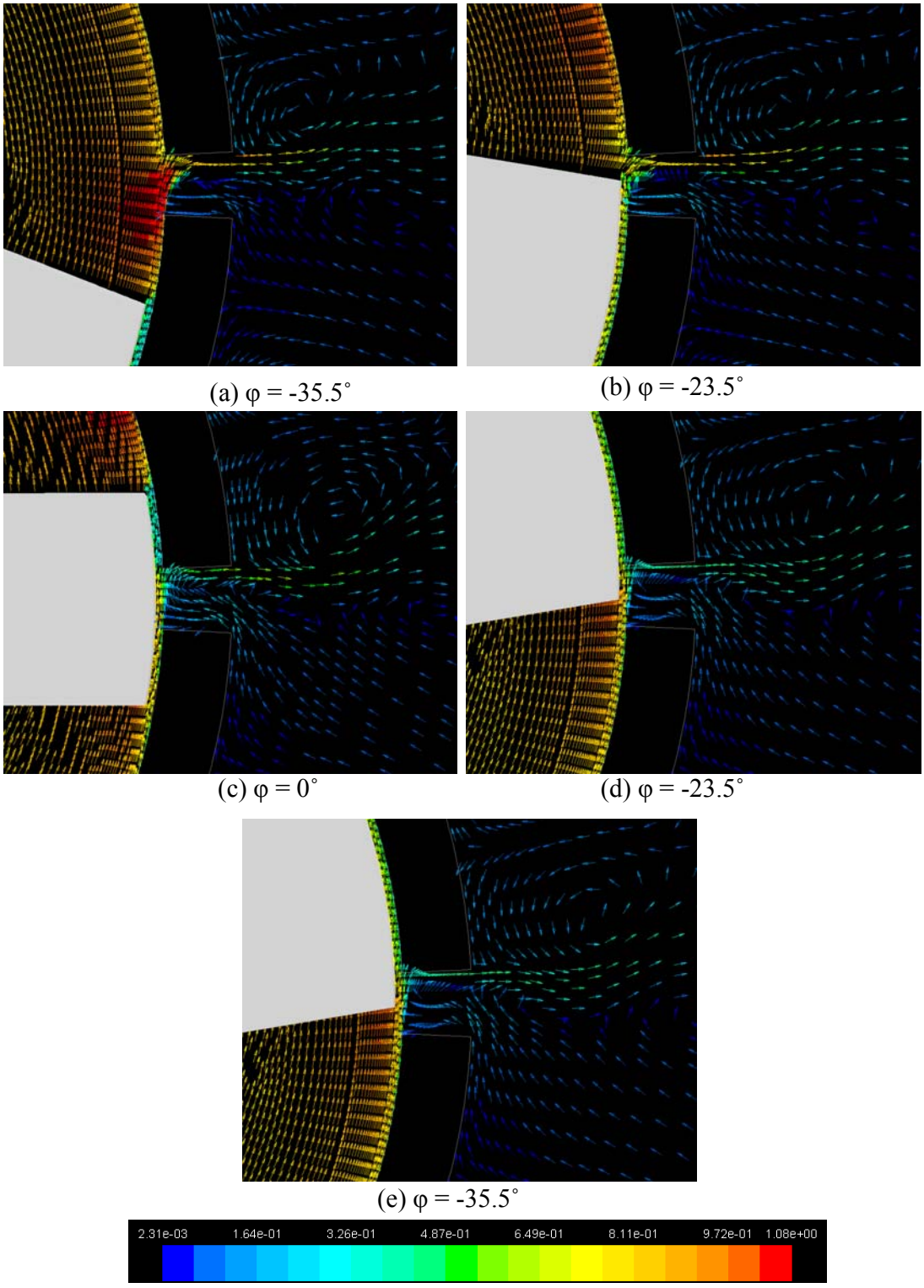

(a) φ = -35.5˚ (b) φ = -23.5˚

(c) φ = 0˚ (d) φ = -23.5˚

(e) φ = -35.5˚

Figure 4-64: Velocity vectors normalized by the rotor tip speed around the stator slot at various blade positions (6000 rpm). The rotor rotates in the anti-clockwise direction.

From these figures it can be found that the flow pattern at 4000 rpm is very similar to that at 6000 rpm. The fluid inside the stator head moves with the rotor in the anti-clockwise direction. Close to the stator slot the fluid pushed by the rotor impinges on the stator teeth. Then the tangentially directed velocity reorients to the radial direction. A strong jet is generated in each stator slot. Regardless the rotor blade position, the jets are always generated close to the leading edge of the stator slot. These jets move further into the bulk of the mixer and tend to move in the anti-clockwise direction, which is opposite to the rotor direction. Meanwhile, outside the stator slots, some fluid is driven backward to enter the stator openings and go back the rotor zone. As a result, there exists a vortex in each stator slot. It is also found that at 6000 rpm, the jets are stronger than those at 4000 rpm, which could be the result of larger pumping capacity at 6000 rpm.

The angularly averaged radial velocity profiles (normalized by rotor tip speed) along line 1 of Figure 4-50 at 4000 and 6000 rpm are shown in Figure 4-65. This figure indicates that the maximum jet radial velocity occurs close to the downstream edge (θ = -3º) of the stator slot 1 and decreases gradually with the distance from the leading edge. At some point near the upstream edge, the radial velocity exhibits a negative value indicating a recirculation region where the liquid flows into the stator slot. Figure 4-65 also suggests that the flow profile at 4000 rpm shows similar trend to that at 6000 rpm.

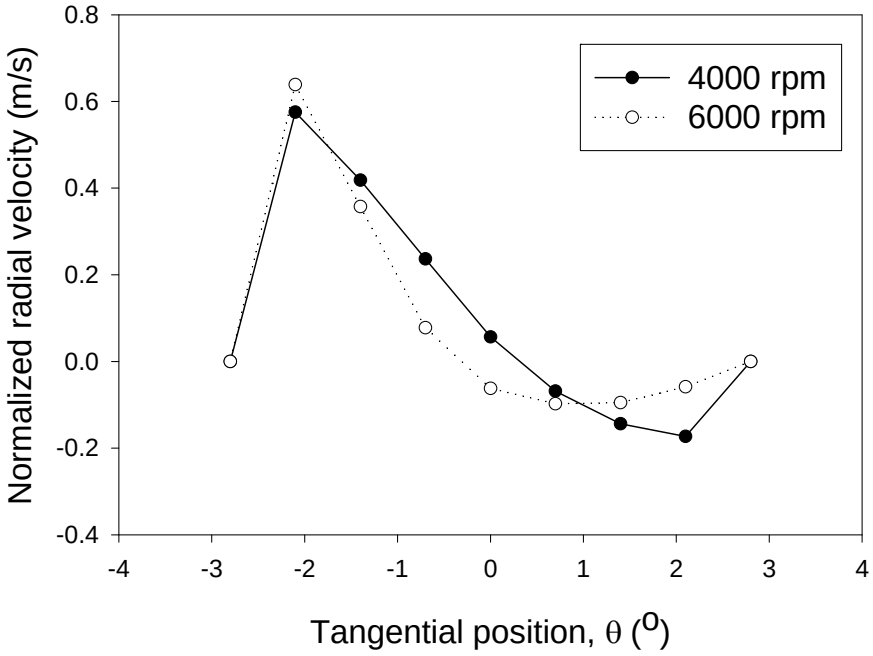

Figure 4-65: Normalized angularly averaged radial velocity profiles along line 1 (Figure 4-50) at 4000 and 6000 rpm.

The angular averaged tangential velocity profiles (normalized by rotor tip speed) along line 1 of Figure 4-50 at 4000 and 6000 rpm are shown in Figure 4-66. This figure indicates that the maximum tangential velocity occurs close to the leading edge of stator slot 1 and decreases gradually with the distance from the leading edge. At some point near the upstream edge, the radial velocity exhibits negative values indicating a vortex existing in the stator slot. Figure 4-65 also suggests that the profile at 4000 rpm gives similar trends to that at 6000 rpm. In contrast to the mean radial velocity profiles, the mean tangential velocity along line 1 does not increase significantly when the rotation rate increases from 4000 to 6000 rpm. In addition, the tangential velocity magnitude is much smaller than the radial velocity magnitude. It may suggest that in the stator slot, the radial velocity is the major velocity component.

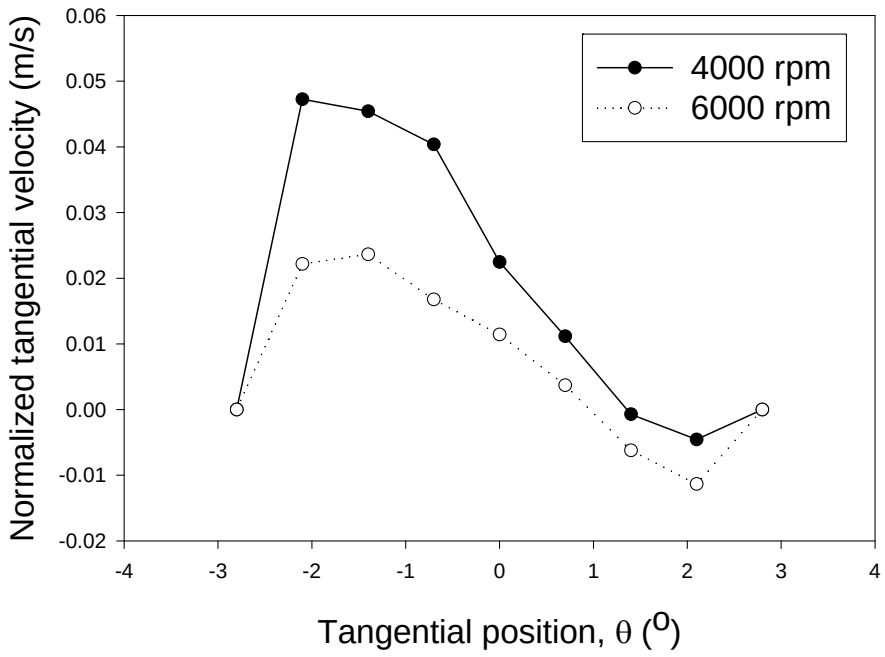

Figure 4-66: Normalized angularly averaged tangential velocity profiles along line 1 (Figure 4-50) at 4000 and 6000 rpm.

4.6.3 The turbulent fields at 4000 and 6000 rpm

The turbulent kinetic energy (TKE) fields on the mid-plane inside the sliding mesh envelope at 4000 and 6000 rpm are shown in Figure 4-67 and the TKE fields outside the sliding mesh envelope are shown as Figure 4-68. The TKE fields are normalized by the tip speed squared (34.68 m/s at 4000 rpm and 78.04 m/s at 6000 rpm). These contours suggest that the TKE fields at 4000 and 6000 rpm are quite similar to each other. The high TKE regions exist in the rotor swept volume and close to the stator slot openings. Outside the envelope, the high TKE magnitude regions coincide with the four jets shown in Figure 4-53.

The TKE fields normalized by the rotor tip speed squared close to the stator slot 1 on the mid-plane (in Figure 4-8) at 4000 and 6000 rpm are shown in Figure 4-69 and 4-70. From these figures, it can be found that the TKE magnitude is affected by the rotor blade position relative to the stator slot openings. The highest TKE occurs in relatively small region close to the leading edges of the stator slot when the rotor blade is approaching the stator slot.

In this research, the turbulent energy dissipation rate fields were investigated. However, it is known that prediction of magnitude and spatial variation of TDR is inaccurate in stirred tanks. It could be the same here.

The turbulent energy dissipation rate (TDR) fields on the mid-plane inside the sliding mesh envelope at 4000 and 6000 rpm are shown in Figure 4-71 and the TDR fields outside the sliding mesh envelope are shown as Figure 4-72. The TDR fields are normalized by N^3D^2, where N is the rotor rotation rate and D is the rotor diameter (234.3 m^2/s^3 at 4000 rpm and 790.7 m^2/s^3 at 6000 rpm). These contours suggest that the TDR fields at 4000 and 6000 rpm are quite similar to each other. The high TDR regions exist in the rotor swept volume and close to the stator slot openings. Outside the envelope, the high TDR magnitude region coincides with the four merged jets shown in Figure 4-53.

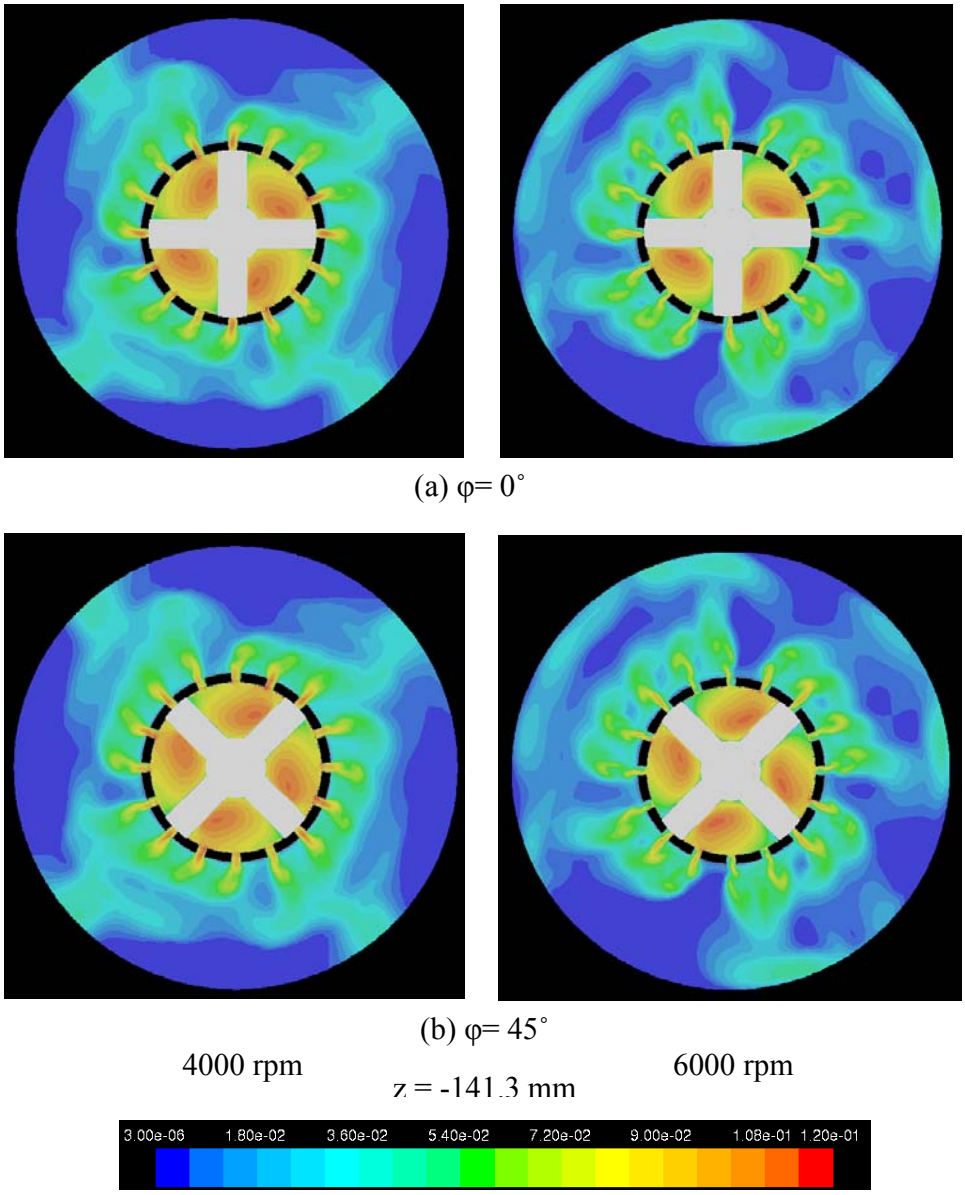

Figure 4-67: Normalized TKE snapshots on mid-plane inside the sliding mesh envelope. The rotor rotates in the anti-clockwise direction.

The TDR fields normalized by N^3D^2 close to the stator slot 1 on the mid-plane (in Figure 4-8) at 4000 and 6000 rpm are shown in Figure 4-73 and 4-74. From these figures, it can be found that the TDR magnitude is affected by the rotor blade position

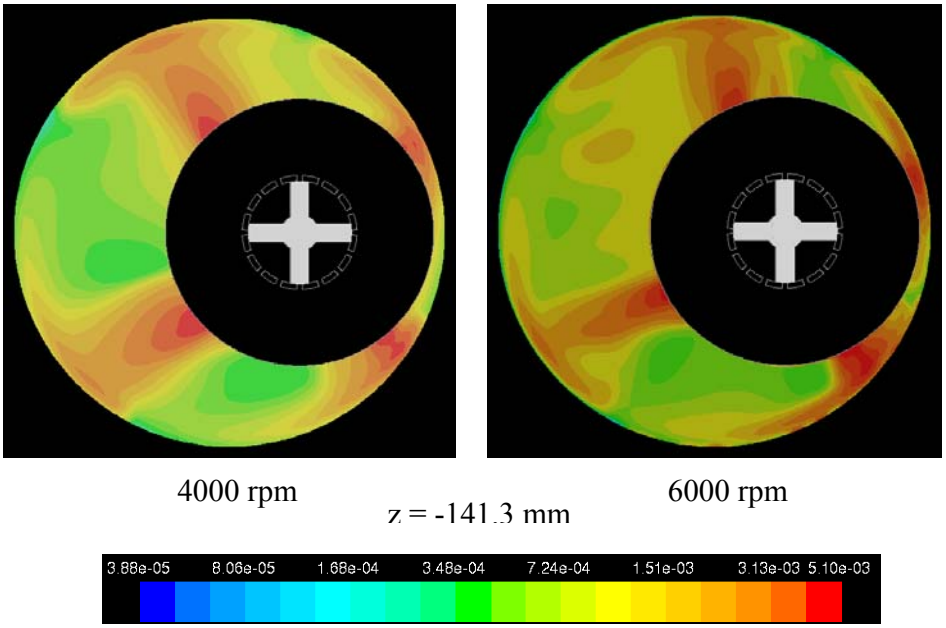

Figure 4-68: Normalized TKE contours at mid-plane outside the sliding mesh envelope.

relative to the stator slot openings. The highest TDR occurs in relatively small region close to the leading edges of the stator teeth when the rotor blade is approaching the stator slot. High turbulent energy dissipation rate is also predicted on the stator teeth wall, which could be the result of the stagnation of fluid on the wall.

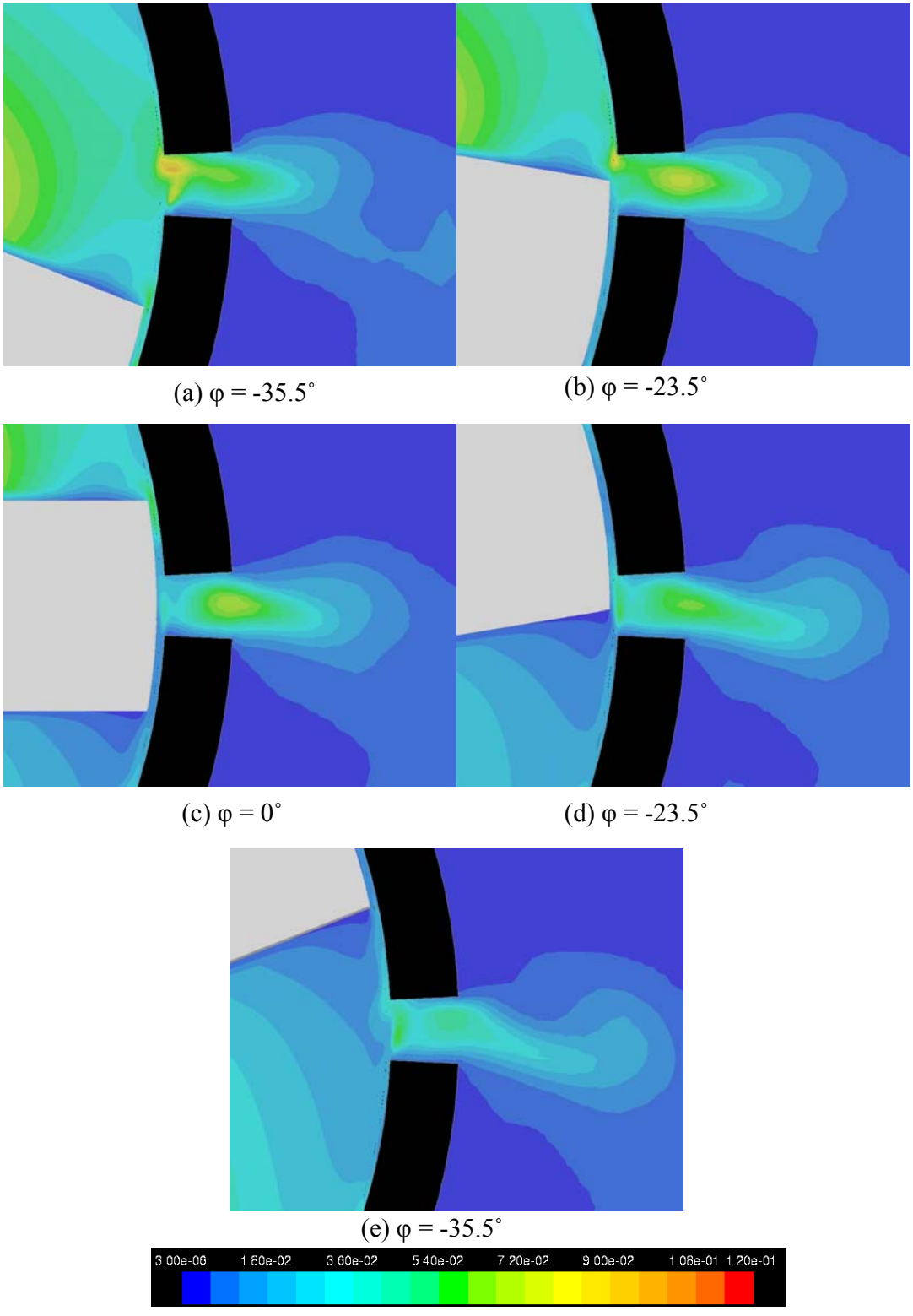

Figure 4-69: Normalized TKE around the stator slot at various blade positions (4000 rpm). The rotor rotates in the anti-clockwise direction.

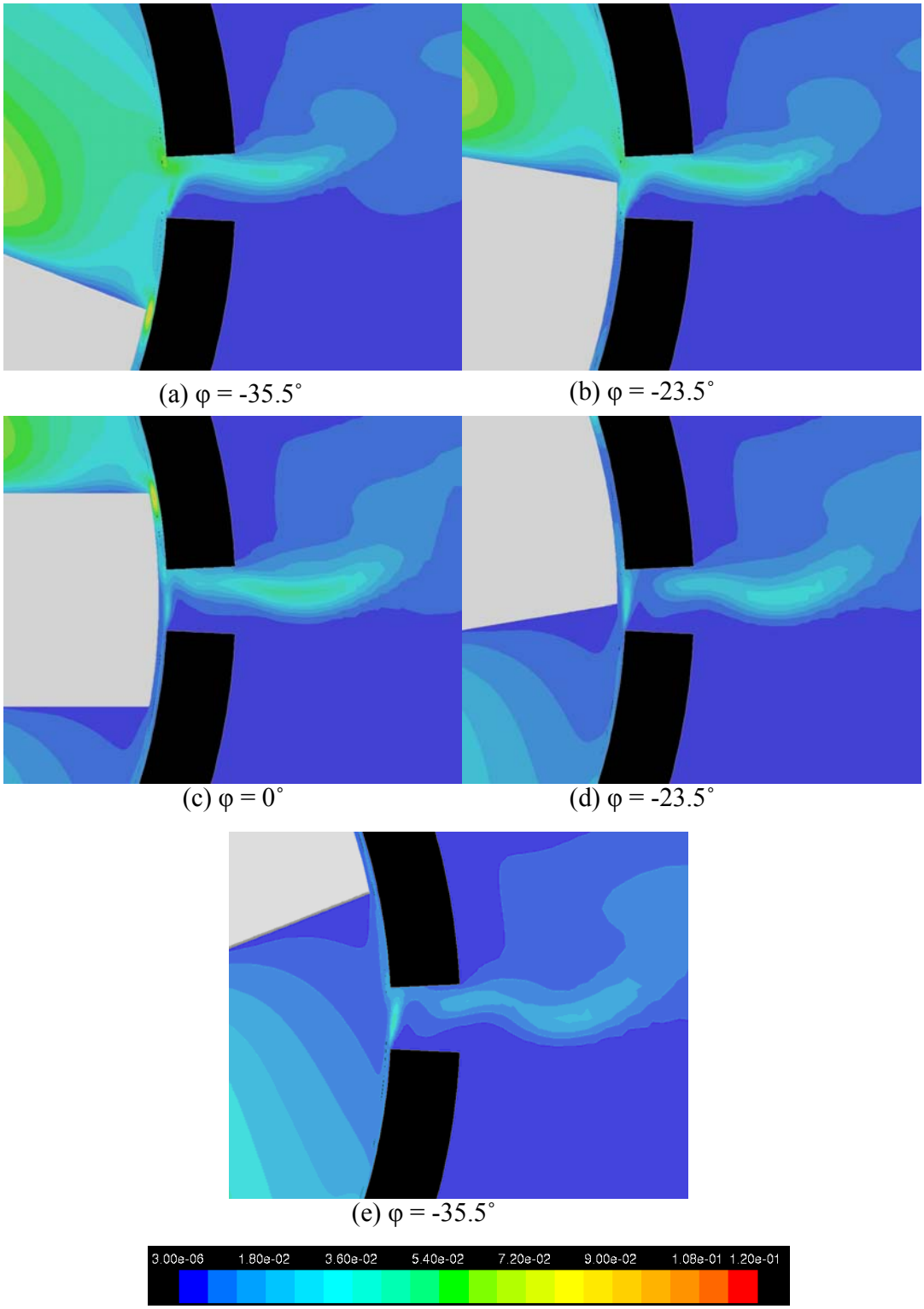

Figure 4-70: Normalized TKE around the stator slot at various blade positions (6000 rpm). The rotor rotates in the anti-clockwise direction.

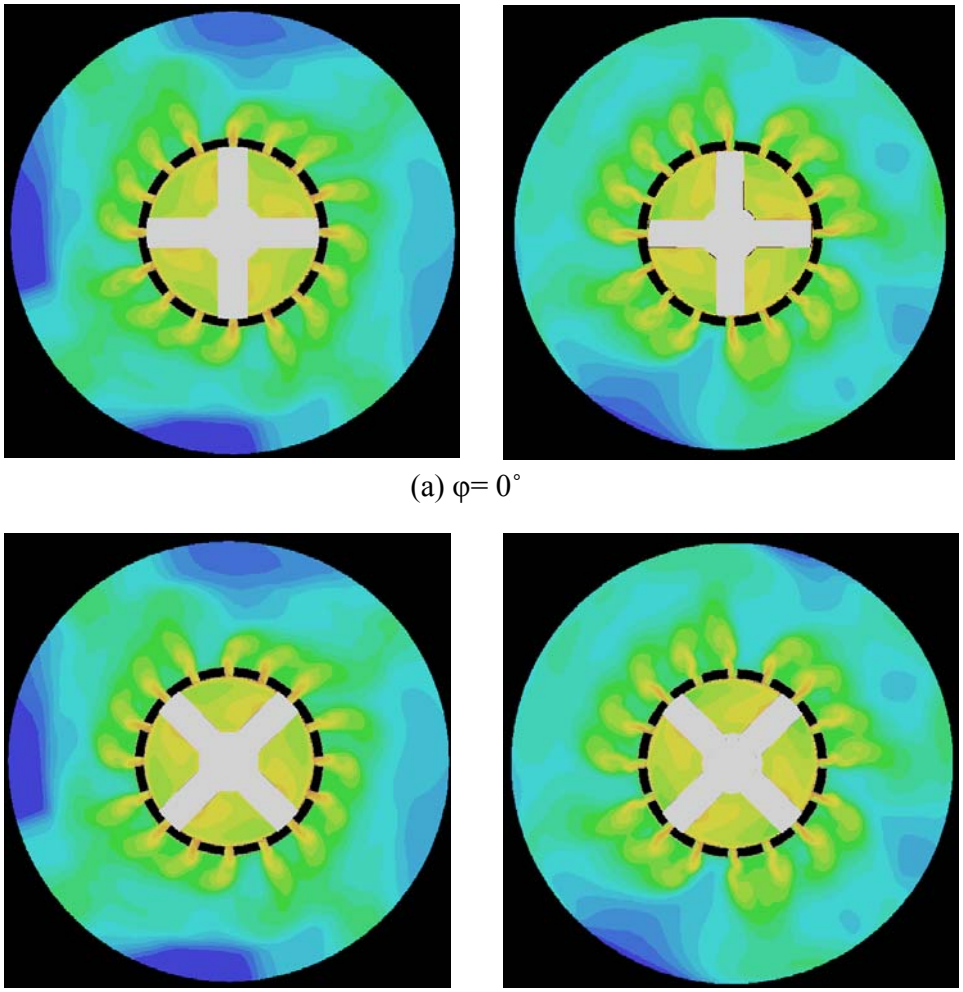

Figure 4-71: Normalized TDR snapshots on mid-plane inside the sliding mesh envelope. The rotor rotates in the anti-clockwise direction.

Figure 4-75 shows different regions in the rotor-stator mixer for turbulent dissipation rate comparisons: rotor swept region, gap region (between the rotor blade and stator teeth), stator slot region and mixer bulk region. Prediction of the distribution of turbulent energy dissipation rate in various region is shown as Table 4-2. Table 4-2

indicates that most of the turbulent energy is dissipated in the region close to the mixing head (about 60% of the total energy). In the mixing head, the majority of the energy is dissipated in the rotor swept volume region while only a small fraction of energy is dissipated in shear gap and stator slot region. The total turbulent energy

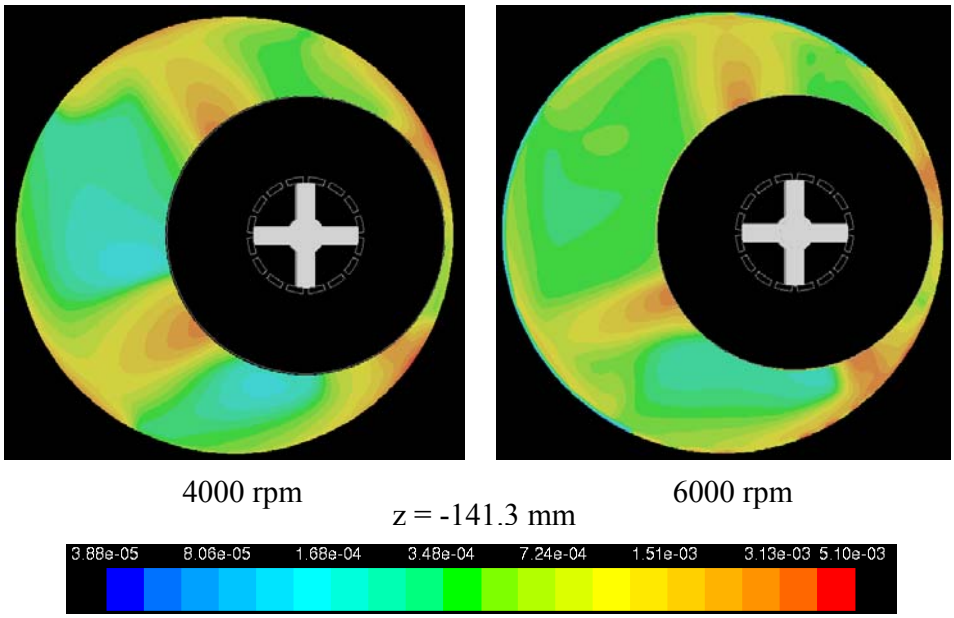

Figure 4-72: Normalized TDR contours at mid-plane outside the sliding mesh envelope.

dissipated in the control volume increase approximately 3.5 times when the rotor rotation rate increase 1.5 times, which indicate that the turbulent energy dissipation rate is proportional to N^3. In addition, the turbulent energy dissipated in the gap region increases from 8.9% at 4000 rpm to 16.3% at 6000 rpm. This may suggest that the turbulent intensity in the high shear gap increase with the rotor speed.

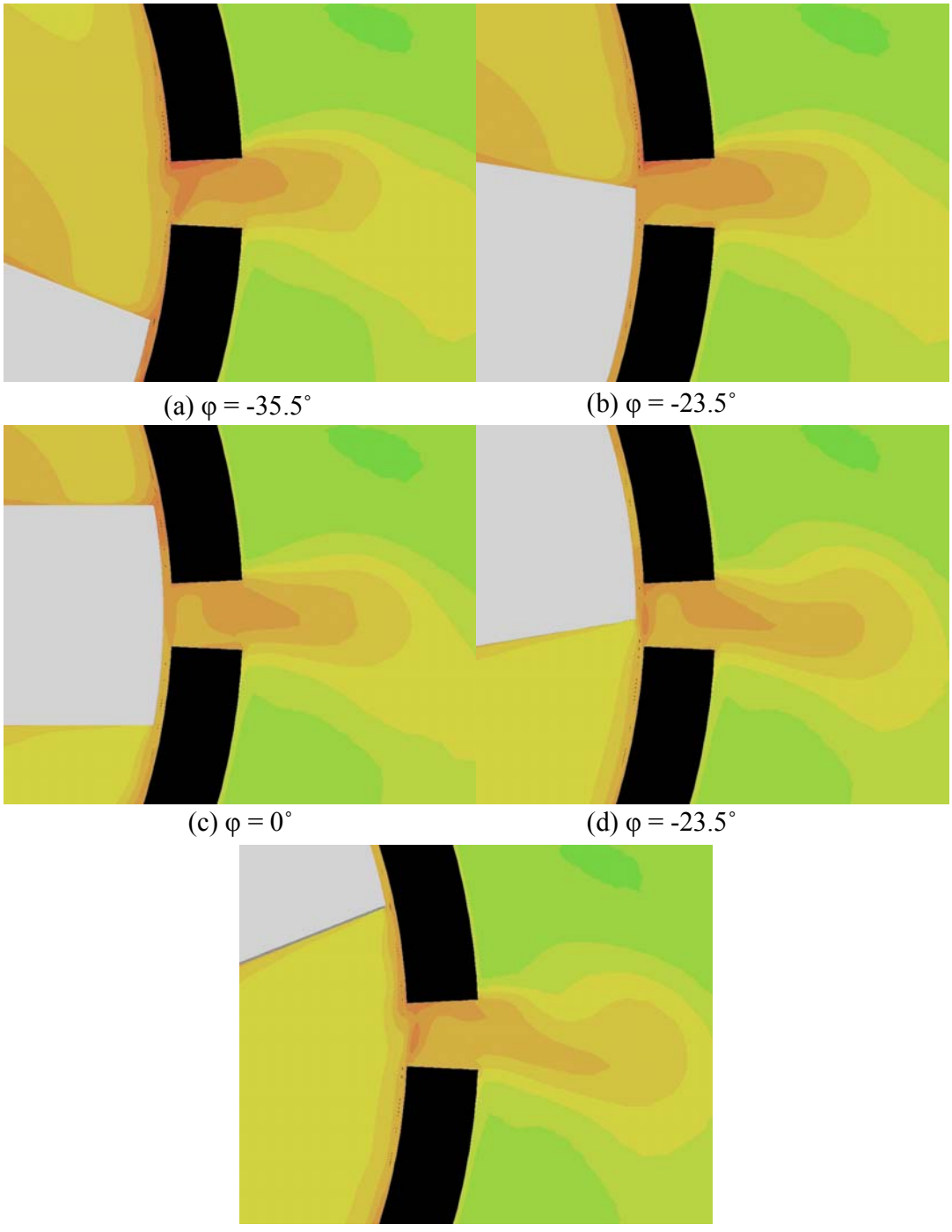

Figure 4-73: Normalized TDR around the stator slot at various blade positions (4000 rpm). The rotor rotates in the anti-clockwise direction.

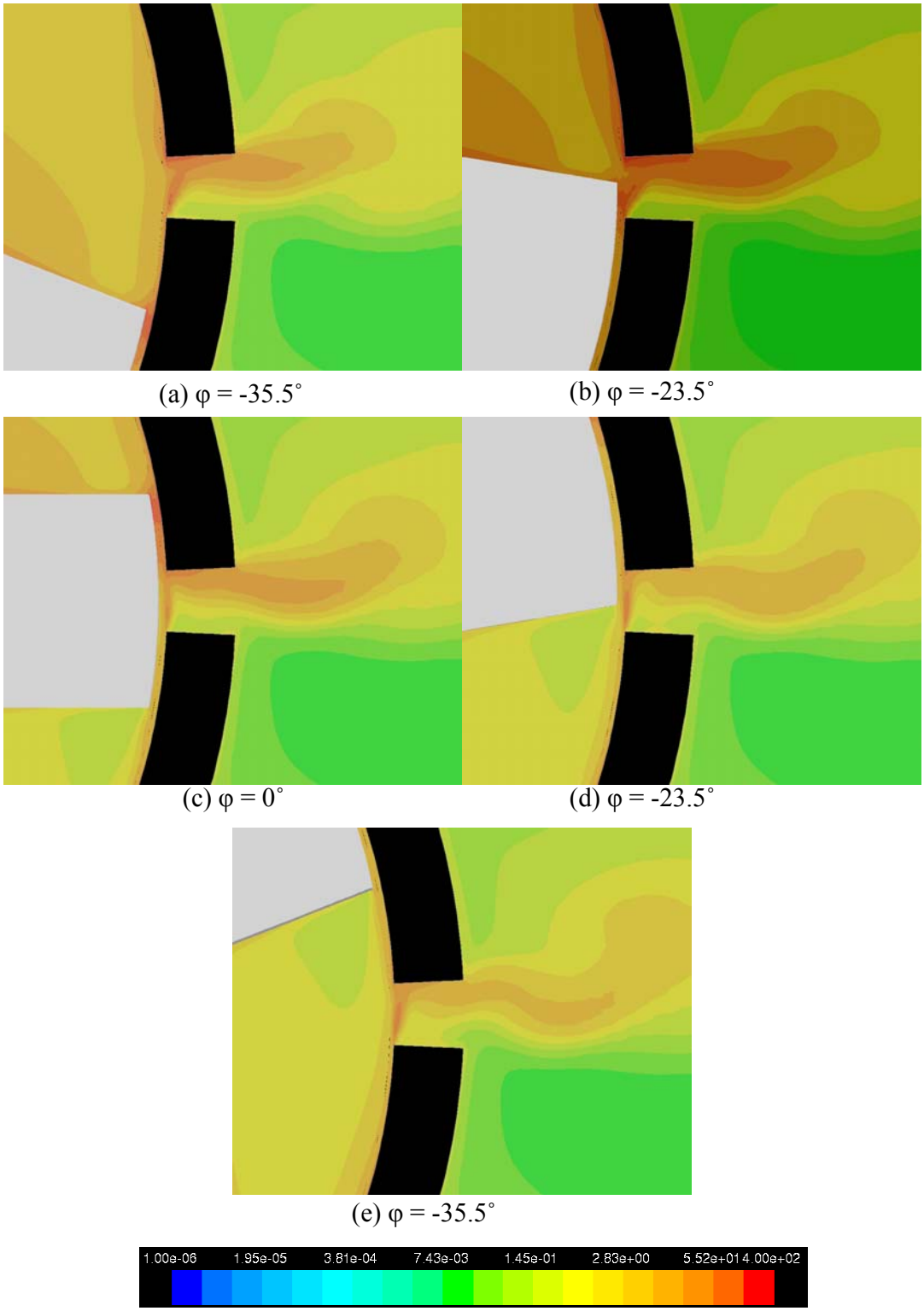

Figure 4-74: Normalized TDR around the stator slot at various blade positions (6000 rpm). The rotor rotates in the anti-clockwise direction.

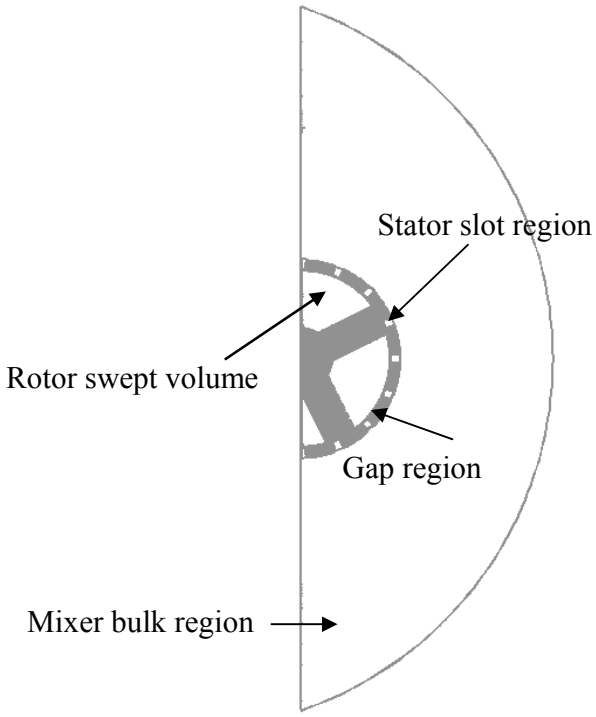

Figure 4-75: Definition of regions in the rotor stator mixer for turbulent dissipation rate comparison.

Table 4-2: Predictions of distributions of turbulent energy dissipated in the tank at 4000 and 6000rpm.

Region	4000 rpm	6000 rpm
Rotor swept volume	0.00287 W (38.2%)	0.00935 W (33.4%)
Gap region	0.00067 W (8.9%)	0.00455 W (16.3%)
Stator slot region	0.00112 W (14.9%)	0.003 W (10.1%)
Mixer bulk region	0.00286 W (38%)	0.0111 W (39.6%)
Total turbulent energy dissipated	0.00752 W (100%)	0.028 W (100%)

4.6.4 The mean deformation fields at 4000 and 6000 rpm

The deformation (shear) fields on the mid-plane inside the sliding mesh envelope at 4000 and 6000 rpm are shown in Figure 4-76 and the mean shear rate fields outside the sliding mesh envelope are shown as Figure 4-77. The shear rate fields are

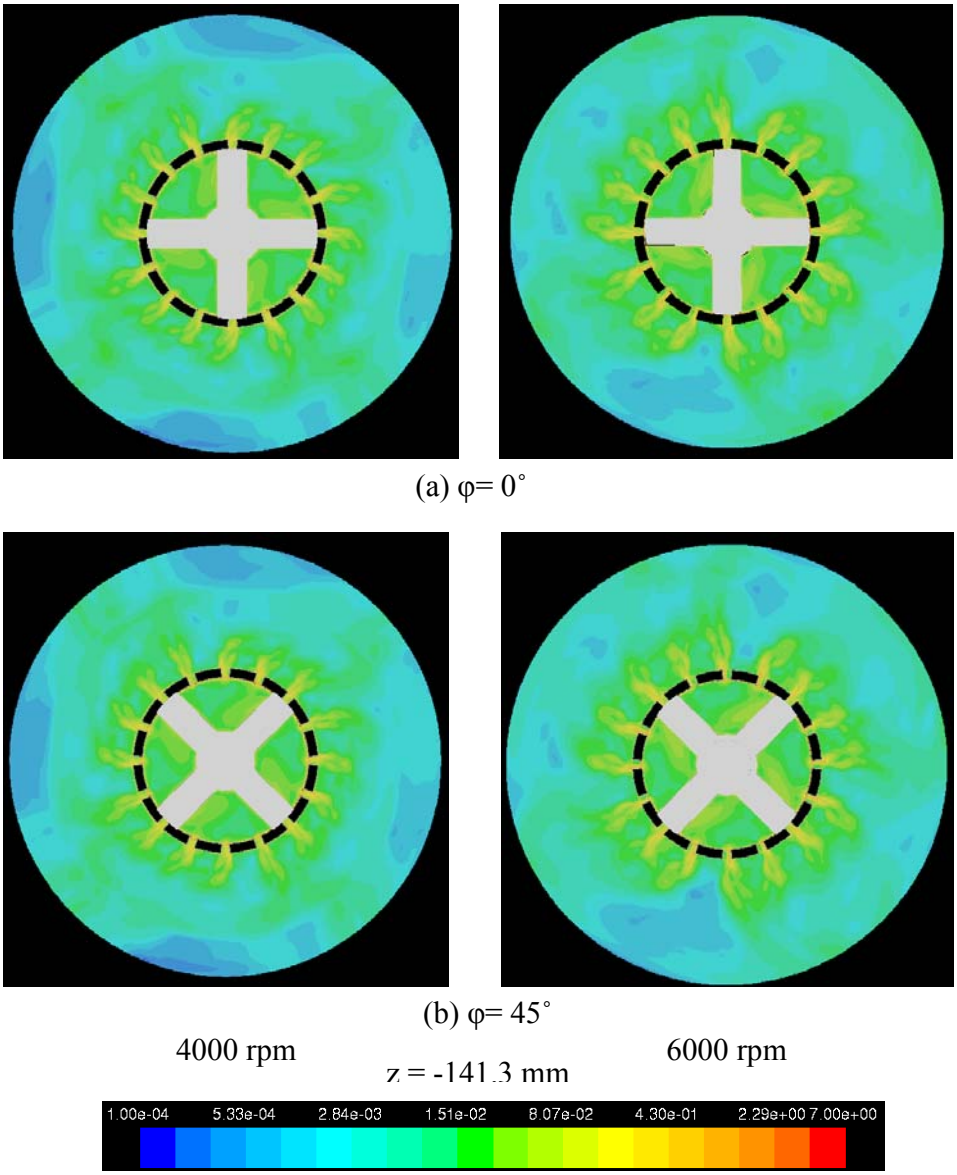

Figure 4-76: Normalized shear rate contours on mid-plane inside the sliding mesh envelope. The rotor rotates in the anti-clockwise direction.

normalizedby nominal shear rate (29450 /s at 4000 rpm and 44175 /s at 6000 rpm), which is defined by Equation 4.6.3, where $\dot{\gamma}$ is the nominal shear rate, V_{tip} is the rotor tip

$$\dot{\gamma} = \frac{V_{tip}}{\delta_{gap}} \tag{4.6.3}$$

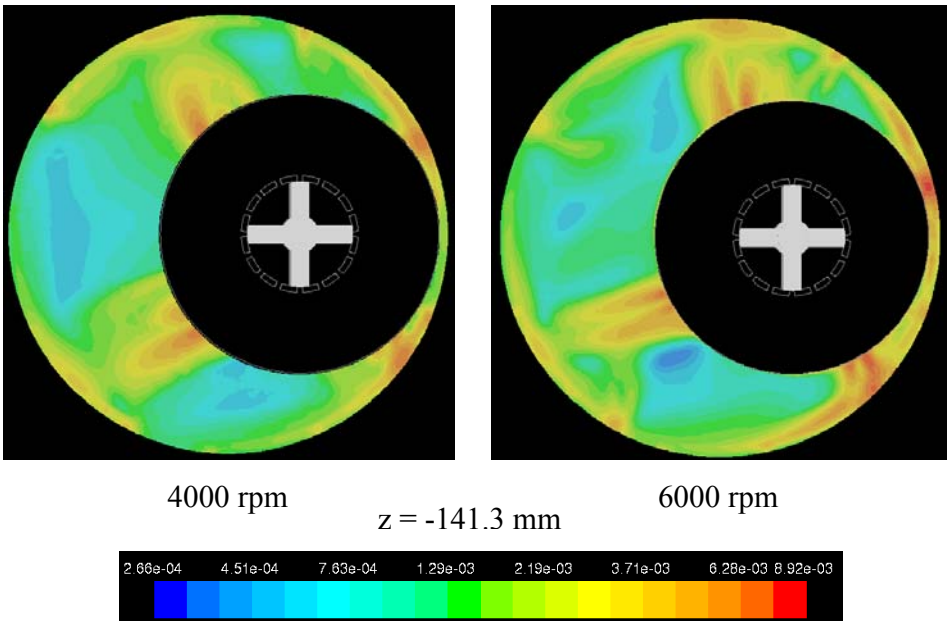

Figure 4-77: Normalized mean shear rate contours at mid-plane outside the sliding mesh envelope.

speed and δ_{gap} is the shear gap size between the rotor blade and stator teeth. These contours suggest that the mean shear rate fields at 4000 and 6000 rpm are quite similar to each other. The high shear rate regions exist in the rotor swept volume and close to the stator slot openings. Outside the envelope, the high shear rate region coincides with the four jets shown in Figure 4-53.

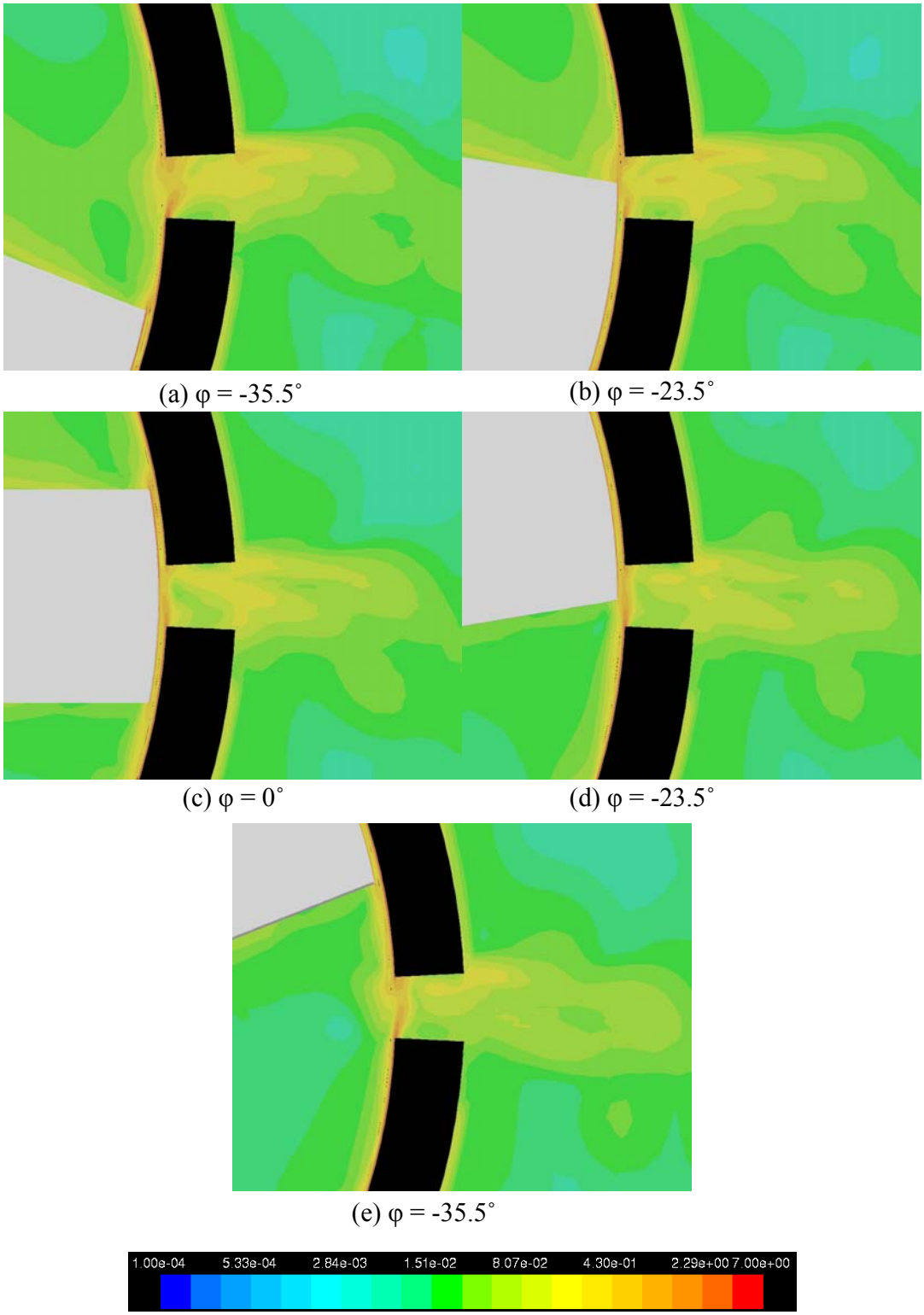

Figure 4-78: Normalized mean shear rate around the stator slot at various blade positions (4000 rpm). The rotor rotates in the anti-clockwise direction.

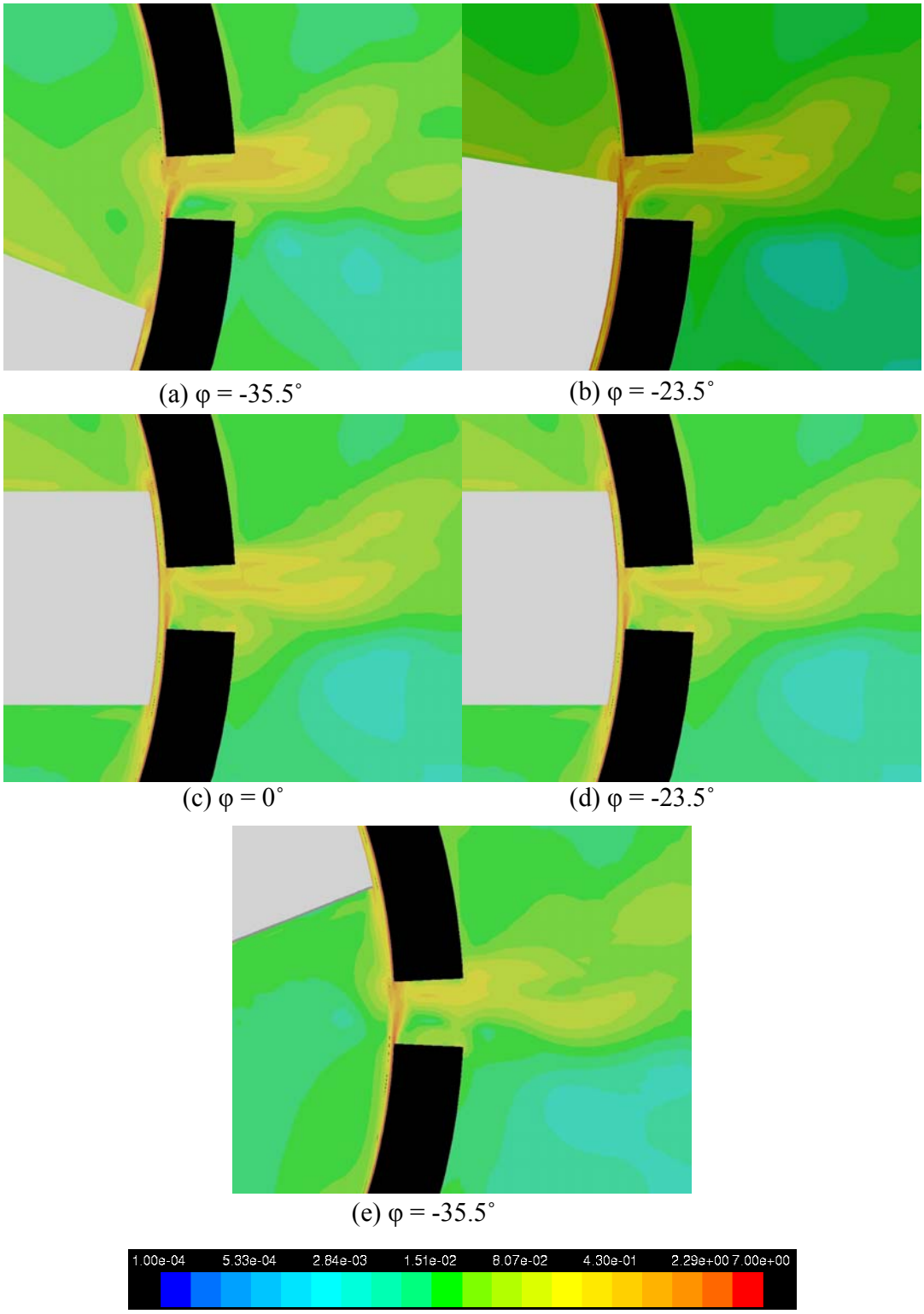

Figure 4-79: Normalized mean shear rate around the stator slot at various blade positions (6000 rpm). The rotor rotates in the anti-clockwise direction.

The mean shear rate fields normalized by nominal shear rate close to the stator slot 1 on the mid-plane (in Figure 4-8) at 4000 and 6000 rpm are shown in Figure 4-78 and 4-79. From these figures, it can be found that the shear rate magnitude is affected by the rotor blade position relative to the stator slot openings. The highest shear rate occurs in a relatively small region close to the leading edges of the stator teeth when the rotor blade is approaching. In addition, the shear rate is also higher at 6000 rpm that at 4000 rpm.

4.6.5 Calculation of solid particles trajectories in Silverson L4R batch rotor-stator mixer

The motion of solid particles in fluid flows is a widely encountered phenomenon in chemical engineering processes such as crystallization, particle breakage, and so on. Also how particle size change with time in chemical engineering process is very important to evaluate and improve the final product qualities. In this work, to investigate solid particle behavior in Silverson L4R batch rotor-stator mixer and the shear stress exerted on these particles, small solid particles are introduced into the fully converged single phase mean flow field. Since in most cases, the size of the particles and their concentration are relatively small, their effect on the flow and the interaction between particles and flow can be neglected. As a result the dynamics of particles has no effect on the fluid flow. It is well known that the particle behavior in a flow can be described by the Basset-Boussinesq-Oseen (BBO) equation which is shown as

$$\frac{d^2\bar{X}_p}{dt^2} = \frac{3\mu \mathrm{Re} C_D}{4d_p^2\rho_p}\left(\frac{d\bar{X}_p}{dt} - \bar{V}_f\right) + \frac{\rho_p - \rho_f}{\rho_p}\bar{g} + \frac{1}{2}\frac{\rho_f}{\rho_p}\left(\frac{D\bar{V}_f}{Dt} - \frac{d^2\bar{X}_p}{dt^2}\right) + \frac{\rho_f}{\rho_p}\frac{D\bar{V}_f}{Dt} \quad (4.6.4)$$

where $\bar{X}_p$ is the coordinate of the particles, t is time, μ is the fluid viscosity, Re is the particle Reynolds number, C_D is the drag coefficient, d_p is the particle diameter, ρ_p is the particle density, $\bar{g}$ is the gravitational acceleration, and $\bar{V}_f$ is the fluid velocity. During the particle tracking calculation process, the flow field, $\bar{V}_f$, is extracted from the fully converged pure water simulations results.

This fast particle tracking code is initially developed in C# by Karl R. Kevala in our group. This method is a one way coupling model. Because of the time periodic behavior in Silveron L4R batch rotor-stator mixer, only 90º (quarter revolution) of the flow field data are required. After 90º of rotation, the flow field will repeat. Since the fully converged 90 º flow field data has been obtained in the previously discussed single phase simulation, only the motion of particles is calculated. As a result particles trajectories can be predicted by this fast particle tracking code in a relatively short time compared with the multi-phase DPM model available in Fluent.

In this work, ten thousand solid spherical particles are released below the rotor. These particles are of neutral buoyancy (density is same as the fluid water, 998.2 kg/m^3) and the diameter is 25 μm. The particles trajectories are recorded for 80 rotor revolutions. Some trajectories of particles at 4000 and 6000 rpm are shown as Figure 4-80 and 4-81 respectively. The shear rate history experienced by the particles can be

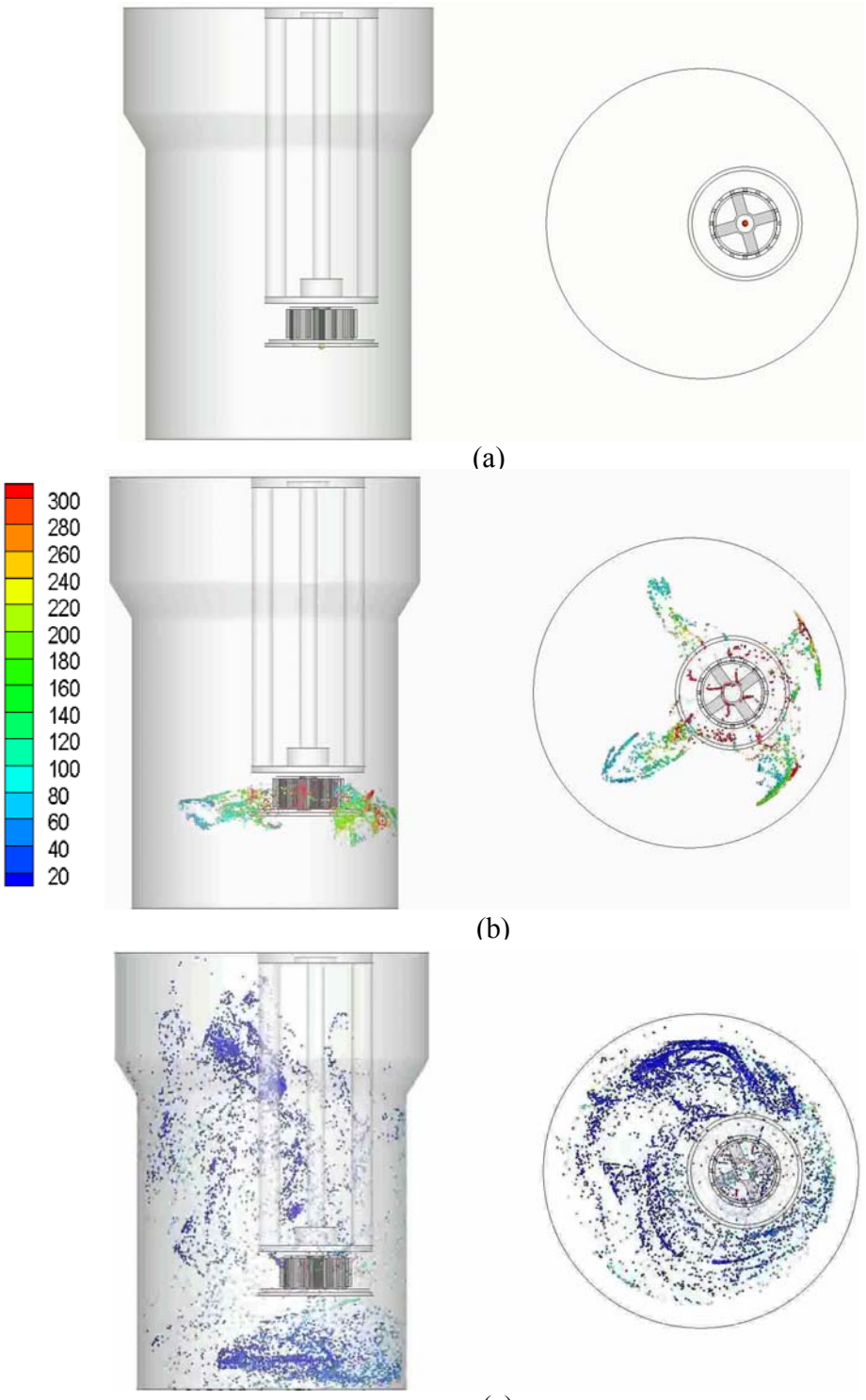

Figure 4-80: Particle tracking at 4000 rpm colored by mean shear rate.

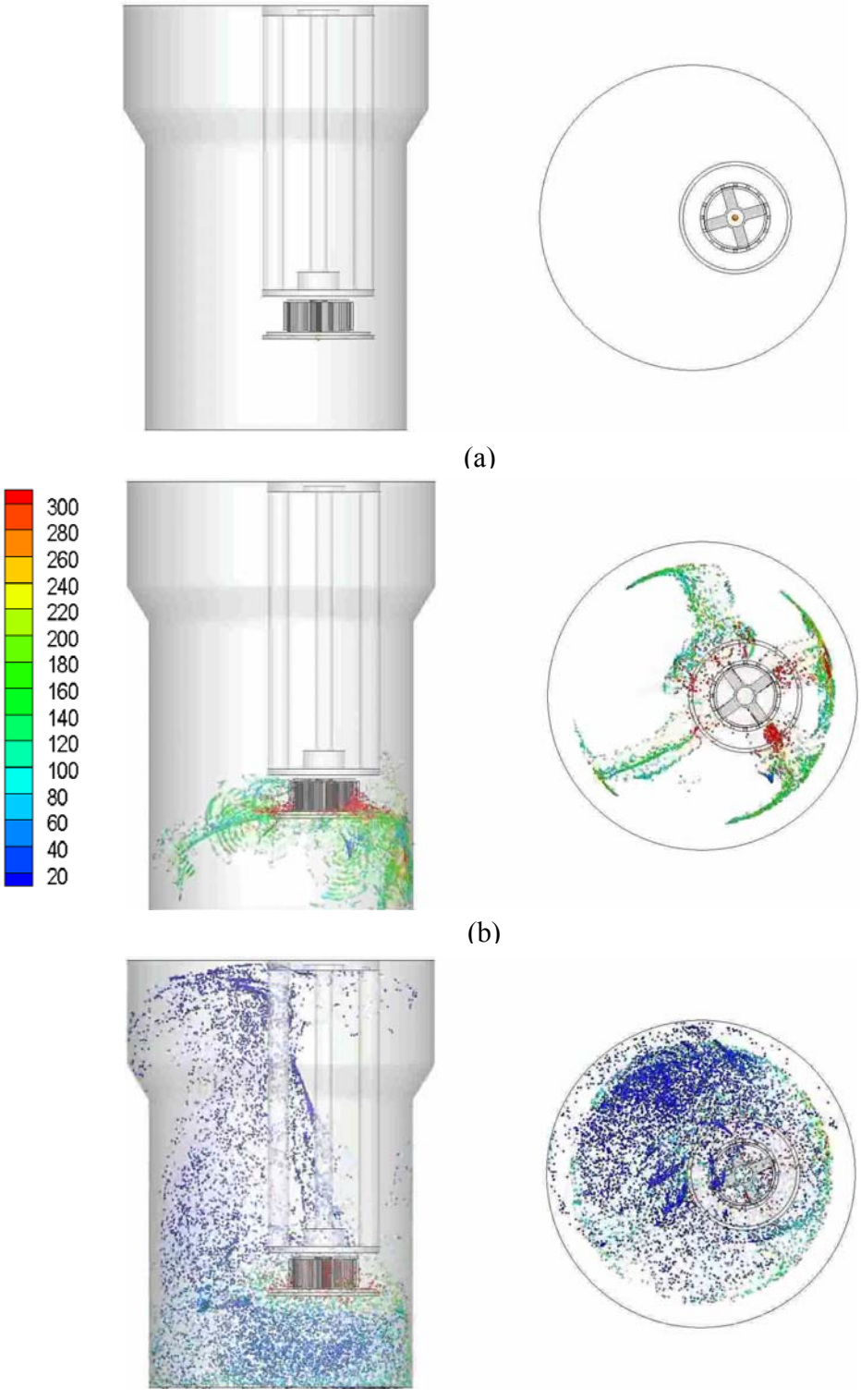

Figure 4-81: Particle tracking at 6000 rpm colored by mean shear rate.

recorded during the simulation by this fast particle tracking model. The legend color shows the deformation rate acting on the particle at its current location. The maximum shear rates are experienced in the high shear region Because only in a small region close to the mill head exhibits high deformation rate, so the lengend is limited to less than 300 /s. Otherwise, there is no color contrast between the particles. From these figures, the particles follows the flow field very well and their trajectories are significantly influenced by the 4 merged jets.

As far as the particle circulation time distribution (CTR) is concerned, thousands of revolutions are required to obtain reasonable statistical CTR data which is unaffordable for our current serial solver particle tracking code. To resolve this difficulty, the fast particle tracking code has to be parallelized, which will be the future work of our group.

Above all, from the simulation results, it can be concluded that this model gives realistic particle trajectory prediction. Since only particles motion need to be calculated, the computational time is reduced significantly. In addition, the particle properties, including particle density and size, and particle introduction position can be adjusted conveniently in the model.

4.6.6 PIV validation of the flow field in Silverson L4R batch rotor-stator mixer

Particle image velocimetry (PIV) is a non-intrusive experimental method for the simultaneous measurement of the instantaneous velocities at numerous points in a flow field[30]. The flow is seeded with particles (called seeding or tracer particles) that are sufficiently small enough so that they can accurately follow the fluid. A light sheet generated by a double-pulsed laser is used to illuminate the tracer particles in a plane along the direction of the flow. The light scattered by the tracer particles is recorded by a CCD camera (the camera view axis is perpendicular to the excitation plane of the light sheet) and two consecutive images corresponding to double-pulse laser light source are obtained. The displacement of trace particles that are carried by the fluid during the given short time is estimated with a cross-correlation technique that analyzes particle-pattern in small sub-domain, or called interrogation window, between the two images. The fluid velocity is determined by dividing the particle displacement by the short time interval.

This work utilized the PIV technique to investigate the flow filed in the Silverson batch mixer at 4000 rpm to aid in validation of the CFD results[31]. In this experiment, a PIV system from LaVision Inc. was used. The system includes a CCD camera, a double-pulsed Nd:YAG laser and an PIV software for image processing. The seeding particles were glass spheres made by Potters Industries Inc. with an average diameter of about 10 micron. A circular laser beam from Nd:YAG laser with a wavelength of 532 nm is shaped into a thin sheet by means of cylindrical lenses. In the experiment,

the laser sheet was shot into the Silverson L4R batch rotor-stator mixer from the side wall and the camera was placed below the mixer bottom to record the images. Because of the limitation of the PIV system memory, only about 80 realizations were allowed, which were not enough for an accurate PIV experiment.

The only purpose of these experiments was to validate the existence of the four steady jets found in the CFD simulation (Figure 4-54), so very crude experiments were

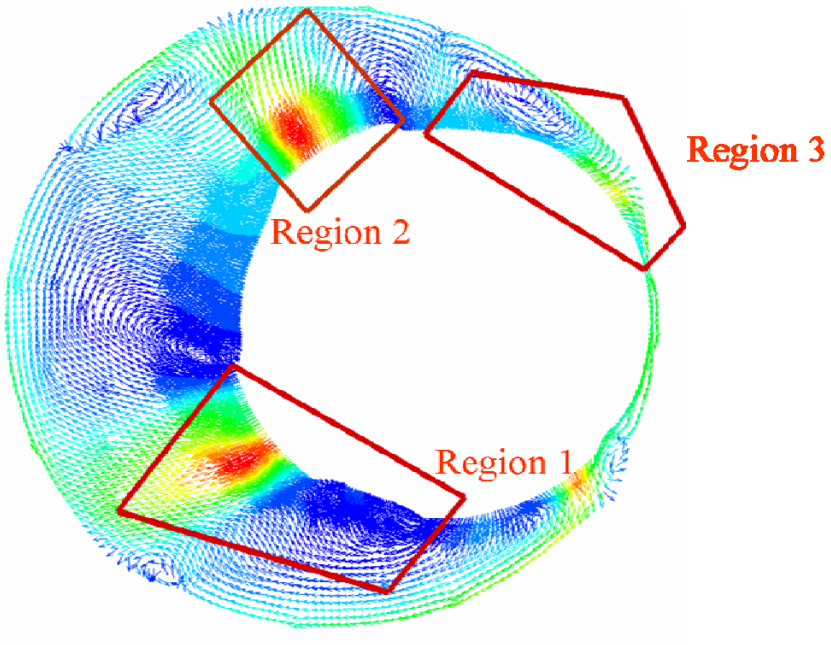

Figure 4-82: The regions focused on in PIV experiments superimposed on the CFD results.

performed. PIV data were acquired in the regions shown in Figure 4-82 on four horizontal planes (mid-plane, 2mm below mid-plane, 4mm below mid-plane and 6mm below mid-plane). These four planes were selected because the traversing system of the PIV is very limited and the mid-pane was the highest level the laser sheet could reach.

The vector maps of RANS simulations and time averaged PIV experiments over-realizations are shown as Figures 4-84, 4-85 and Figure 4-86. It is found from these figures that the predicted results are qualitatively similar to the PIV results. The steady jets in region 1, 2 and 3 are found both in the simulations and the experiments. It is also seen from the figures that the results in region 2 and 3 are better than those in region 1. This may result from the experiment operation. In the measurement of region 2 and 3, the tank was kept stationary relative to the mixing head. However, during the measurement of region 1, the tank was rotated to capture the merged jets, but the mill head was kept stationary. As a results, the relative position of the vertical screws connecting the top and bottom plate to hold the stator was different for each experiment. The regions where the jets exist move correspondingly so that the regions actually measured in the experiments are not the targeted regimes where the jets are.

4.7 Summary

This chapter presents the CFD simulation and validation of the flow field in a Silverson L4R batch rotor-stator mixer. A mesh independence test was performed to determine suitable cell number for the simulation. As a result, a well constructed 3D mesh composed of 4.6 million hexahedral cells was created. Hybrid technique was developed to allow the simulation to reach convergence at reasonable computational expense, which reduced the computation time dramatically compared with the traditional sliding mesh technique. The hybrid simulations have been completed at 4000 and 6000 rpm. Macroscopic properties, including pumping capacity, pumping

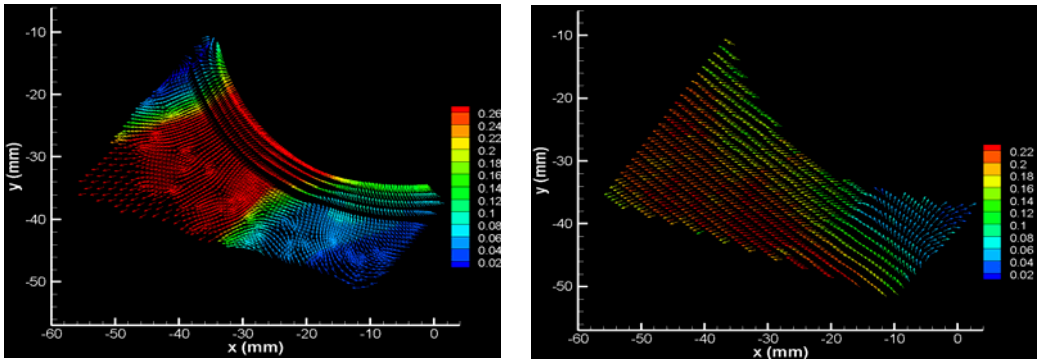

Vector field on mid-plane (z = -141.3 mm)

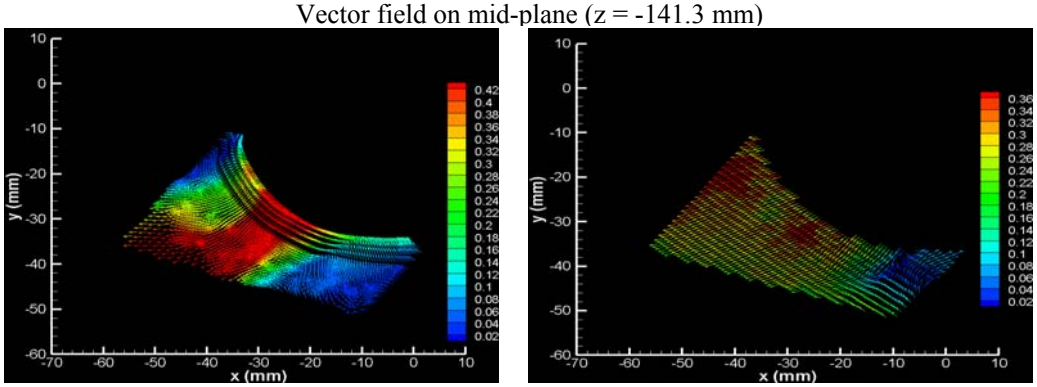

Vector field on the plane 2 mm below mid-plane (z = -143.3 mm)

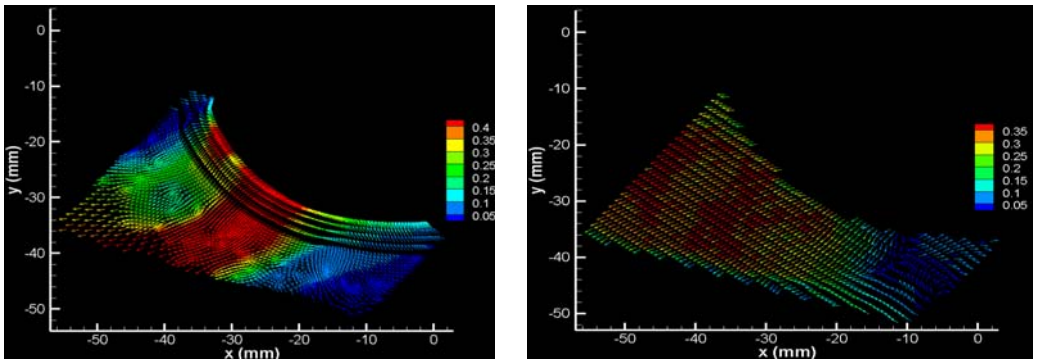

Vector field on the plane 4 mm below mid-plane (z =-145.5 mm)

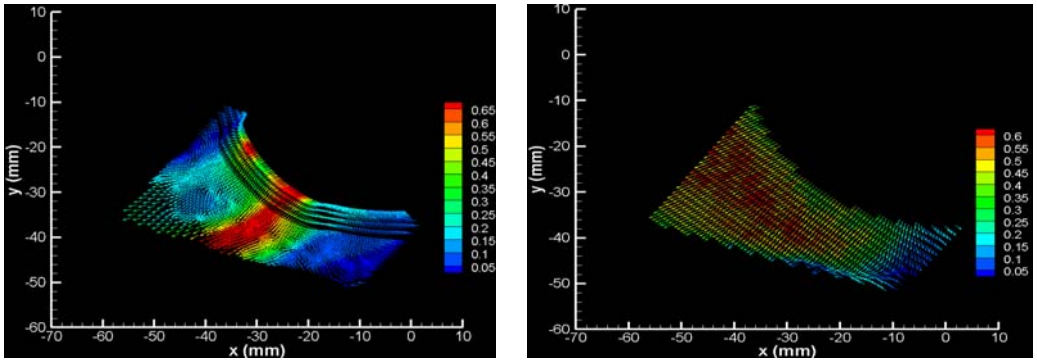

Vector field on the plane 6 mm below mid-plane (z =-147.5 mm)

(a) RANS simulation (b) PIV experiment

Figure 4-83: Vector fields of RANS simulation and PIV in region 1.

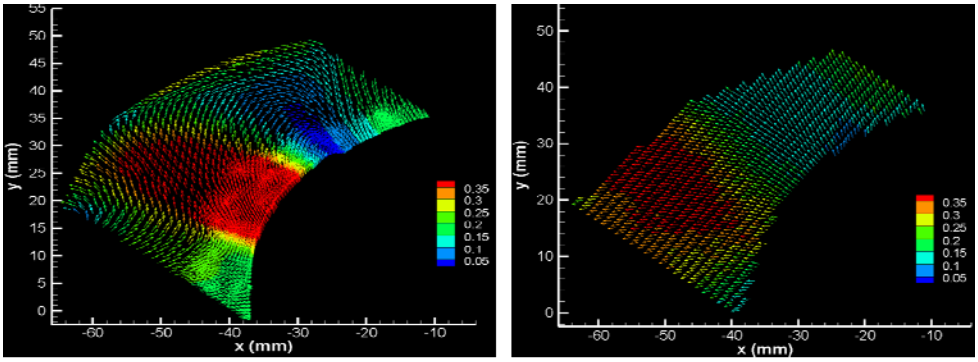

Vector field on mid-plane (z = -141.3 mm)

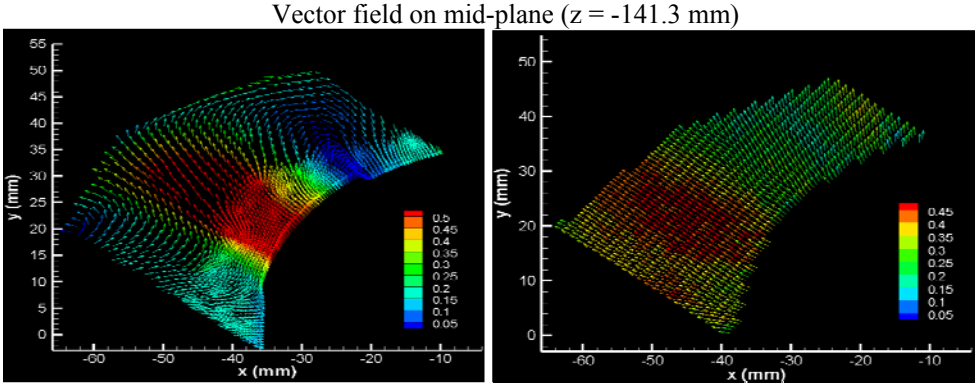

Vector field on the plane 2 mm below mid-plane (z = -143.3 mm)

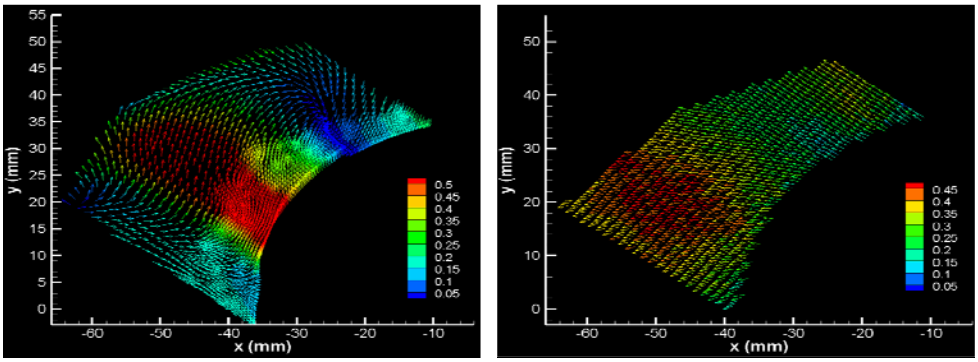

Vector field on the plane 4 mm below mid-plane (z =-145.5 mm)

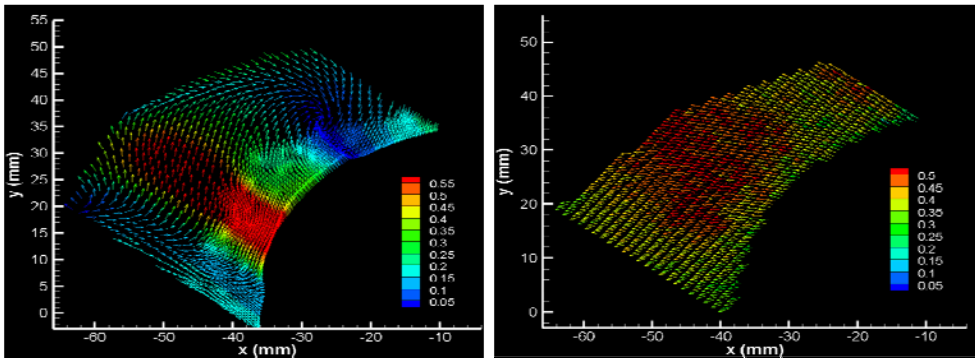

Vector field on the plane 6 mm below mid-plane (z =-147.5 mm)

(a) RANS simulation (b) PIV experiment

Figure 4-84: Vector fields of RANS simulation and PIV in region 2.

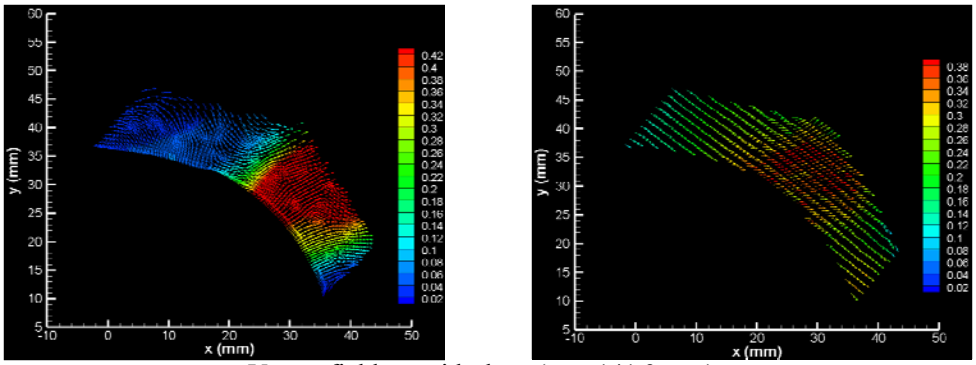

Vector field on mid-plane (z = -141.3 mm)

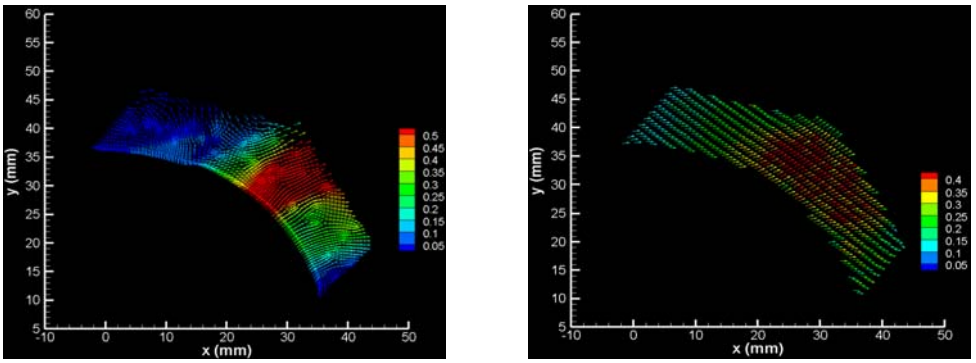

Vector field on the plane 2 mm below mid-plane (z = -143.3 mm)

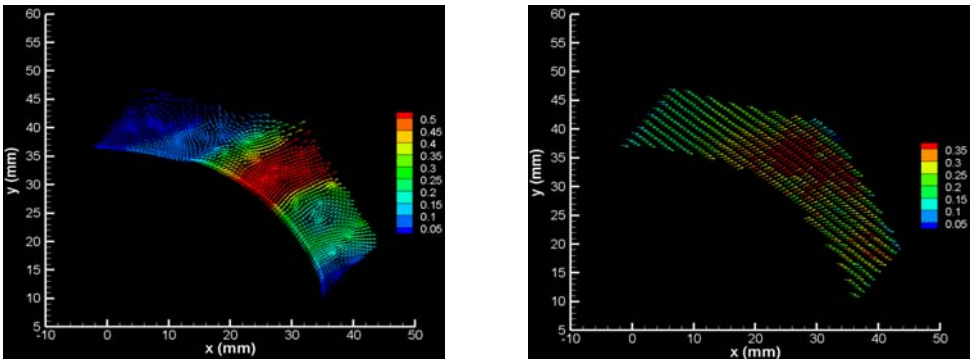

Vector field on the plane 4 mm below mid-plane (z = -145.3 mm)

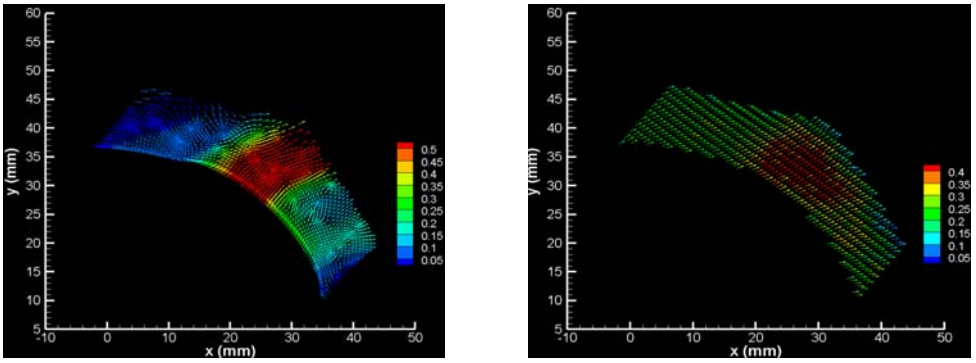

Vector field on the plane 6 mm below mid-plane (z = -147.3 mm)

(a) RANS simulation (b) PIV experiment

Figure 4-85: Vector fields of RANS simulation and PIV in region 3.

number and power number, are computed based on the simulation results. The simulated power number compares favorably with experimental data. The mean velocity, turbulence and deformation rate field were also investigated and discussed. After the well converged flow field is obtained, neutrally buoyant solid spherical particles are introduced into the flow field. Particle trajectories and shear rate history are predicted by a fast particle tracking model, which decreases the computation time significantly compared with traditional multi-phase DPM model. PIV experiments were conducted to validate the flow pattern in the mixer at 4000 rpm. It is found that the results were disappointing and only 1 jet was captured.

Chapter 5: RANS Simulation of Silverson Inline Rotor-Stator Mixer at Lab, Pilot and Plant Scale

For general scale-up process, constant nominal shear rate (tip speed over Rotor-Stator gap width) is maintained as the scale up criterion. In the simulation, when the rotation rate for the Silverson L4R, 450LS and 600LS are 8000, 2100 and 1575 rpm respectively, the tip speed is the same, 12.6 m/s, for the 3 mixers. The gap width is constant so that the nominal shear rate is constant. In this chapter, the scale up effect on the flow properties based on constant nominal shear rate (tip speed) is discussed.

This chapter also presents the results of CFD simulation of the flow field in Silverson inline rotor-stator mixers at lab, pilot and plant scales. The grids of these mixers were generated by use of the automated mesh generator Harpoon in conjunction with Gambit and Tgrid. Macroscopic properties are predicted and compared with experimental results. The mean velocity, turbulent and deformation rate fields of the 3 different scale mixers are also predicted and compared. To investigate the inlet flow rate effect, a simulation of the Silverson inline 450LS at 2100 rpm was performed at the same flow rate per slot condition as the L4R at 8000 rpm.

5.1 Geometries and flow conditions

5.1.1 Geometry of Silverson L4R inline lab scale rotor-stator mixer

The lab scale inline high shear mixer, Silverson L4R, investigated herein is shown in Figure 5-1 and several parts in the simulation are shown as Figure 5-2. The rotor is a 4 blade impeller of diameter 31.24 mm. The high shear gap between the rotor and stator, where the highest shear rate exists, is 0.2 mm. The square hole stator head was used in this study . There are 104 square hole slots on the stator head. The size of the opening in the stator head is 2.4 mm * 2.4 mm * 2 mm. The thickness of the stator is 2 mm. The height and diameter of the stator are 18.9 mm and 31.5 mm, respectively.

5.1.2 Geometry of Silverson 450LS inline pilot scale rotor-stator mixer

The pilot scale inline high shear mixer, Silverson 450LS, investigated is herein shown

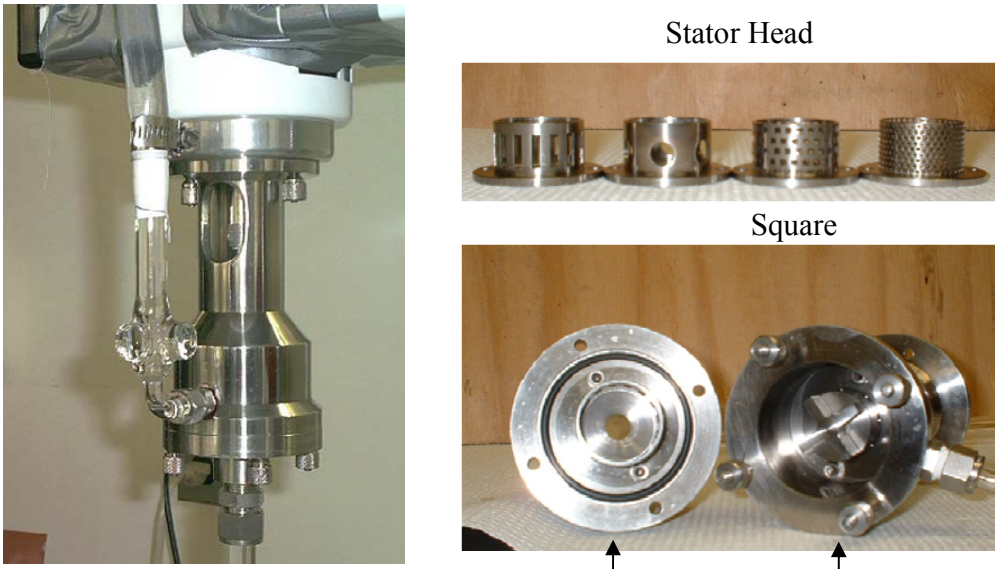

Figure 5-1: Silverson Inline Lab Scale L4R Rotor Stator Mixer.

in Figure 5-3 and several parts in the simulation are shown as Figure 5-4. The rotor is a 4 blade impeller of diameter 114.3 mm whose geometry is different from that of the

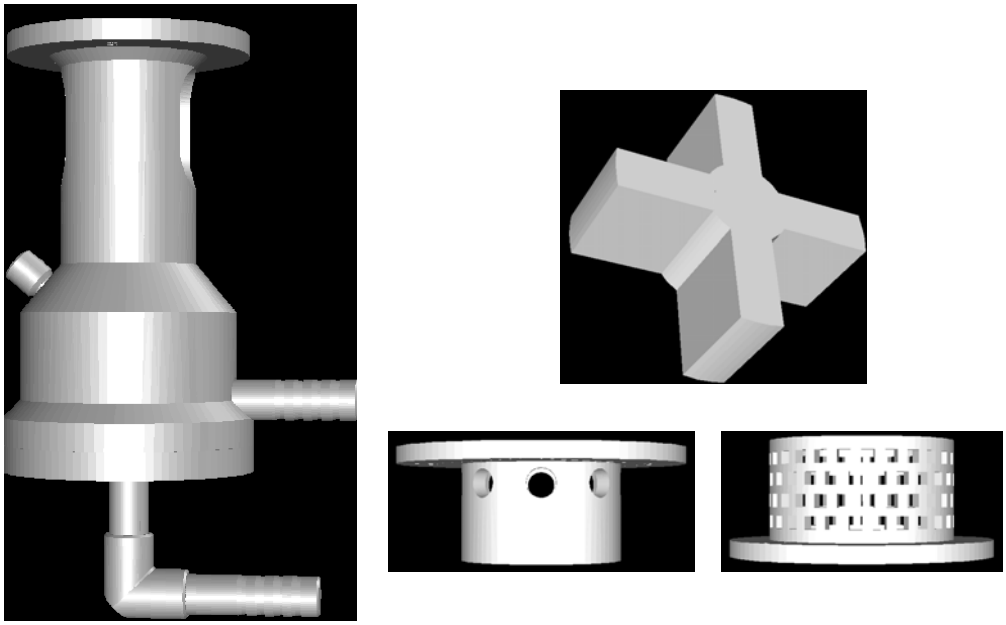

Figure 5-2: Silverson L4R batch rotor-stator mixer geometry.

Silverson inline 450LS
Rotor-Stator Mixer Assembly

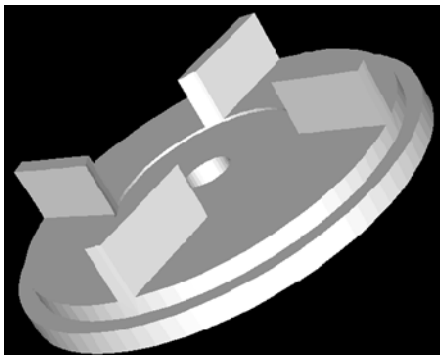

Rotor

Figure 5-3: Silverson Inline Pilot Scale 450LS Rotor Stator Mixer.

lab scale L4R mixer. The high shear gap between the rotor and stator, where the highest shear rate exists, is 0.2 mm. The square hole stator head was used in this study too . There are 560 square hole slots on the stator head. The size of the stator opening is the same as that of L4R. The thickness of the stator is 2 mm. The height and diameter of the stator are 30.9 mm and 114.6 mm, respectively.

5.1.3 Geometry of Silverson 600LS inline plant scale rotor-stator mixer

The plant scale inline high shear mixer, Silverson 600LS, is very similar to the

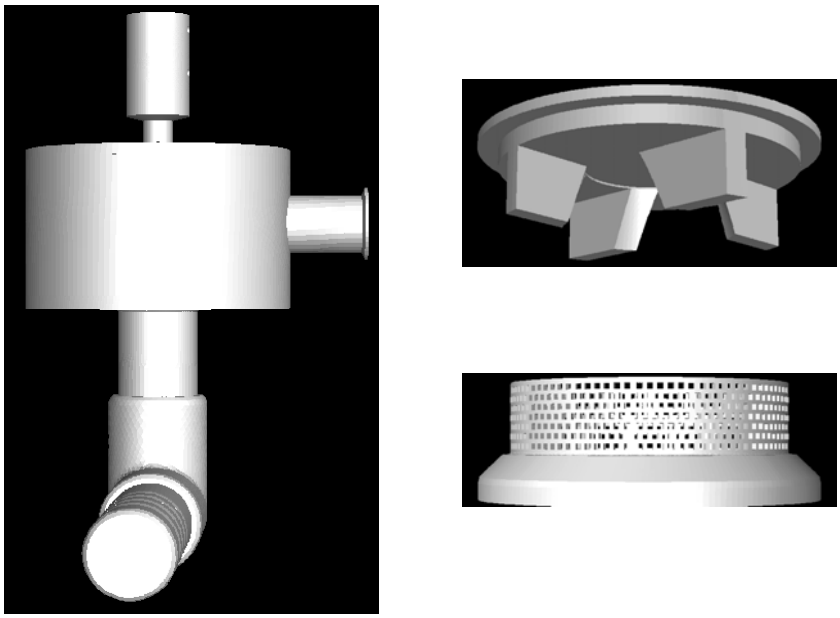

Figure 5-4: Silverson L4R batch rotor-stator mixer geometry.

Silverson pilot scale rotor-stator 450LS, except that the size increases significantly. The rotor is a 4 blade impeller of diameter 152.4. The high shear gap between the rotor and stator, where the highest shear rate exists, is 0.2 mm. The square hole stator

head was also used in this study too . There are 980 square hole slots on the stator head. The size of the stator opening is the same as that of L4R. The thickness of the stator is 2 mm. The height and diameter of the stator are 36.6 mm and 152.7 mm, respectively.

5.1.4 Flow conditions

In these simulations, the rotor rotates clockwise from the top view and the rotation rates are 4000 and 8000 rpm in lab scale Silverson L4R mixer simulations. For pilot scale 450LS and plant scale 600LS mixer simulations, the rotation rates are 2100 and 1575 rpm respectively, so that the tip speed of these larger scale mixers is same as that of lab scale mixer at 8000 rpm, which is 12.6 m/s. A Cartesian coordinate system is used to describe the geometry. The working fluid is water and its density and viscosity is 998.2 Kg/m^3 and 0.001003 Pa·s. The z-axis coincides with the vertical axis of the shaft. The origin of the coordinate system is located on the mid-plane of the rotor and the positive z direction is upward.

5.2 Grid generation

It is well known that the grid used during the simulation determines the convergence and the accuracy of the simulation. Because the geometries of these mixers are very complicated, the grid generation is very challenging. In addition, although the smallest size of these 3 mixers are the same which is 0.2 mm shear gap, the overall size of the mixer increases significantly from the lab scale L4R mixer to the plant

scale 600LS mixer. As a result, the cell number increases dramatically. However because of the limitation of the accessible computational resources, the total cell number is required to be less than 15 million for every grid.

In addition, it requires a lot of experience to create a good quality mesh for a complicated system. It could take tremendous time for a beginner to build a complex grid using traditional mesh generation software such as Gambit. Currently there have been several automatic grid generation algorithms which are claimed to enable the user with little mesh building experience to create acceptable grid in short time. In this section, the automated mesh generator Harpoon is used with Gambit and Tgrid Wrappler to create the 3 dimensional volume mesh for L4R, 450LS and 600LS rotor-stator mixers. By Tgrid, the whole high shear mixer is divided into several individual parts such as rotor, stator, volute. Gambit is used to improve the surface mesh of the high shear mixer.

5.2.1 Grid generation procedure

The mesh of L4R, 450LS and 600LS are built by use of Harpoon, Gambit and Tgrid and the procedure is as following:

- The geometry files (SLT file) are provided by Silverson machines, Ltd. The original STL file is imported into Tgrid and the whole assembly is divided into several individual parts such as rotor, stator, inlet, outlet etc.

- Examine the geometry of each part in Tgrid and repair the geometry to satisfy the grid generation requirement. Useless holes are filled, and screws and unnecessary gaps resulting from the artifact of STL file are deleted.
- Each individual part is imported into Gambit where the surface mesh is improved until the mesh quality is acceptable (the skewness of the meshed surface is less than 0.9).
- All the parts are merged together by Tgrid and the final assembly has to be fully closed. The interfaces are also created in Tgrid, which divides the whole domain into several cell zones that are required by the following MRF and sliding mesh simulation.
- The whole assembly is imported into the automated mesh generator Harpoon. An acceptable 3 dimensional hex dominated volume mesh is created by carefully selecting the process parameters. The holes are filled and unnecessary cell zones (most of time, these zones are solid zones) are deleted.

5.2.2 Mesh of Silverson L4R, 450LS and 600LS

The mesh of Silverson L4R, 450LS and 600LS on the mid-plane are shown in Figure 5-5, 5-7 and 5-9 respectively. The interface is highlighted by the red color. The interface divides the whole domain into a stationary zone and a rotating zone. The mesh close to the inlet and outside of the mixing head are shown in Figure 5-6, 5-8 and 5-10. As shown in the figures, small cells are used close to the mixing head to capture the intense change of the flow field while larger cells are used in the region

far from the mixing head to reduce the total mesh size. Finally, the total cell number of Silverson L4R, 450LS and 600LS are 4.3, 13 and 13 million.

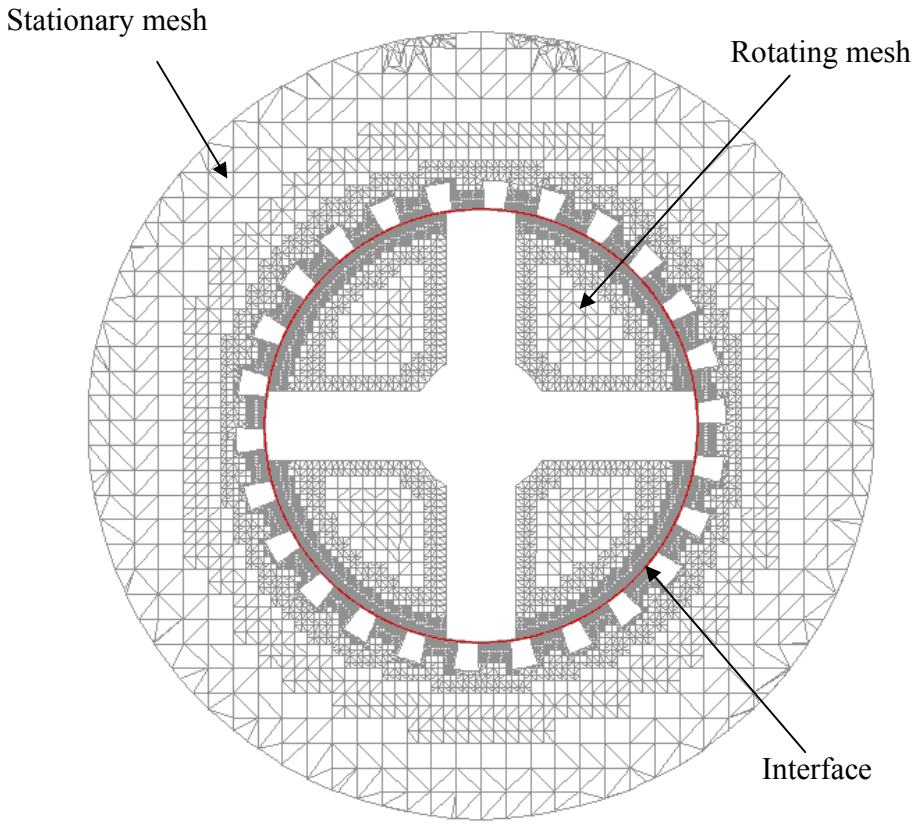

Figure 5-5: Rotating and fixed mesh on the mid-plane of Silverson inline L4R mixer.

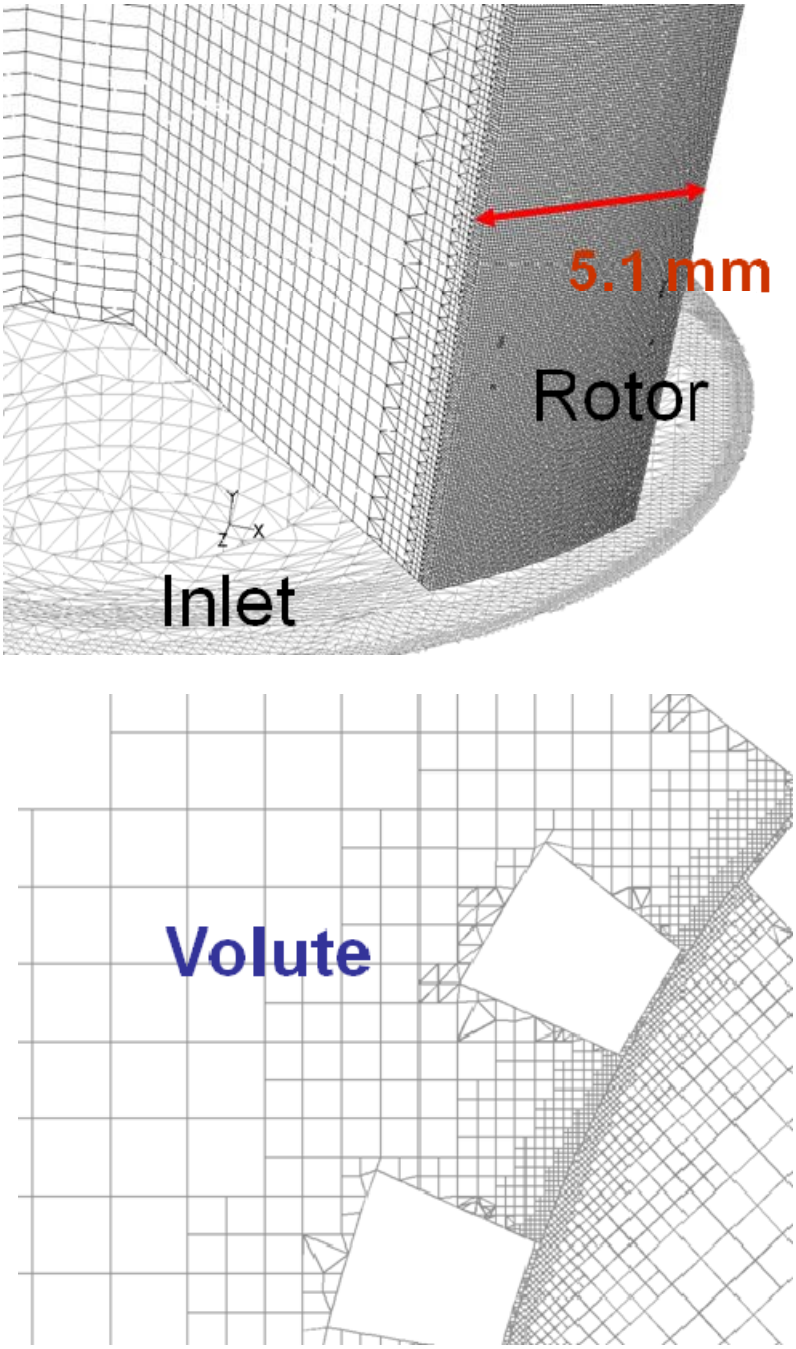

Figure 5-6: Mesh of Silverson inline L4R mixer.

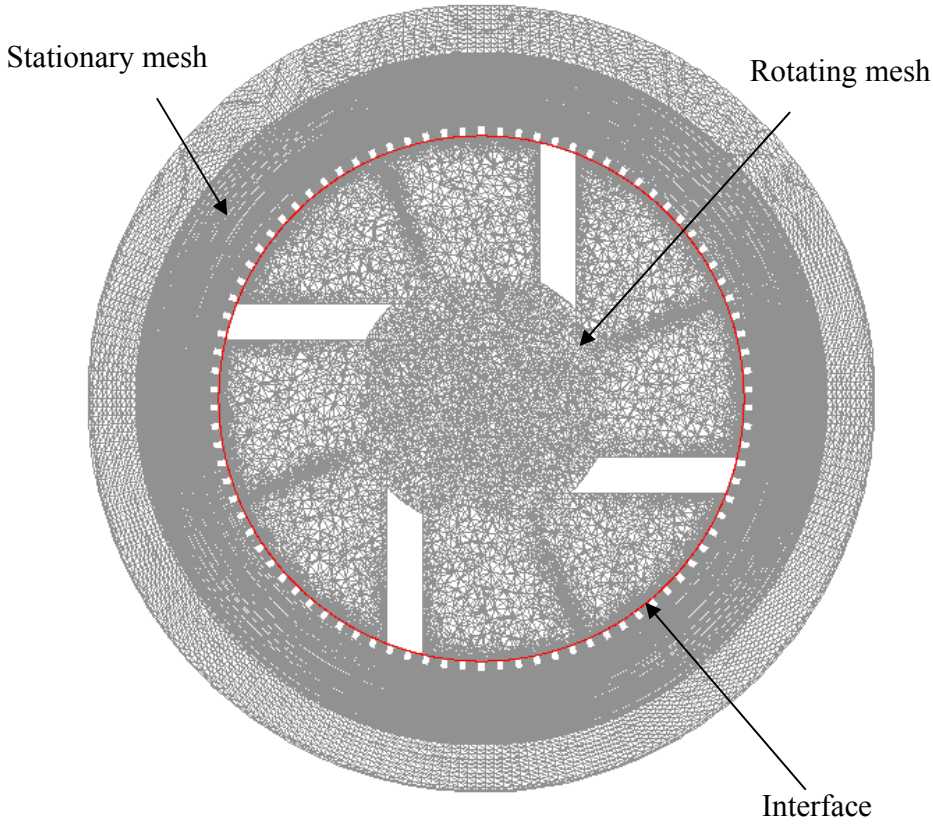

Figure 5-7: Rotating and fixed mesh on the mid-plane of Silverson inline 450LS mixer.

Mesh quality is a very important aspect of the CFD simulation and the skewness is one of the most important indicators to evaluate the mesh quality. A grid with Skewness smaller then 0.97 is considered to be acceptable. The mesh skewness of

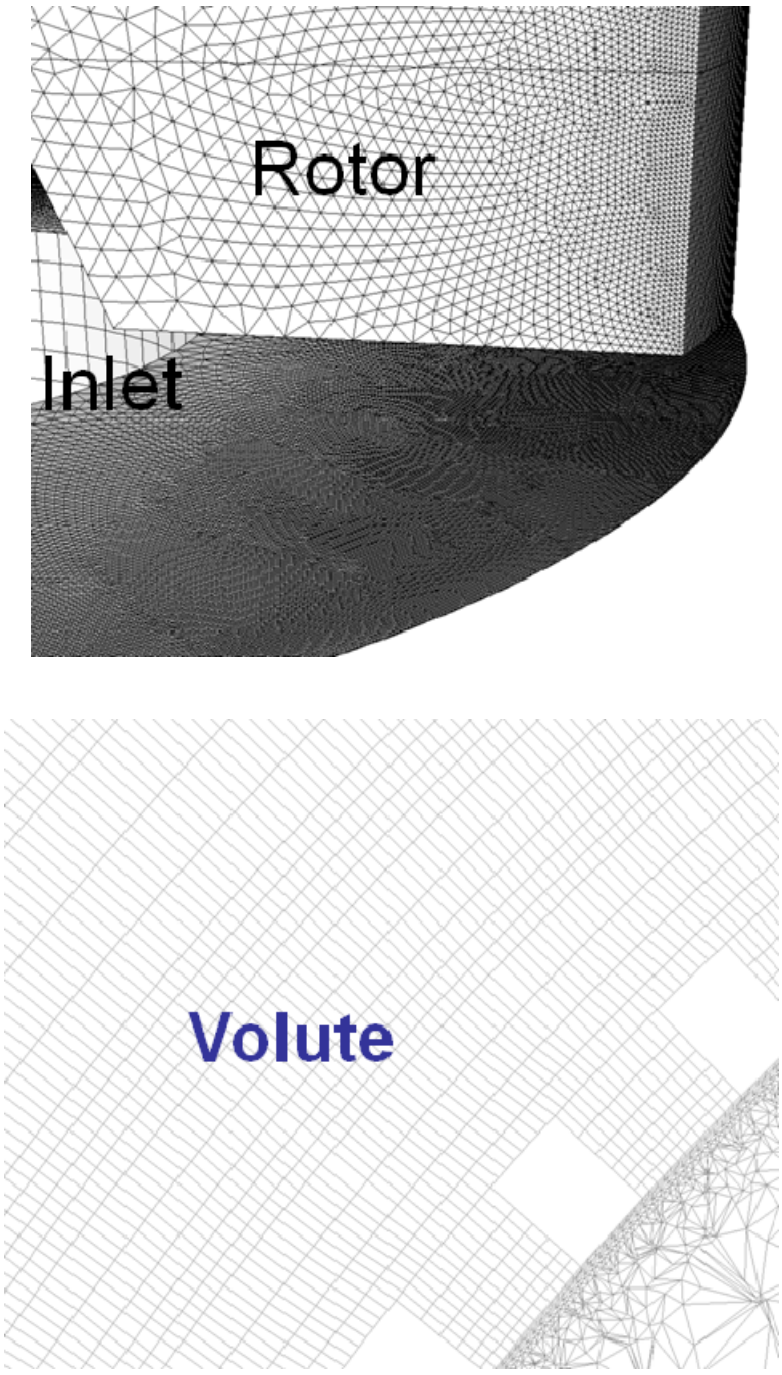

Figure 5-8: Mesh of Silverson inline 450LS mixer.

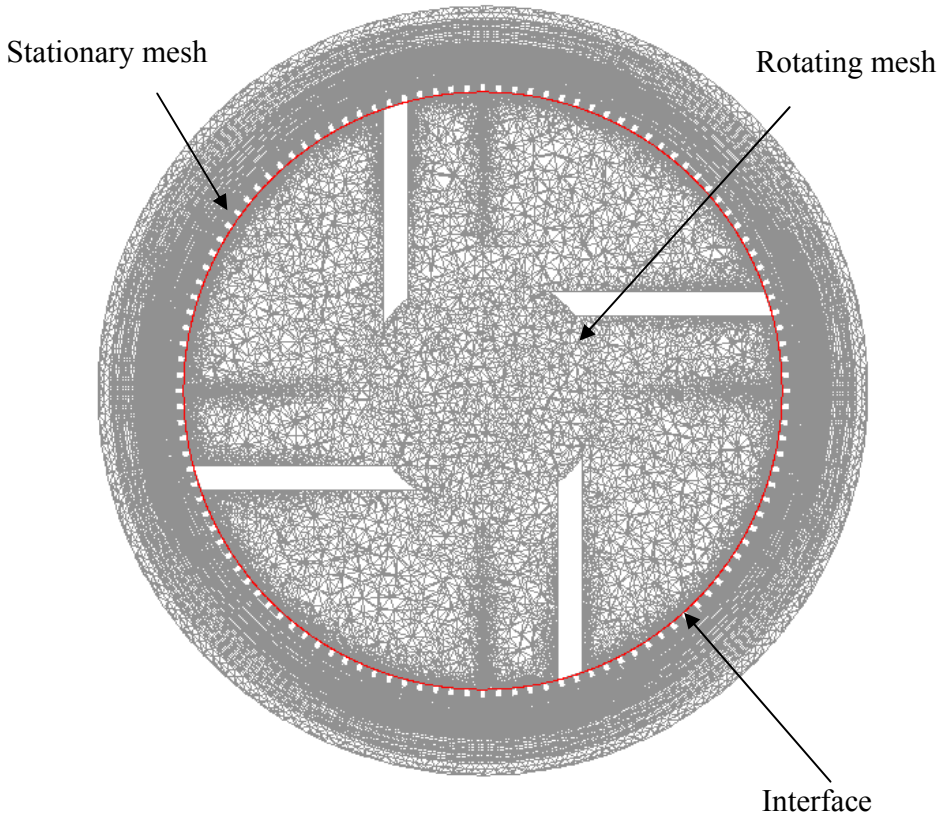

Figure 5-9: Rotating and fixed mesh on the mid-plane of Silverson inline 600LS mixer.

Silverson L4R, 450LS and 600LS mixers are shown in Figures 5-11, 5-12 and 5-13. From these figures, it can be found that the mesh used in the simulation is satisfactory.

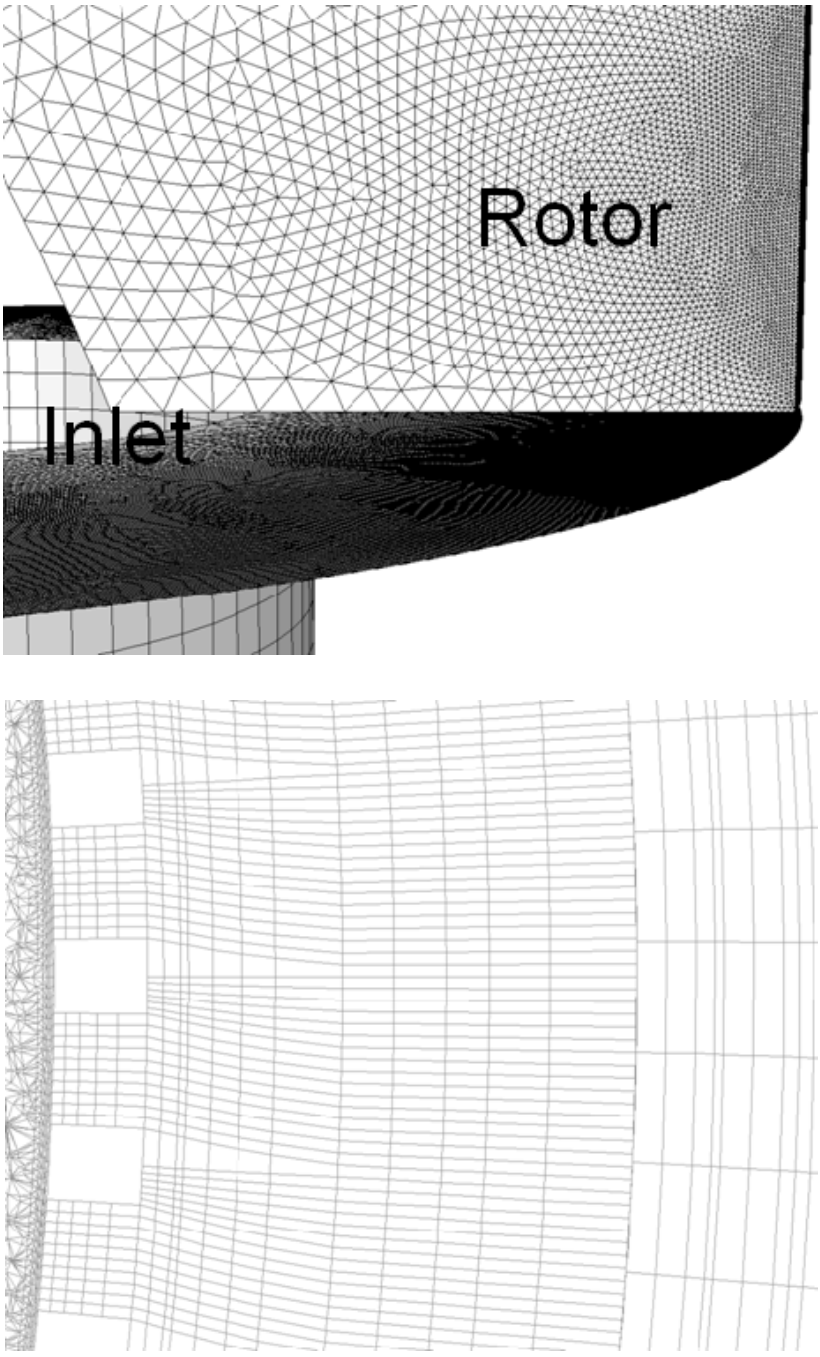

Figure 5-10: Mesh of Silverson inline 450LS mixer.

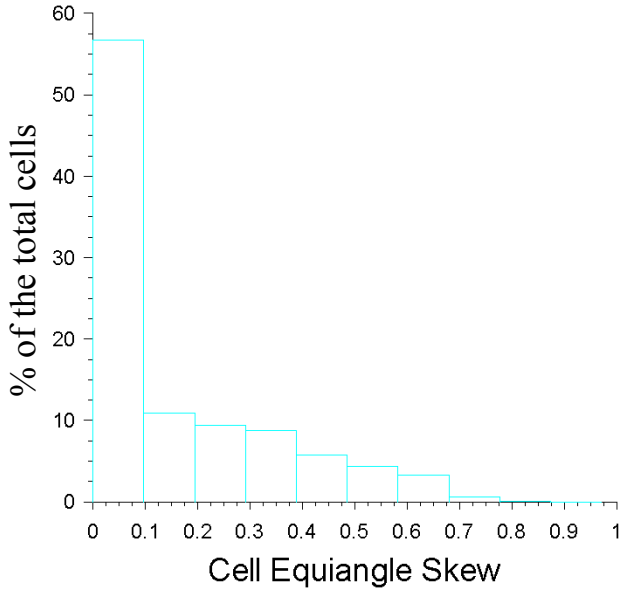

Figure 5-11: Histgram of the skewness of Silverson L4R mixer.

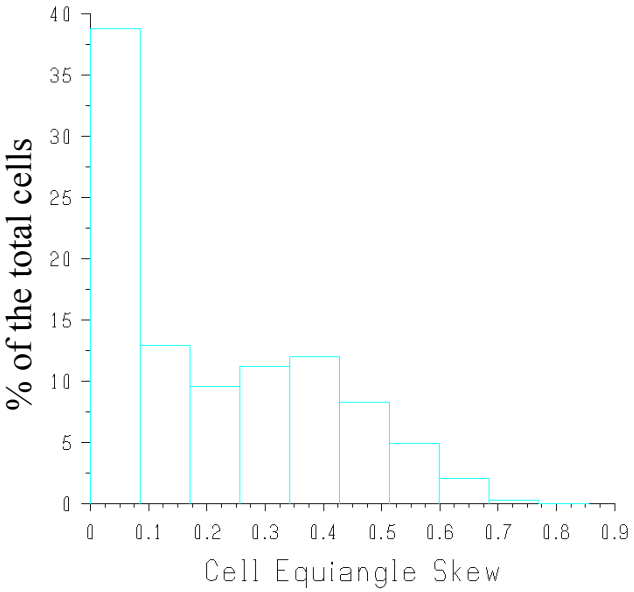

Figure 5-12: Histgram of the skewness of Silverson 450LS mixer.

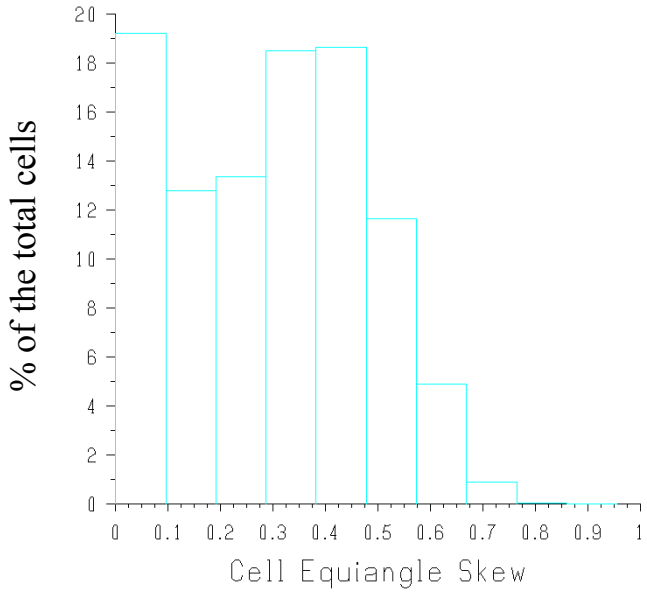

Figure 5-13 Histgram of the skewness of Silverson 600LS mixer.

5.3 CFD model settings

In this chapter, all the simulations have been carried out using the commercially available software package FLUENT 12. The discretized form of the governing equations for each cell is obtained such that the conservation principles are satisfied on each cell. The second-order implicit scheme is used for time discretization in all the turbulence models. Second-order upwind difference scheme was used for spatial discretization. All the discretized equations were solved in a segregated solver with the PISO algorithm which is believed to have better performance in unsteady simulations. In this work, the convergence criterion is that all residuals are required to reach a value smaller than 10^{-6} before proceeding to the next time step. Here, the residual R is calculated as the imbalance in the algebraic equations summed overall the computational cells.

Standard model constants have been used for all the turbulence models. Realizable k-ε model is used to model the turbulence. For the reference frame, the sliding mesh method is selected to account for the relative rotation between the rotor and the stator. The time step size is the time the rotor blades take to rotate 0.5º. The non-equilibrium wall functions are applied for the wall treatment because of the capability to partly account for the effects of pressure gradients and departure from equilibrium.

Simulations of Silverson inline L4R mixer were performed at 4000 and 8000 rpm. To investigate the scale up effect, constant tip speed is required at lab, pilot and plant scale simulations. As a result, the rotation rates of the Silverson 450LS and 600LS are 2100 and 1575 rpm respectively so that the tip speed of Silverson 450LS and 600LS mixers is same as that of Silverson L4R mixer at 8000 rpm which is 12.6 m/s.

In the simulation, pressure boundary conditions are enforced at the inlet and outlet, which is 1 atmosphere pressure. Therefore, the flow or pumping rate can be predicted by the simulation.

During the simulation, a steady MRF model is used at the beginning until the flow field does not change significantly with the iteration. Then, the fully transient sliding mesh method is turned on. The velocity magnitude change with time is monitored to check if the time periodic flow field has been reached. It is found that after about 35 rotor revolutions, the fully converged time periodic flow field is obtained.

5.4 Results and discussion

5.4.1 Macro scale properties

Based on the CFD simulation, macro scale properties of the Silverson inline L4R, 450LS and 600 LS mixers are investigated.

The shear frequency S_{freq} is defined by equation 5.4.1[23] and those of Silverson inline L4R, 450LS and 600LS mixers at several rotation rates are shown in Table 5-1.

$$S_{freq} = Rotation\ Rate \times \text{Number of Blades on Rotor} \times \text{Number of Stator Slots along the Perimenter} \quad (5.4.1)$$

Table 5-1: Shear frequency of the Silverson inline L4R, 450LS and 600LS mixers.

Silverson inline mixer	L4R		450LS	600LS
Rotation Rate (rpm)	4000	8000	2100	1575
No. of blades on Rotor	4	4	4	4
No. of Stator Slots along perimeter	26	26	80	123
Shear Frequency	4E+5	8E+5	6E+5	8E+5
Aspect Ratio of Stator*	0.6	0.6	0.27	0.24

* Aspect Ratio of Stator = Height of the Stator/Diameter of the stator

The predicted pumping rate Q_v, flow number N_Q and flow rate per slot of Silverson inline L4R, 450LS and 600LS mixers at several rotation rates are shown as Table 5-2. The flow number is defined by the following equation:

$$N_Q = \frac{Q_v}{ND^3} \tag{5.4.2}$$

The flow rate of the Silverson inline L4R mixer measured in the experiments that will be discussed in Chapter 6 is shown in Figure 5-14. From Figure 5-14, it can be found that the flow rates of Silverson inline L4R mixer at 4000 and 8000 rpm are 6.38 and 13.98 L/min respectively, which correspond to 0.11 and 0.23 L/s. Therefore the predicted result compares favorably with experiment for the Silverson inline L4R mixer. This result also make the author confident in the simulation method applied to the Silverson inline 450LS and 600LS mixers.

Table 5-2: Predicted flow rate and flow number of the Silverson inline L4R, 450LS and 600LS mixers.

Silverson inline mixer	L4R		450LS	600LS
Rotation Rate (rpm)	4000	8000	2100	1575
Flow Rate (L/s)	0.11	0.22	6.9	13.9
Flow Number	0.05	0.05	0.13	0.15
Flow Rate per Slot (L/s)	0.0011	0.0021	0.012	0.014
Number of Stator Slots	104	104	560	980

By equation 4.3.1 and 4.3.2, power and power number of Silverson inline L4R, 450LS and 600LS mixers can be predicted. Specific energy *SE* is defined by equation 5.4.3:

$$SE = \frac{P}{\rho Q} \tag{5.4.3}$$

The predicted power, power number, power per slot, specific energy and specific energy per slot are shown in Table 5-3.

The measured power and power number of the Silverson inline L4R mixer is shown in Figure 5-15[9]. The Reynolds number at 4000 and 8000 rpm

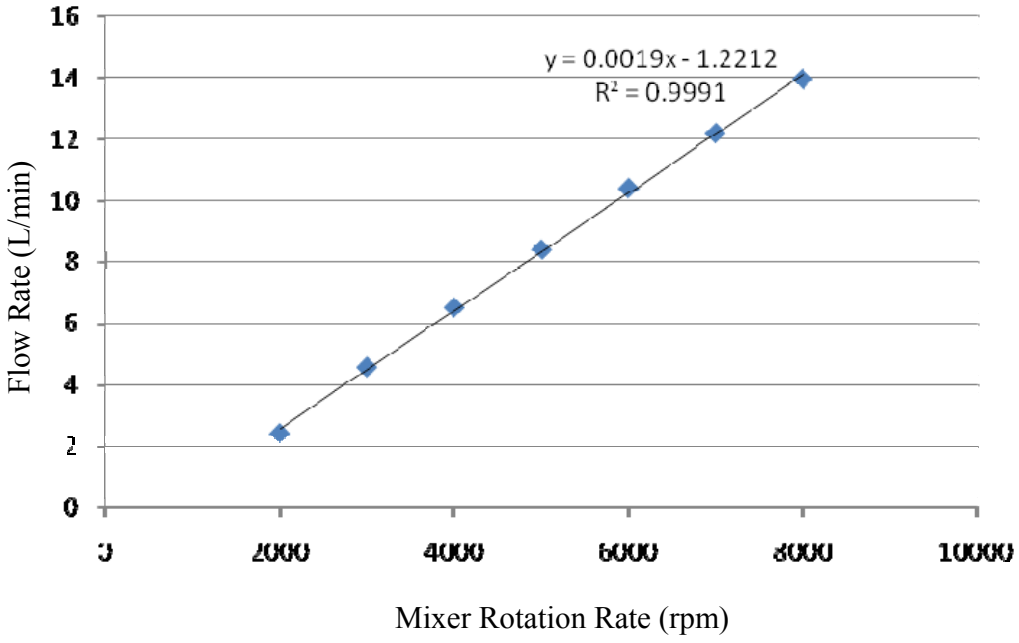

Figure 5-14: Experimental flow rate of Silverson inline L4R rotor-stator mixer.

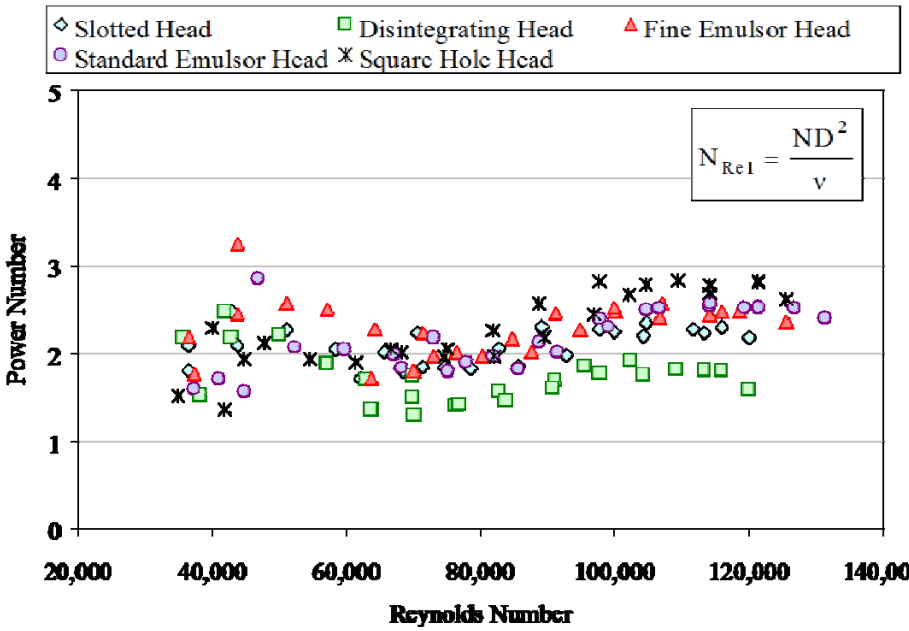

Figure 5-15: Experimental power number data of Silverson inline L4R rotor-stator mixer[9].

Table 5-3: Predicted power properties of the Silverson inline L4R, 450LS and 600LS mixers.

Silverson inline mixer	L4R		450LS	600LS
Rotation Rate (rpm)	4000	8000	2100	1575
Power (W)	20	164	1075	1845
Power per Slot (W)	0.19	1.58	1.94	1.88
Power Number	2.2	2.3	1.3	1.2
SE (J/kg)	182	757	157	133
SE per Slot (J/kg)	1.75	7.18	0.28	0.14
Power per Swept Volume (W/m^3)	1.38E+6	1.13E+7	3.39E+6	2.76E+6

are 63,760 and 127,520 respectively. From Figure 5-15, it can be found that the averaged power number of Silverson inline L4R mixer with square hole stator head at 4000 and 8000 rpm are both 2.3, which compare favorably with the CFD prediction for the Silverson inline L4R mixer.

In Table 5-1, 5-2 and 5-3, when the result of Silverson inline L4R mixer at 8000 rpm is compared with those of Silverson inline 450LS and 600LS mixers, it can be concluded that the flow rate, flow number, flow rate per slot and power per slot increase significantly with the size of the mixers; specific energy per slot decreases with the size of the mixers. The flow rate per slot of the Silverson inline 450LS and 600LS mixers, however, is very similar to each other. This may suggest that it be fine to scale up from the pilot scale mixer to the plant scale mixer based on the constant nominal shear rate criterion. However, considering the rotor tip speed alone may lead to a significant discrepancy when scale up from lab scale to pilot scale. The predicted mean velocity, turbulence and deformation rate fields, discussed below, will further bear this out.

In wet milling processes, higher shear frequency, power per slot or specific energy per slot can result in smaller particles while lower flow rate leads to longer residence time, which generates smaller particles. Therefore, although the theoretical mechanism for the rotor-stator mixer scale up is unknown, the dominating parameters that control this scale up process can be found by the CFD simulation in conjunction

with experiments. If smaller particles are found in larger scale mixer, it may suggest that it is power per slot that is the controlling parameter for scale up. Otherwise, if smaller particles are found in smaller scale mixer, specific energy per slot could be the controlling parameter.

5.4.2 Flow fields of the Silverson inline L4R, 450LS and 600LS mixers

Mean flow field of the Silverson inline L4R mixer

The coordinate used in the Silverson inline L4R mixer is shown in Figure 5-16 where φ is the angle between centerline of the rotor blade and the x axis and θ is tangential coordinate. The rotor rotates in the clockwise direction.

The flow fields on the mid-plane of the Silverson inline L4R mixer at 4000 and 8000 rpm are shown in Figure 5-17. The flow fields are normalized by the tip speed (6.56 m/s at 4000 rpm and 12.6 m/s at 8000 rpm). From the vector plots, it is found that the flow pattern of 4000 rpm is very similar to that of 8000 rpm. Close to each stator slot, a strong jet exists in both cases. The rotor rotates in the clockwise direction while the fluid leaving the stator and entering the bulk of the tank tends to move in the anti-

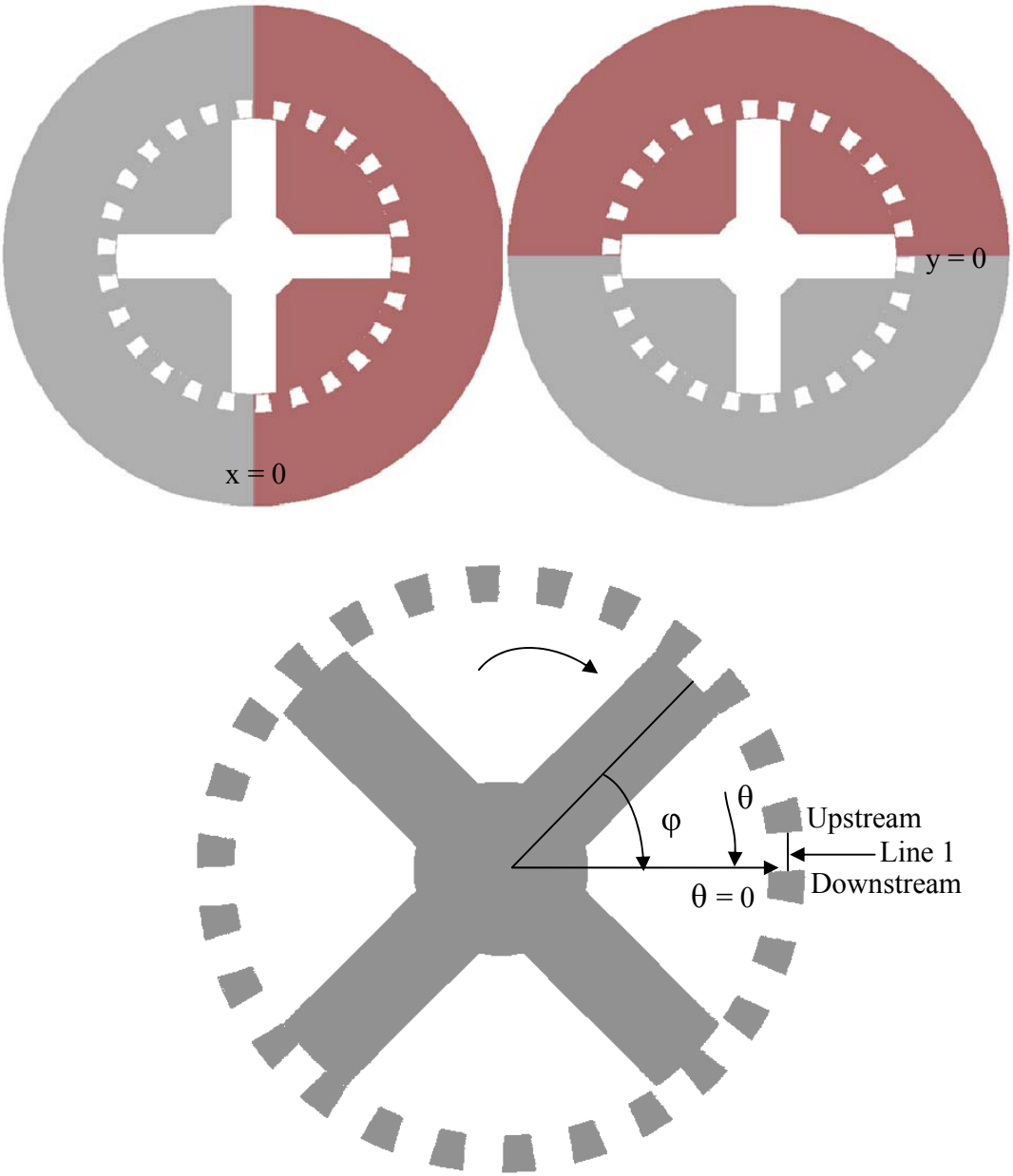

Figure 5-16: The coordinate on the mid-plane of Silverson inline rotor-stator mixers. The tangential coordinate of Line 1 is from -8.1˚to 0˚ in the L4R mixer, from-2.4˚ to 0˚ in the 450LS mixer and from -1.8˚ to 0˚ in the 600LS mixer.

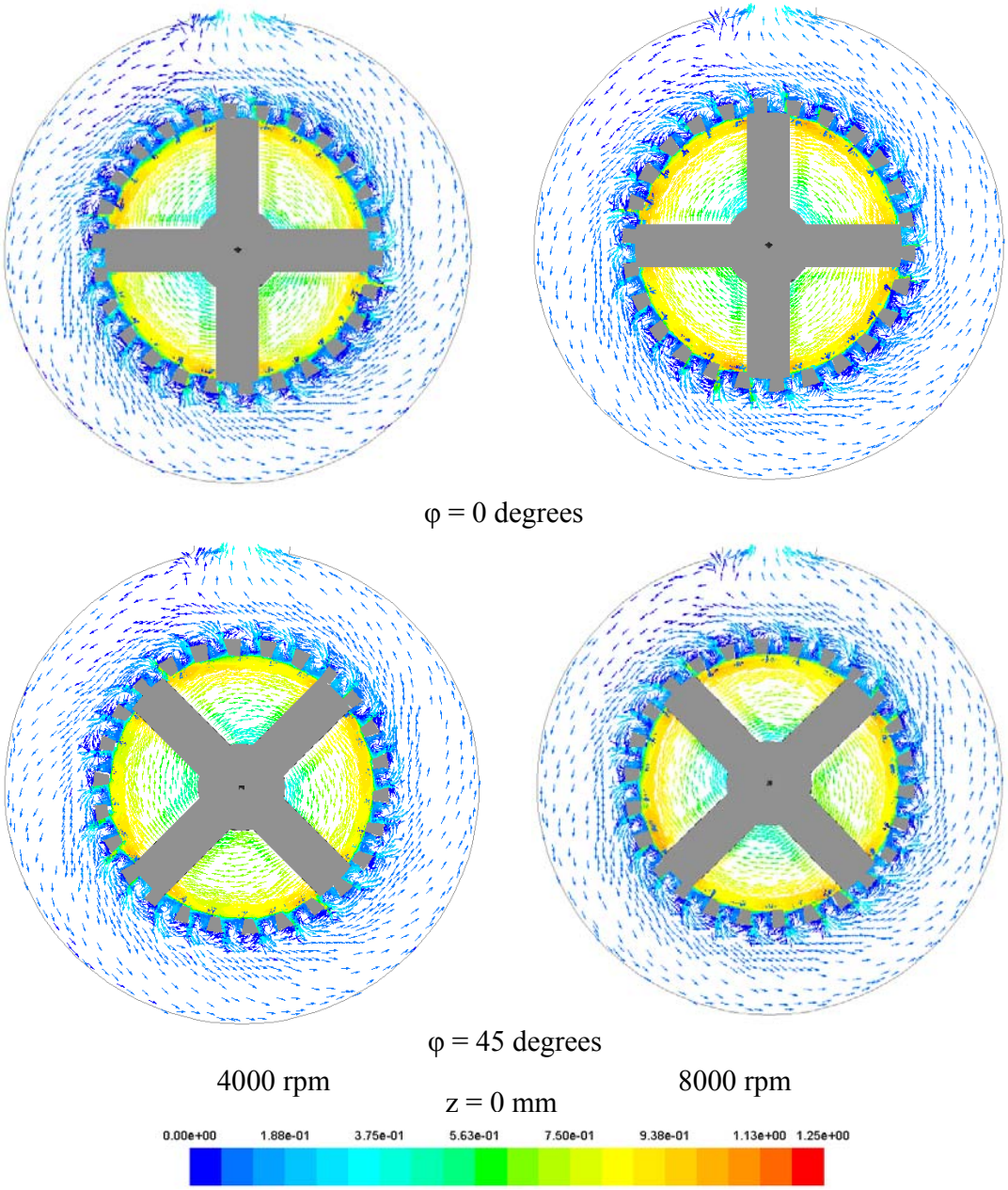

Figure 5-17: Normalized velocity magnitude snapshots on mid-plane of Silverson inline L4R mixer at 4000 and 8000 rpm.

clockwise direction, which is opposite to the rotation direction of rotor. This finding is consistent with what we found in the Silverson L4R Batch rotor-stator mixer.

The flow fields on plane y=0 (see Figure 5-16) at 4000 and 8000 rpm are shown in Figure 5-18, where the rotor blade orientations are the same as Figure 5-16. From the vector plots, it is found that the flow pattern at 4000 rpm is very similar to that at 8000 rpm. The fluid enters the rotor from the bottom and top, and is pumped rapidly out of the stator from the side. Therefore, vortices between the rotor blades are generated in the vertical plane. There are big vortex structures generated outside the mixing head in the bulk of the volute.

The flow fields at different z coordinates are shown in Figure 5-20 and 5-21, respectively. Plane z = 23 mm is close to the mixer top while plane z = -9 mm is below the rotor (see Figure 5-19).

In Figure 5-20, the fluid rotates with the shaft in the clockwise direction in the center of the figure. In the bulk of the tank, the fluid tends to move in the anti-clockwise direction. In addition, in contrast to the flow close to the mixing head, the velocity

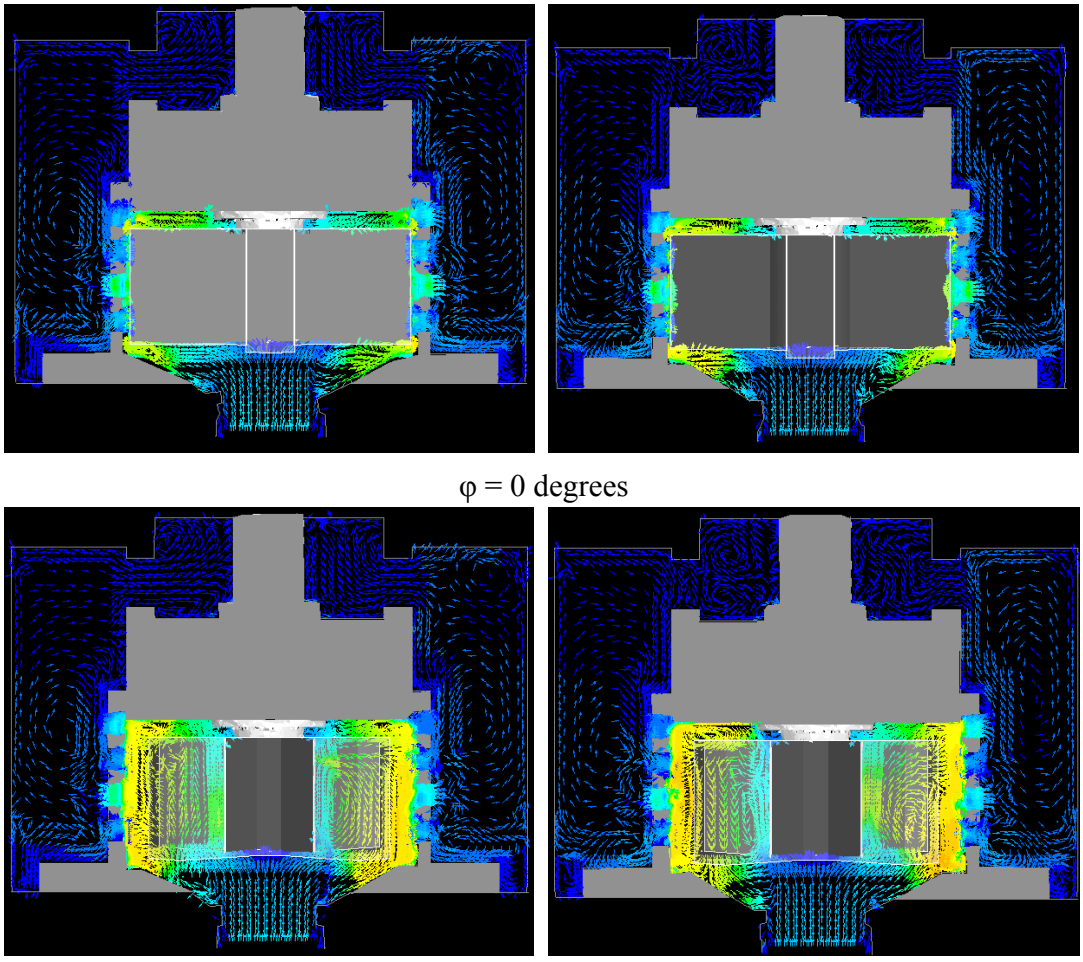

Figure 5-18: Normalized velocity magnitude snapshots at plane y = 0 in Silverson inline L4R rotor-stator mixer.

profile at the horizontal plane above the mixing head is dominated by tangential flow. It is also found that at different rotor blade orientations, the flow fields above the mixing head almost remain unchanged. This may suggest that the flow field at this position could be simulated by the steady solver MRF method.

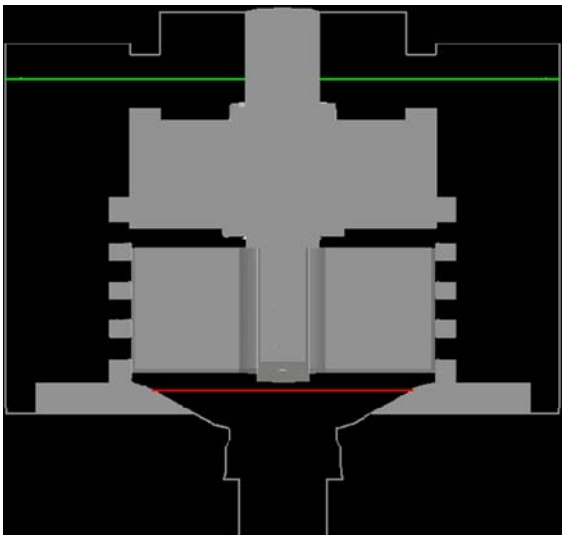

Figure 5-19: The z coordinate in the Silverson inline L4R rotor-stator mixer.

In Figure 5-21, the fluid enters the rotor zone from the inlet pipe and then move in clockwise direction with the rotor. It is also found that at different rotor blade orientation, the flow fields below the mixing head almost remain unchanged. In the center of the flow field, the fluid mainly moves in the radial direction while the velocity profile is dominated by tangential flow outside.

The velocity filed normalized by the rotor tip speed (6.56 m/s at 4000 rpm and 12.6 m/s at 8000 rpm) close to the stator slot 1 on the mid-plane (in Figure 5-22) at 4000 and 8000 rpm is given in Figure 5-24 and 5-25. Five different rotor positions are shown (shown in Figure 5-23). From these figures it can be found that the flow

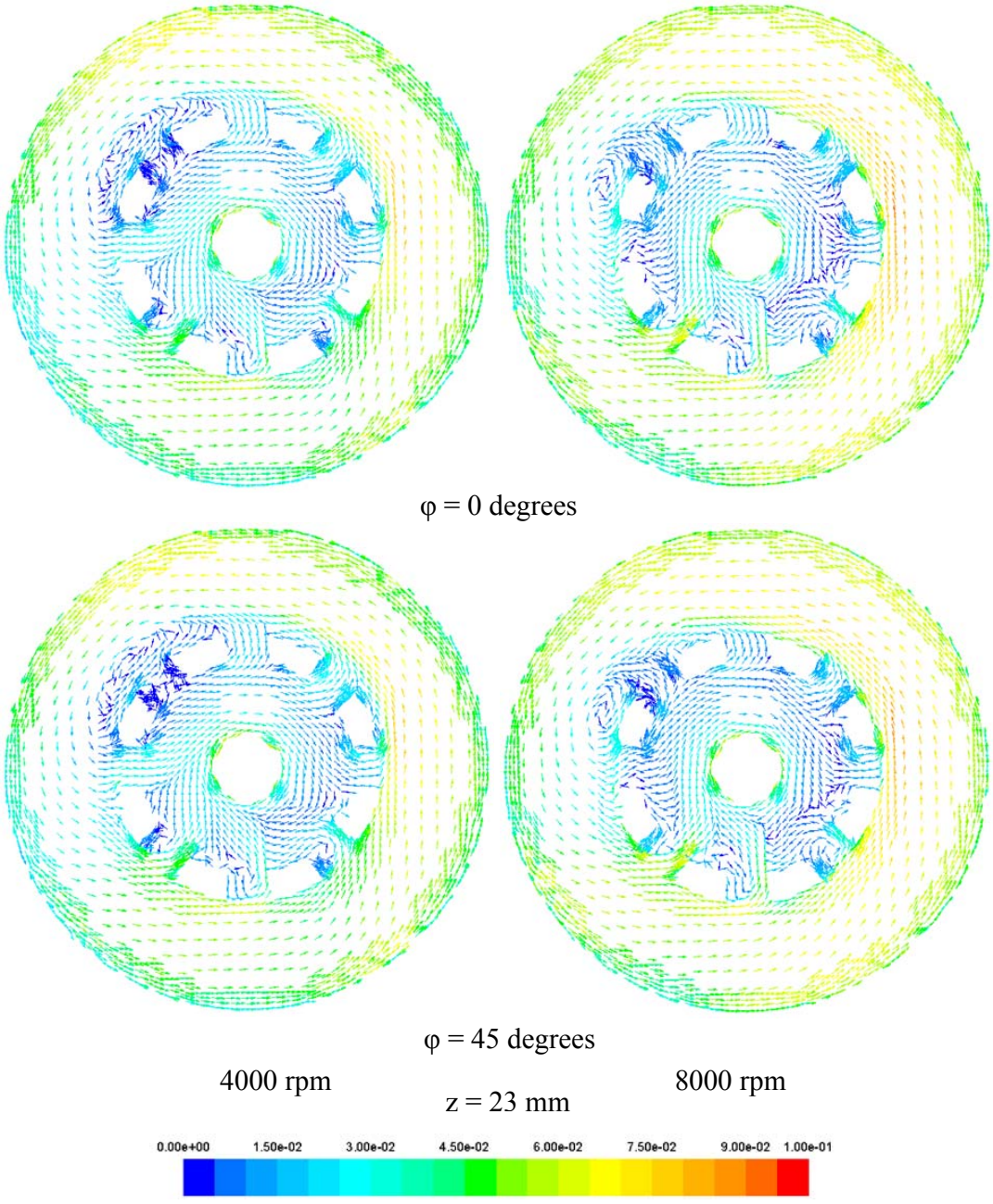

Figure 5-20: Normalized velocity magnitude vector plots at plane z = 23 mm (close to the volute top).

pattern at 4000 rpm is very similar to that at 8000 rpm. The fluid inside the stator head moves with the rotor in the clockwise direction while outside the mixing head, it tends to move in the anti-clockwise direction. Close to the stator slot the fluid pushed

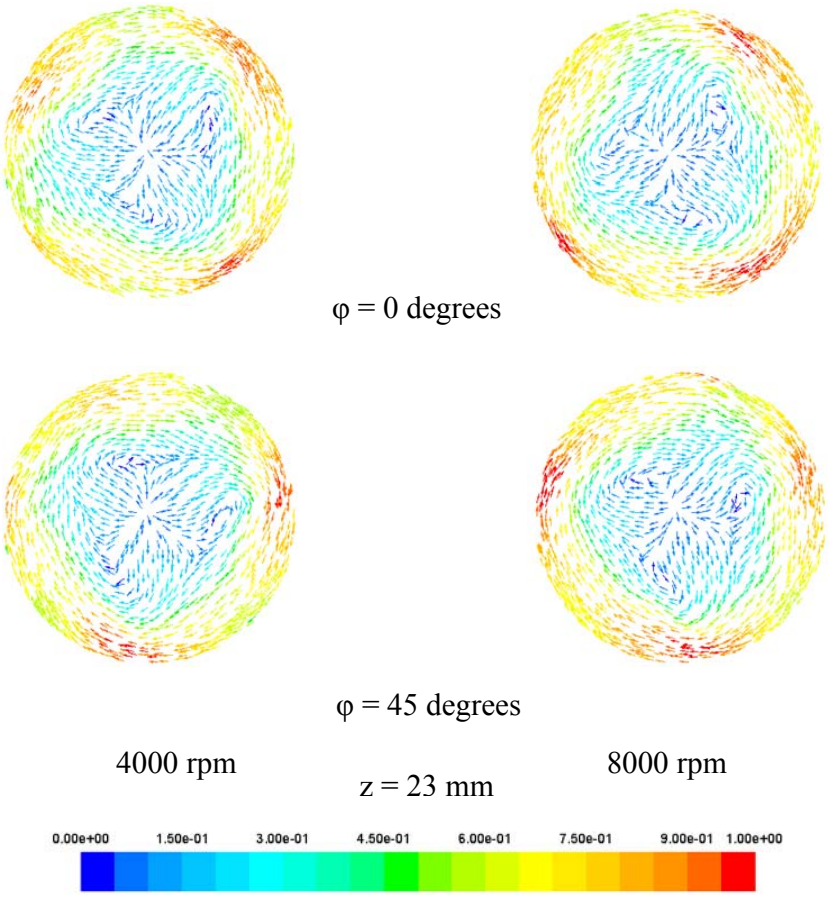

Figure 5-21: Normalized velocity magnitude vector plots at plane z = -9 mm (in the inlet pipe).

by the rotor hits the stator teeth. Then, the tangential direction velocity is changed to radially directed velocity. A strong jet is generated in each stator slot. Regardless of the rotor blade position, the jets are always generated close to the downstream edge of

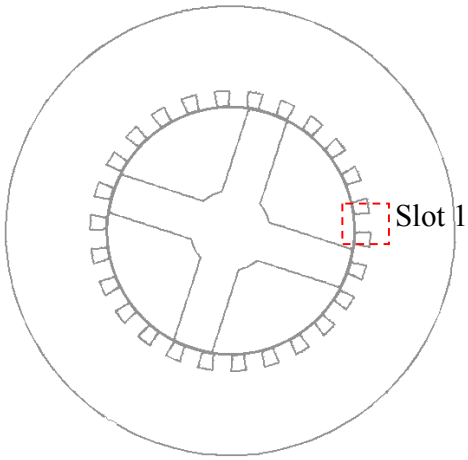

Figure 5-22: The monitored stator slot 1 on the mid-plane of Silverson inline L4R rotor-stator mixer

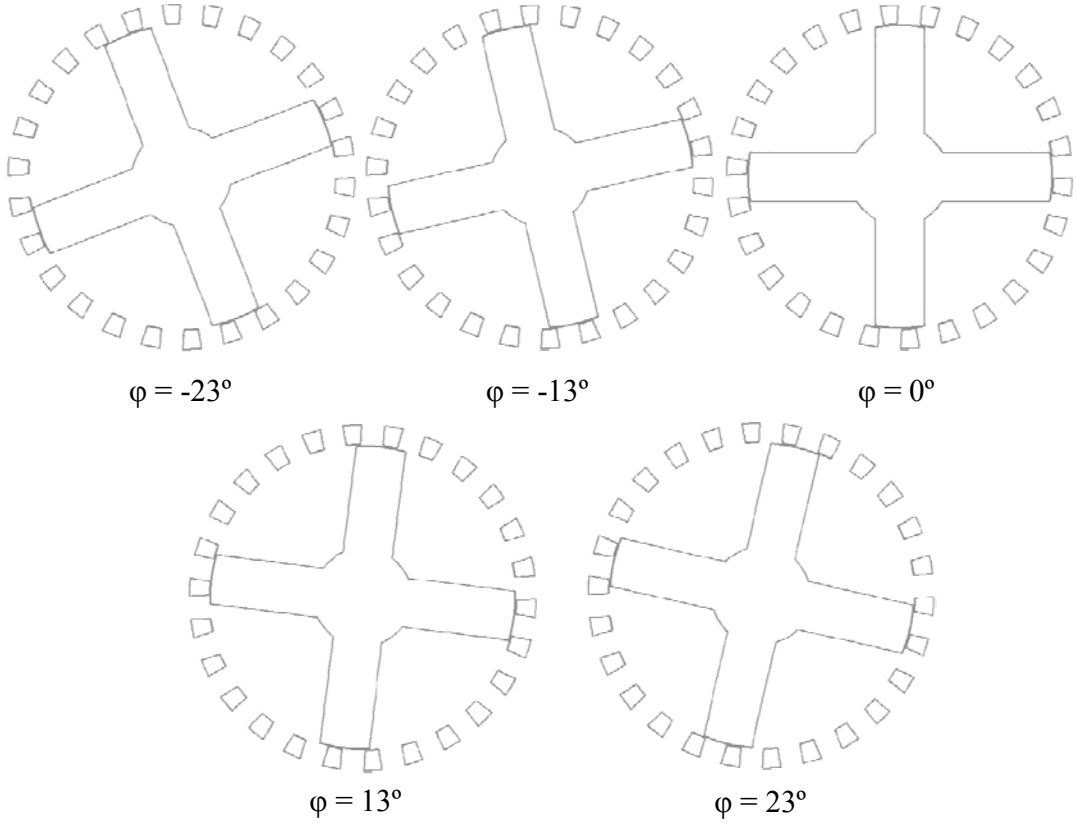

Figure 5-23: Position of the rotor blades relative to stator slot 1.

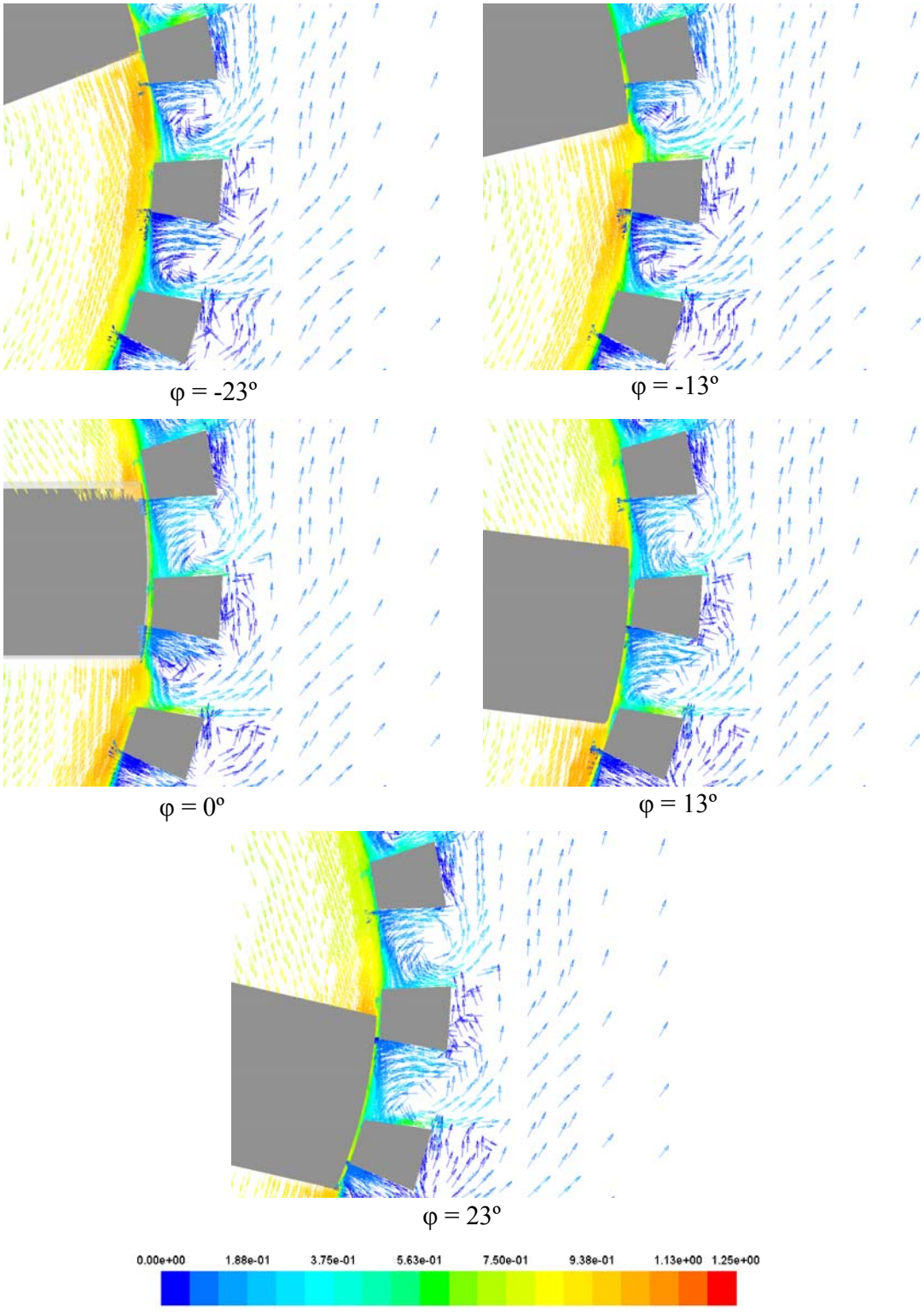

Figure 5-24: Velocity vectors normalized by the rotor tip speed around the stator slot at various blade positions (4000 rpm).

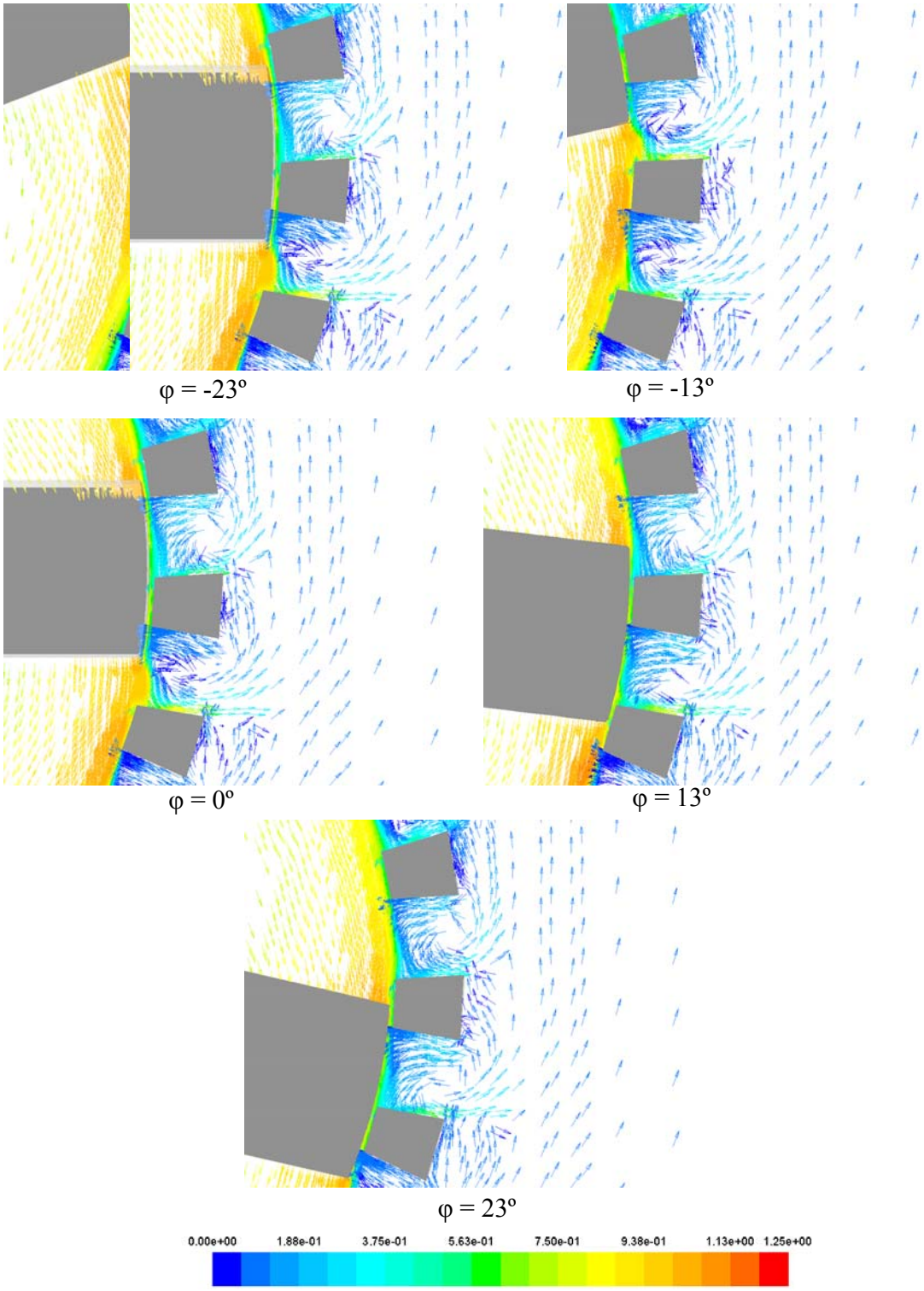

Figure 5-25: Normalized velocity vectors normalized around the stator slot at various blade positions (8000 rpm).

the stator slot. These jets move further into the bulk of the mixer and tends to move in the anti-clockwise direction which is opposite to the rotor direction. Meanwhile outside the stator slots, some fluid is driven to enter the openings and then go into the rotor zone. Therefore a vortex is generated in each stator slot.

The angularly averaged radial velocity profiles (normalized by rotor tip speed) along line 1 (shown in Figure 5-16) at 4000 and 8000 rpm are shown in Figure 5-26. From the figure it can be found that the profiles at 4000 and 8000 rpm are quite similar. This figure also indicates that the maximum jet radial velocity occurs close to the downstream edge ($\theta = 0^o$) of the stator slot 1 and decreases gradually with the

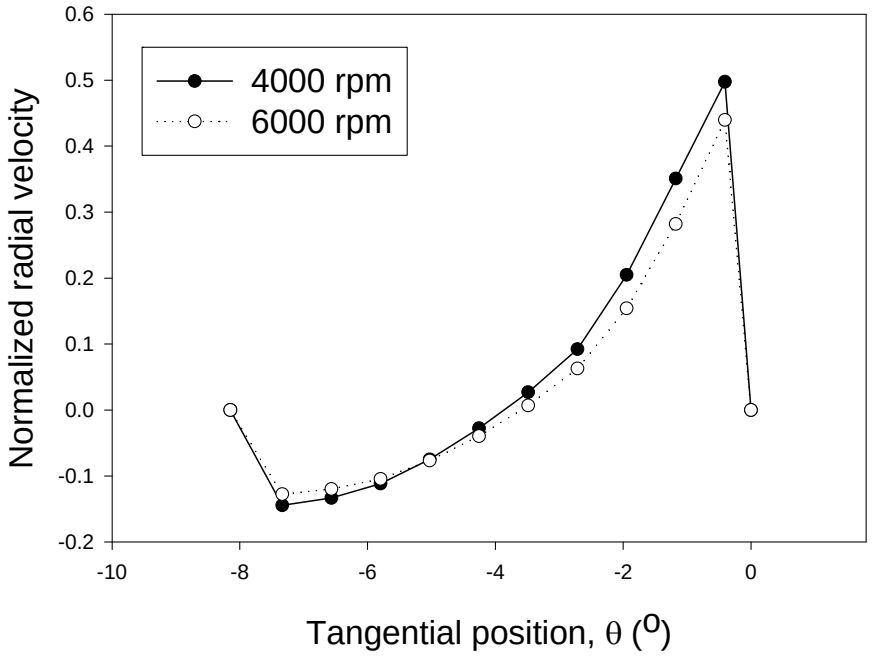

Figure 5-26: Normalized angularly averaged radial velocity profiles along line 1 (Figure 5-16) at 4000 and 8000 rpm in Silverson L4R inline mixer. The downstream edge of the stator tooth is at $\theta = 0^o$ and the upstream edge is at $\theta = -8^o$.

distance from the downstream edge. At some point near the upstream edge, the radial velocity exhibits negative values indicating a recirculation region existing where the liquid flows back into stator slot 1.

The angularly averaged tangential velocity profiles (normalized by rotor tip speed) along line 1 (Figure 5-16) at 4000 and 8000 rpm are shown in Figure 5-27. The tangential velocity profile shows similar trends at both 4000 and 8000 rpm. In this figure, similar to Figure 5-26, the normalized tangential velocity is proportional to the rotor tip speed. This figure indicates that the maximum tangential velocity occurs at θ = 2.87º close to the middle of the stator slot 1. Moreover, at the downstream edge, the tangential velocity is almost zero which may suggest that most of the tangential flux

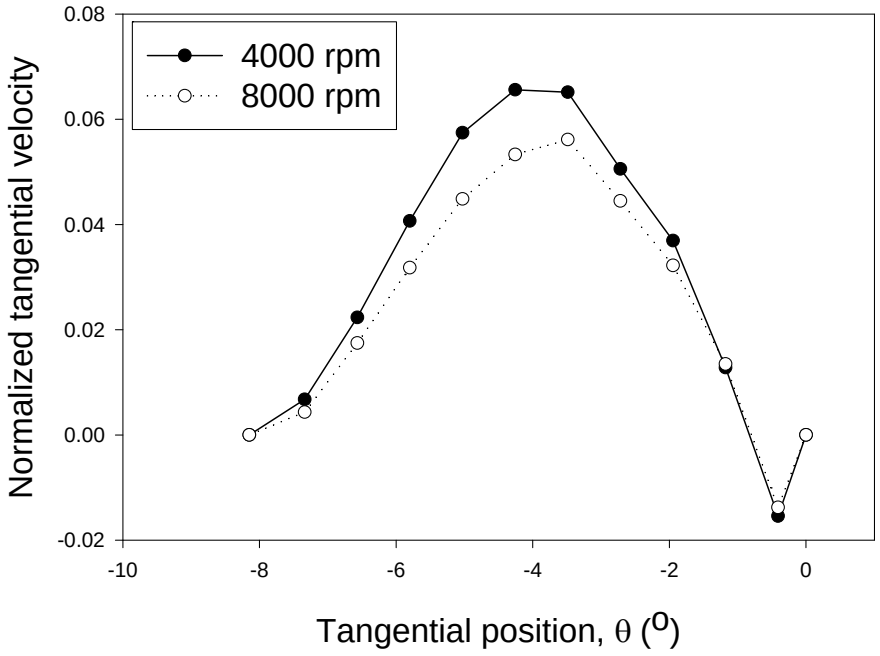

Figure 5-27: Normalized angularly averaged tangential velocity profiles along line 1 (Figure 5-16) at 4000 and 8000 rpm in Silverson L4R inline mixer. The downstream edge is at θ = 0º and upstream edge is at θ = -8º.

is converted into a radial momentum flux when the fluid impinges on the downstream edge of the stator.

Figure 5-28 and 5-29 show the radial velocity profiles along line 1 in Figure 5-16 at various rotor blade positions at 4000 and 8000 rpm. As the blade approaches the downstream edge, the jet radial velocity at the downstream edge increases and reaches the maximum just before the blade encounters stator slot 1. When the blade moves away from the downstream edge of the slot, the radial velocity starts to decrease. In addition, when the blade move towards the downstream edge, the circulation region widens as the blade blocks the fluid in the rotor region from passing through the stator slot. The

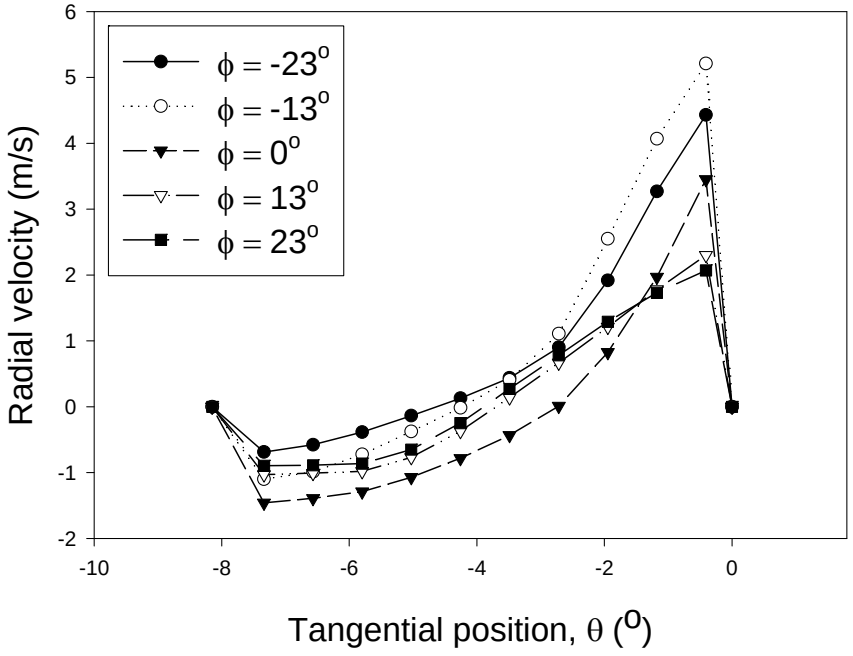

Figure 5-28: Radial velocity profiles along line 1 (Figure 5-16) at 4000 rpm in the Silverson L4R inline mixer. The downstream edge of the stator tooth is at θ = 0º and upstream edge is at θ = -8º.

circulation region reaches its maximum when the stator slot is fully closed by the rotor blade.

In Figure 5-31, normalized angularly averaged results on the radial and tangential velocity along line 2, which is shown in Figure 5-30, parallel to the z axis outside the stator head, predicted by the simulations, are shown. Two stator slots are in the range of Line 2. Both the radial and tangential velocity profiles exhibit similar trend at 4000 and 8000 rpm. The jet from stator slot 1 on the mid-plane is shown in the figure and the magnitude of radial and tangential velocity are very similar.

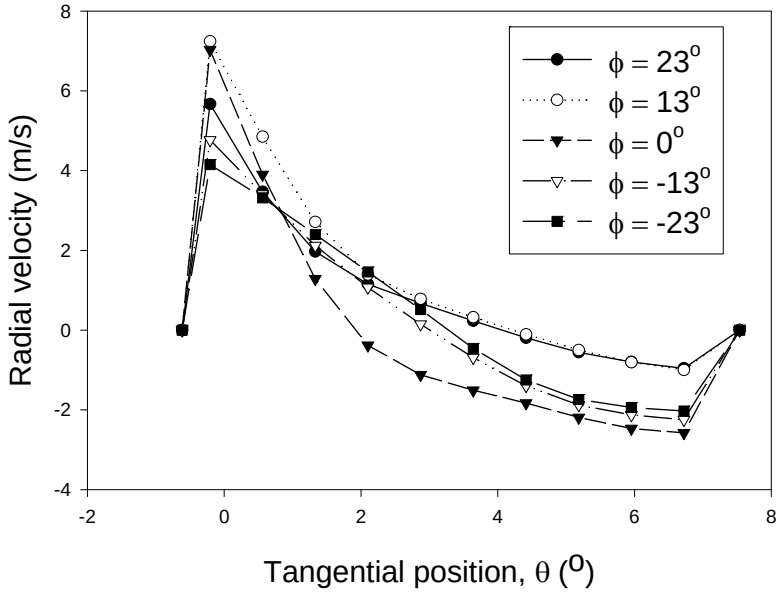

Figure 5-29: Radial velocity profiles along line 1 (Figure 5-16) at 8000 rpm in Silverson L4R inline mixer. The downstream edge of the stator tooth is at θ = 0º and upstream edge is at θ = -8º.

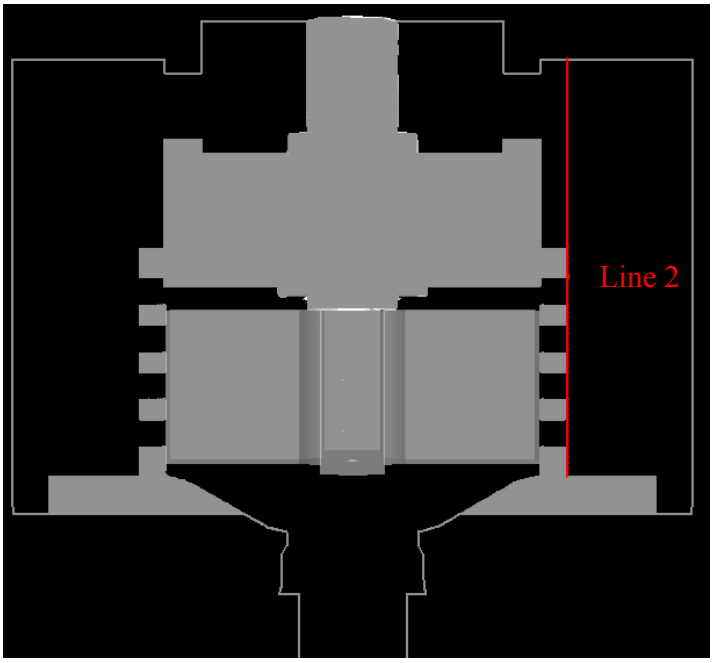

Figure 5-30: Line 2 monitored in the simulation.

Flow field of Silverson inline 450LS mixer

The flow fields on the mid-plane of Silverson inline 450LS mixer at 2100 rpm are shown in Figure 5-32. The coordinate system used for the 450LS is the same as that for the L4R except the dimensions are larger. The flow fields are normalized by the rotor tip speed which is 12.6 m/s, the same as Silverson inline L4R mixer at 8000 rpm. From the vector plots, it is found that close to each stator slot, there exists a strong jet. The rotor rotates in the clockwise direction while the fluid that leaves the stator and enters the bulk of the volute tends to move in the anti-clockwise direction, which is opposite to the rotation direction of the rotor. This finding is consistent with our previous results.

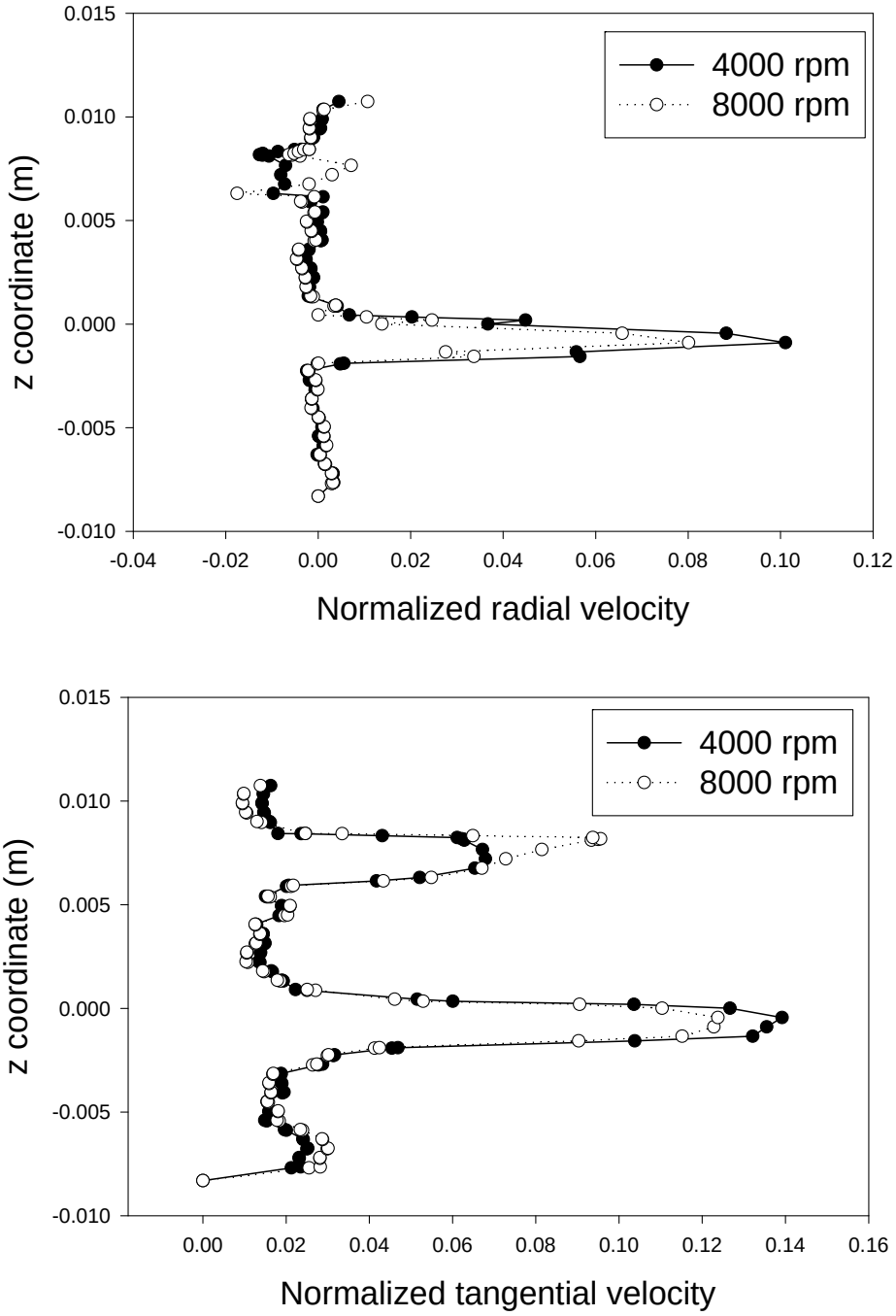

Figure 5-31: Axial profiles of the Normalized angularly averaged radial and tangential velocity component along line 2 (Figure 5-30) at 4000 and 8000 rpm in Silverson L4R inline mixer.

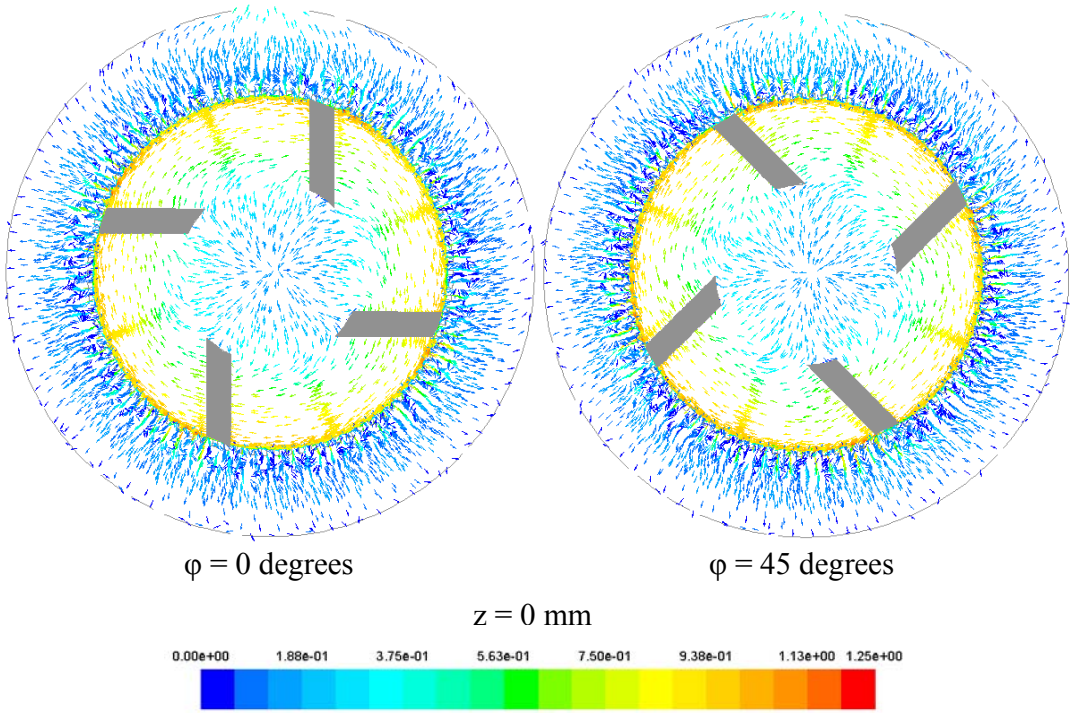

Figure 5-32: Normalized velocity magnitude snapshots on mid-plane of the Silverson inline 450LS mixer at 2100 rpm.

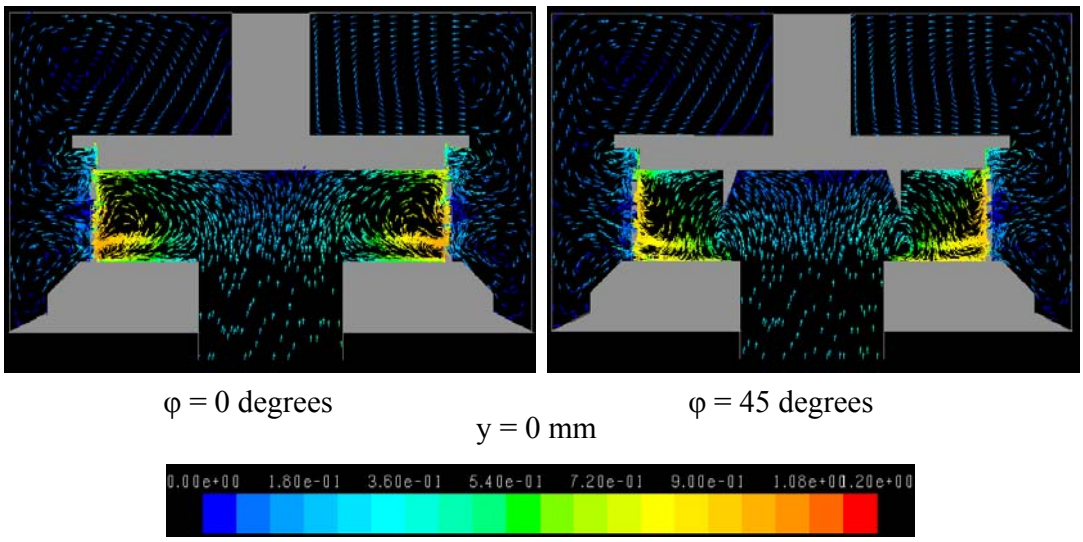

Figure 5-33: Normalized velocity magnitude snapshots at plane y=0 in the Silverson inline 450LS rotor-stator mixer.

The flow fields on plane y = 0 at 2100 rpm are shown in Figure 5-33, where the rotor blade positions are φ = 0 and 45 degrees. The fluid enters the rotor from the bottom and top, and is pumped rapidly out of the stator from the side. Therefore, vortices between the rotor blades are generated in the vertical plane. There are also some large vortex structures generated outside the mixing head at the corners of the mixer.

The flow fields at different z coordinates are shown in Figure 5-35 and 5-36 respectively, where the rotor blade positions are φ = 0 and 45 degrees. Plane z = 55 mm is close to the mixer top while plane z = -37 mm is below the rotor in the inlet pipe (see Figure 5-34).

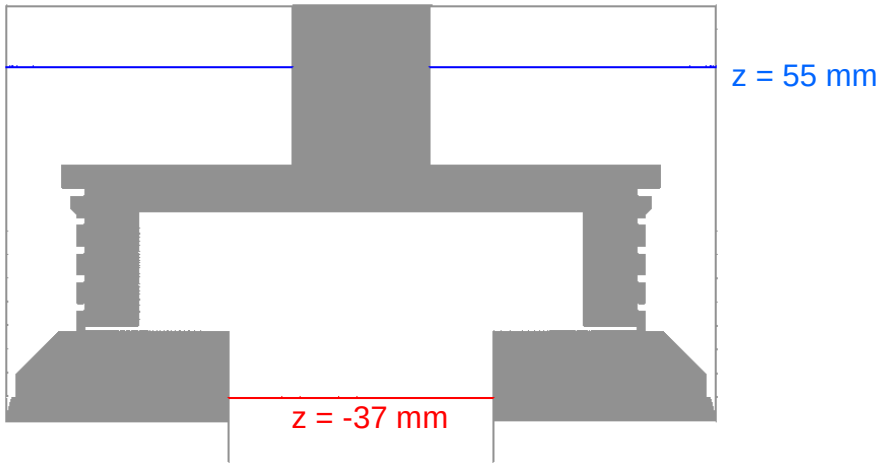

Figure 5-34: The z coordinate in Silverson inline 450LS rotor-stator mixer.

Figure 5-35 shows the flow field below the rotor in the inlet pipe. The fluid enters the rotor zone from the inlet pipe and then moves in a clockwise direction with the rotor. Similar to the flow field of the Silverson inline L4R mixer (Figure 5-21), two vortex

structures exist. The different vortex positions between the two scale mixers may result for the difference between the geometry of the rotors. It is also found that at different rotor blade orientation, the flow fields below the mixing head almost remain the same.

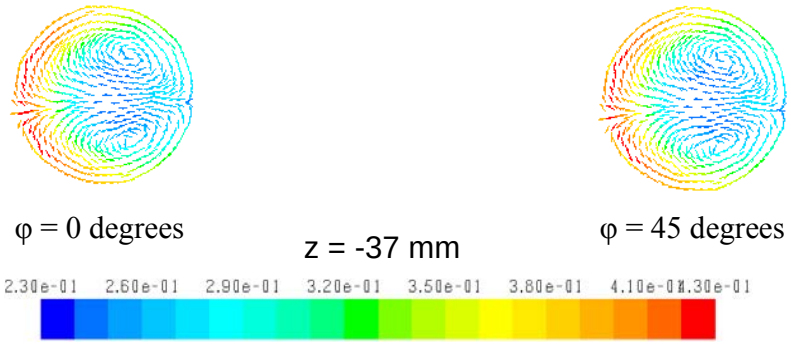

Figure 5-35: Normalized velocity magnitude vector plots at plane z = -34 mm (in the inlet pipe) in the 450LS mixer.

Along the y = 0 centerline, the fluid mainly moves in the radial direction while the profile is dominated by tangential flow near the inlet pipe wall.

In Figure 5-36, the fluid rotates with the shaft in the clockwise direction near the center of the flow field. There is a low velocity magnitude stream originating from the shaft extending to the mixer wall, which may be the result of the effect of the outlet close to the plane at z = 55 mm. It is also found that at different rotor blade orientations, the flow fields above the mixing head almost remain unchanged.

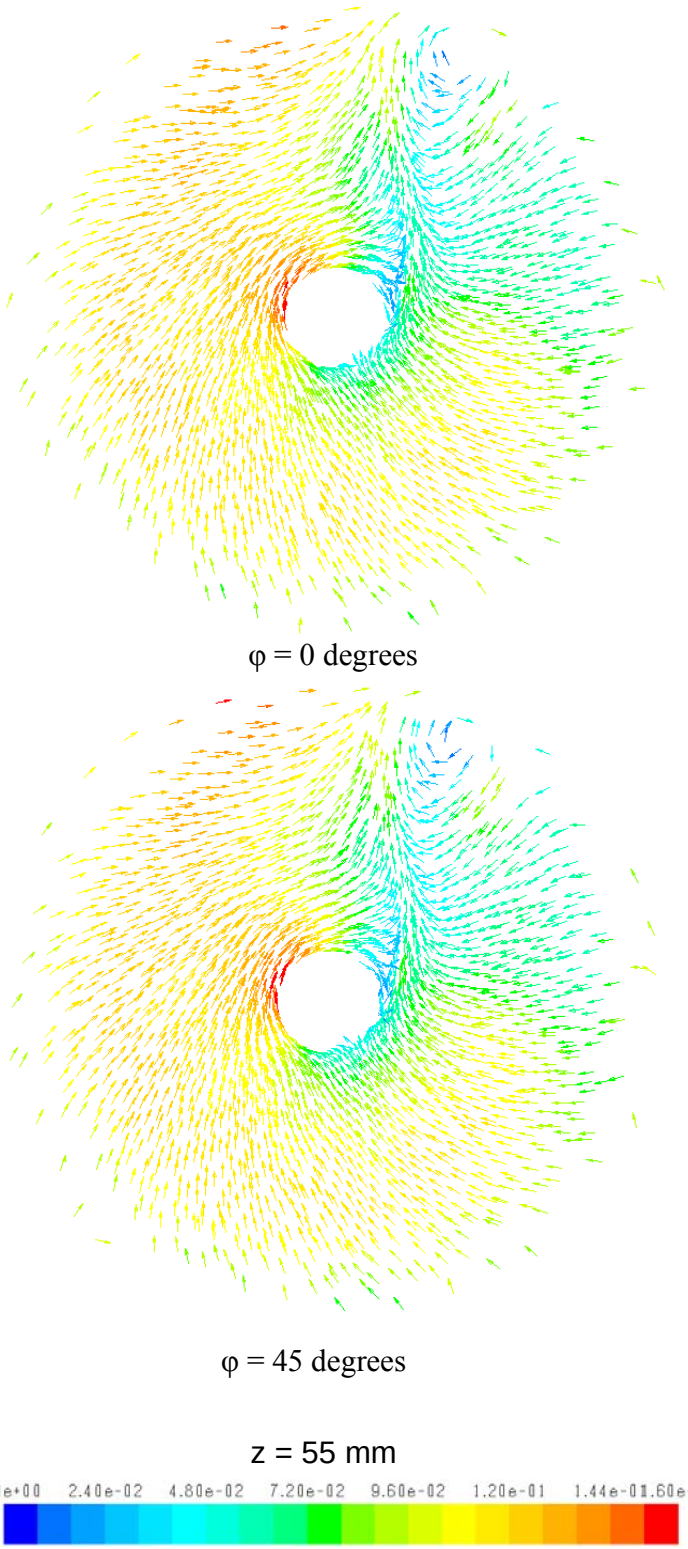

Figure 5-36: Normalized velocity magnitude vector plots at plane z = 62 mm (close to the volute top) in the 450LS mixer.

Figure 5-37 shows five different rotor position relative to stator slot 1.

The velocity filed normalized by the rotor tip speed (12.6 m/s) close to stator slot 1 on the mid-plane at 2100 rpm is given in Figure 5-38. Five different rotor positions are investigated (see Figure 5-37). From these figures it is seen that the fluid inside the stator head moves with the rotor in the clockwise direction, then it impinges on the

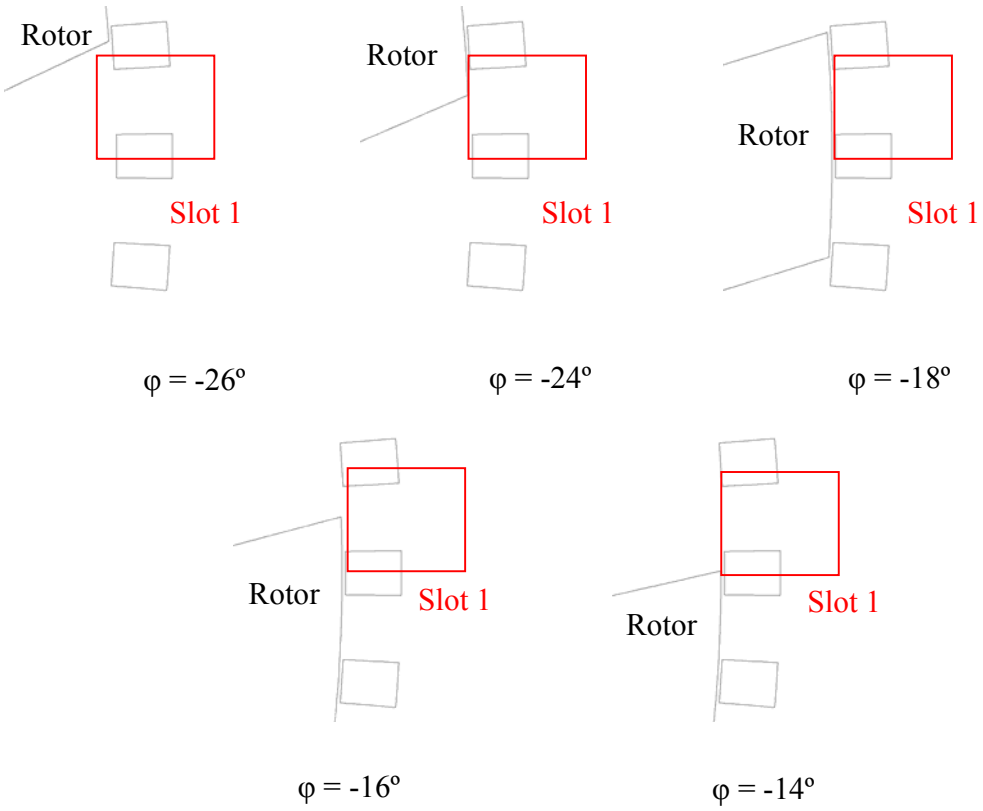

Figure 5-37: Position of the rotor blades relative to stator slot 1 in the 450LS mixer.

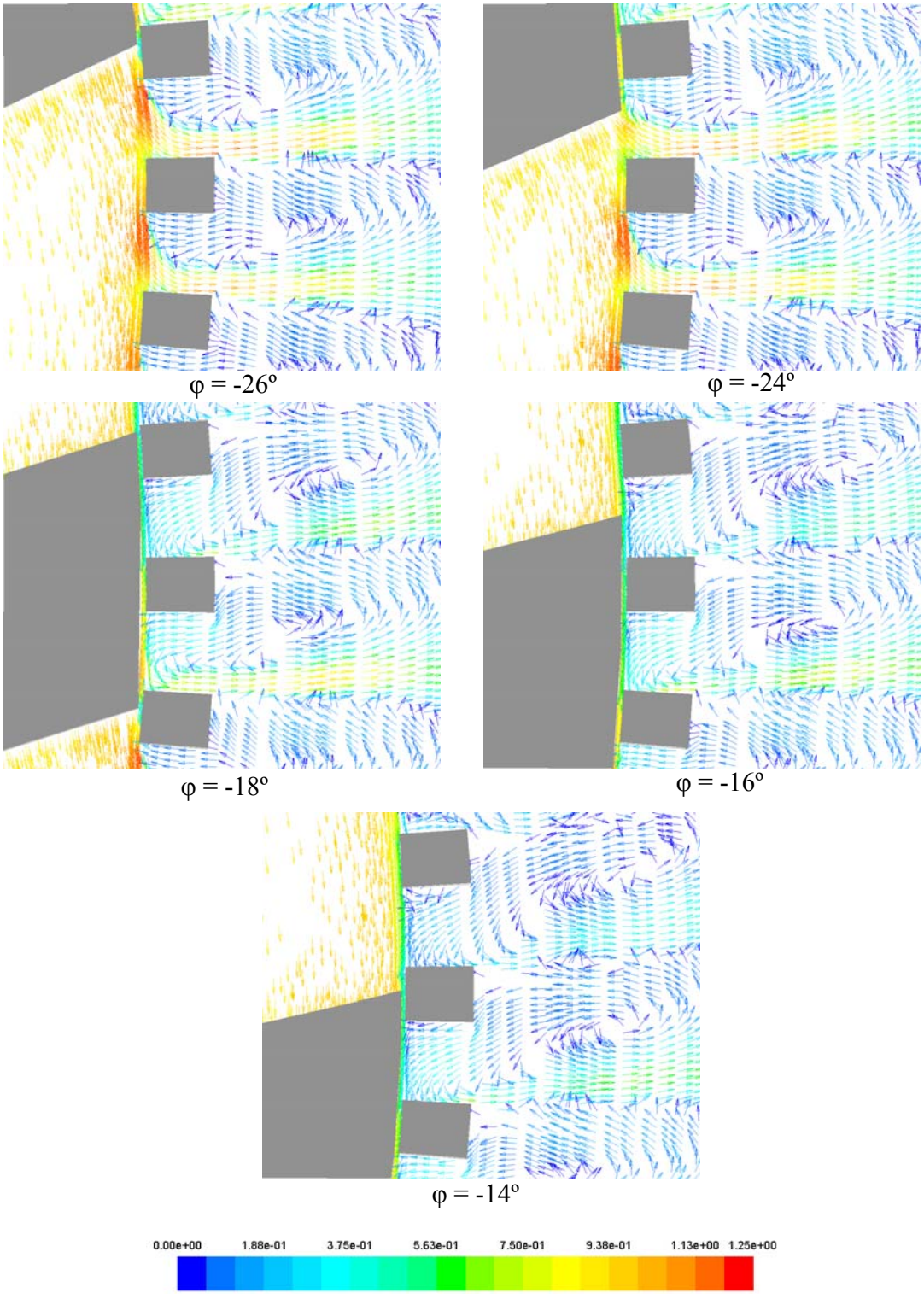

Figure 5-38: Normalized velocity vectors normalized around the stator slot at various blade positions (2100 rpm) in the 450LS mixer.

stator teeth (pushed by the rotor blade). The tangential velocity is changed to radial direction velocity. A strong radial jet is generated near each stator slot. Regardless of the rotor blade position, the jets are always generated close to the downstream edge of the stator slot. Meanwhile, outside the stator slots, the fluid is driven to re-enter the stator openings and move back into the rotor zone. Therefore, a vortex is generated close to each stator slot.

Compared with the flow field for the Silverson inline L4R mixer (in Figure 5-25), Figure 5-38 shows that the vortex structure is not in the stator slot, but is centered further outside in the volute. In addition, the jets close to the downstream edge of stator are much stronger than those in the Silverson inline L4R mixer. These difference result from the larger flow rate in the Silverson inline 450LS mixer (Table 5-2).

The angularly averaged radial velocity profile (normalized by rotor tip speed) along line 1 (the position of line 1 is similar to Figure 5-16) at 2100 rpm is shown in Figure 5-39. This figure indicates that the maximum jet radial velocity occurs close to the downstream edge ($\theta = 0^{o}$) of the stator slot 1 and decreases gradually with distance from the downstream edge. At some point near the upstream edge, the radial velocity exhibits negative values indicating a recirculation region existing where the liquid flows back into the stator slot 1. Compared with Figure 5-26, the normalized radial velocity increases about 20% percent.

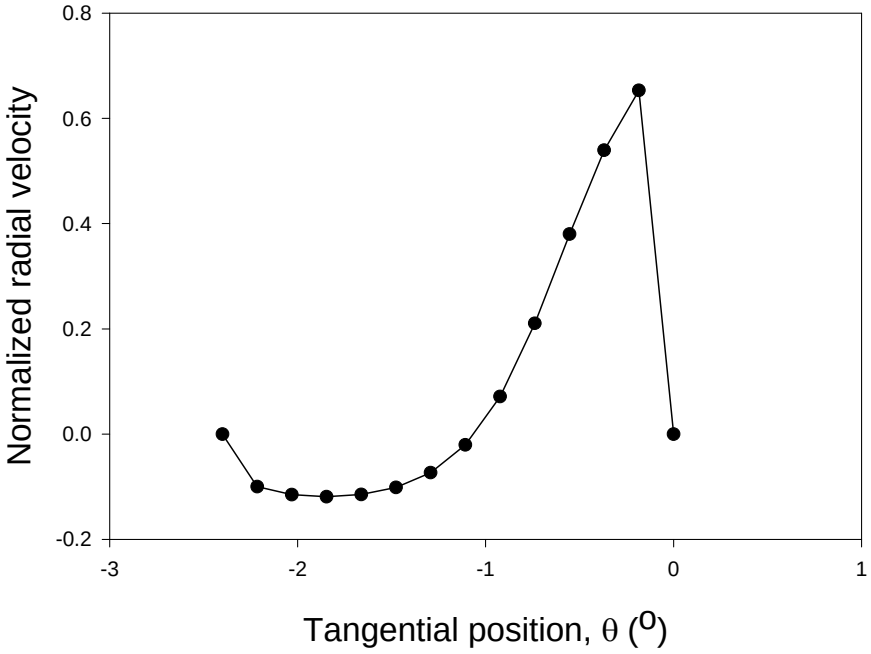

Figure 5-39: Normalized angularly averaged radial velocity profiles along line 1 (Figure 5-16) at 2100 rpm in Silverson inline 450LS mixer. The downstream edge is at θ = 0º and upstream edge is at θ = -2.4º.

The angularly averaged tangential velocity profile (normalized by rotor tip speed) along line 1 (Figure 5-16) at 2100 rpm is shown in Figure 5-40. This figure indicates that the maximum tangential velocity occurs at θ = -0.55º close to the middle of the stator slot 1. Moreover, at the downstream edge, the tangential velocity is relatively small which suggests that most of the tangential flux is converted into radial momentum flux when the fluid impinges on the downstream stator edge. Compared with Figure 5-27, the normalized tangential velocity also increases about 20% percent.

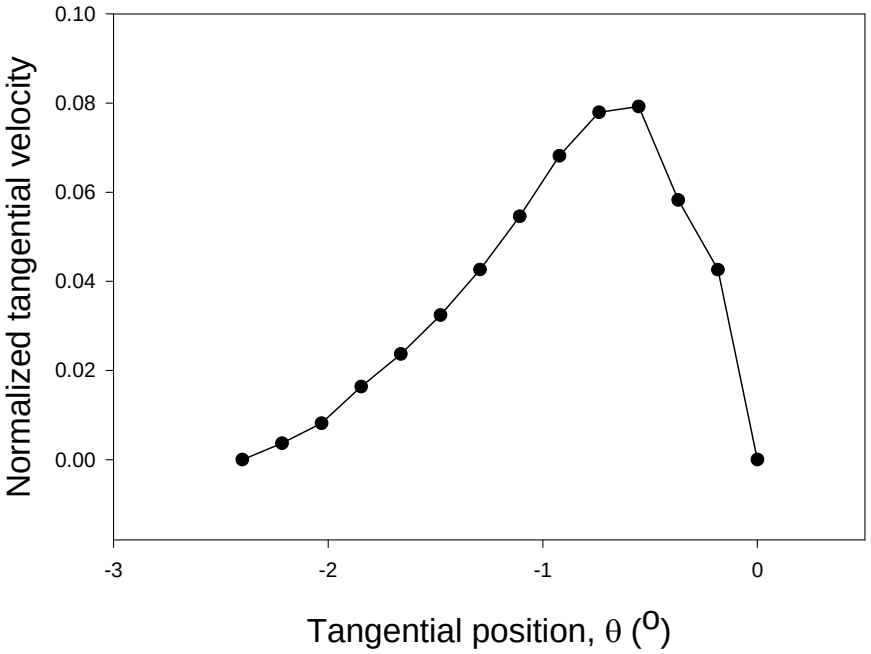

Figure 5-40: Normalized angularly averaged tangential velocity profiles along line 1 (Figure 5-16) at 2100 rpm in Silverson inline 450LS mixer. The downstream edge is at $\theta = 0^{o}$ and upstream edge is at $\theta = -2.4^{o}$.

Figure 5-41 presents the radial velocity profiles along line 1 in Figure 5-16 at various rotor blade positions at 2100 rpm. As the blade approaches the downstream stator edge, the jet radial velocity at the downstream edge increases and reaches a maximum just before the blade blocks stator slot 1. When the blade move away from the downstream edge, the radial velocity starts to decrease. In addition, when the blade moves towards the downstream edge, the circulation region widens as the blade blocks the fluid in the rotor region from passing through the stator slot. The circulation region reaches its maximum when the stator slot is fully blocked by the rotor blade.

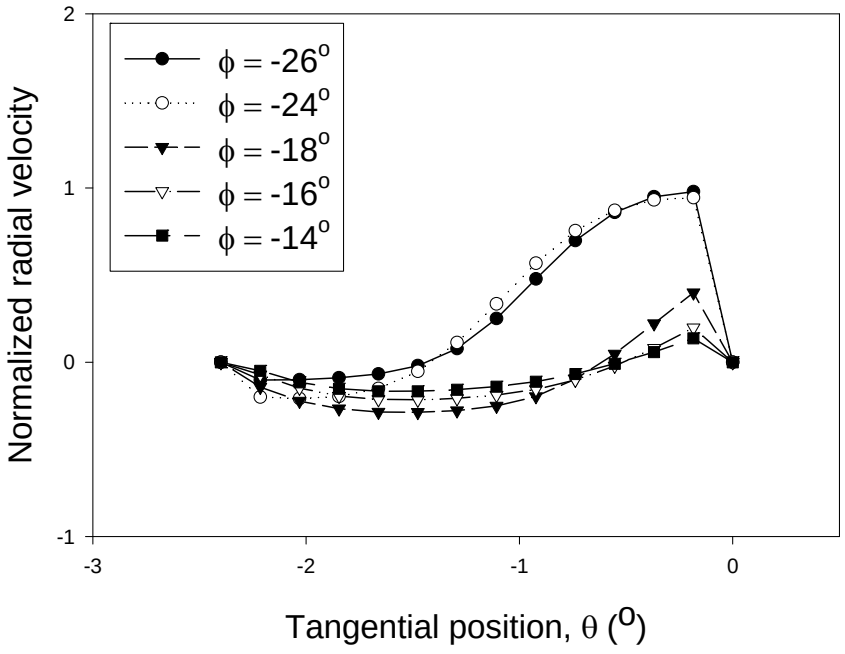

Figure 5-41: Normalized radial velocity profiles along line 1 (Figure 5-16) at 2100 rpm in Silverson inline 450LS mixer. The downstream edge of the stator slot is at θ = 0º and the upstream edge is at θ = -2.4º.

Figure 5-42 shows the position of Line 2 in the 450LS mixer.

In Figure 5-43, normalized angularly averaged results for the radial and tangential velocity along line 2, (see Figure 5-42), parallel to the z axis outside the stator head. Four stator slots are in the range of Line 2. The existence of the radial jet from stator slot 1 (z = 0) on the mid-plane is shown dramatically in the figure. It is also found that the jets along line 2 are much stronger than those in Figure 5-30 (L4R mixer).

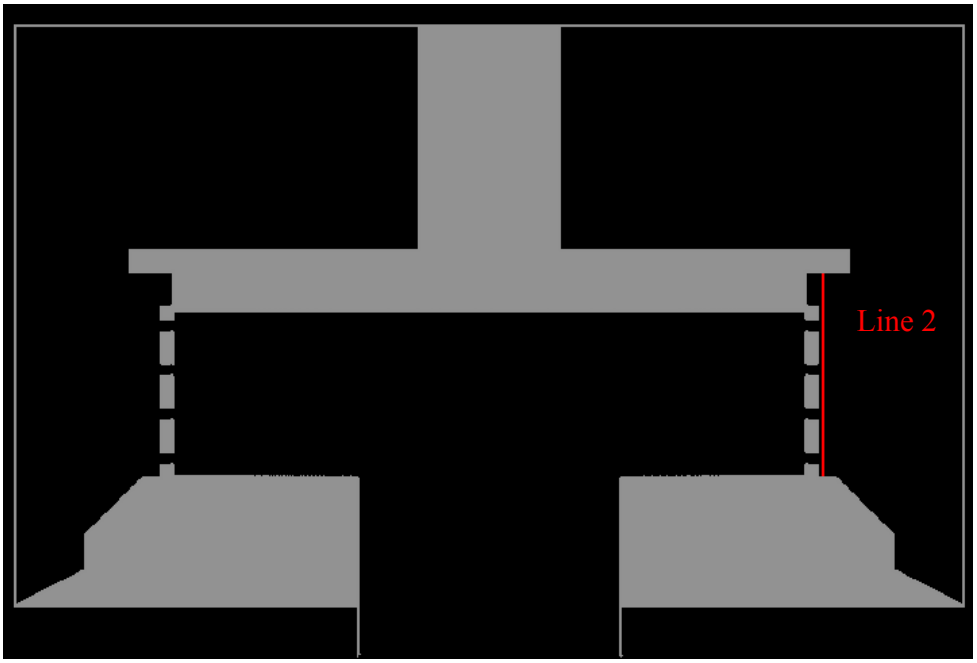

Figure 5-42: Line 2 monitored in the simulation.

Mean flow field of Silverson inline 600LS mixer

The mean flow fields on the mid-plane of the Silverson inline 600LS mixer at 1575 rpm are shown in Figure 5-44. The flow fields are normalized by the rotor tip speed which is 12.6 m/s the same as the Silverson inline L4R mixer at 8000 rpm and the 450LS mixer at 2100 rpm. From the vector plots, it is found that close to each stator slot, there exists a strong jet. The rotor rotates in the clockwise direction while the fluid that leaves the stator and enters the bulk of the volute tends to move in the anti-clockwise direction, which is opposite to the rotation direction of the rotor.

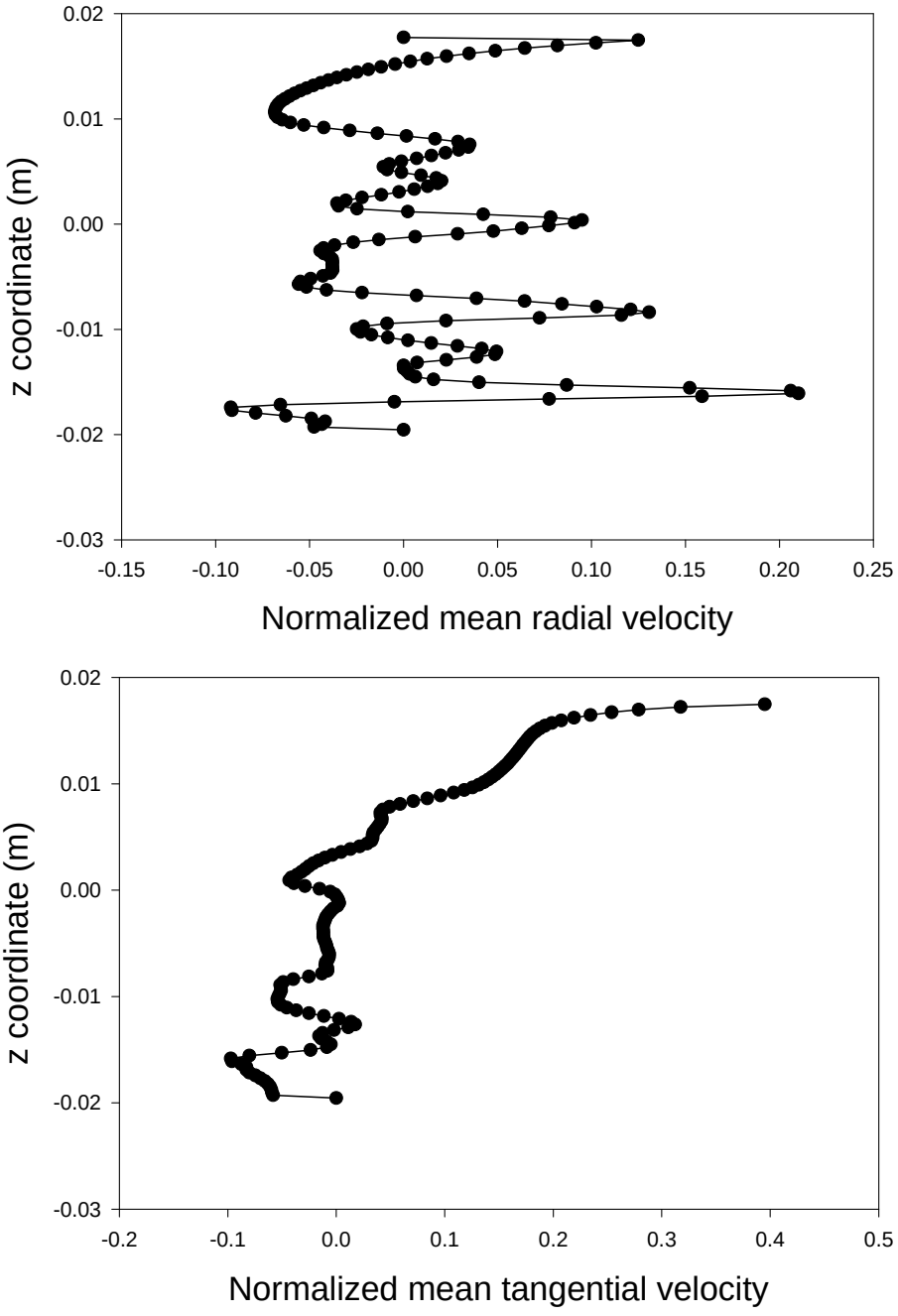

Figure 5-43: Axial profiles of the normalized angularly averaged radial and tangential velocity component along line 2 (Figure 5-42) at 2100 rpm in the Silverson inline 450LS mixer.

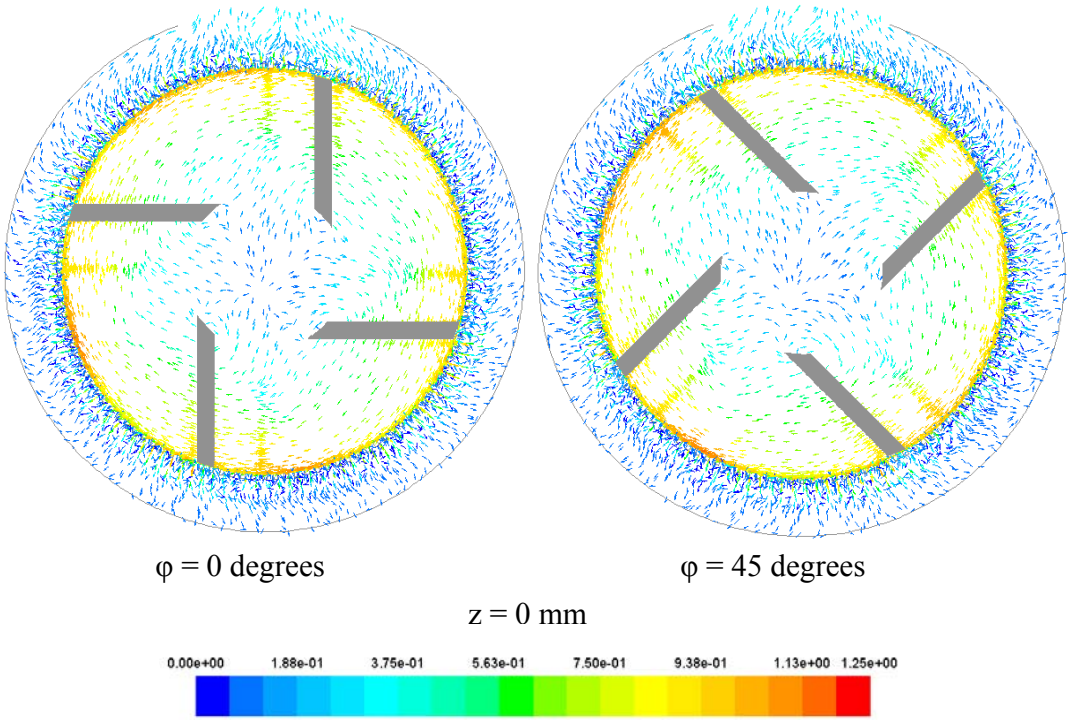

Figure 5-44: Normalized velocity magnitude snapshots on mid-plane of Silverson inline 600LS mixer at 1575 rpm.

The mean flow fields on plane y = 0 (see Figure 5-16) at 1575 rpm are shown in Figure 5-45, where the rotor blade positions are φ = 0 and 45 degrees. The fluid enters the rotor from the bottom and top, and is pumped rapidly out of the stator from the side. Therefore, vortices between the rotor blades are generated in the vertical plane. There are also some large vortex structures generated outside the mixing head at the corners of the mixer.

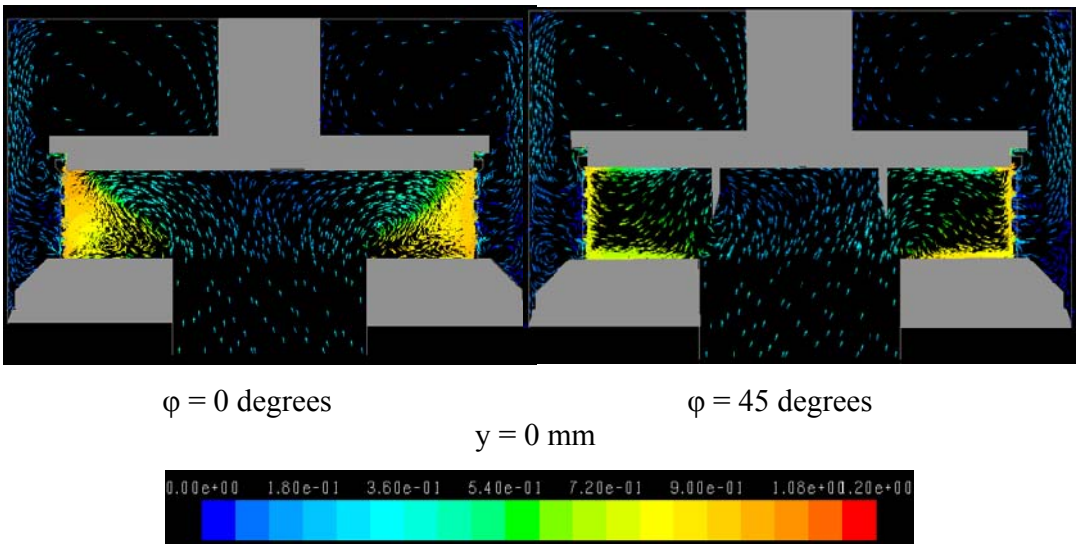

Figure 5-45: Normalized mean velocity vector snapshots at plane y = 0 in the Silverson inline 600LS rotor-stator mixer.

The flow fields at different z coordinates are shown in Figures 5-47 and 5-48 respectively, where the rotor blade positions are φ = 0 and 45 degrees. Plane z = 55 mm is close to top of the mixer while plane z = -37 mm is below the rotor (see Figure 5-46).

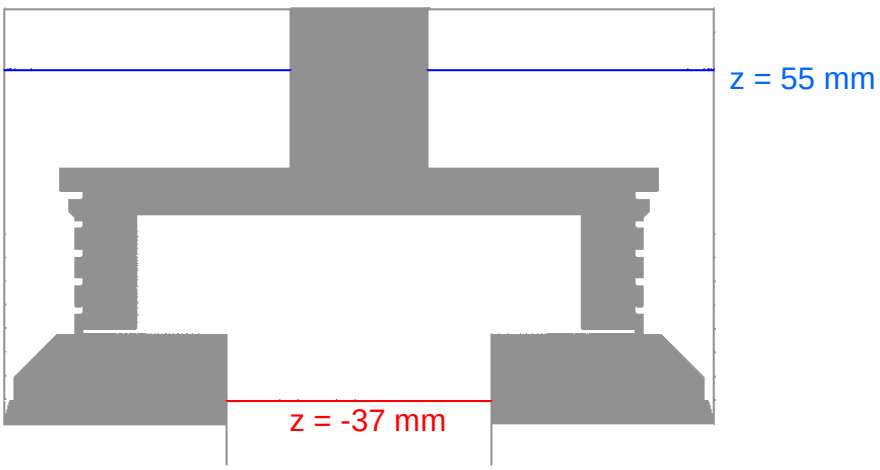

Figure 5-46: The z coordinate in Silverson inline 600LS rotor-stator mixer.

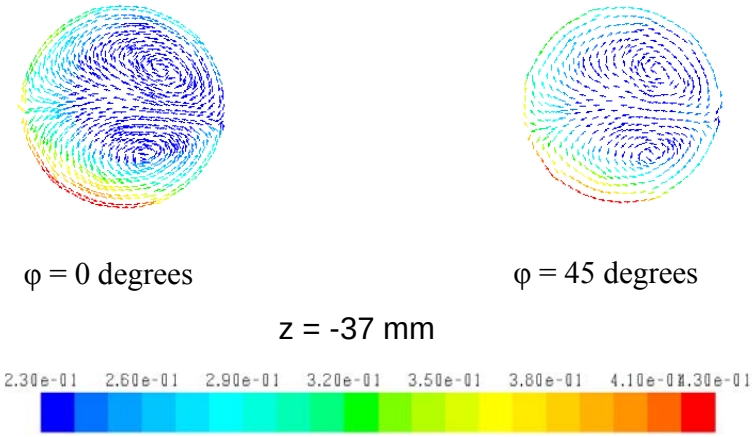

Figure 5-47: Normalized mean velocity vector plots at plane z = -37 mm (in the inlet pipe) in the 600LS mixer.

Figure 5-47 shows the flow field below the rotor in the inlet pipe. The fluid enters the rotor zone from the inlet pipe and then moves in a clockwise direction with the rotor. Similar to the flow field of Silverson inline L4R and 450LS mixers (Figure 5-21 and 5-35), two vortex structures exist. It is also found that at different rotor blade locations, the flow fields below the mixing head almost remain same. Along the y = 0 centerline, the fluid mainly moves in a radial direction while the velocity profile is dominated by tangential flow near the inlet pipe wall. The flow pattern of the Silverson inline 600LS mixer is quite similar to that of the Silverson inline 450LS mixer. However, there is a significant difference between the larger scale and the lab scale mixer.

In Figure 5-48, the fluid rotates in the clockwise direction close to the shaft. It is also seen that there is a low velocity magnitude stream originating from the shaft

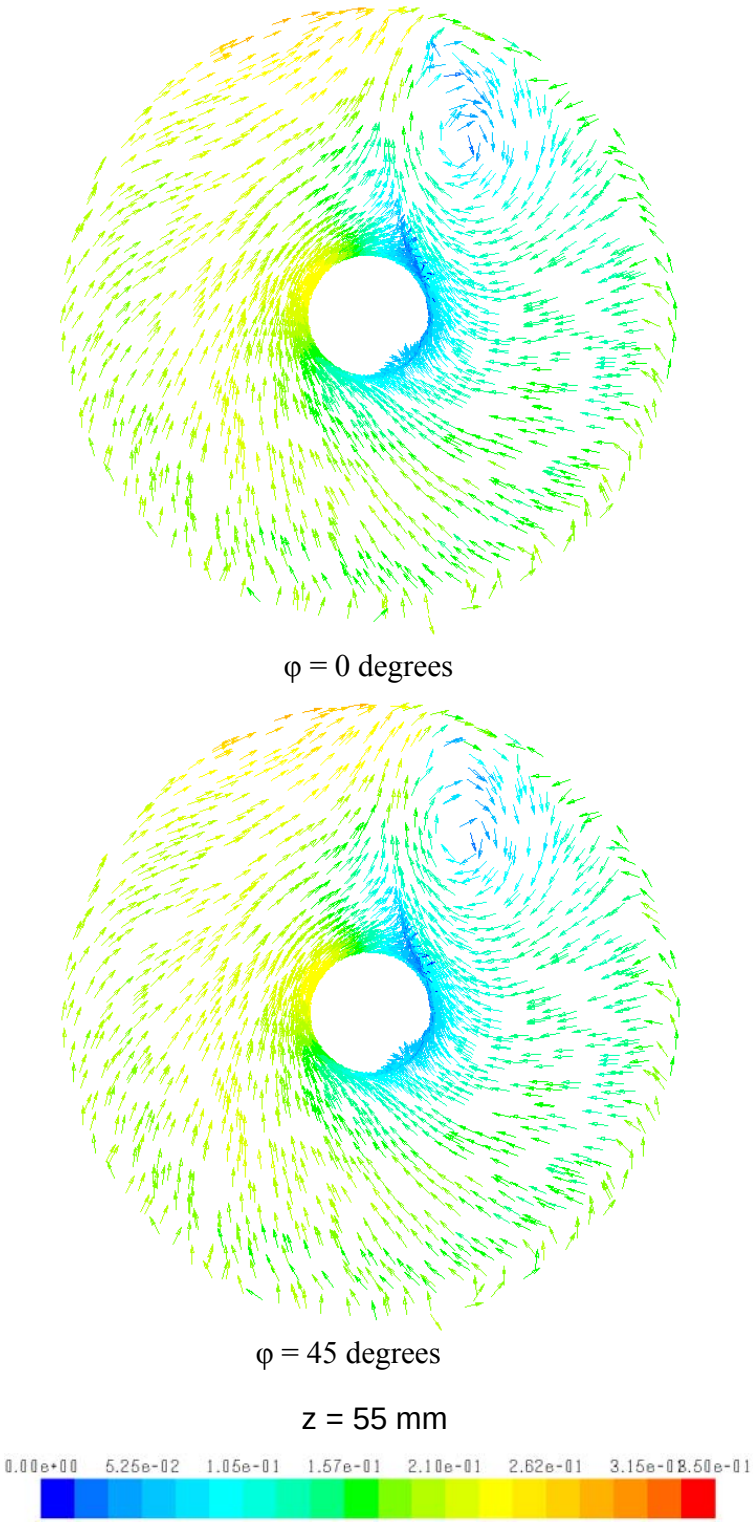

Figure 5-48: Normalized velocity magnitude vector plots at plane z = 55 mm (close to the volute top).

extending to the mixer wall, similar to the case of the Silverson 450LS mixer. The flow structures in the Silverson 600LS mixer are closer to those in the 450LS mixer than those in the L4R mixer.

Figure 5-49 shows five different rotor position relative to stator slot 1.The velocity filed normalized by the rotor tip speed (12.6 m/s) close to stator slot 1 on the mid-plane at 2100 rpm are shown in Figure 5-50. Five different rotor positions are investigated (shown in Figure 5-49). The flow pattern is very similar to the Silverson inline 450LS mixer (Figure 5-38). However, compared with the Silverson inline L4R mixer, the radial jet originating from each stator slot is much stronger and the position of the vortex is different.

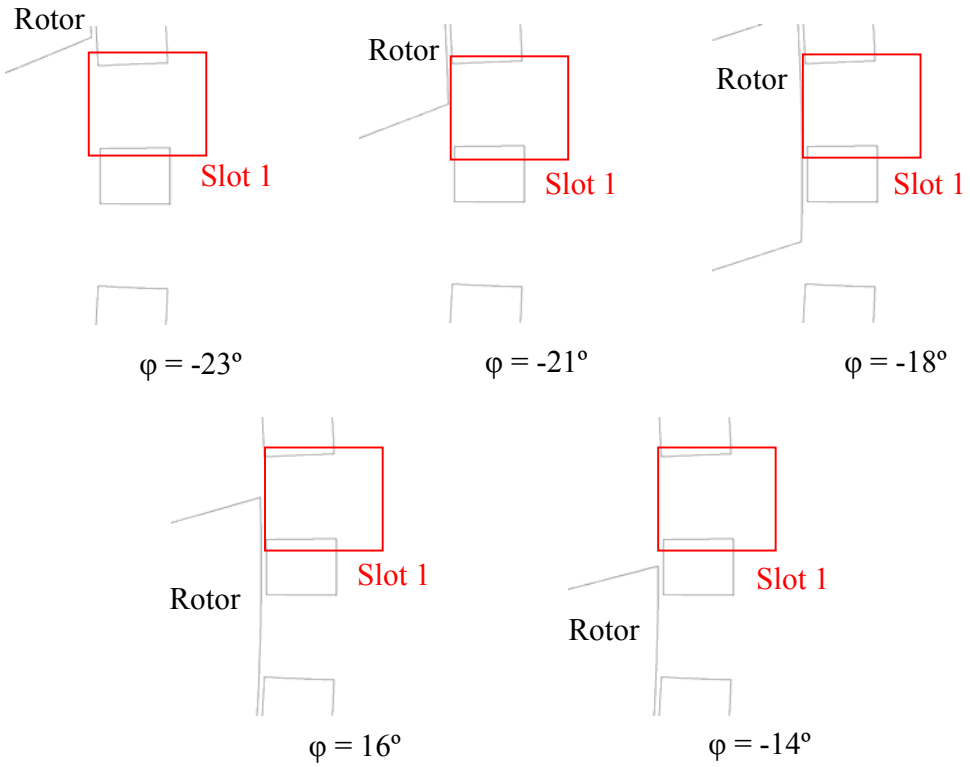

Figure 5-49: Position of the rotor blades relative to stator slot 1 in the 600LS mixer.

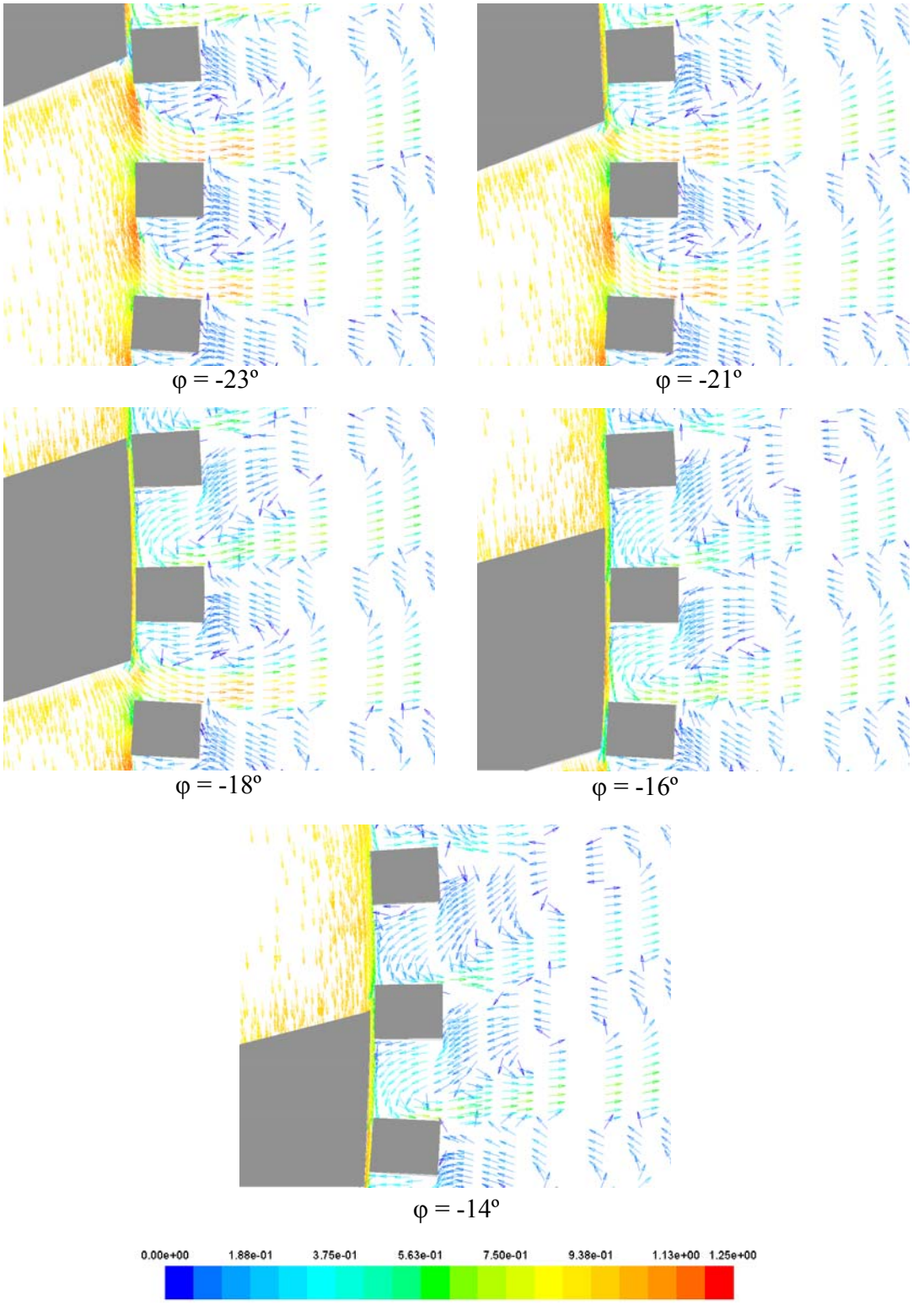

Figure 5-50: Normalized velocity vectors normalized around the stator slot at various blade positions (1575 rpm) in the 600LS mixer.

The angularly averaged radial velocity profile (normalized by rotor tip speed) along line 1 (the position of line 1 is similar to Figure 5-16) at 1575 rpm is shown in Figure 5-51. This figure shows that the maximum jet radial velocity occurs close to the downstream edge ($\theta = 0^o$) of stator slot 1, and decreases gradually with distance from the downstream edge. At some point near the upstream edge, the radial velocity

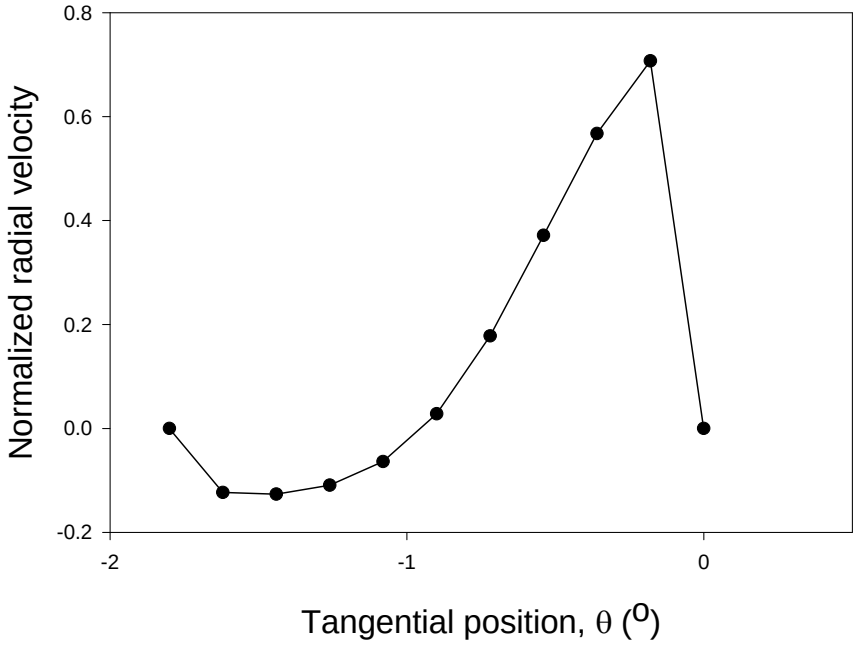

Figure 5-51: Normalized angularly averaged radial velocity profiles along line 1 (Figure 5-16) at 1575 rpm in the Silverson inline 600LS mixer. The downstream edge of the stator slot is at $\theta = 0^o$ and the upstream edge is at $\theta = -1.8^o$.

exhibits negative values indicating a recirculation region where the liquid flows back into the stator slot. Compared with Figure 5-39, the radial velocity profile of the Silverson inline 600LS mixer is quite close to that of the Silverson inline 450LS mixer. However, the maximum value of normalized jet mean velocity increases about 20% percent compared with the bench scale L4R mixer.

The angularly averaged tangential velocity profile (normalized by rotor tip speed) along line 1 (Figure 5-16) at 1575 rpm is shown in Figure 5-52. This figure indicates that the maximum tangential velocity occurs at θ = -0.54º close to the middle of the stator slot 1. Compared with Figure 5-27 and 5-40, the maximum value of normalized jet mean velocity increases with the size of the mixer.

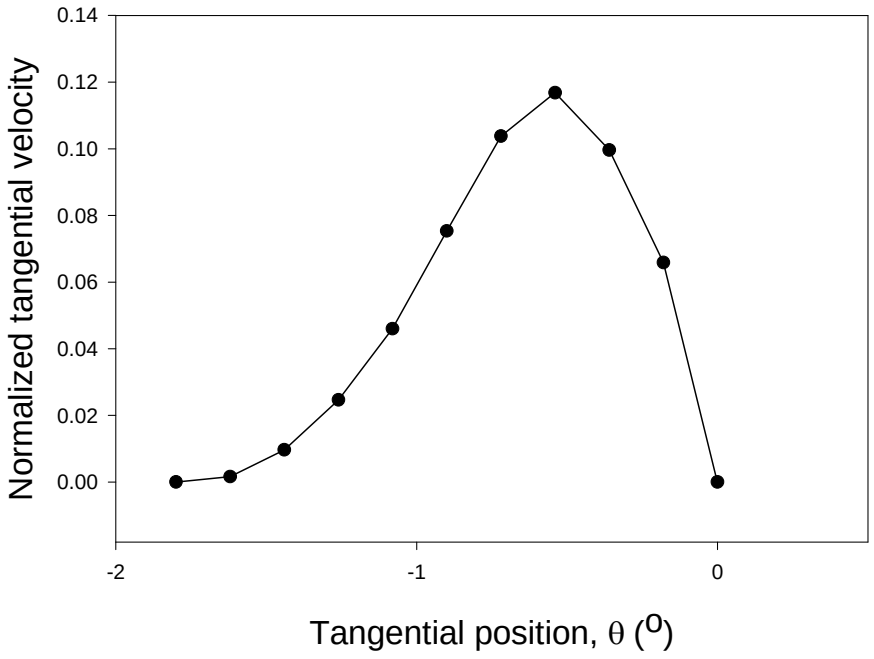

Figure 5-52: Normalized angularly averaged radial mean velocity profiles along line 1 (Figure 5-25) at 1575 rpm in Silverson inline 600LS mixer. The downstream edge of the stator slot is at θ = 0º and the upstream edge is at θ = -1.8º.

Figure 5-53 presents the radial velocity profiles along line 1 in Figure 5-25 at various rotor blade positions at 1575 rpm. It shows similar trend as Figures 5-29 and 5-41.

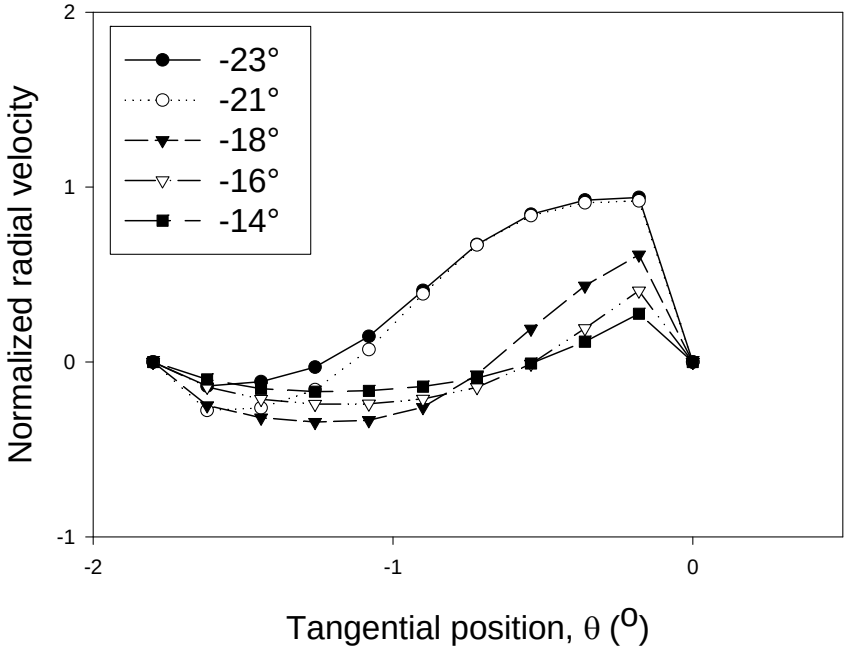

Figure 5-53: Normalized radial mean velocity profiles along line 1 (Figure 5-16) at 1575 rpm in Silverson inline 600LS mixer. The downstream edge of the stator slot is at $\theta = 0^{o}$ and the upstream edge is at $\theta = -1.8^{o}$.

Figure 5-54 shows the position of Line 2 in the 600LS mixer.

In Figure 5-55, normalized angularly averaged results for the radial and tangential mean velocity along line 2, which is shown in Figure 5-54, parallel to the z axis outside the stator head, are shown. Four stator slots are in the range of Line 2. The existence of the jet from stator slot 1 on the mid-plane (z = 0) is shown dramatically in the figure. It is also found that the jets along line 2 are much stronger than those in Figure 5-31 for the Silverson inline L4R mixer.

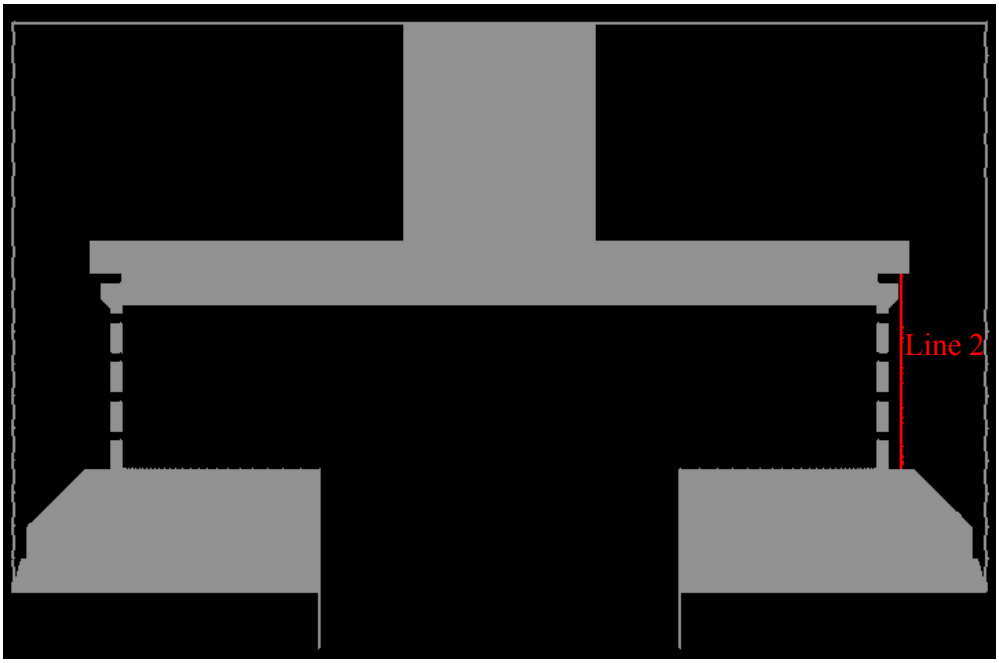

Figure 5-54: Line 2 monitored in the simulation.

5.4.3 Turbulent flow field of the Silverson inline L4R, 450LS and 600LS mixers

Turbulent flow field of the Silverson inline L4R mixer

The TKE fields on the mid-plane of the Silverson inline L4R mixer at 4000 and 8000 rpm are shown in Figure 5-56. The TKE fields are normalized by the tip speed squared (43.0336 m^2/s^2 at 4000 rpm and 158.76 m^2/s^2 at 8000 rpm). These contours suggest that the normalized TKE fields at 4000 and 8000 rpm are quite similar to each other. High TKE regions exist in the rotor swept volume and close to the stator slot openings.

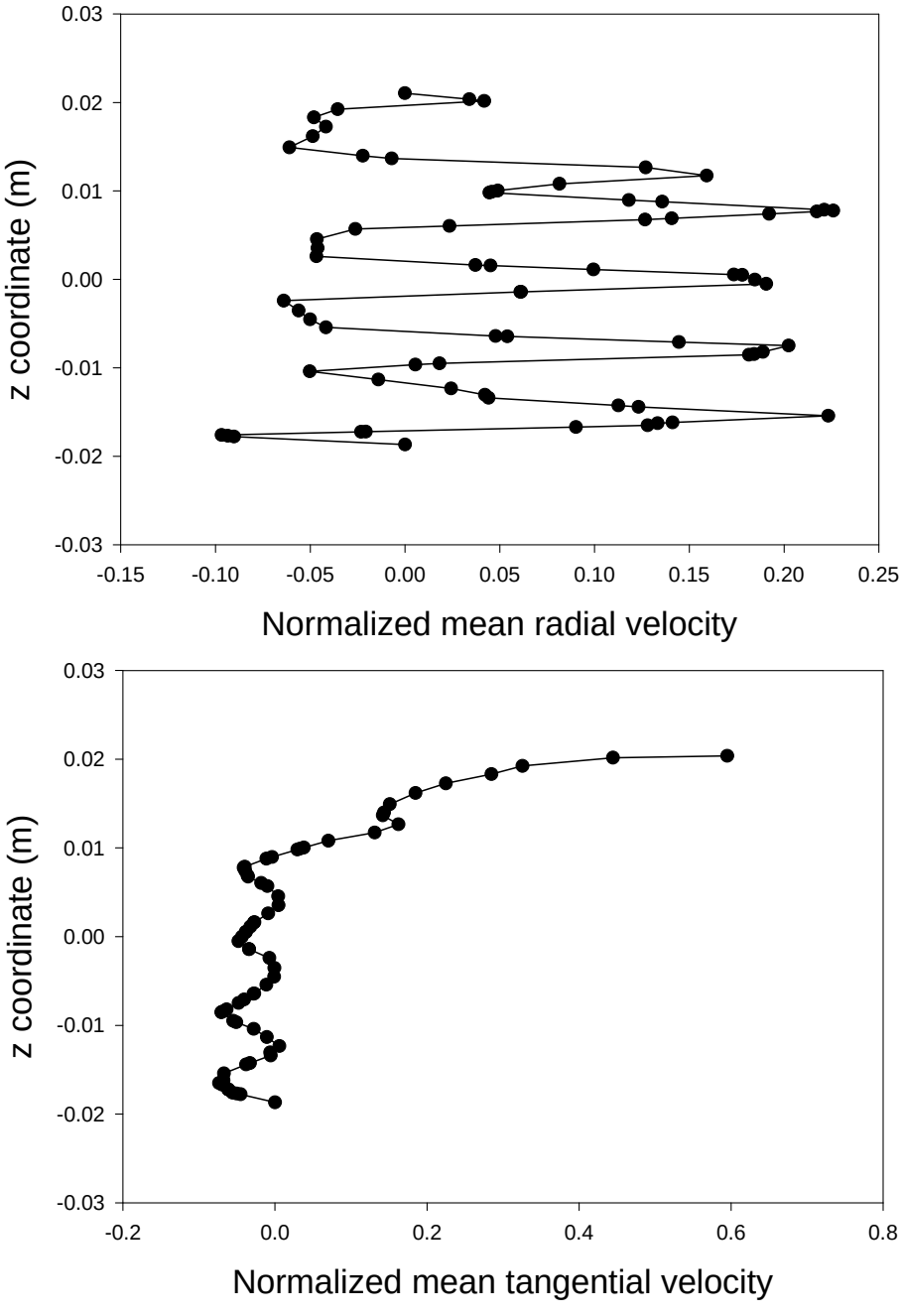

Figure 5-55: Axial profiles of the normalized angularly averaged mean radial and tangential velocity components along line 2 (Figure 5-54) at 1575 rpm in the Silverson inline 600LS mixer.

The TKE fields normalized by the rotor tip speed squared close to stator slot 1 (see Figure 5-22) on the mid-plane at 4000 and 8000 rpm are shown in Figure 5-57 and 5-58. From these figures, it can be found that the TKE magnitude is affected by the rotor blade position relative to the stator slot openings. The highest TKE occurs in relatively small region close to the downstream edges of the stator slots when the rotor blade is approaching. The high TKE region is limited to the small region close to the stator slot.

Figure 5- 59 presents the normalized angularly averaged results on TKE along line 2, shown in Figure 5-30. The TKE profiles at 4000 and 8000 rpm show similar trend. The jet (z = 0 m) from stator slot 1 on the mid-plane is shown dramatically in the figure.

The TDR fields on the mid-plane of the Silverson inline L4R rotor-stator mixer at 4000 and 8000 rpm are shown in Figure 5-60. The TDR fields are normalized by N^3D^2, where N is the rotor rotation rate and D is the rotor diameter (285 m^2/s^3 at 4000 rpm and 2280 m^2/s^3 at 8000 rpm). These contours suggest that the normalized TDR fields at 4000 and 8000 rpm are quite similar to each other. High TDR regions exist adjacent to the rotor blades in the rotor swept volume and close to the stator slot openings.

The TDR fields normalized by N^3D^2 close to the stator slot 1 on the mid-plane (in Figure 5-16) at 4000 and 8000 rpm are shown in Figure 5-61 and 5-62. From these

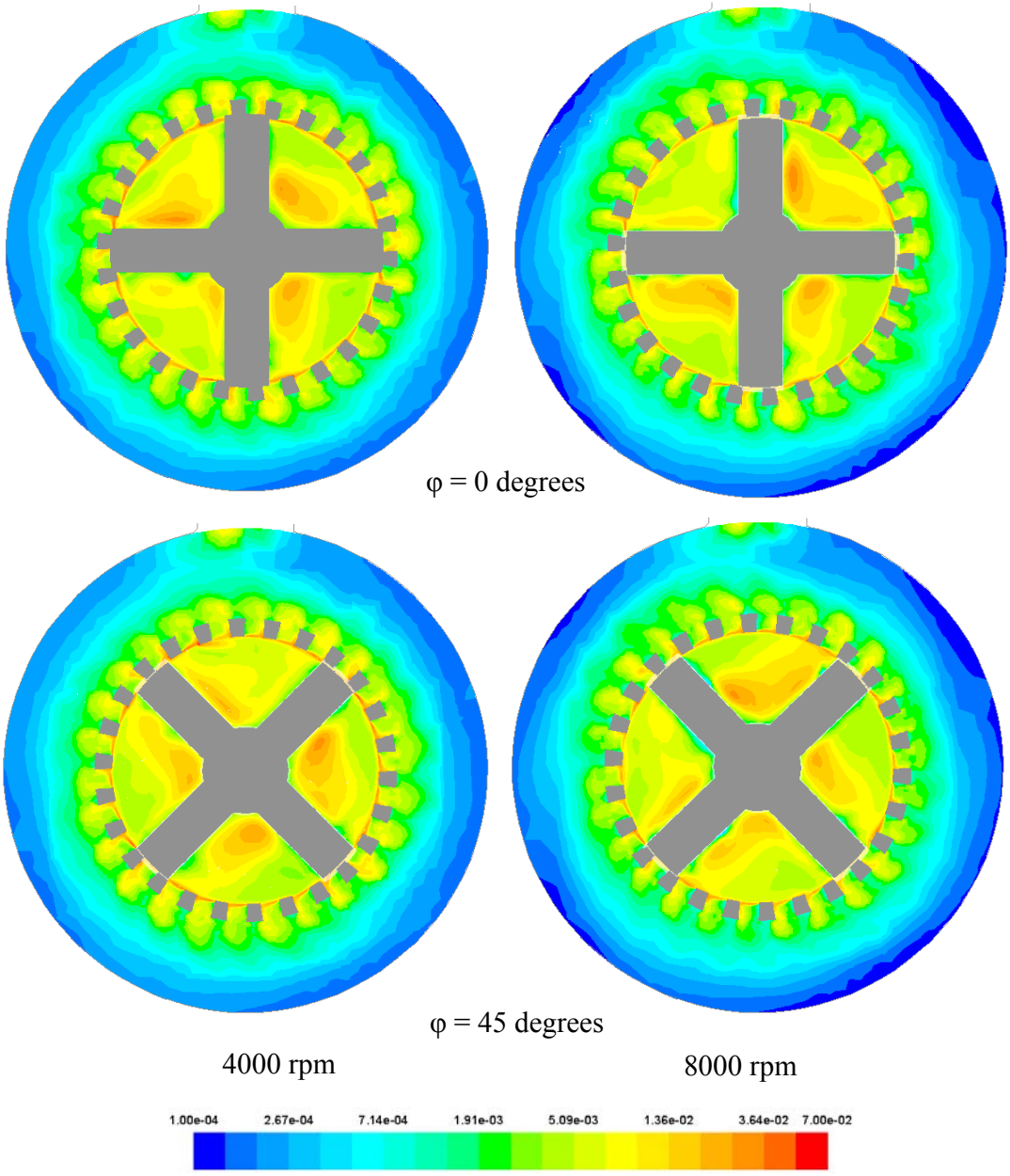

Figure 5-56: Normalized TKE contours at 4000 and 8000 rpm on the mid-plane of the Silverson inline L4R rotor-stator mixer.

figures, it can be seen that the TDR magnitude is affected by the rotor blade position relative to the stator slot openings. The highest TDR occurs in a relatively small region close to the downstream edges of the stator teeth when the rotor blade is

approaching the stator slot. High turbulent dissipation rate is also predicted on the stator slots edges, which could be the results of the stagnation of fluid on this wall.

The TDR distributed in the rotor swept region, gap region, stator slot region and mixer bulk region (which are similar to the regions in Figure 4-76) for the Silverson inline L4R mixer are shown as Table 5-4. It is found that the majority of the turbulent energy is dissipated in the mixing head region (about 84% of the total energy). In the mixing head, the turbulent energy is consumed almost evenly in rotor swept, gap and stator slot regions. The TDR increases significantly with rotation rate. With doubled rotation rate, the proportion of TDR in the gap region increases about 9% while the proportion of TDR in the stator slot region decreases about 7%.

Turbulent flow field of the Silverson inline 450LS mixer

The TKE fields on the mid-plane of the Silverson inline 450LS mixer at 2100 rpm are shown in Figure 5-63. The TKE fields are normalized by the rotor tip speed squared (158.76 m^2/s^2 same as that of the Silverson inline L4R mixer at 8000 rpm). These contours suggest that high TKE regions exist in the rotor swept volume and close to the stator slot openings. It is also seen that the magnitude of the TKE in Silverson inline 450LS mixer is much larger than that in the Silverson inline L4R mixer.

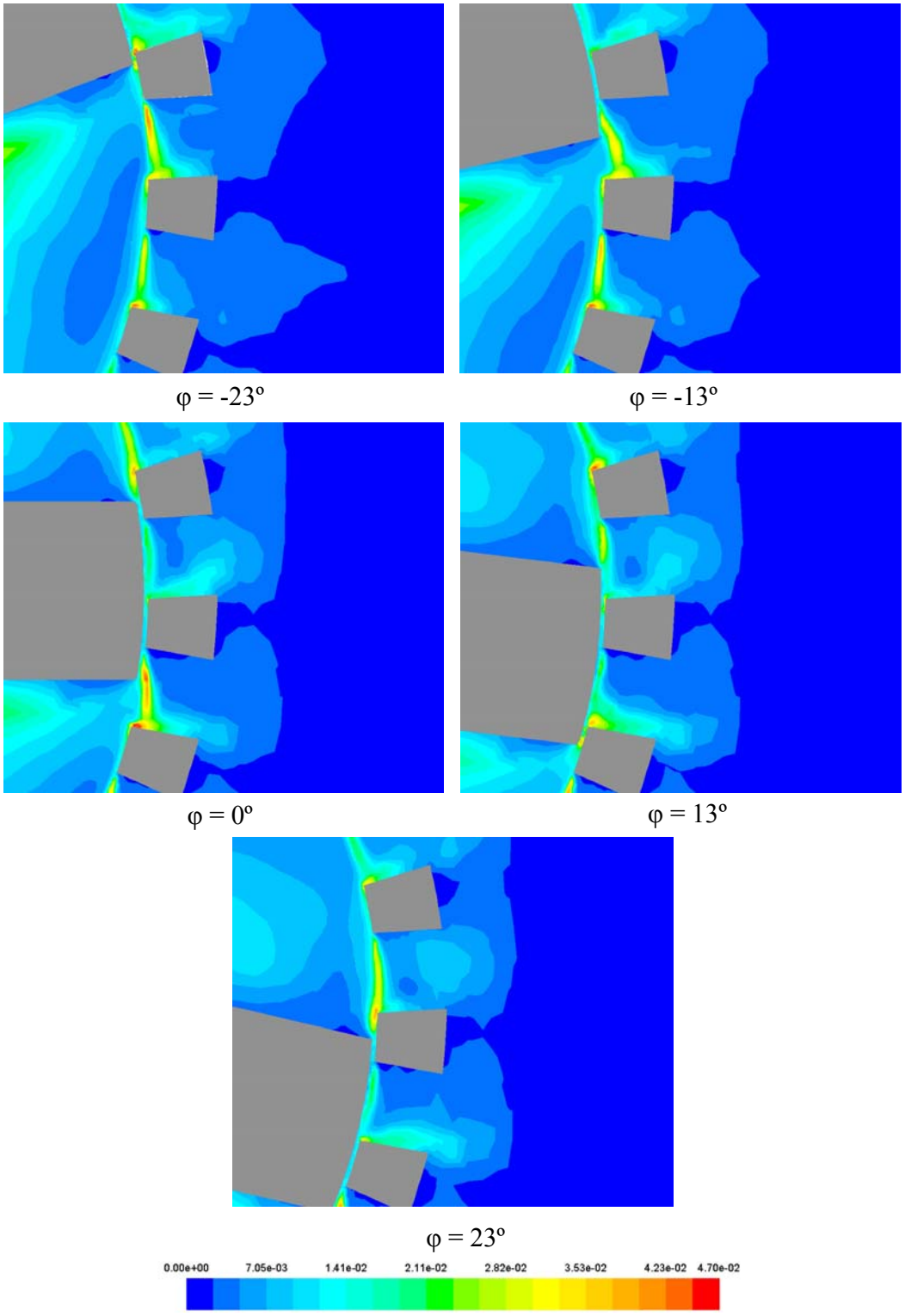

Figure 5-57: Normalized TKE around the stator slot at various blade positions at 4000 rpm in the Silverson inline L4R mixer.

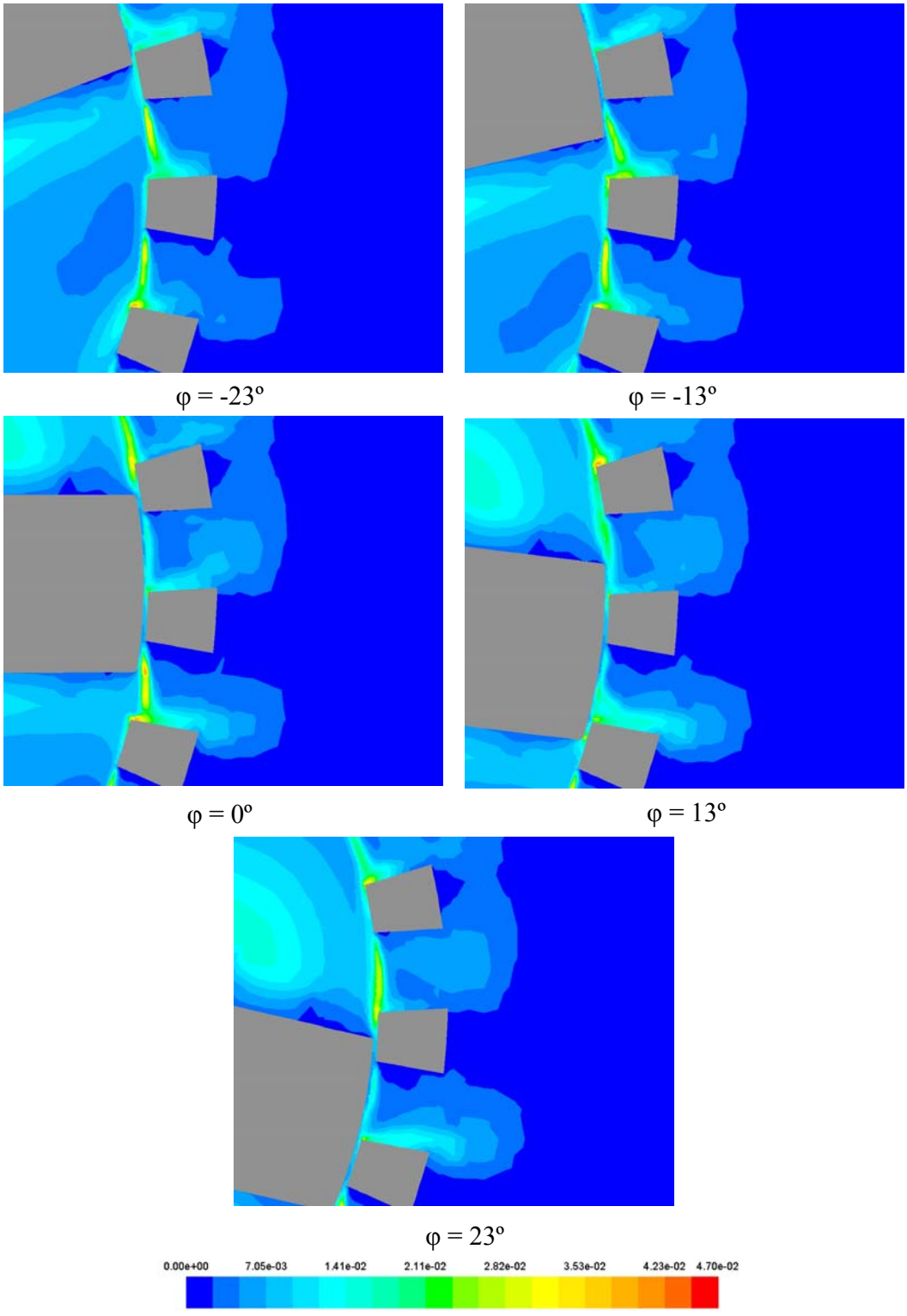

Figure 5-58: Normalized TKE around the stator slot at various blade positions at 8000 rpm in the Silverson inline L4R mixer.

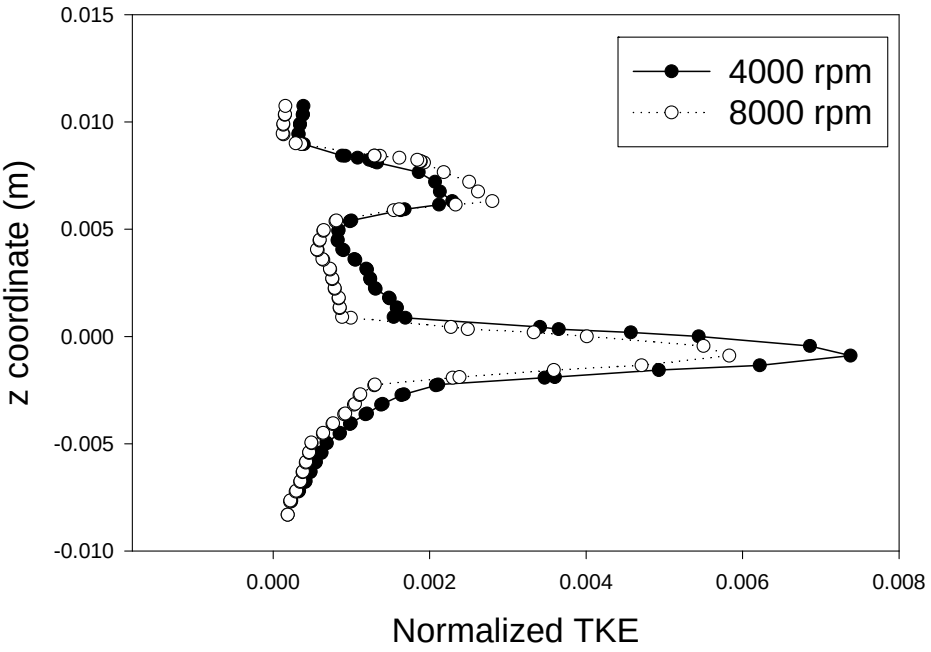

Figure 5-59: Axial profiles of the normalized angularly averaged TKE along line 2 (Figure 5-30) at 4000 and 8000 rpm in the Silverson L4R inline mixer.

The TKE fields normalized by the rotor tip speed squared close to the stator slot 1 on the mid-plane (in Figure 5-16) at 2100 rpm are shown in Figure 5-64. From these figures, it can be found that the TKE magnitude is affected by the rotor blade position relative to the stator slot openings. The highest TKE occurs in the high shear gap close to the rotor blade and in the region close to the downstream edges of the stator slot when the rotor blade is approaching the stator slot. Compared with the TKE field

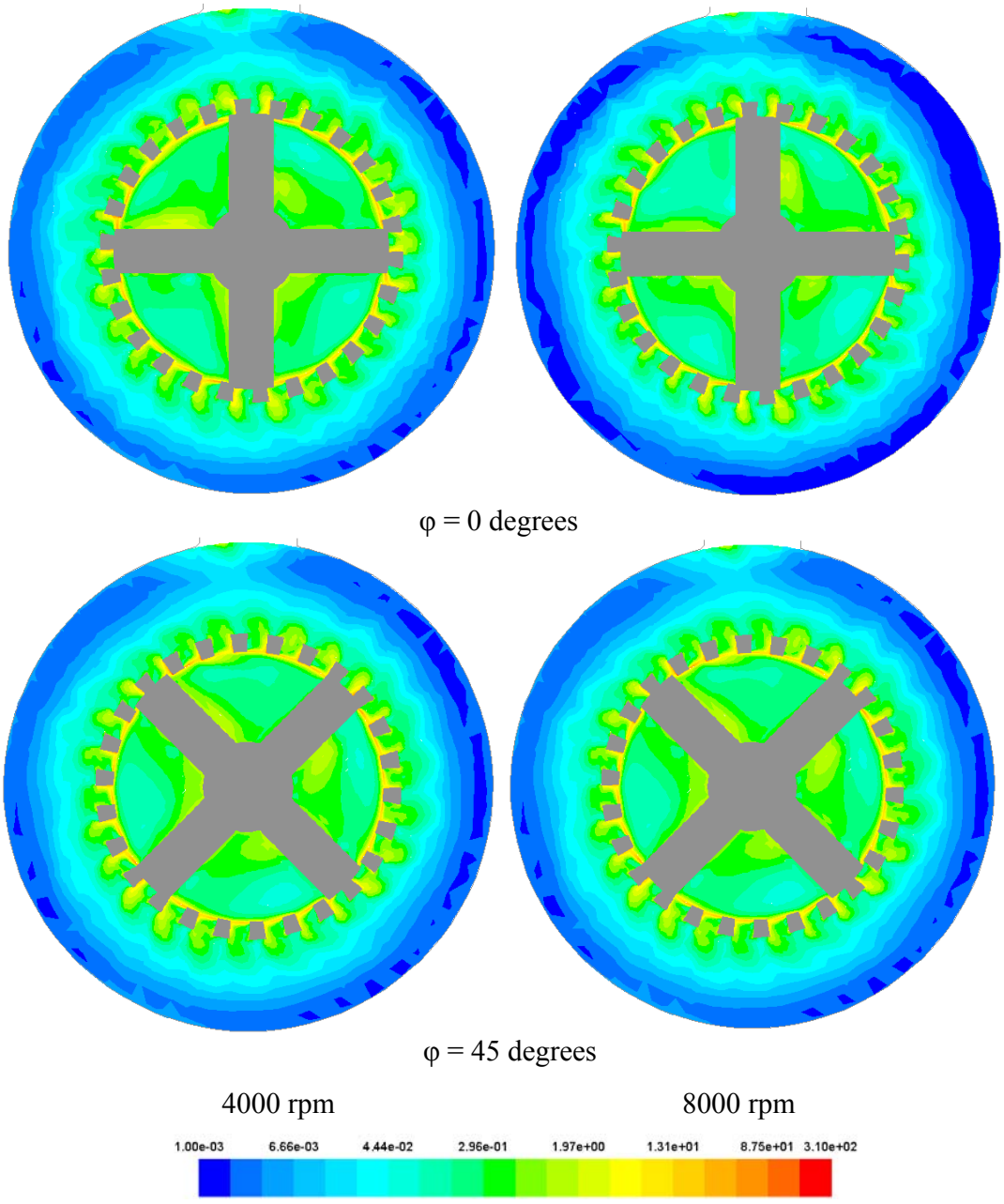

Figure 5-60: Normalized TDR contours at 4000 and 8000 rpm on the mid-plane of the Silverson inline L4R rotor-stator mixer.

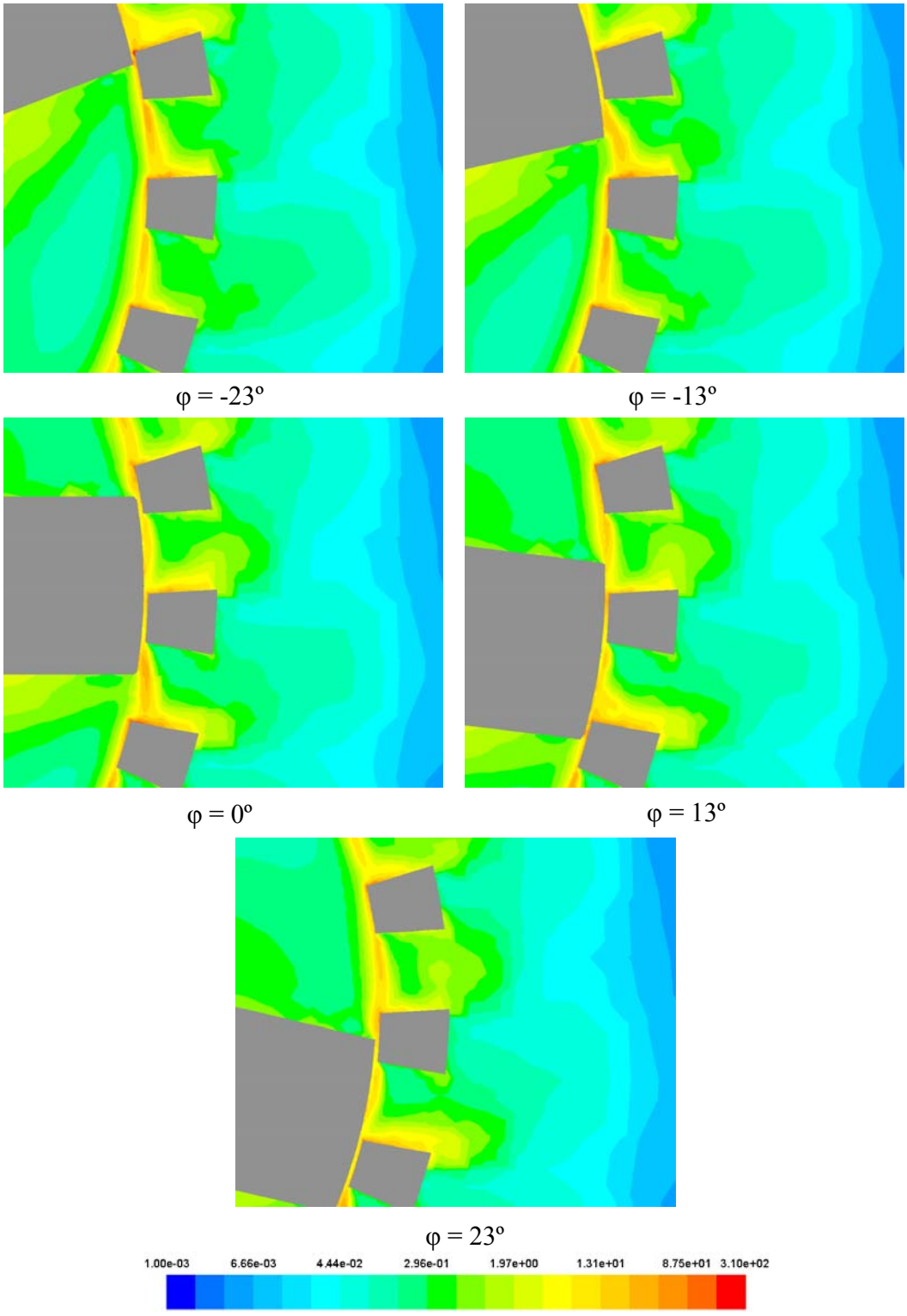

Figure 5-61: Normalized TDR around the stator slot at various blade positions at 4000 rpm in the Silverson inline L4R mixer.

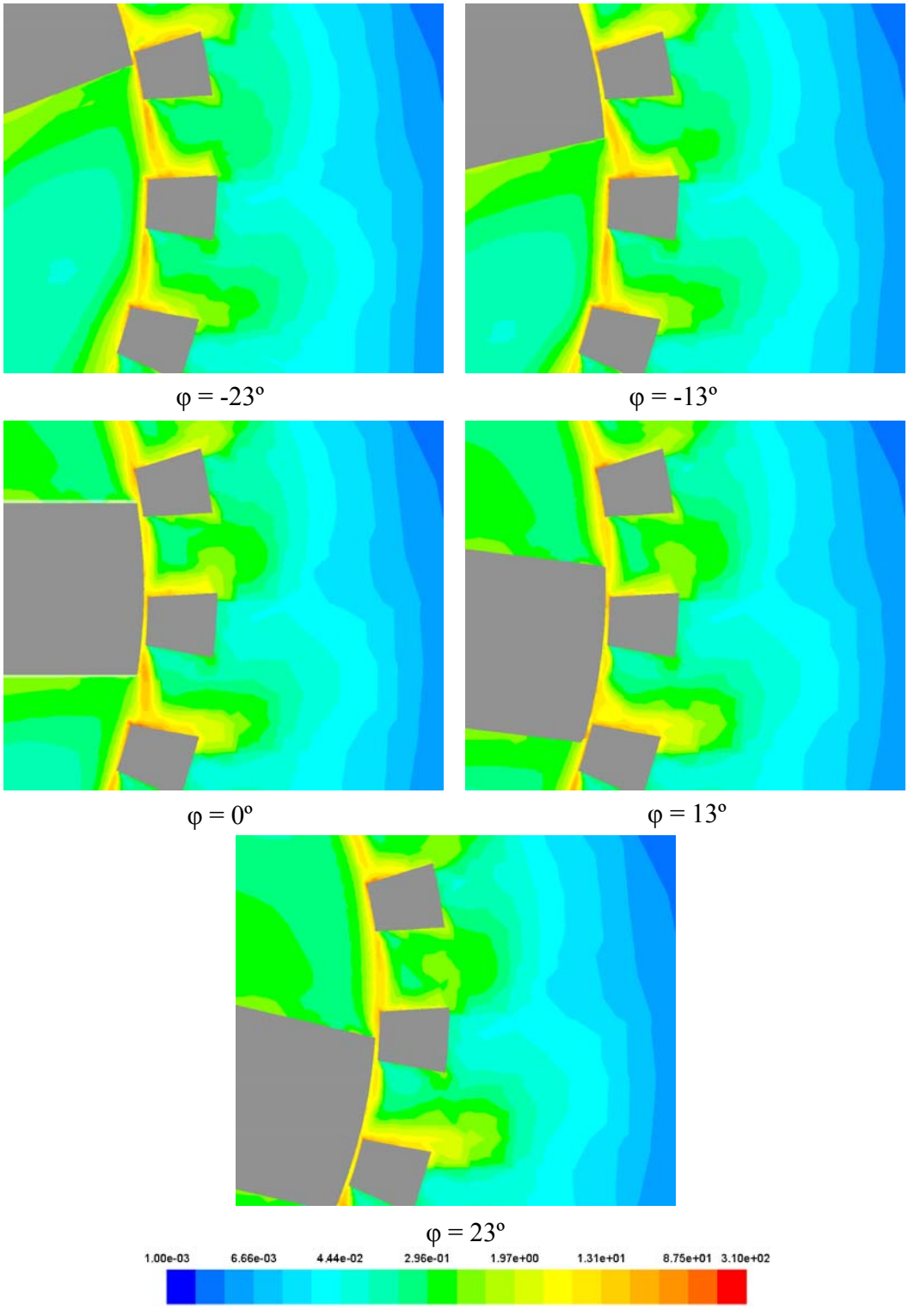

Figure 5-62: Normalized TDR around the stator slot at various blade positions at 8000 rpm in the Silverson inline L4R mixer.

Table 5-4: Predictions of distributions of turbulent energy dissipation in the Silverson inline L4R mixer at 4000 and 8000rpm.

Region	4000 rpm	8000 rpm
Rotor swept volume	0.81337 W (27.5%)	4.96768 W (26.2%)
Gap region	0.73755 W (25.0%)	6.53274 W (34.5%)
Stator slot region	0.92955 W (31.5%)	4.42895 W (23.4%)
Mixer bulk region	0.44313 W (15.0%)	3.03117 W (15.9%)
Total turbulent energy dissipated	2.9536 W (100%)	18.96054 W (100%)

*It is known that prediction of magnitude and spatial variation of TDR is inaccurate in stirred tanks. It could be the same here.

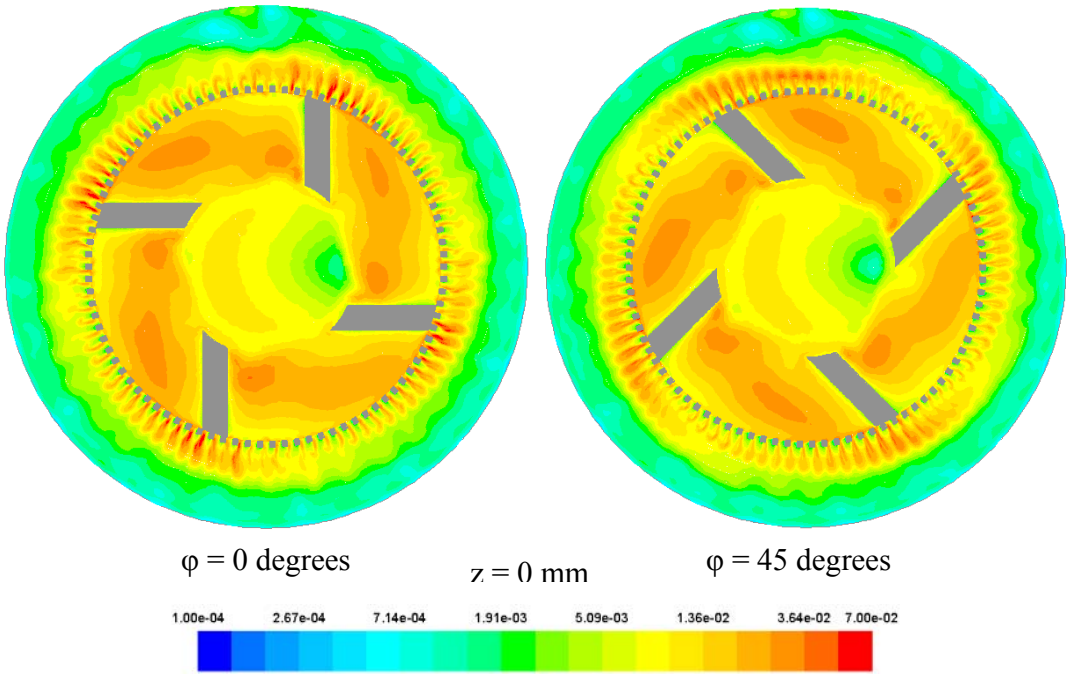

Figure 5-63: Normalized TKE contours at 2100 rpm on the mid-plane of the Silverson inline 450LS rotor-stator mixer.

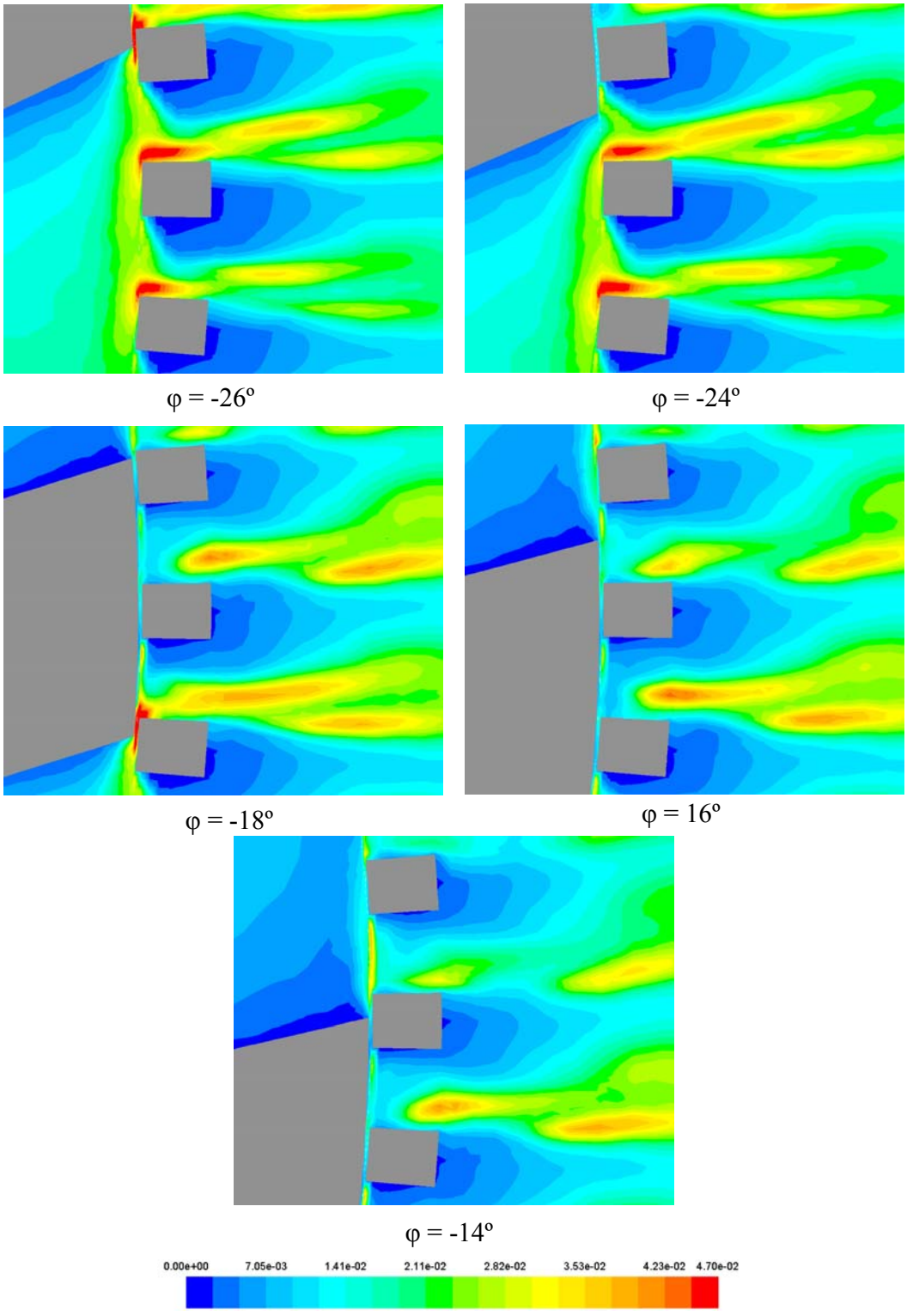

Figure 5-64: Normalized TKE around the stator slot at various blade positions at 2100 rpm in Silverson inline 450LS mixer.

of the Silverson inline L4R mixer, it exhibits higher TKE magnitude and the high TKE region is not limited to the volume close to the stator, but extends further into the bulk region.

Figure 5- 65 presents the normalized angularly averaged results for TKE along line 2, shown in Figure 5-42. The jet (z = 0 m) from stator slot 1 on the mid-plane is shown dramatically in the figure and it is much stronger than that of the Silverson inline L4R mixer (Figure 5-59).

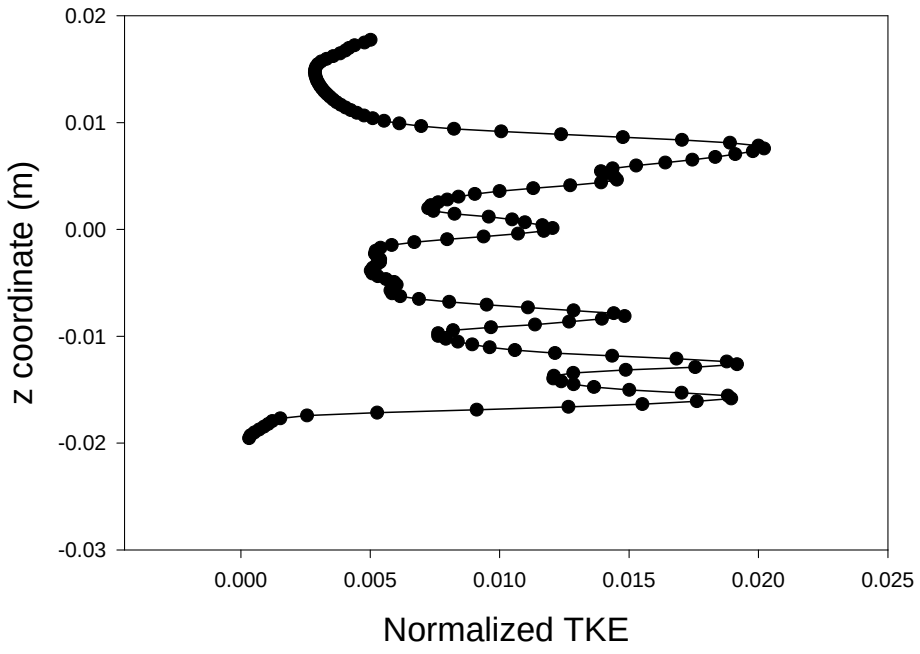

Figure 5-65: Axial profiles of the normalized angularly averaged TKE along line 2 (Figure 5-42) at 2100 rpm in the Silverson 450LS inline mixer.

The TDR fields on the mid-plane of the Silverson inline 450LS rotor-stator mixer at 2100 rpm are shown in Figure 5-66. The TDR fields are normalized by N^3D^2 (560

m^2/s^3). The high TDR regions exist in the rotor swept volume and in stator slots. Compared to Figure 5-60, it is found that the magnitude of the normalized TDR is higher than that of the Silverson inline L4R mixer and the extent of the high shear region is larger.

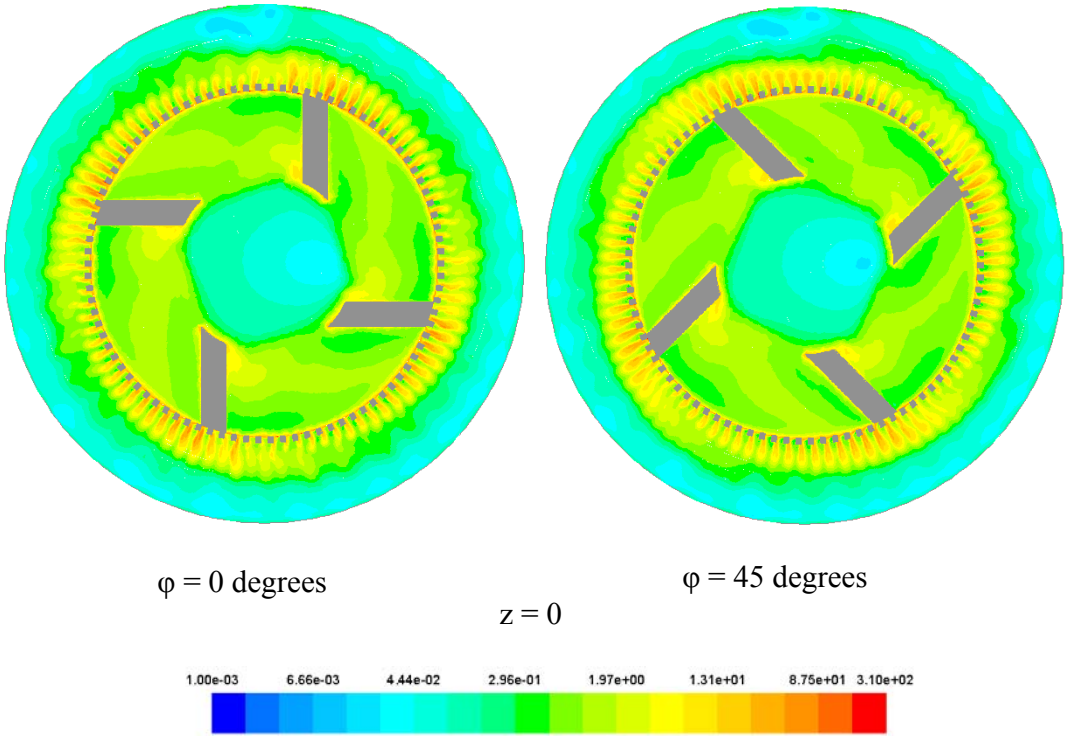

Figure 5-66: Normalized TDR contours at 2100 rpm on the mid-plane of the Silverson inline 450LS rotor-stator mixer.

The TDR field normalized by N^3D^2 close to stator slot 1 on the mid-plane (in Figure 5-16) at 2100 rpm is shown in Figure 5-67. From the figures, it can be seen that the TDR field is affected by the rotor blade position relative to the stator slot openings. The highest TDR occurs in the region close to the downstream edges of the stator slot when the rotor blade is approaching the stator slot. Compared with Figure 5-52, it

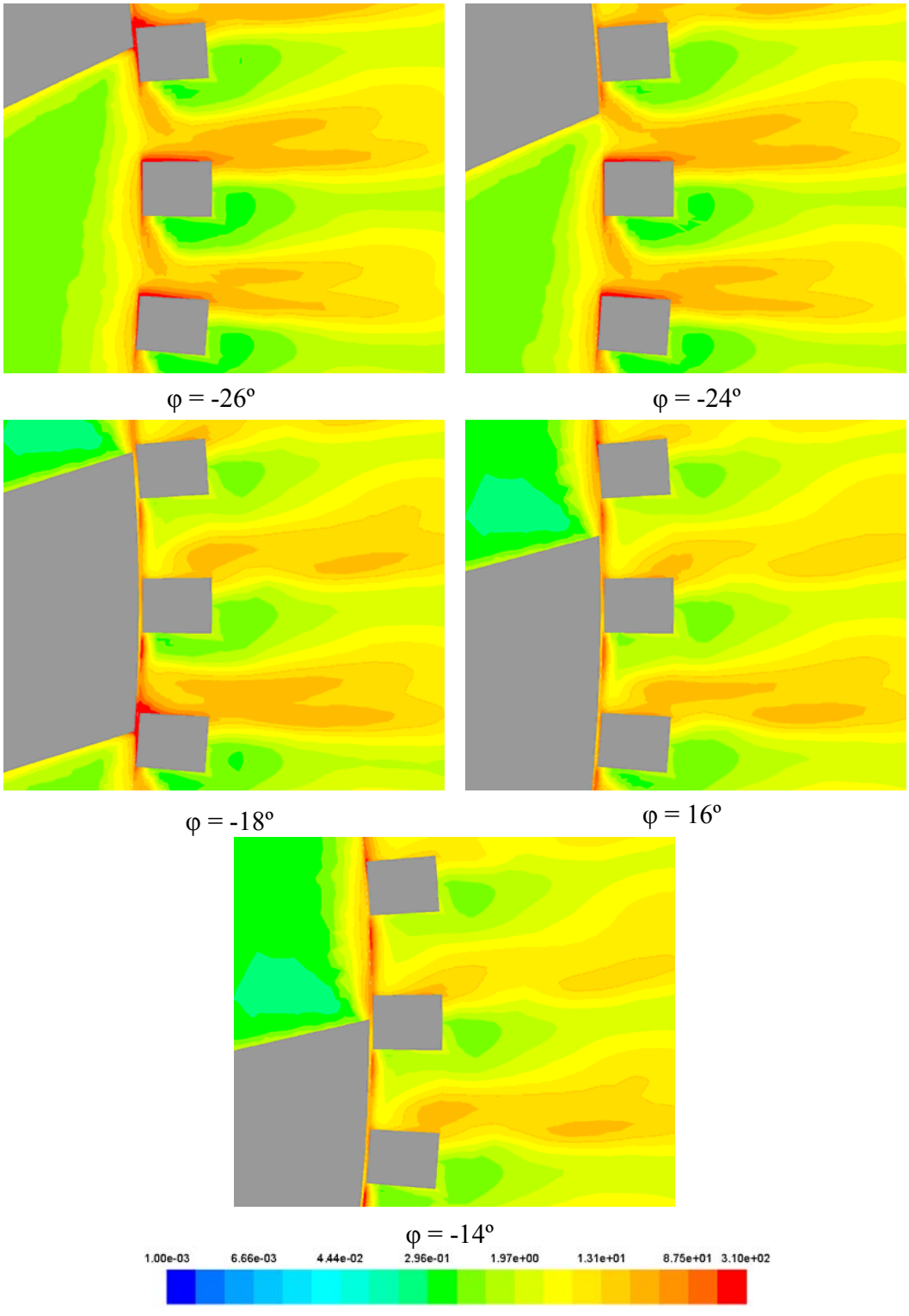

Figure 5-67: Normalized TDR around the stator slot at various blade positions at 2100 rpm in the Silverson inline 450LS mixer.

is evident that the normalized TDR of the Silverson inline 450LS mixer is much stronger than that of the Silverson inline L4R mixer. The high shear region not only exists close to the stator slot, but extends into the bulk of the mixer.

The TDR distributed in the rotor swept region, gap region, stator slot region and volute bulk region (which are similar to the regions in Figure 4-76) of the Silverson inline 450LS mixer are shown in Table 5-5. It is found that about 47% the turbulent energy is dissipated in the mixing head region (about 75% of the total energy). In the mixing head, the majority of turbulent energy is consumed in rotor swept region.

Table 5-5: Predictions of distributions of turbulent energy dissipation in the Silverson inline 450LS mixer at 2100rpm.

Region	2100 rpm
Rotor swept volume	212.4581 W (33.7%)
Gap region	29.0454 W (5.6%)
Stator slot region	52.2876 W (8.3%)
Mixer bulk region	335.9623 W (53.4%)
Total turbulent energy dissipated	582.2237 W (100%)

*It is known that prediction of magnitude and spatial variation of TDR is inaccurate in stirred tanks. It could be the same here.

Turbulent flow field of the Silverson inline 600LS mixer

The TKE fields on the mid-plane of the Silverson inline 600LS mixer at 1575 rpm are shown in Figure 5-68. The TKE fields are normalized by the rotor tip speed squared (158.76 m^2/s^2, the same as that of the Silverson inline 450LS and L4R at 8000 rpm). These contours indicate that the high TKE regions exist in the rotor swept volume and close to the stator slot openings. It is also seen that the magnitude of the TKE in Silverson inline 600LS mixer is much larger than that in Silverson inline L4R mixer.

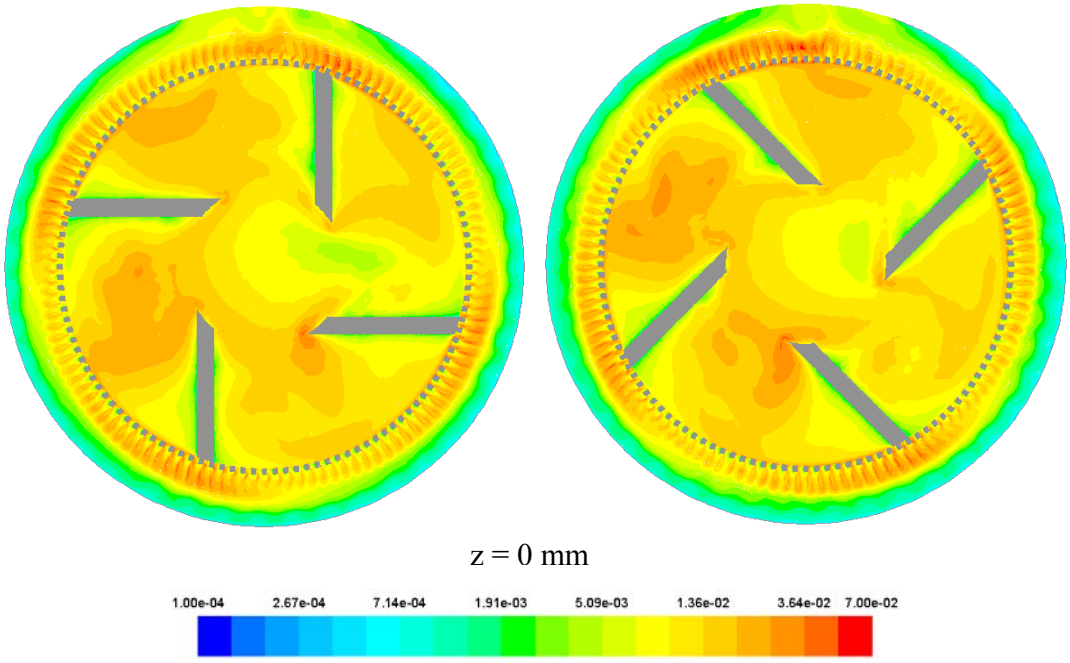

Figure 5-68: Normalized TKE contours at 1575 rpm on the mid-plane of the Silverson inline 600LS rotor-stator mixer.

The TKE fields normalized by the rotor tip speed squared close to the stator slot 1 on the mid-plane (in Figure 5-16) at 1575 rpm are shown in Figure 5-69. From these figures, it can be found that the TKE field is affected by the rotor blade position relative to the stator slot openings. The highest TKE occurs in the high shear gap

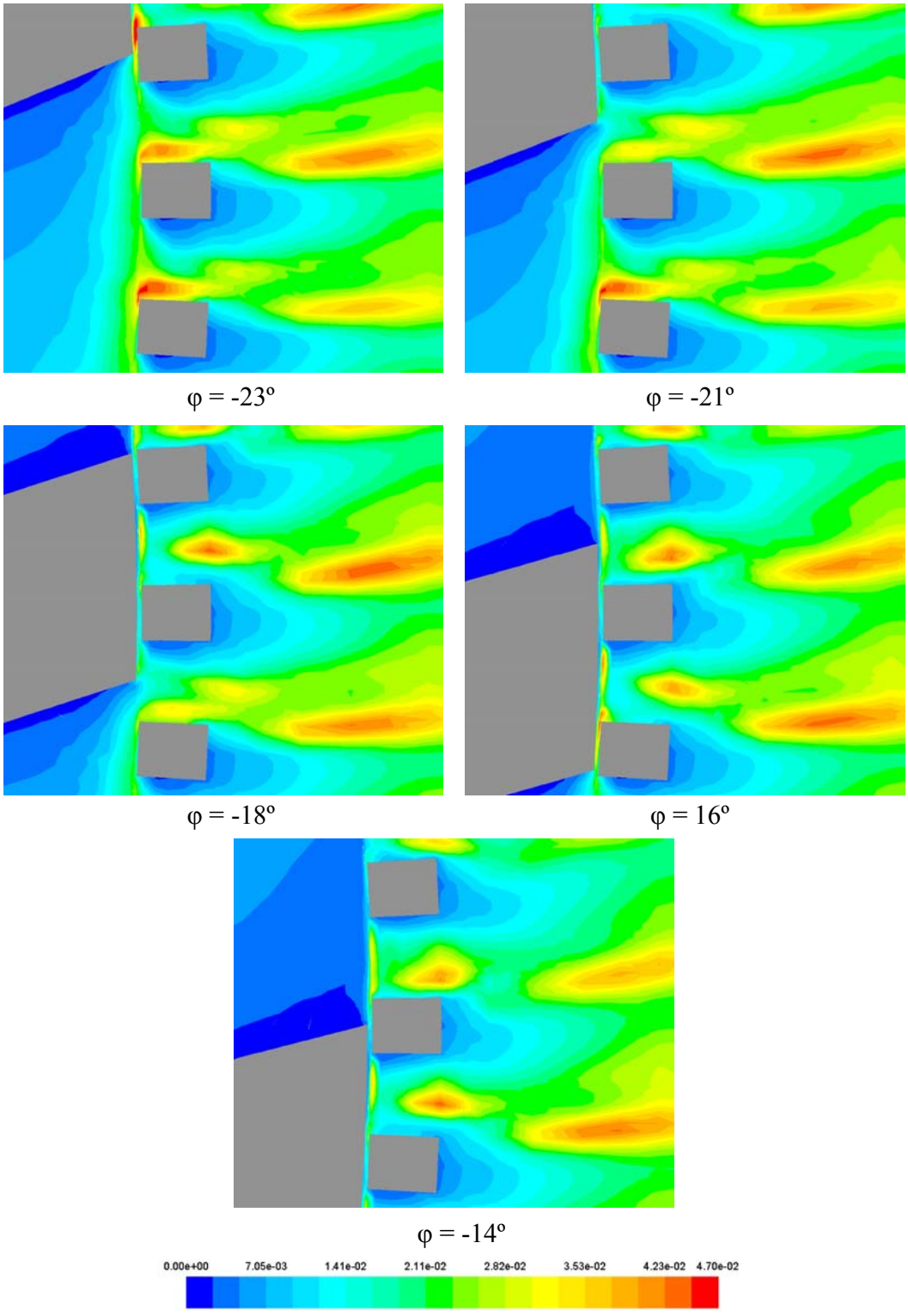

Figure 5-69: Normalized TKE around the stator slot at various blade positions at 1575 rpm in the Silverson inline 600LS mixer.

close to the rotor blade and in a relatively small region close to the downstream edges of the stator slot when the rotor blade is approaching the slot. Compared with the Silverson inline L4R (Figure 5-58) and 450LS mixers (Figure 5-64), the TKE field of the Silverson 600LS mixer is similar to 450LS, but significant differently from the L4R mixer.

Figure 5- 70 shows the normalized angularly averaged results for TKE along line 2, shown in Figure 5-54. The jet from stator slot 1 on the mid-plane can be clearly seen in this figure. This jet is much stronger than that of the Silverson inline L4R mixer (Figure 5-59).

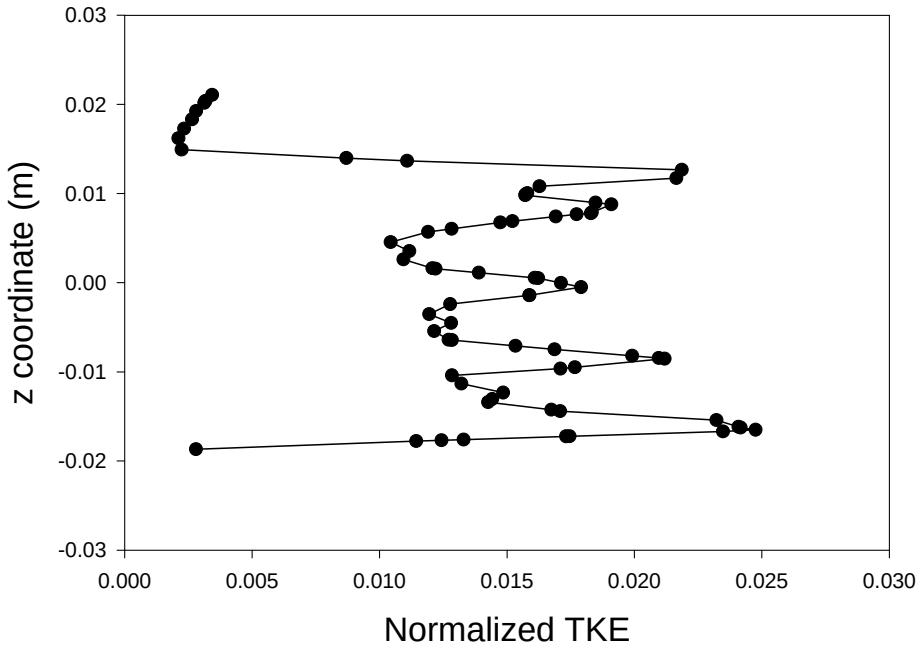

Figure 5-70: Axial profiles of the normalized angularly averaged TKE along line 2 (Figure 5-54) at 1575 rpm in the Silverson 600LS inline mixer.

The TDR fields on the mid-plane of the Silverson inline 600LS rotor-stator mixer at 1575 rpm are shown in Figure 5-71. The TDR fields are normalized by N^3D^2 (420 m^2/s^3). The high TDR regions are in the rotor swept volume and in stator slots. Compared with Figure 5-60, it is found that the magnitude of the TDR is higher than that of the Silverson inline L4R mixer and the extent of the high shear region is larger.

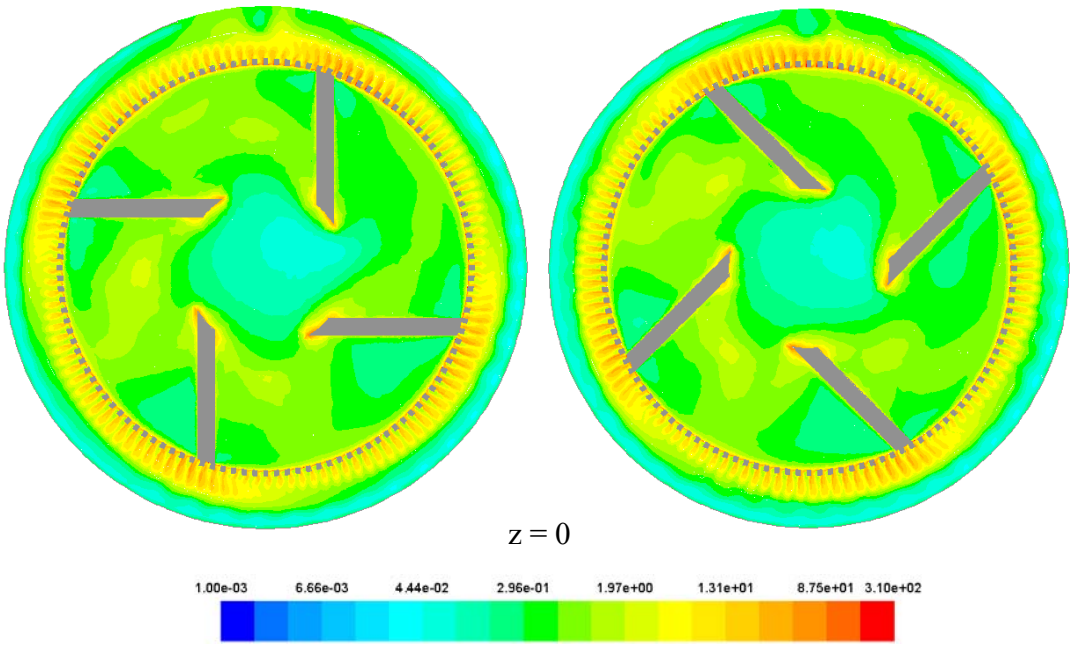

Figure 5-71: Normalized TDR contours at 1575 rpm on the mid-plane of the Silverson inline 600LS rotor-stator mixer.

The TDR field normalized by N^3D^2 close to stator slot 1 on the mid-plane (in Figure 5-16) at 1575 rpm is shown in Figure 5-72. From the figure, it can be seen that the TDR field is influenced by the rotor blade position relative to the stator slot openings. The highest TDR occurs in the region close to the downstream edges of the stator slot when the rotor blade is approaching the slot. It is also found that the magnitude of the

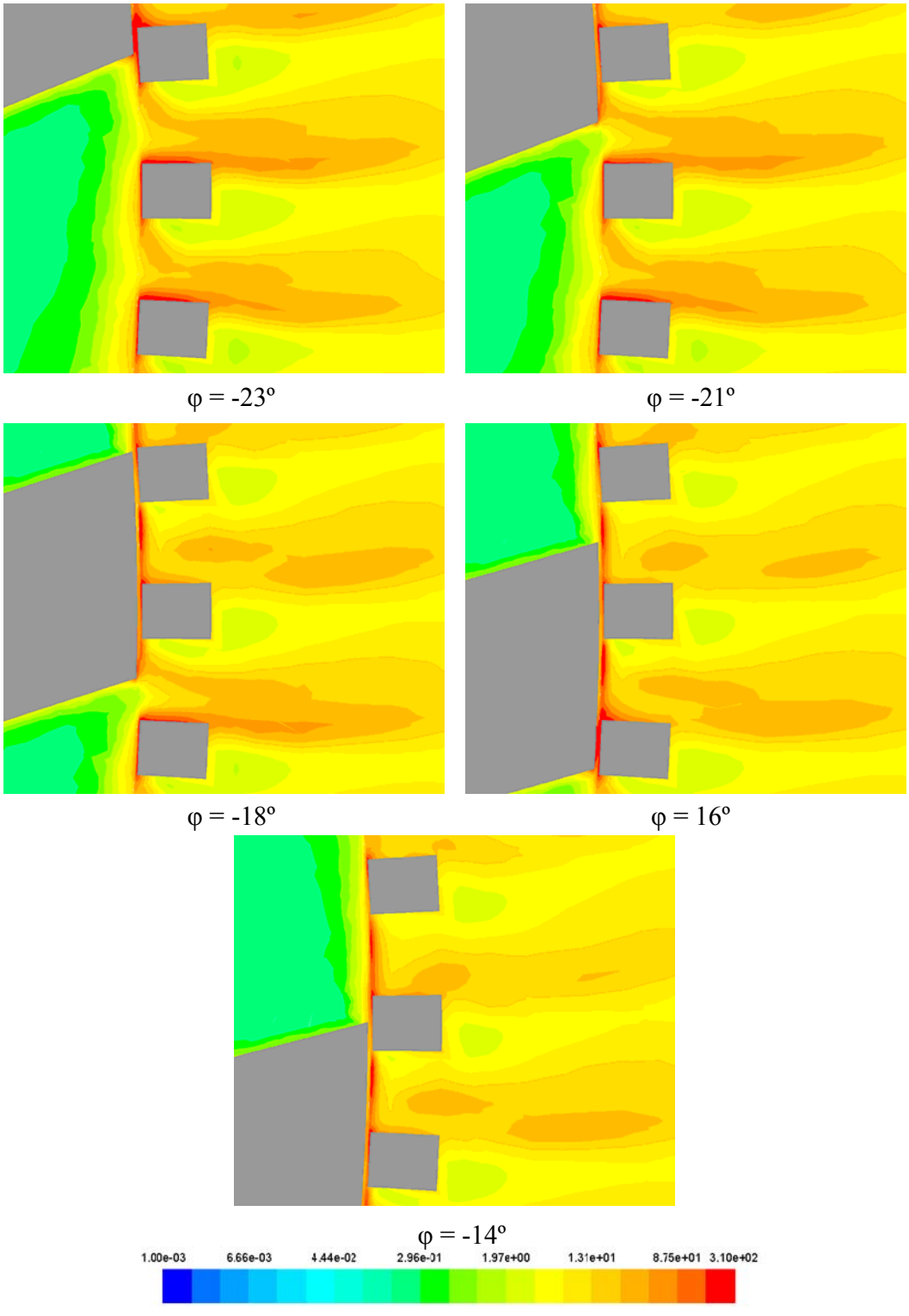

Figure 5-72: Normalized TDR around the stator slot at various blade positions at 1575 rpm in the Silverson inline 600LS mixer.

TDR in the Silverson inline 600LS mixer is much larger than that in the Silverson inline L4R mixer.

The TDR distributed in the rotor swept region, gap region, stator slot region and mixer bulk region (which are similar to the regions in Figure 4-76) of the Silverson inline 600LS mixer are shown in Table 5-6. It is found that about 42% of the turbulent energy is dissipated in the mixing head region. In the mixing head, the majority of turbulent energy is consumed in rotor swept region.

Table 5-6: Predictions of distributions of turbulent energy dissipation in the Silverson inline 600LS mixer at 1575 rpm.

Region	1575 rpm
Rotor swept volume	231.8558 W (26.3%)
Gap region	50.2264 W (5.7%)
Stator slot region	81.6931 W (9.3%)
Mixer bulk region	519.1291 W (58.8%)
Total turbulent energy dissipated	882.9044 W (100%)

*It is known that prediction of magnitude and spatial variation of TDR is inaccurate in stirred tanks. It could be the same here.

5.4.4 The mean deformation rate field of the Silverson inline L4R, 450LS and 600LS mixers

The mean deformation rate field of the Silverson inline L4R mixer

The deformation (shear) fields on the mid-plane of the Silverson inline L4R rotor-stator mixer at 4000 and 8000 rpm are shown in Figure 5-73. The deformation rate fields are normalized by nominal shear rate (32800 /s at 4000 rpm and 65600 /s at 8000 rpm), which is defined by Equation 4.6.3. These contours suggest that the shear rate fields at 4000 and 8000 rpm show quite similar patterns to each other. The high shear rate regions exist adjacent to the rotor blade and the stator slot openings.

The mean deformation rate fields normalized by nominal shear rate close to the stator slot 1 on the mid-plane (in Figure 5-22) at 4000 and 8000 rpm are shown in Figure 5-74 and 5-75. From these figures, it can be found that the shear rate magnitude is affected by the rotor blade position relative to the stator slot openings. The highest shear rate occurs in relatively small region close to the downstream edges of the stator slot when the rotor blade is approaching the slot.

The mean deformation rate field of the Silverson inline 450LS mixer

The mean deformation rate (shear) fields on the mid-plane of the Silverson inline 450LS rotor-stator mixer at 2100 rpm are shown in Figure 5-76. The shear rate fields are normalized by nominal shear rate (65600 /s same as that of Silverson inline L4R mixer at 8000 rpm), which is defined by Equation 4.6.3. These contours suggest that

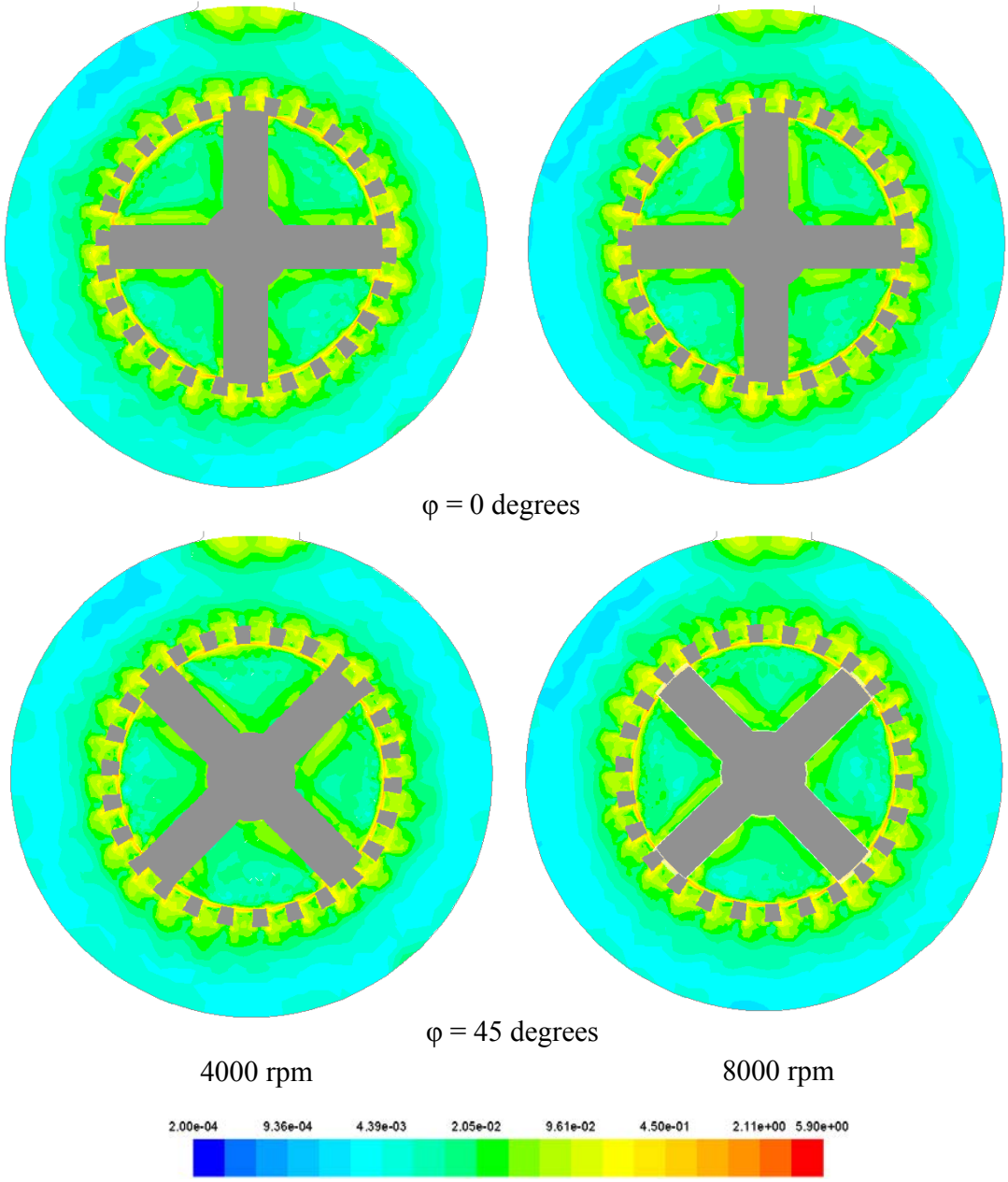

Figure 5-73: Normalized mean deformation rate contours at 4000 and 8000 rpm on the mid-plane of the Silverson inline L4R rotor-stator mixer.

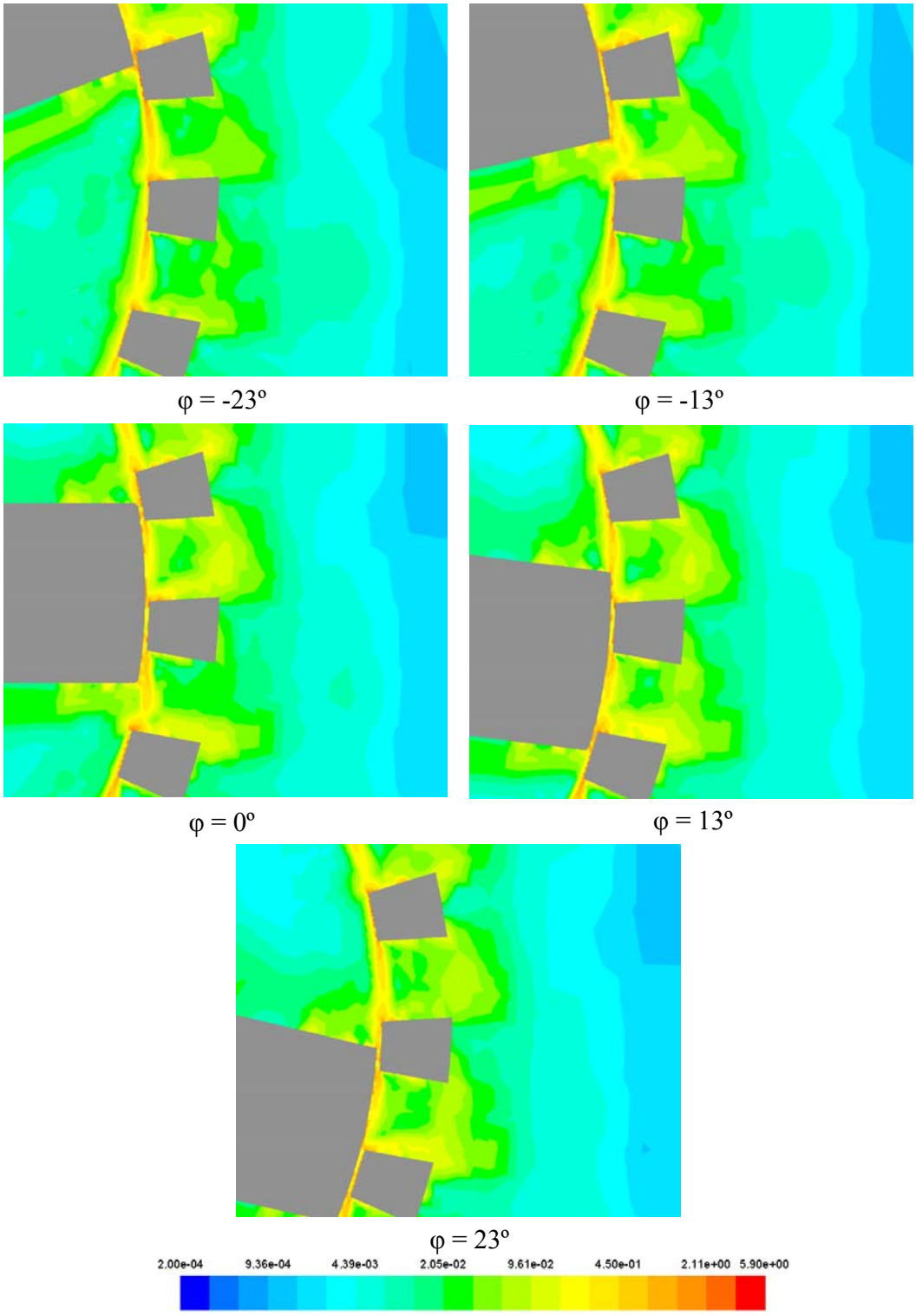

Figure 5-74: Normalized mean deformation rate around the stator slot at various blade positions at 4000 rpm in the Silverson inline L4R mixer.

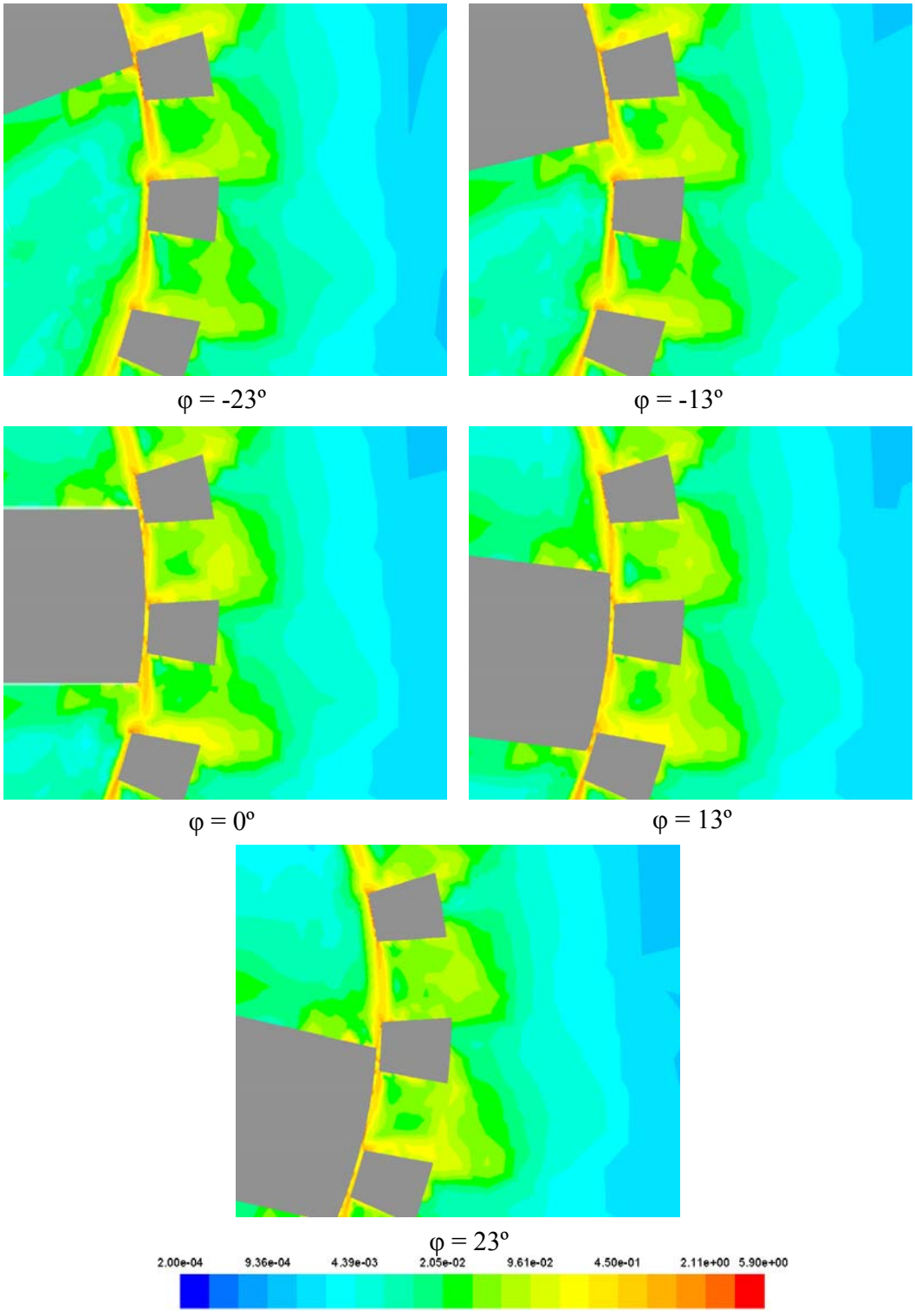

Figure 5-75: Normalized mean deformation rate around the stator slot at various blade positions at 8000 rpm in the Silverson inline L4R mixer.

high shear rate regions exist adjacent to the rotor blade and the stator slot openings.

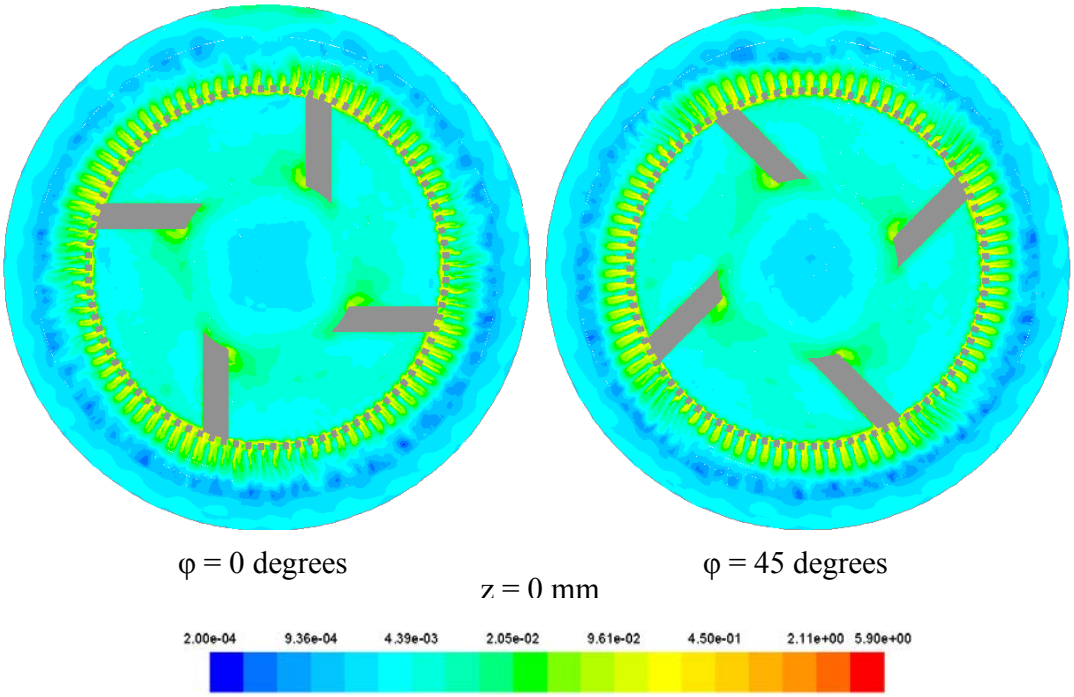

Figure 5-76: Normalized mean deformation rate contours at 2100 rpm on the mid-plane of the Silverson inline 450LS rotor-stator mixer.

The shear rate fields normalized by nominal shear rate close to stator slot 1 on the mid-plane (in Figure 5-22) at 2100 rpm are shown in Figure 5-77. From the figure, it can be seen that the shear rate magnitude is affected by the rotor blade position relative to the stator slot openings. The highest shear rate occurs in the high shear gap with the presence of the rotor blade and in the region close to the downstream edges of the stator slot when the rotor blade is approaching the slot. Compared with the

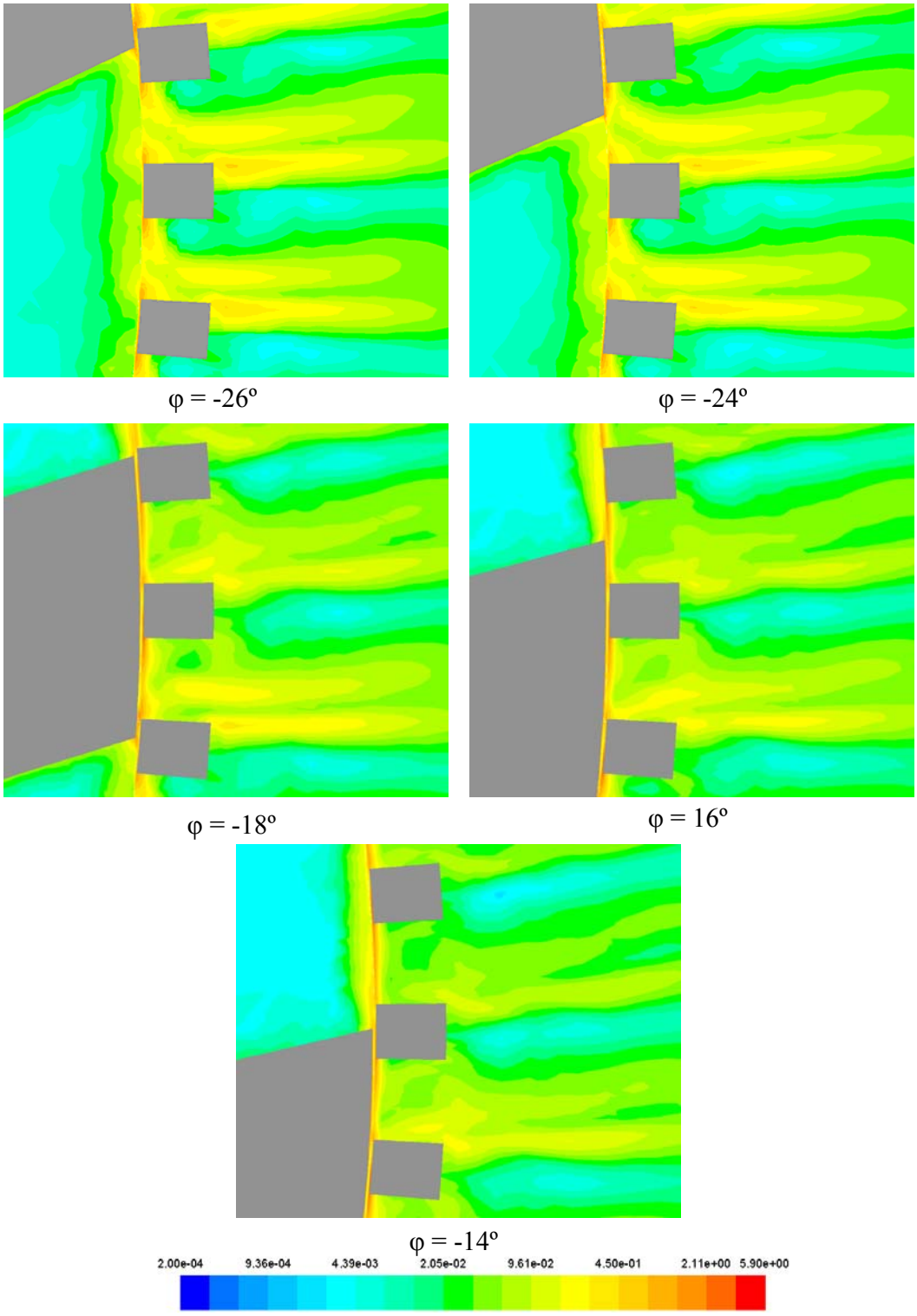

Figure 5-77: Normalized mean deformation rate around the stator slot at various blade positions at 2100 rpm in the Silverson inline 450LS mixer.

deformation rate field of the Silverson inline L4R mixer (Figure 5-75), the deformation rate field of the Silverson 450LS is much larger and extends further into the bulk of the volute.

The mean deformation rate field of the Silverson inline 600LS mixer

The mean deformation rate (shear) fields on the mid-plane of the Silverson inline 600LS rotor-stator mixer at 1575 rpm are shown in Figure 5-78. The shear rate fields are normalized by nominal shear rate (65600 /s the same as that of the Silverson inline L4R mixer at 8000 rpm and 450LS mixer), which is defined by Equation 4.6.3. These contours suggest that the high shear rate regions exist adjacent to the rotor blade and the stator slot openings.

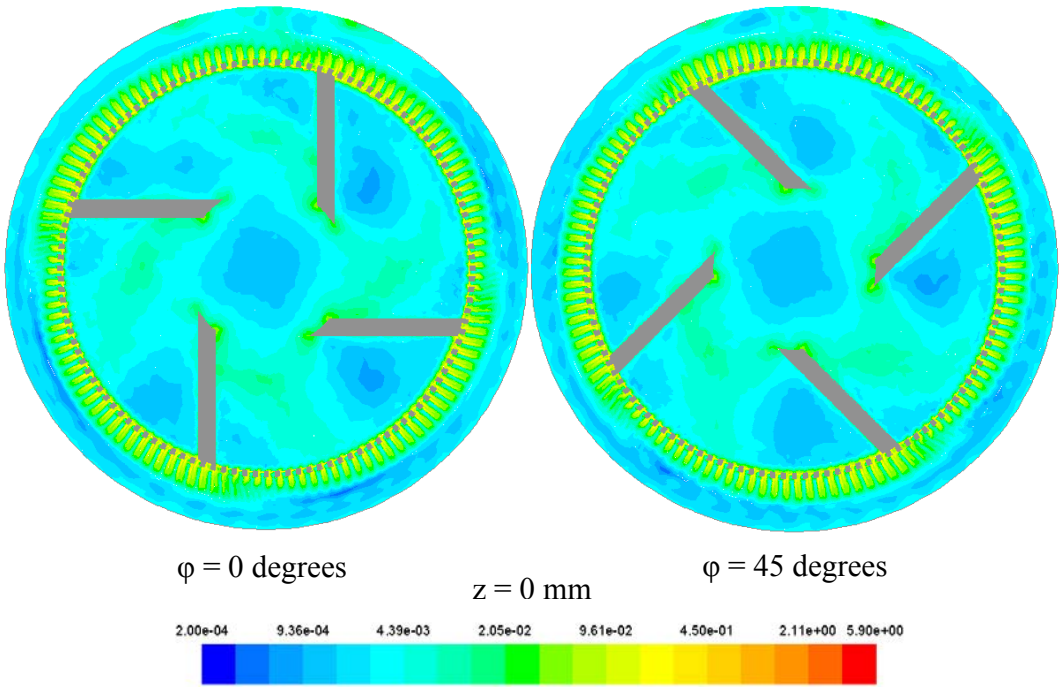

Figure 5-78: : Normalized mean deformation rate contours at 1575 rpm on the mid-plane of the Silverson inline 600LS rotor-stator mixer.

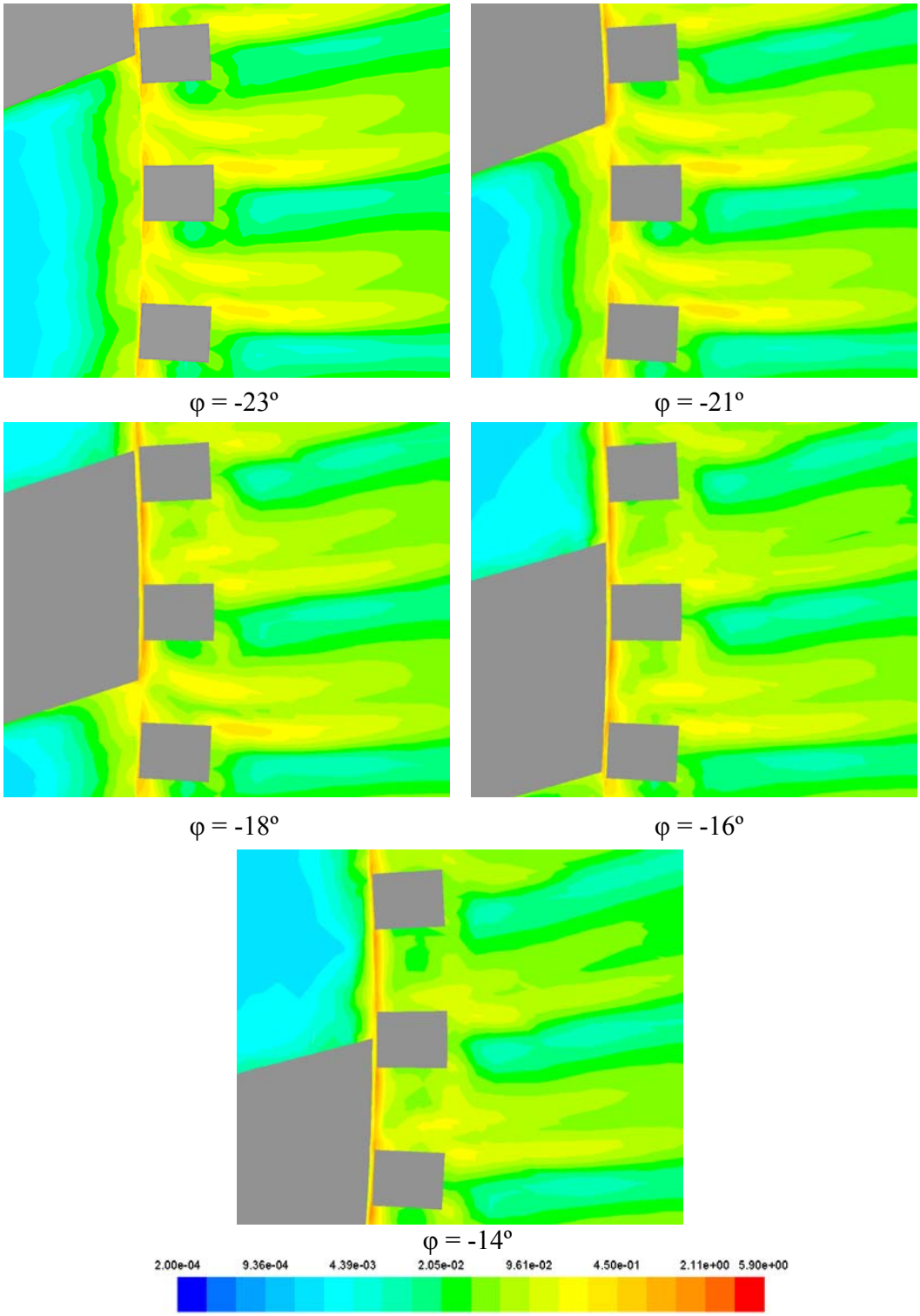

Figure 5-79: Normalized mean deformation rate around the stator slot at various blade positionsat 1575 rpm in the Silverson inline 600LS mixer.

The shear rate fields normalized by nominal shear rate close to the stator slot 1 on the mid-plane (in Figure 5-22) at 1575 rpm are shown in Figure 5-79. Compared with the deformation rate field of Silverson inline L4R (Figure 5-75) and 450LS (Figure 5-77) mixer, the deformation field of the Silverson 600LS mixer is very similar to that of Silverson 450LS mixer, but it is significantly different from that of the Silverson L4R mixer.

5.4.5 Effect of flow rate at constant tip speed

To investigate the effect of flow rate at constant tip speed, the flow field in Silverson inline 450LS mixer is simulated at 2100 rpm with a flow rate of 1.2 L/s. As a result the flow rate per slot is 0.0021 L/s, which is same as the flow rate of Silverson inline L4R mixer at 8000 rpm. In the simulation, velocity inlet boundary condition is used instead of pressure inlet condition. In addition, another simulation for the Silverson L4R mixer at the same flow rate as the 450LS mixer at the free pumping condition was also performed. But the pressure drop was out of bounds, which is not realistic.

The flow fields on mid-plane and y = 0 plane are shown as Figure 5-80 and 5-81. Compared with Figure 5-17, 5-18, 5-32 and 5-33, it is found that the jets in Figure 5-75 are much weaker than those in Figure 5-32 and they are more similar to Figure 5-17 for the L4R mixer. The jets are limited to the regions close to stator slots. Also, the magnitude of the velocity is closer to that in the lab scale mixer.

The velocity filed normalized by the rotor tip speed (12.6 m/s) close stator slot 1 on the mid-plane (the position of slot 1 is same as that in Figure 5-37) at 2100 rpm are shown in Figure 5-82. Compared with Figure 5-38, the jet is much weaker than

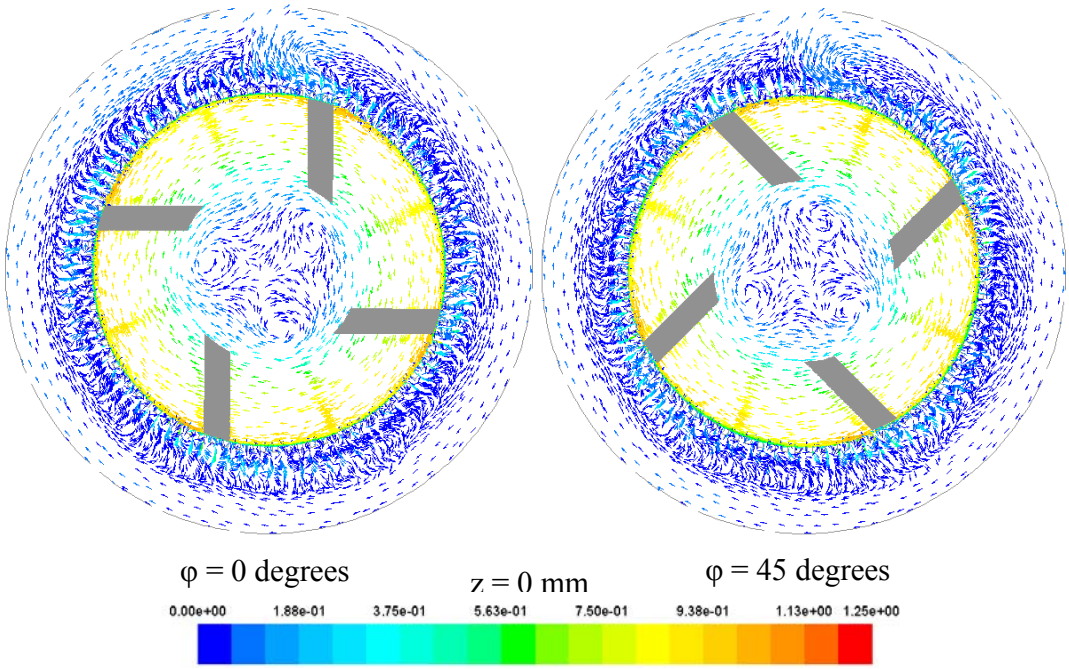

Figure 5-80: Normalized mean velocity magnitude snapshots on the mid-plane of the Silverson inline 450LS mixer at 2100 rpm with a flow rate of 1.2 L/s.

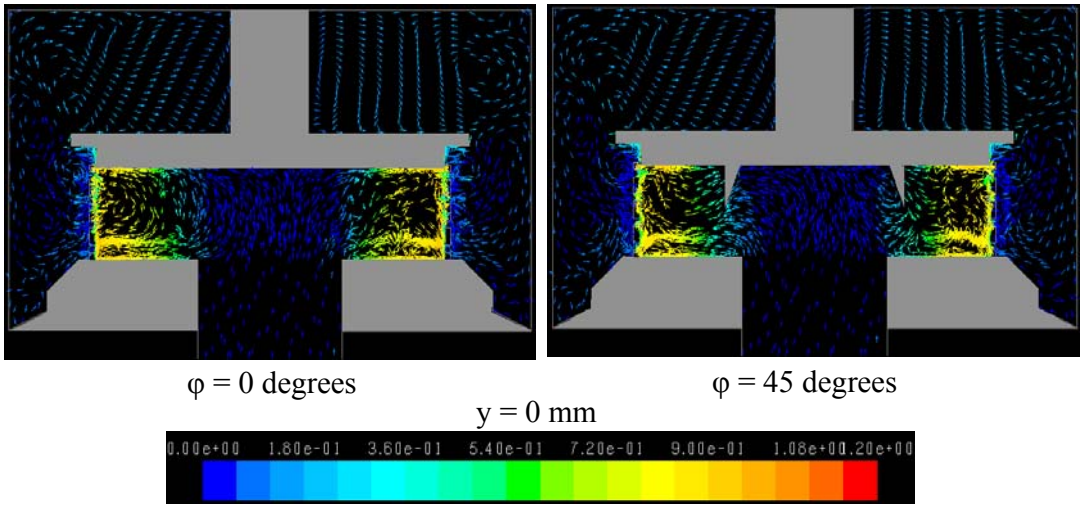

Figure 5-81: Normalized mean velocity magnitude snapshots at plane y = 0 in the Silverson inline 450LS rotor-stator mixer with a flow rate of 1.2 L/s.

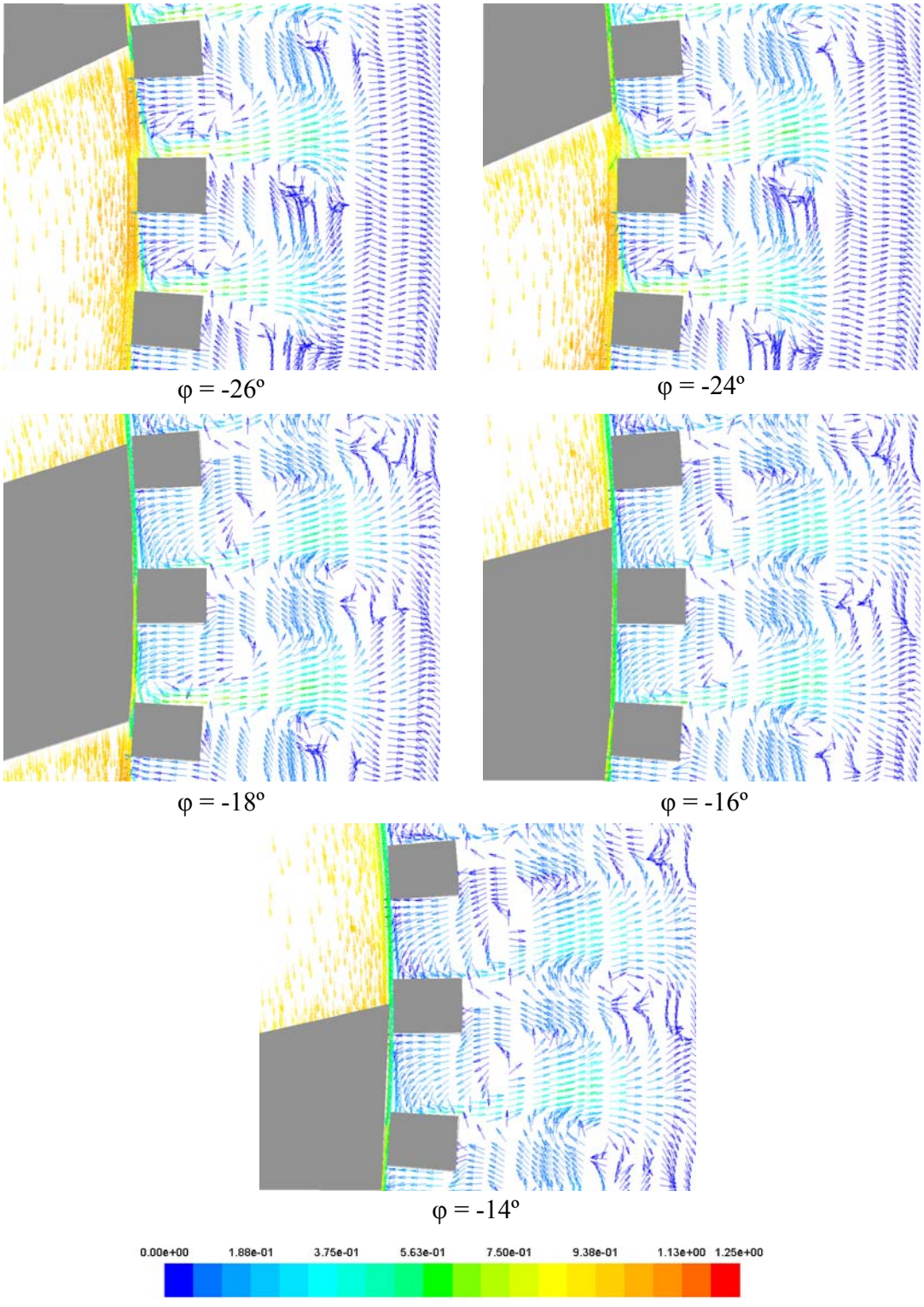

Figure 5-82: Normalized mean velocity vectors near the stator slot at various blade positions (2100 rpm) with a flow rate of 1.2 L/s.

that at the free pumping condition, and it exists in the region closer to the stator slot, which is more similar to Figure 5-24. The difference between this simulation and the bench scale mixer simulation may result from the different geometry of mixing head, such as the shape of the rotor, the width of the rotor blade and aspect ratio.

The TKE fields on the mid-plane of the Silverson inline 450LS mixer at 2100 rpm are shown in Figure 5-83. The TKE fields are normalized by the rotor tip speed squared. Compared with the TKE contour of lab scale mixer at 8000 rpm (Figure 5-56) and 450LS at free pumping condition (Figure 5-63), it is found that the magnitude of these contours are more similar to the TKE fields in the L4R mixer.

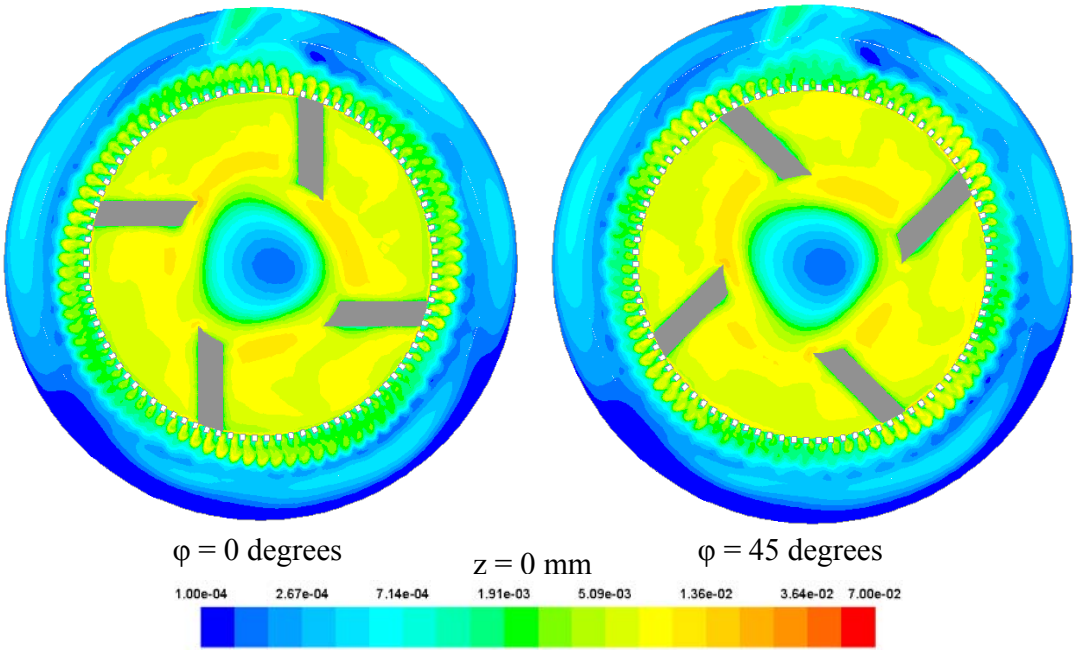

Figure 5-83: Normalized TKE contours at 2100 rpm with a flow rate of 1.2 L/s on the mid-plane of Silverson inline 450LS rotor-stator mixer.

The TKE fields normalized by the rotor tip speed squared close to stator slot 1 (see Figure 5-37) on the mid-plane at 2100 rpm with a flow rate of 1.2 L/s are shown in Figure 5-84. Compared with Figure 5-58 and 5-64, the area of high TKE regions is smaller than that of Figure 5-64 and is more similar to Figure 5-58. In addition, the magnitude of the TKE is almost the same as that in Figure 5-58.

The TDR fields on the mid-plane of the Silverson inline 450LS mixer at 2100 rpm with a flow rate of 1.2 L/s are shown in Figure 5-85. The TDR fields are normalized by N^3D^2. Compared with the TDR contours of the lab scale mixer at 8000 rpm (Figure 5-60) and 450LS at free pumping condition (Figure 5-66), it is found that the magnitude of these contours are more similar to the TDR field in L4R mixer.

The TDR distributed in the rotor swept region, gap region, stator slot region and volute bulk region (which are similar to the regions in Figure 4-76) of the Silverson inline 450LS mixer with a flow rate of 1.2 L/s are shown in Table 5-7. It is found that compared with Table 5-5, the fraction of the energy dissipated in the mill head increases about 20%, which is more similar to that in the L4R mixer at 8000 rpm (see Table 5-4. The majority of the turbulent energy is dissipated in the mixing head region (about 68% of the total energy). In the mixing head, the majority of turbulent energy is consumed in rotor swept region.

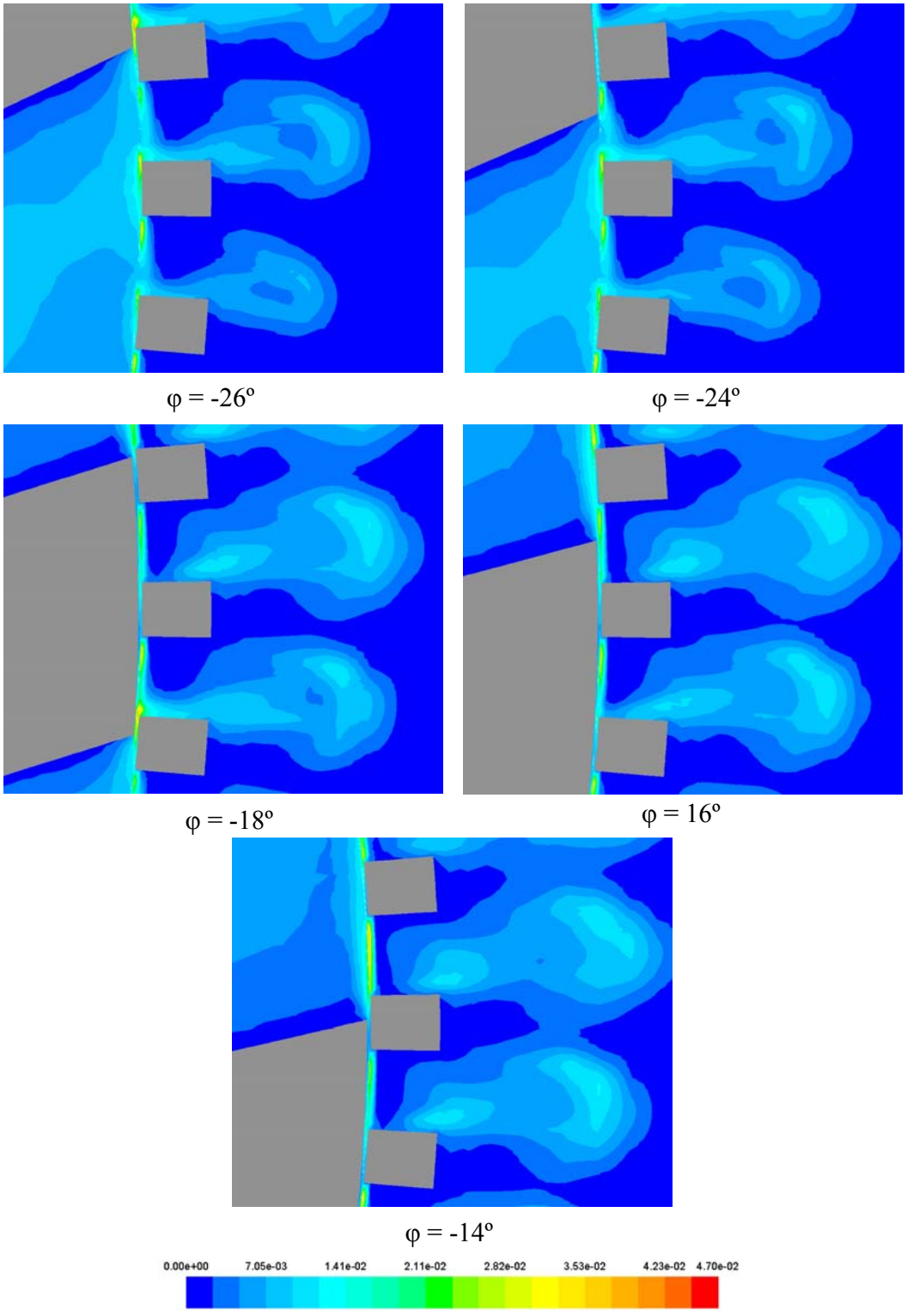

Figure 5-84: Normalized TKE around the stator slot at various blade positions at 2100 rpm with a flow rate of 1.2 L/s in the Silverson inline 450LS mixer.

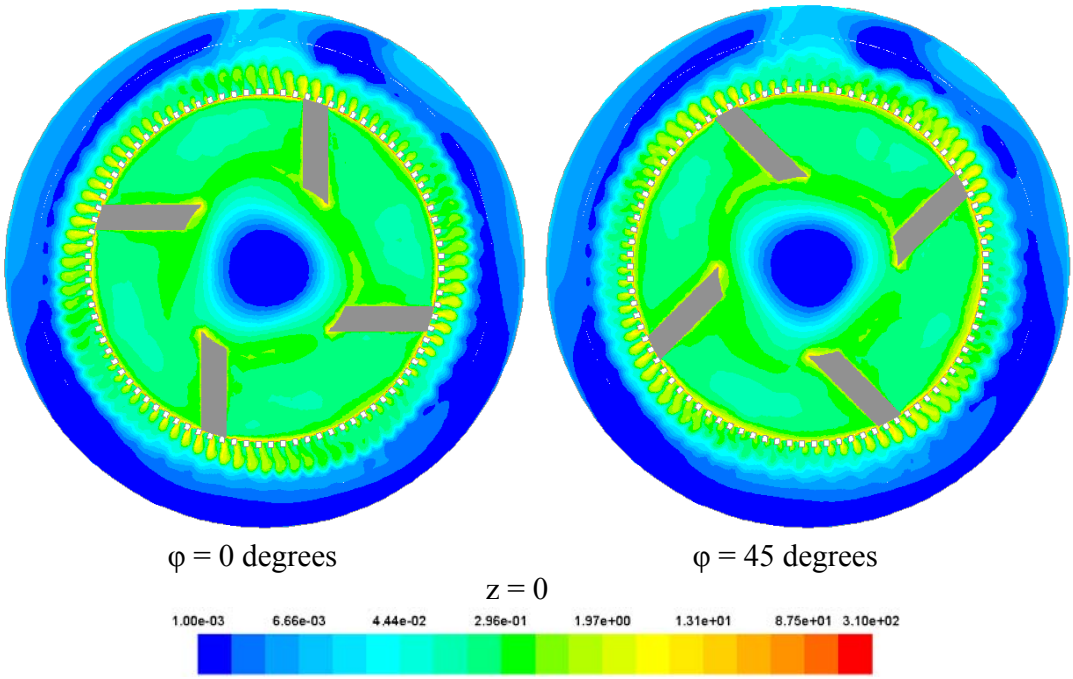

Figure 5-85: Normalized TDR contours at 2100 rpm with a flow rate of 1.2 L/s on the mid-plane of the Silverson inline 450LS rotor-stator mixer.

Table 5-7 Predictions of distributions of turbulent energy dissipation in the Silverson inline 450LS mixer with a flow rate of 1.2 L/s at 2100rpm.

Region	2100 rpm
Rotor swept volume	51.5 W (41.4%)
Gap region	21.2 W (17.1%)
Stator slot region	11.1 W (8.9%)
Mixer bulk region	40.5 W (32.6%)
Total turbulent energy dissipated	124.3 W (100%)

*It is known that prediction of magnitude and spatial variation of TDR is inaccurate in stirred tanks. It could be the same here.

The normalized TDR fields close to the stator slot 1 on the mid-plane (in Figure 5-37) at 2100 rpm with a flow rate of 1.2 L/s are shown in Figure 5-86. Compared with Figures 5-62 and 5-67, the area of the high TDR regions is smaller than that of Figure 5-67 and is more similar to that of Figure 5-62. In addition, the magnitude of TKE is almost same as that in Figure 5-62.

The mean deformation rate (shear) fields on the mid-plane of the Silverson inline 450LS rotor-stator mixer at 2100 rpm with a flow rate of 1.2 L/s are shown in Figure 5-87. Compared with the deformation rate contours of the lab scale mixer at 8000 rpm (Figure 5-73) and the 450LS at free pumping condition (Figure 5-76), it is found that the magnitude of these contours close to the mixing head are more similar to the shear rate field in the L4R mixer.

The shear rate fields normalized by nominal shear rate close to stator slot 1 on the mid-plane (in Figure 5-37) at 2100 rpm with a flow rate of 1.2 L/s are shown in Figure 5-88. Compared with Figure 5-75 and 5-77, the area of the high shear rate regions is smaller than that of Figure 5-77 and is more similar to Figure 5-75. In addition, the magnitude of shear rate is almost the same as that in Figure 5-75.

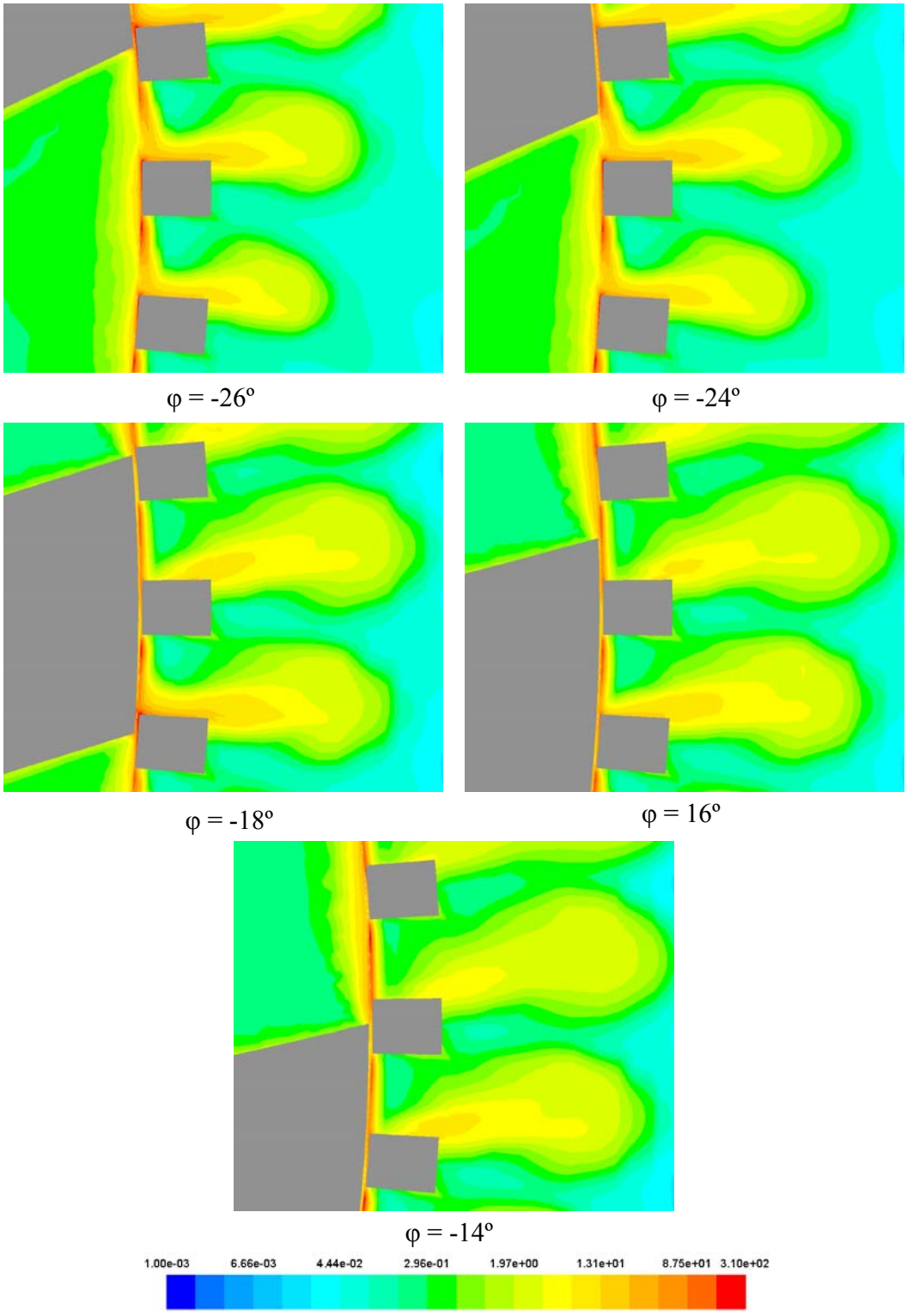

Figure 5-86: Normalized TDR near the stator slot at various blade positions at 2100 rpm with a flow rate of 1.2 L/s in the Silverson inline 450LS mixer.

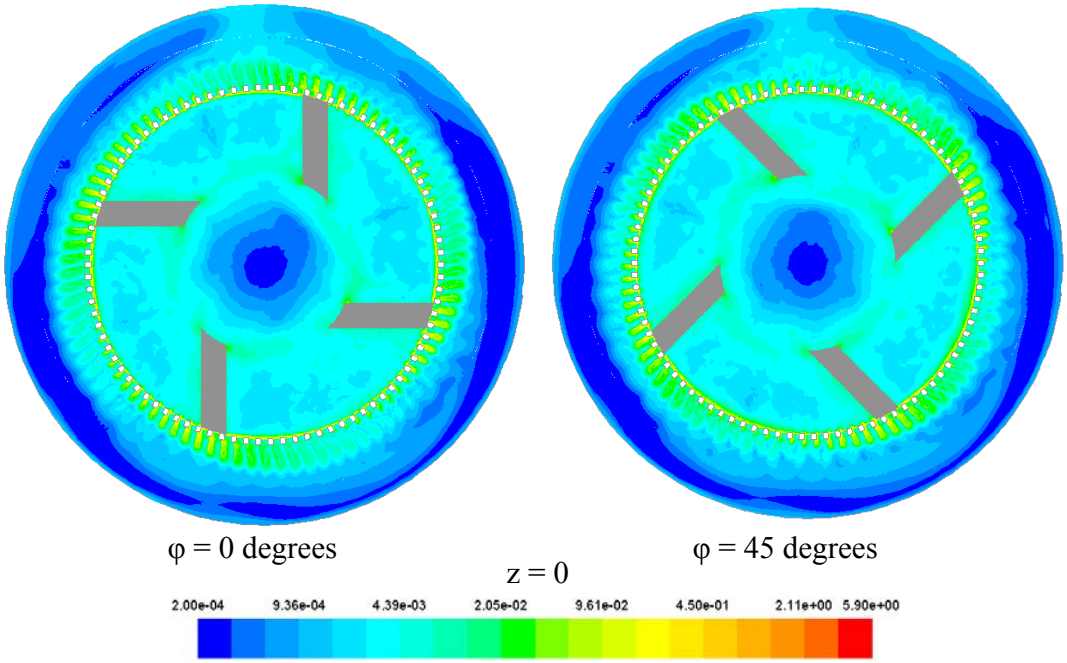

Figure 5-87: Normalized mean deformation rate field around the stator slot at various blade positions at 2100 rpm with a flow rate of 1.2 L/s in the Silverson inline 450LS mixer.

5.5 Summary

The CFD simulation study for the scale up of the Silverson inline rotor-stator mixers was covered in this chapter. Hex dominated 3D volume meshes are prepared by use of Harpoon, an automatic mesh generator. RANS simulations are performed for the Silverson inline L4R (lab scale), 450LS (pilot scale) and 600LS (plant scale) mixers. The simulation of the Silverson L4R mixer are carried out at 4000 and 8000 rpm and the simulation of the Silverson 450LS and 600LS are performed at 2100 and 1575 rpm, respectively, so that the tip speed is 12.6 m/s same as L4R at 8000 rpm. Macroscopic properties, including flow rate, power and shear frequency were calculated based on the simulation. The flow rate and power number of the Silverson

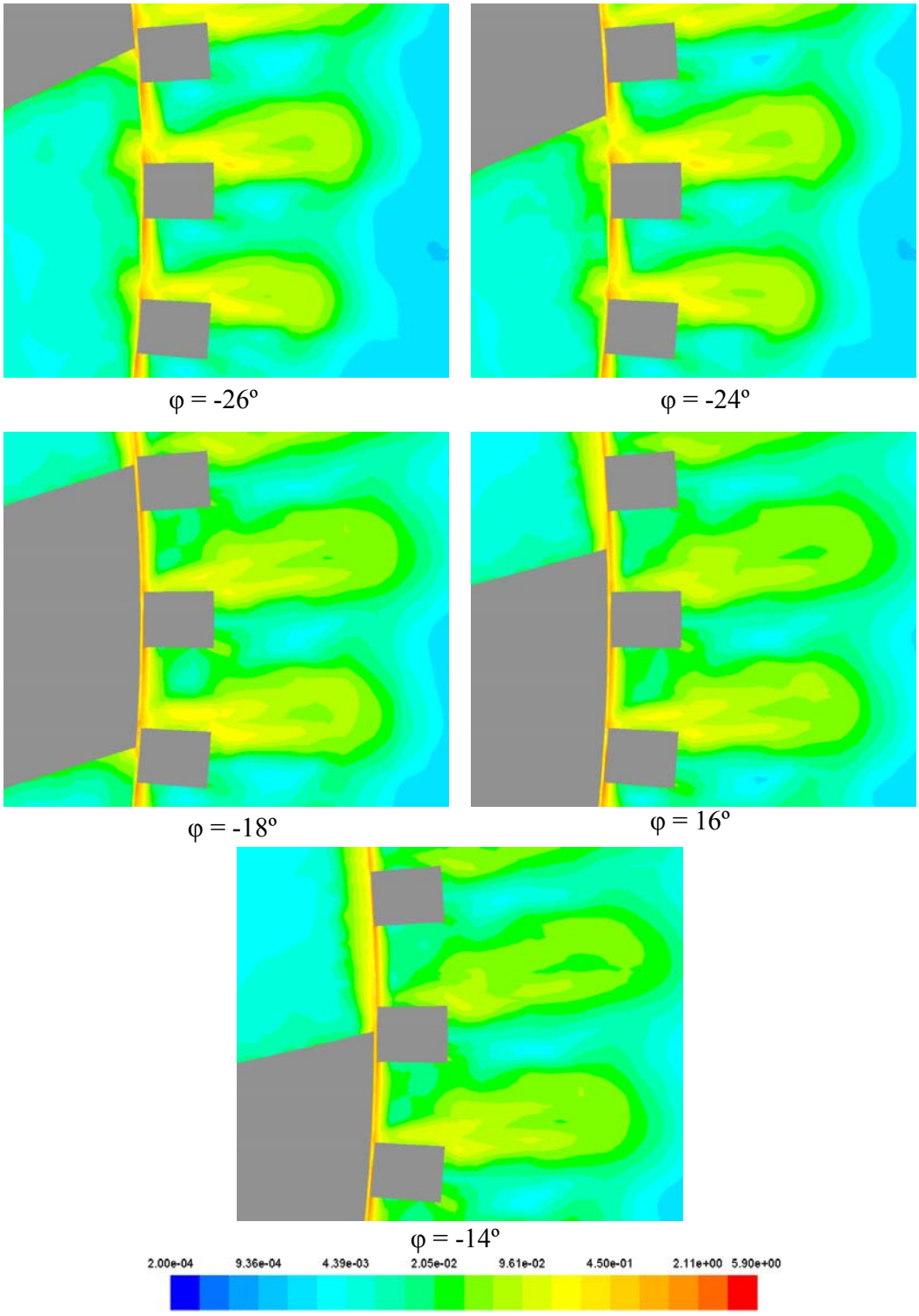

Figure 5-88: Normalized mean deformation rate near the stator slot at various blade positions at 2100 rpm with a flow rate of 1.2 L/s in the Silverson inline 450LS mixer.

L4R mixer compared favorably with the experimental data. It was found that shear frequency increases with the size of mixer. Flow rate, flow number and flow rate per slot increases with the size of mixer; power increases with the size of mixer; power per slot and power numbers of 450LS and 600LS are almost same but larger than that of L4R; specific energy and specific energy per slot decreases with the size of mixer.

The velocity, turbulence and mean deformation rate fields are were investigated and compared. The results indicate that the velocity, turbulence and deformation rate field of 450LS and 600LS are quite similar but they are significant different from the L4R. To investigate the effect of inlet flow rate, a simulation of the Silverson inline 450LS mixer was performed at 2100 rpm with a decreased inlet flow rate of 1.2 L/s from the flow rate of 6.9 L/s at free pumping condition. As a result the flow rate per slot is the same as that of the Silverson inline L4R mixer free pumping at 8000 rpm. Compared with the L4R mixer at 8000 rpm and 450LS at free pumping condition, it is found that with the decrease of flow rate, the difference between the flow field of L4R and 450LS is diminished significantly. The velocity, turbulence and mean deformation rate fields are also investigated.

Above all, the macroscopic properties, velocity, turbulence and mean deformation rate fields at the free pumping condition, when the tip speed is constant, all indicate that it may reasonable to scale up from the pilot scale to plant scale based on the constant tip speed scale up criterion. However, considering the tip speed alone may lead to a significant discrepancy between the bench scale and the larger scales. To

scale up high shear mixers, the flow rate per stator slot is also required to be kept constant beside the constant tip speed.

Chapter 6: Wet Milling of Crystals in the Silverson L4R Inline Rotor-Stator Mixer

To provide experimental data for a wet milling process in the bench scale rotor stator mixer, wet milling experiments were performed in the Silverson inline L4R mixer at 4000, 6000 and 8000 rpm. Two crystal-antisolvent systems were investigated: sucrose in isopropyl alcohol; and mannitol in ethyl alcohol. Images of crystal samples removed at different times during the milling process, were taken by video microscopy and analyzed by an automatic program developed in ImageJ. In the experiments, the effects of rotation rate and flow rate on the wet milling process were investigated. To this end, the flow rate at different rotation rates was measured. These were also compared with the simulation results.

6.1 Equipment

The complete wet milling process experimental set up is shown in Figure 6-1. The Silverson L4R inline rotor-stator mixer with a square hole stator head used in the wet milling process is shown in Figure 5-1. A 2 liter glass reactor tank with a cooling jacket is used as the holding vessel. A four pitched blade impeller was in the center of the holding vessel to insure good mixing and suspension of the crystal slurry. Four baffles were attached to the wall of the holding vessel to promote better mixing. There are 3 openings on the top of the holding vessel. Two of them were used to hold the baffles and another one was the sample removal port. The inlet of the holding vessel, which is connected to the return line of the high shear mixer is on the baffle.

There is a valve and opening at the bottom of the holding vessel. The valve was used to control the flow rate and the opening was connected to the inlet of the high shear mixer.

Video microscopy is used to capture the crystal images for size analysis. This video technique combines the traditional optical microscope with a digital camera, which is linked to a computer so that the images taken are digitalized and transferred to the computer for later analysis. Generally, one of the most significant limitations of the video technique is that to determine particle size distribution, a large amount of particles need to be analyzed, which is quite time consuming and labor intensive.

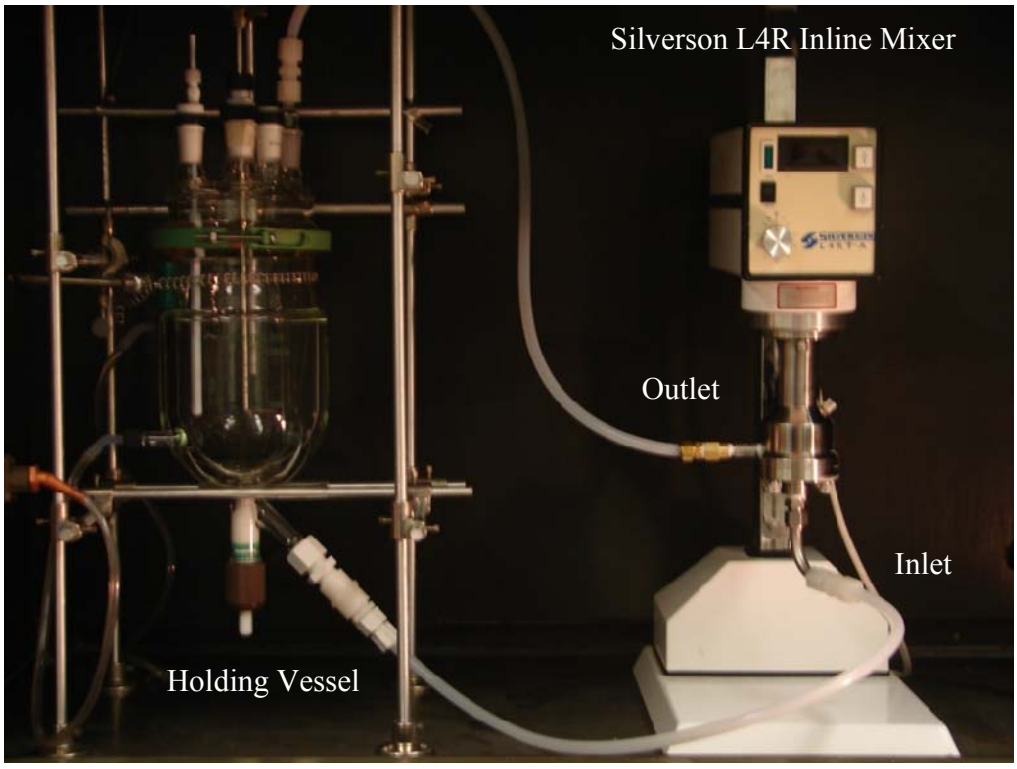

Figure 6-1: The wet milling process experiment set up.

However, in conjunction with a digital image processing, this method becomes more powerful in particle characterization.

6.2 Material

Two crystal-antisolvent systems are investigated: sucrose in isopropyl alcohol; and mannitol in ethyl alcohol. Antisolvents were used to insure that crystal size reduction was solely due to mechanical milling. Therefore, there is no dissolution or crystallization happening in the experiments. Sucrose and mannitol are selected as the crystals because they have well known crystal habits, easily accessible solubility data and they are non-toxic, readily available and relatively inexpensive. The criterion for antisolvent selection is that the solubility of the investigated crystal in the corresponding solvent is so small that dissolution is not significant in our wet milling process. Moreover, the antisolvent is non-toxic. As a result, isopropyl alcohol and ethyl alcohol are selected for sucrose and mannitol crystals, respectively[32,33].

The density of sucrose[34] is 1.587 g/cm^3 and the solubility of sucrose in isopropyl alcohol is 0.0036 (mole fraction) at 283 K[32]. The viscosity of isopropyl alcohol is 2.86 cP at 288 K[35]. The density of mannitol[35] is 1.52 g/cm^3 and the solubility of mannitol in ethyl alcohol is 0.0018 (grams per gram of solution)[33]. The viscosity of ethyl alcohol is 0.0012 Pa s at 293 K[35].

Figure 6-2: Microscope camera arrangement[9].

6.3 Image analysis

ImageJ Software is used for the image analysis process. This software is a public Java image processing program inspired by NIH Image. There is a built-in function for particle analysis in ImageJ. However, to use this function, the images have be to adequately prepared and ImageJ can only analyze one image at a time. To resolve this limitation, an automated macro was developed. The image preparation consists of two steps: background subtraction and thresholding.

The background subtraction step is to remove from the sample image any spots resulting from dirt attached to the optical system, which may be confused with particles by the image analysis algorithm. Before any sample images are analyzed, a picture of what is seen through the microscope without the sample is taken. Then, this image is subtracted from all the sample images by the macro.

After the background is removed from the sample images, the edges of new images are re-constructed by ImageJ and the contrast is enhanced in order to make it easier to distinguish between particles and the background of the images. Then the Threshold function in ImageJ is used to separate particles from the background. Finally, the built-in Particle Analysis function is called to calculate particle properties, such as area, perimeter, etc.

This method is used to obtain two dimensional information about the particles. In this work, the third dimension is selected to be the smaller scale between the width and length. As a result, when the third dimension scale is significantly different from the second dimension scale, this method can be inaccurate. In addition, the smallest scale that can be measured is 1.5 micron.

6.4 Wet milling experimental procedure

The procedure for the wet milling experiments is:

- Fill the holding vessel with 2 liters of antisolvent.
- Open the feed tank valve and begin stirring in the holding vessel.

- Turn on the Silverson inline L4R rotor-stator mixer and initiate flow through the mixer from the holding tank.
- Turn off the rotor-stator mixer and close the feed valve.
- Charge 200 g of crystals into the holding vessel.
- Turn on the Silverson inline L4R rotor-stator mixer again and open the feed valve.
- Remove samples from the feed tank at given times and use the video microscope to analyze crystal size.

6.5 Image analysis procedure

The procedure for image analysis is as follows

- Import the images taken by the video microscope into ImageJ.
- Use the automated image analysis macro to obtain 2D geometry information for the crystal particles.
- Select the smaller scale between width and length as the 3rd dimension of size of the crystals to calculate the crystal volume.
- Calculate the equivalent spherical diameter of the crystal based on the volume.

The main limitation of this technique is that when the third dimension is significantly different from the width of the particle, such as plate shaped crystals, this method will lead to a large discrepancy.

6.6 Results and discussion

High shear wet milling is an import chemical engineering process. However, to the author's knowledge, only two papers were published[23, 24] on this area. In these papers, only particle size reduction with time data are presented. This chapter presents the wet milling of crystals in the Silverson inline L4R rotor stator mixer and the operating parameters influence on the performance of the high shear wet mill.

6.6.1 Pumping rate of the Silverson inline L4R rotor-stator mixer

The experimental set up is shown in Figure 6-3. The Silverson L4R rotor-stator mixer inlet is connected to a constant head tank. The amount of time to fill a second

Figure 6-3: The flow rate measurement experiment set up

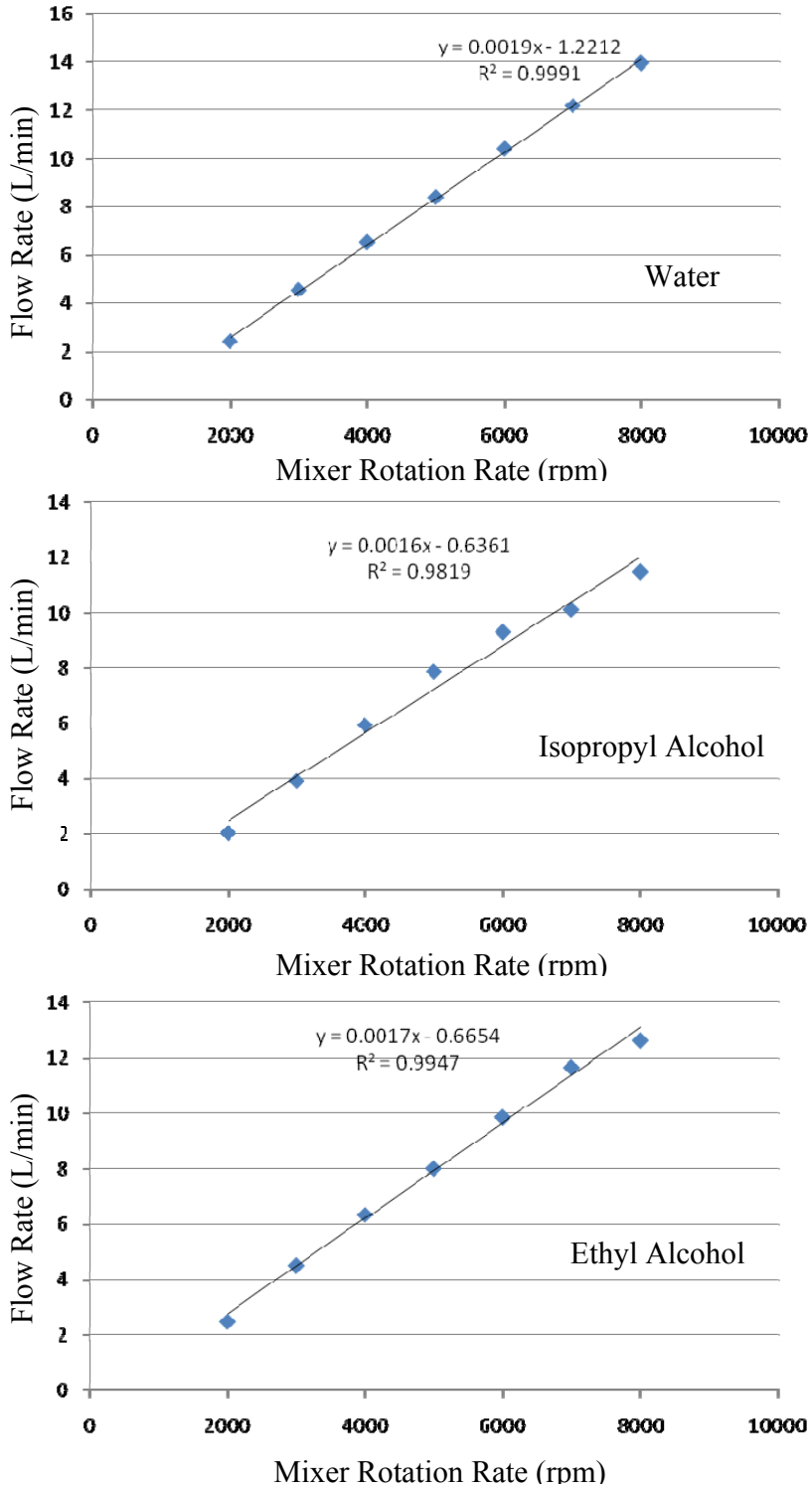

Figure 6-4: Flow rate in Silverson inline L4R mixer

container of known volume is recorded by a stop watch. The flow rate vs. rotation rate for water, isopropyl alcohol and ethyl alcohol are shown in Figure 6-4. The feed tank height was kept at the same level as in the high shear mixer.

The flow number is 0.06 at 8000 rpm when the working fluid is water, which is calculated by equation 5.4.2. These experiments results compares favorably with the simulation results (see section 5.4).

6.6.2 Wet milling of Sucrose

Free pumping wet milling experiments

In this research, two kinds of sucrose are investigated: raw sucrose and granulated sucrose. The experiments were performed at 4000, 6000 and 8000 rpm. No flow rate controller was used and the fluid was free pumped by the Silverson inline L4R mixer itself. The initial size of these crystals are shown as Figure 6-5.

The granulated sucrose samples removed at different time intervals at 4000, 6000 and 8000 rpm are shown in Figures 6-6, 6-7 and 6-8. From these figures, it is found that the crystal size decreases significantly and the particle size reduces with the rotation rate.

Table 6-1 shows the change in particle size D_{32} with number of particle counts at 8000 rpm. The sample was removed 1 minute after wet milling was initiated. From this table, it is found that 1000 particles are enough to perform the analysis.

Table 6-1 Particle size calculated at different number of particles at 8000 rpm

# of Particles	1000	1200	1700	2000	2200	2400
D_{32} (micron)	432	429	438	437	436	435

The granulated sucrose crystal size reduction profiles with time at 4000, 6000 and 8000 rpm at the free pumping condition in the Silverson inline L4R mixer are shown in Figure 6-9 and the number of passes the crystals exhibit at specific times is shown in Table 6-1. From this figure, it can be found that the crystal size is reduced

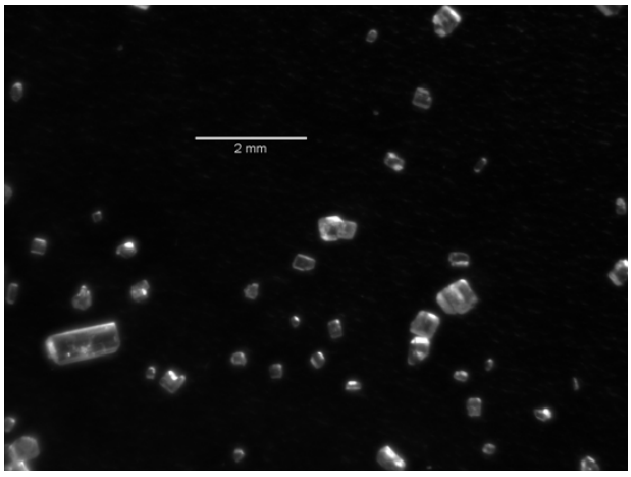

Raw Sucrose

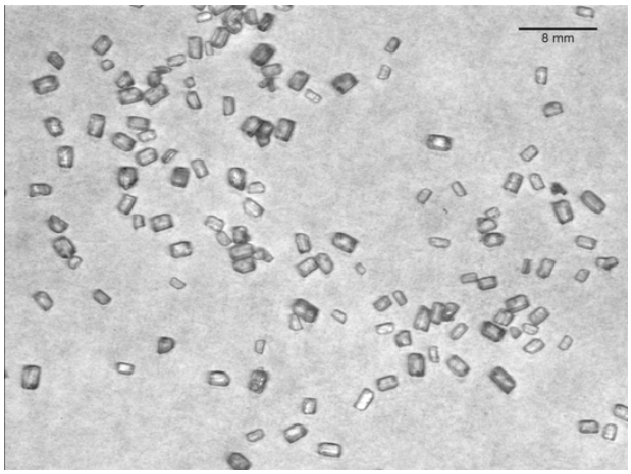

Granulated Sucrose

Figure 6-5: Initial sucrose crystals before wet milling experiments.

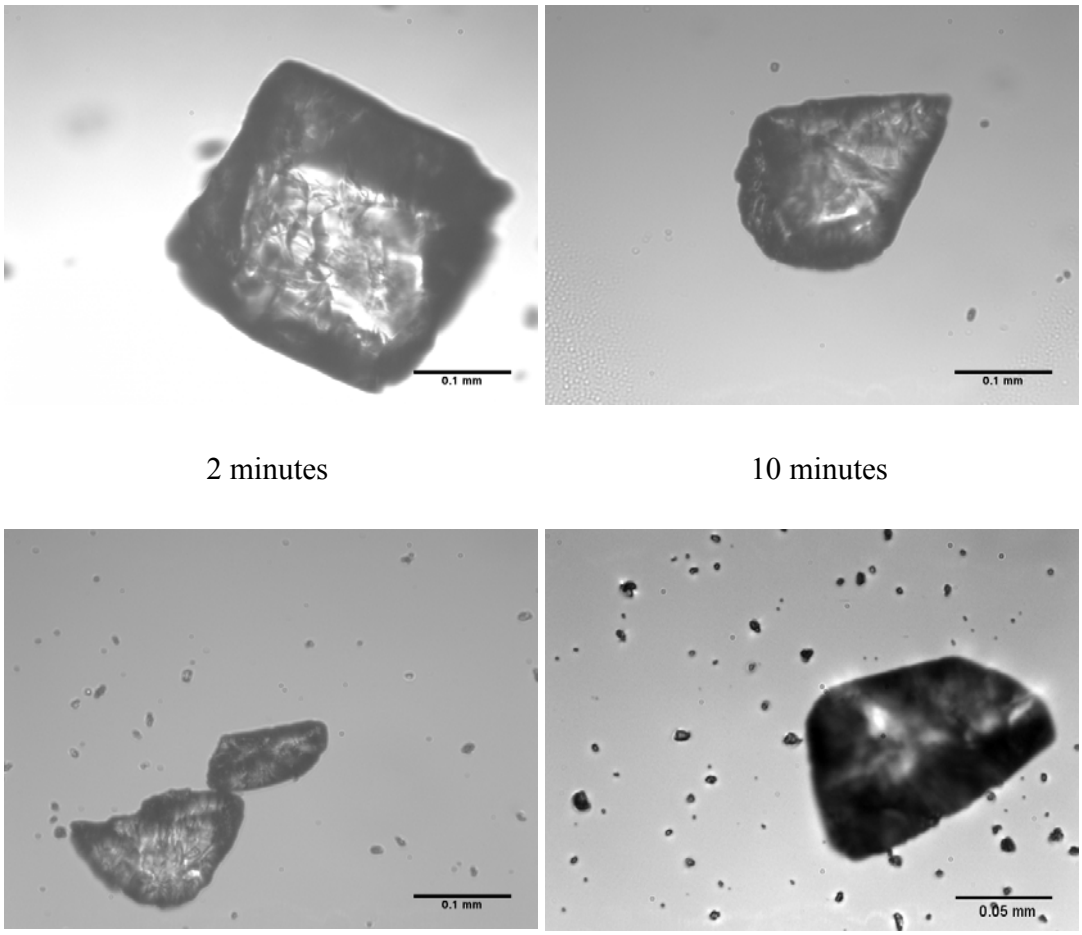

2 minutes 10 minutes

40 minutes 120 minutes

Figure 6-6: Granulated sucrose crystals removed at different times at 4000 rpm in the Silverson inline L4R rotor-stator mixer.

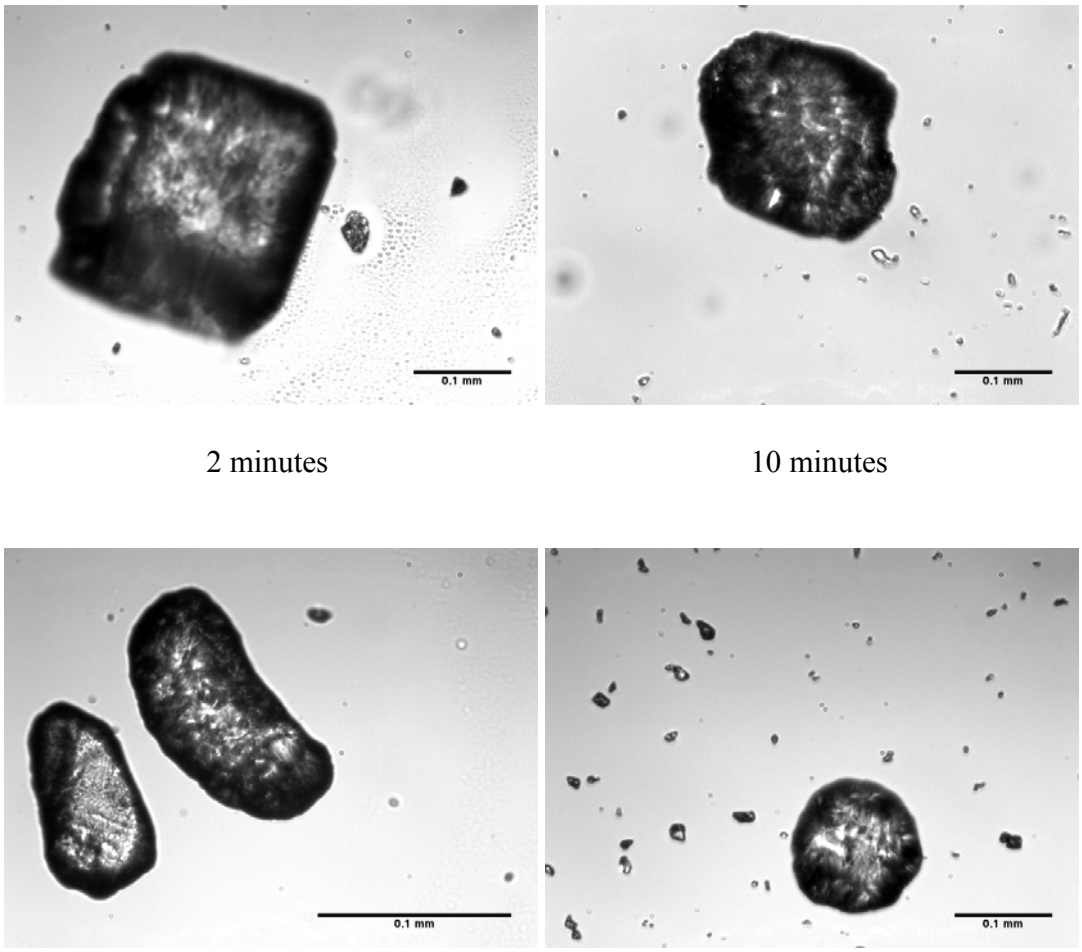

2 minutes 10 minutes

40 minutes 120 minutes

Figure 6-7: Granulated sucrose crystal removed at different times at 6000 rpm in Silverson inline L4R rotor-stator mixer.

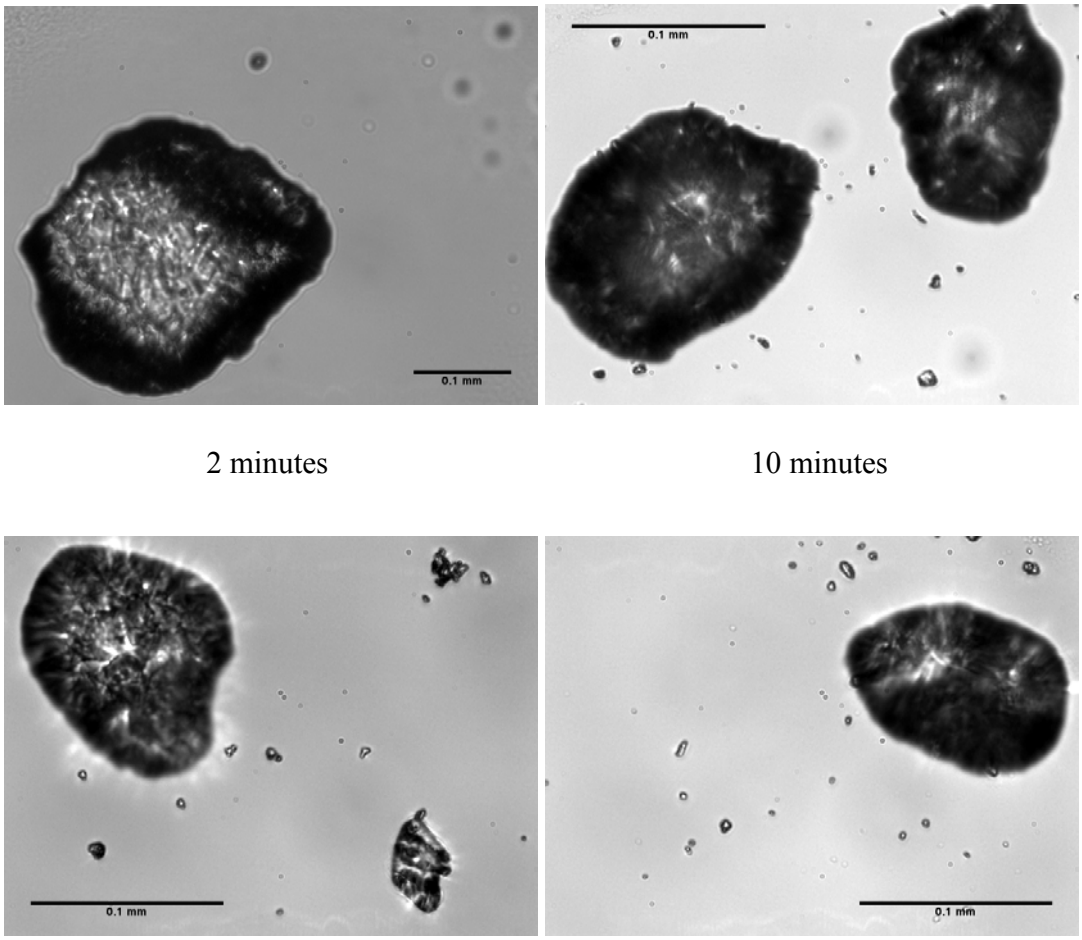

2 minutes 10 minutes

40 minutes 120 minutes

Figure 6-8: Granulated sucrose crystals removed at different times at 8000 rpm in the Silverson inline L4R rotor-stator mixer.

significantly at the beginning. After about 16 minutes, the size reduction rate is slowed. As a result, two different regimes are captured, which are the mass fracture regime and the attrition region. In the mass fracture region, particle size decreases dramatically with time while in the attrition region, the size reduction process is almost negligible. At the free pumping conditions, the crystal size decreases with the increase of rotation rate or nominal shear rate.

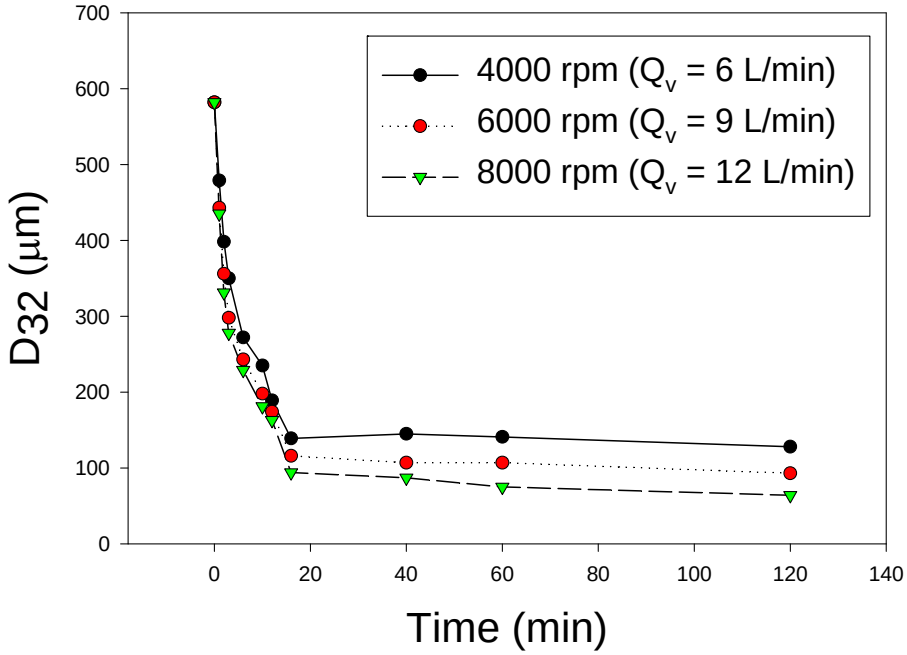

Figure 6-9: Granulated sucrose crystal size reduction with time at 4000, 6000 and 8000 rpm in Silverson inline L4R rotor-stator mixer.

Table 6-2: Number of passes of sucrose crystals at specific times.

	Flow Rate (L/min)	2 min	10 min	40 min	120 min
4000 rpm	6	6	30	120	360
6000 rpm	9	9	45	180	540
8000 rpm	12	12	60	240	720

The probability density function (PDF) of initial granulated sucrose is shown in Figure 6-10. PDF is defined by the following equation:

$$PDF(D) = \frac{F(D+\Delta D) - F(D)}{\Delta D}$$
$$\int PDF(D)dD = 1 \qquad (6.6.1)$$

It is the number fraction of the particles divided by the bin width, so Figure 6-10 is not a histogram. The PDF at different time intervals at 4000, 6000 and 8000 rpm are shown in Figures 6-11, 6-12 and 6-13, respectively. It is found that in the mass

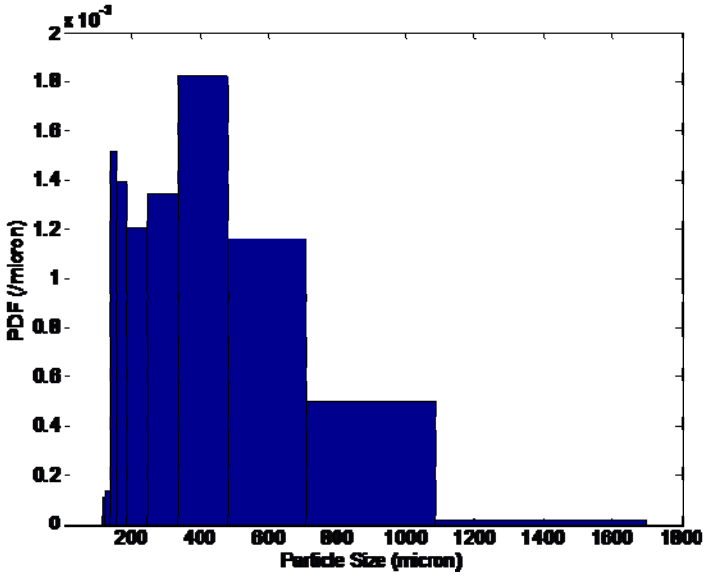

Figure 6-10: The normalized PSD of initial granulated sucrose.

fracture region, the number of larger particles decreases significantly from 2 min to 10 min while in the attrition region, the density of small particles increases from 40 min to 120 min. It is also seen from the particle images, such as Figure 6-8, that in the mass fracture region, the particles were broken in the middle, which sharp edges of the particle (the sample removed after 2 minutes). In the attrition region, it is seen that a large amount of small particles chipping from the particle edges are generated and the edge of particles are close to round.

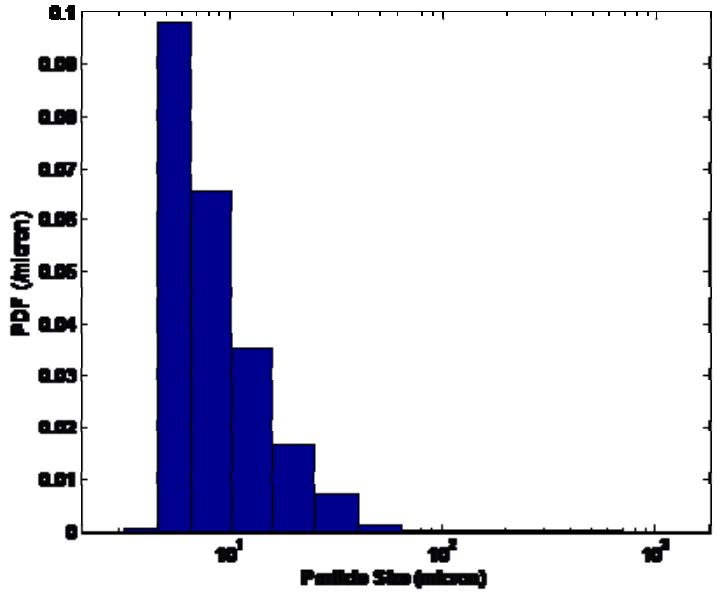

(a) 2 minutes

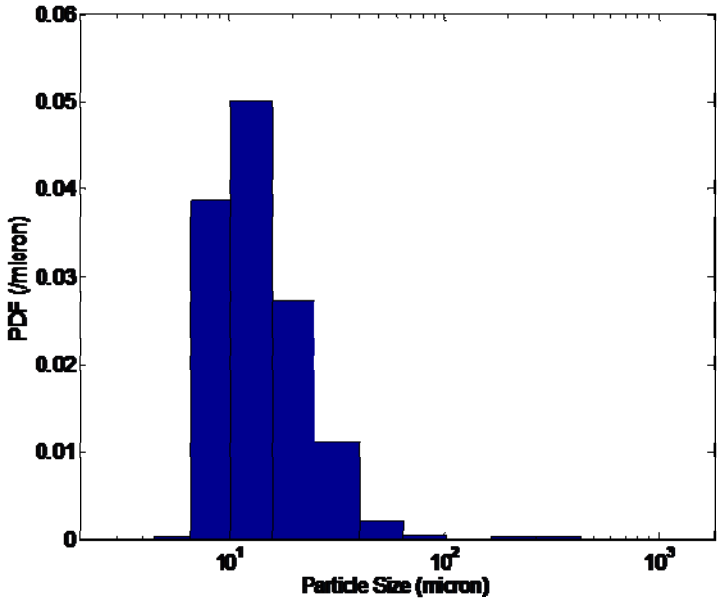

(b) 10 minutes

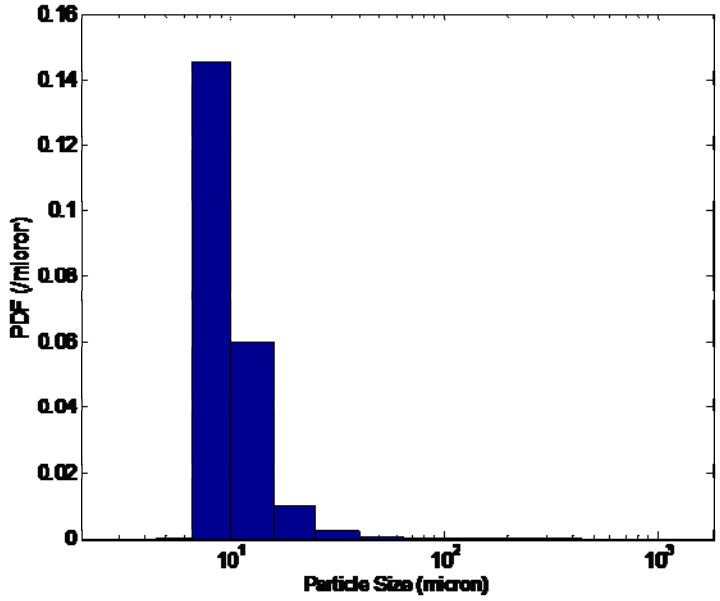

(c) 40 minutes

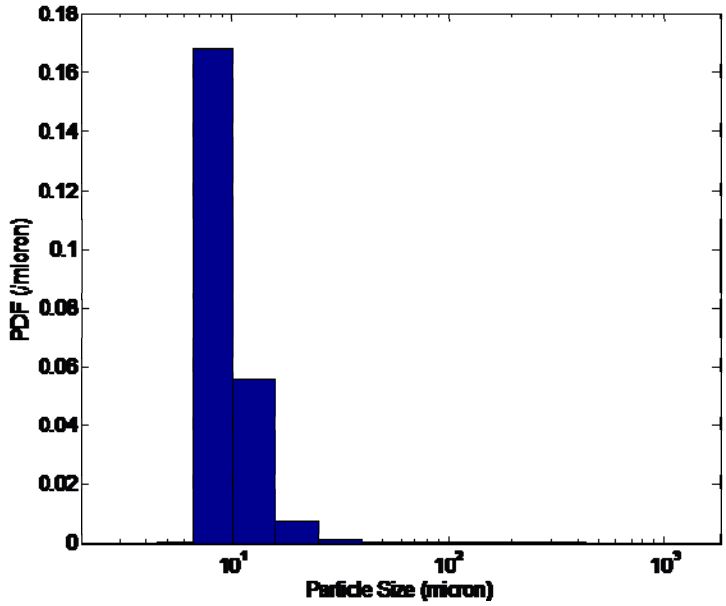

(d) 120 minutes

Figure 6-11: The PDF of granulated sucrose at 4000 rpm.

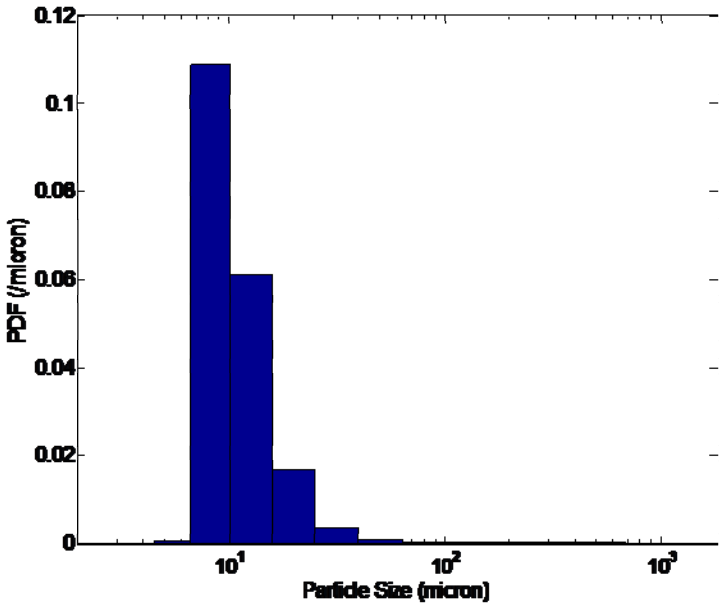

(a) 2 minutes

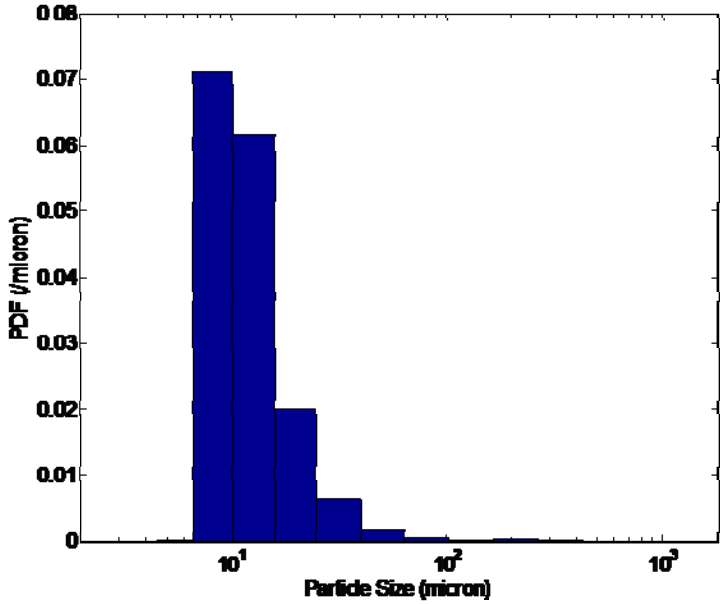

(b) 10 minutes

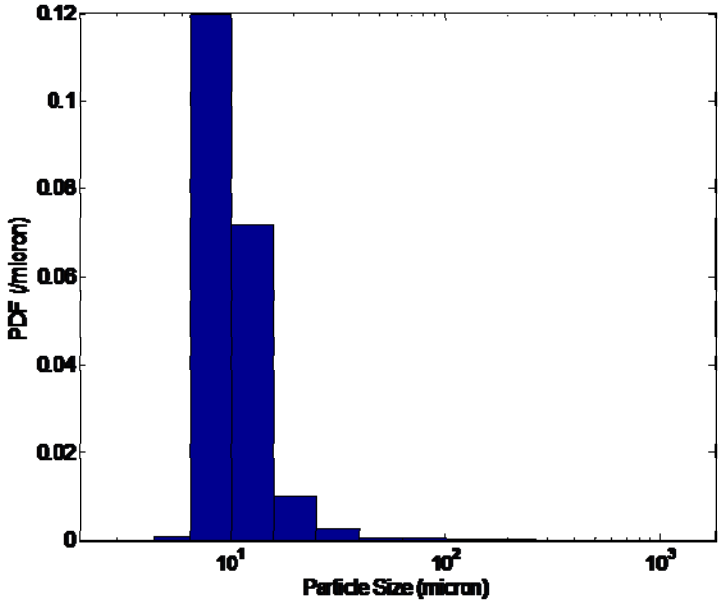

(c) 40 minutes

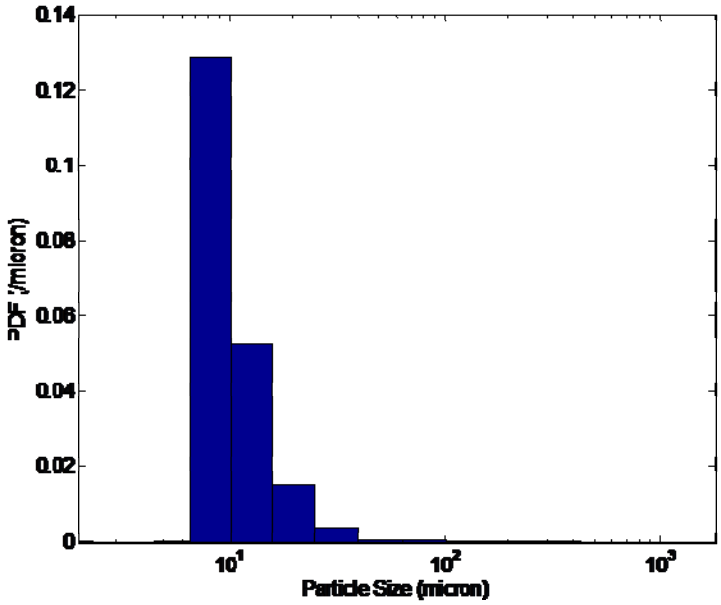

(d) 120 minutes

Figure 6-12: The PDF of granulated sucrose at 6000 rpm.

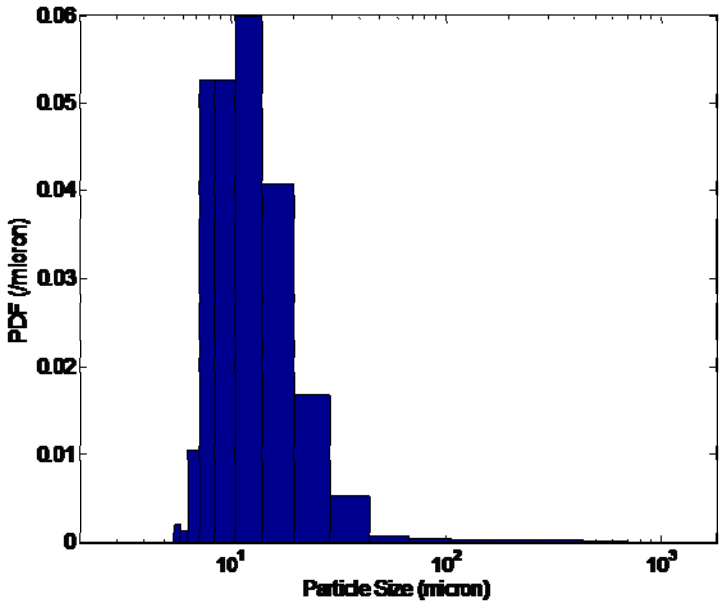

(a) 2 minutes

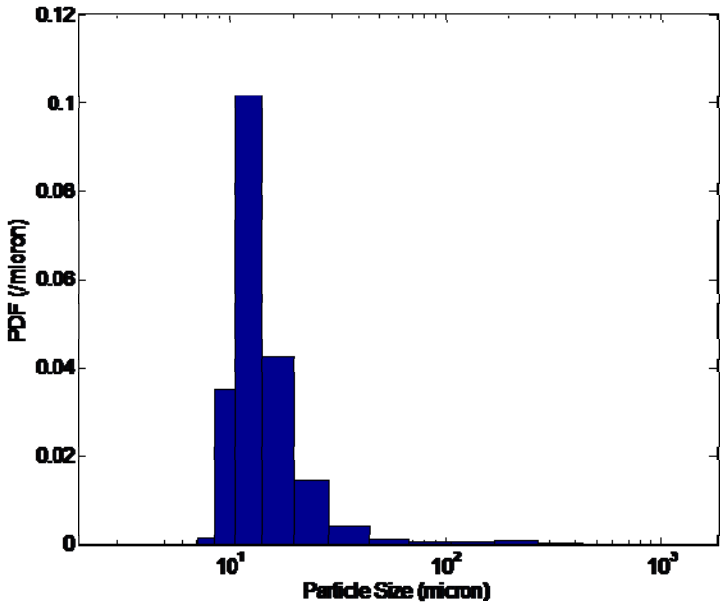

(b) 10 minutes

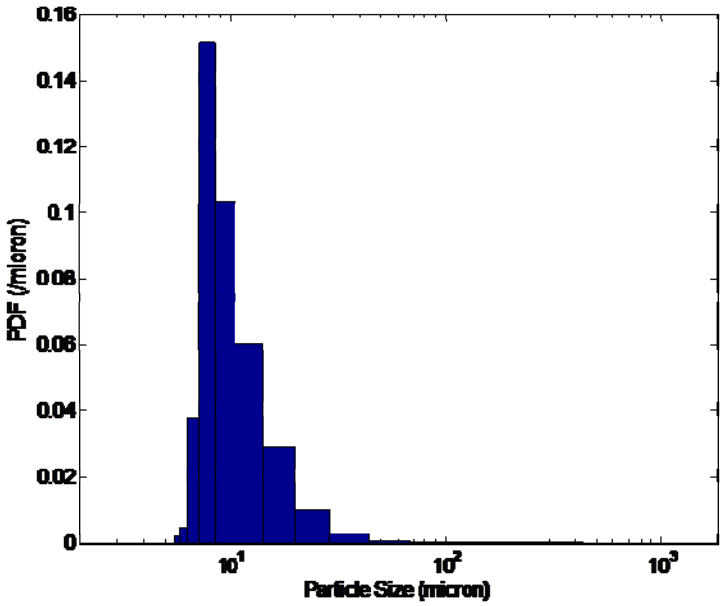

(c) 40 minutes

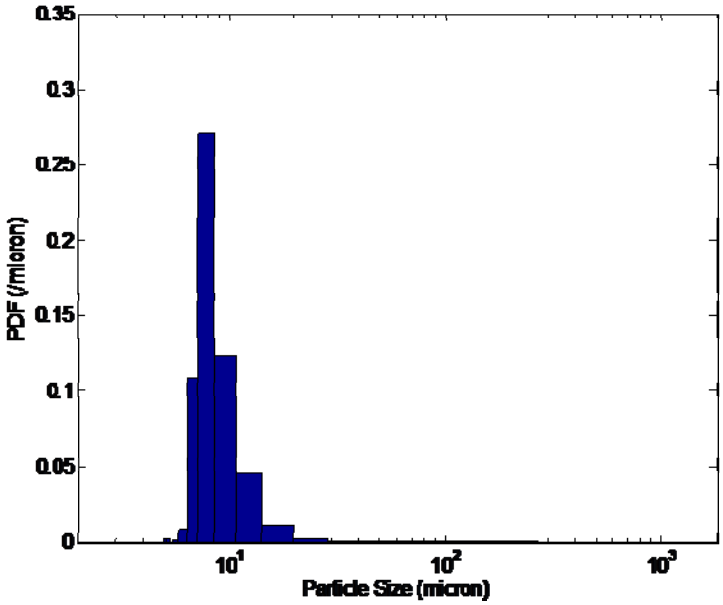

(d) 120 minutes

Figure 6-13: The normalized PSD of granulated sucrose at 8000 rpm.

The raw sucrose samples removed at different time intervals at 4000, 6000 and 8000 rpm are shown as Figure 6-14, 6-15 and 6-16. From these figures, the similar trend can be found for granulated sucrose.

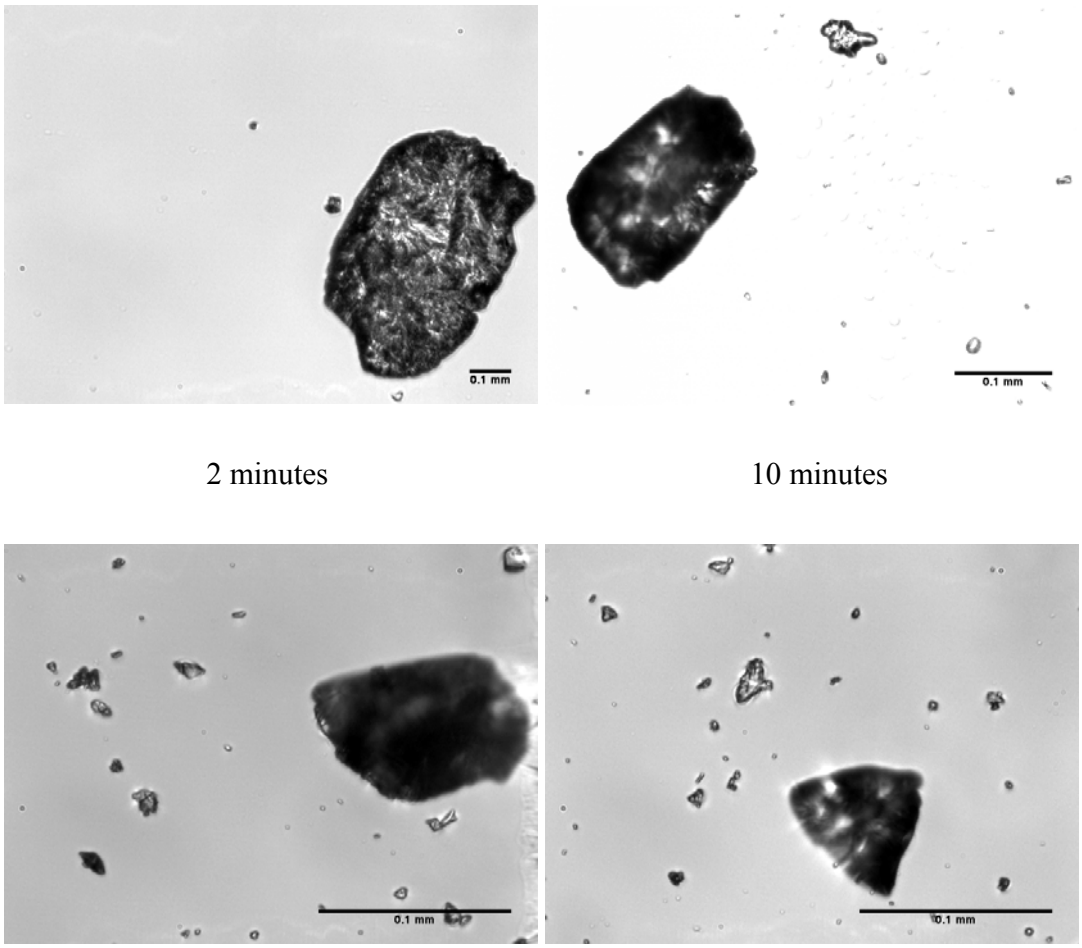

2 minutes 10 minutes

40 minutes 120 minutes

Figure 6-14: Raw sucrose crystals removed at different times at 4000 rpm in the Silverson inline L4R rotor-stator mixer.

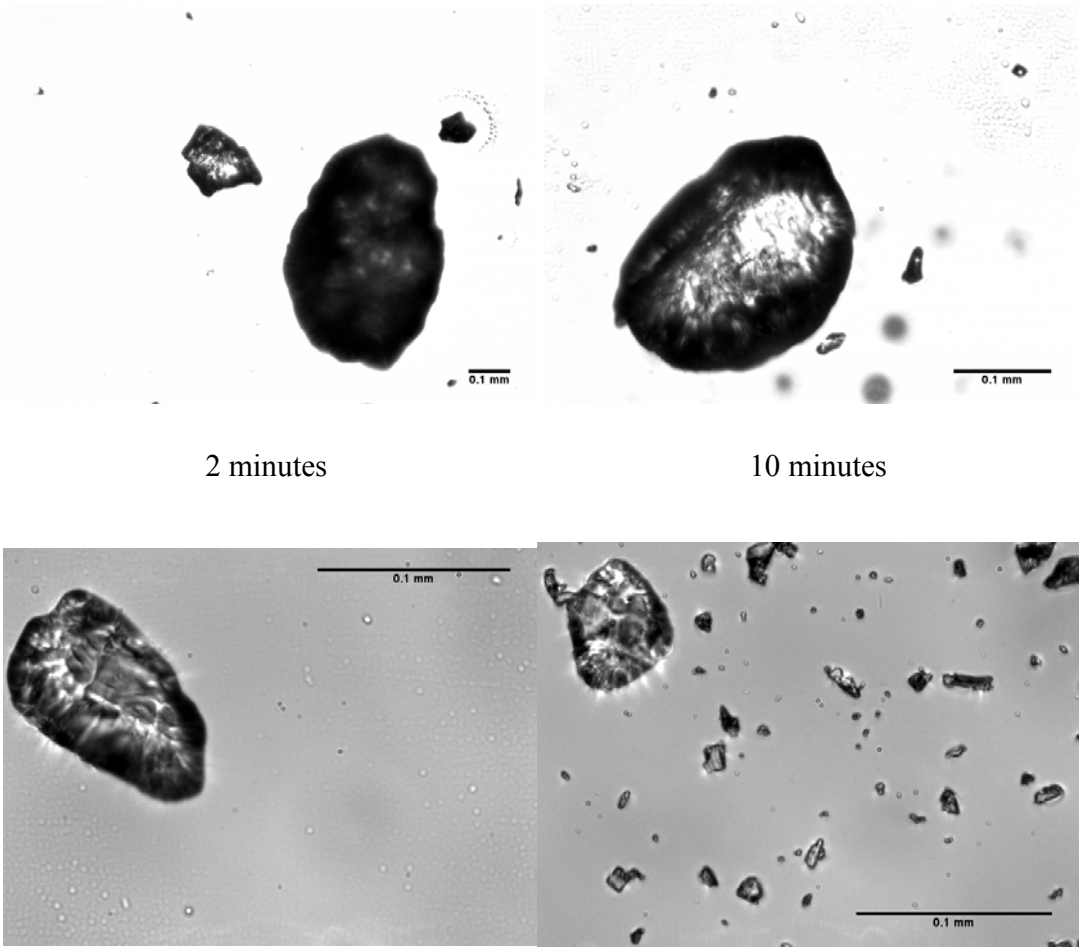

2 minutes

10 minutes

40 minutes

120 minutes

Figure 6-15: Raw sucrose crystals removed at different times at 6000 rpm in the Silverson inline L4R rotor-stator mixer.

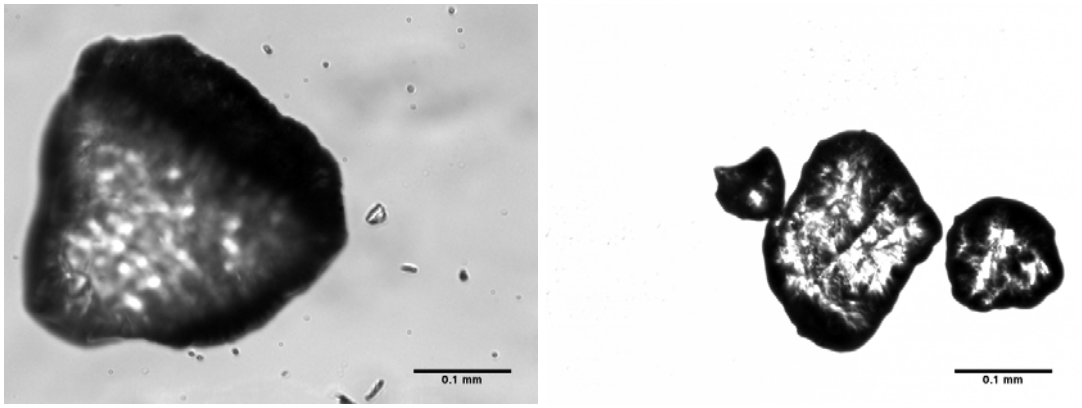

2 minutes 10 minutes

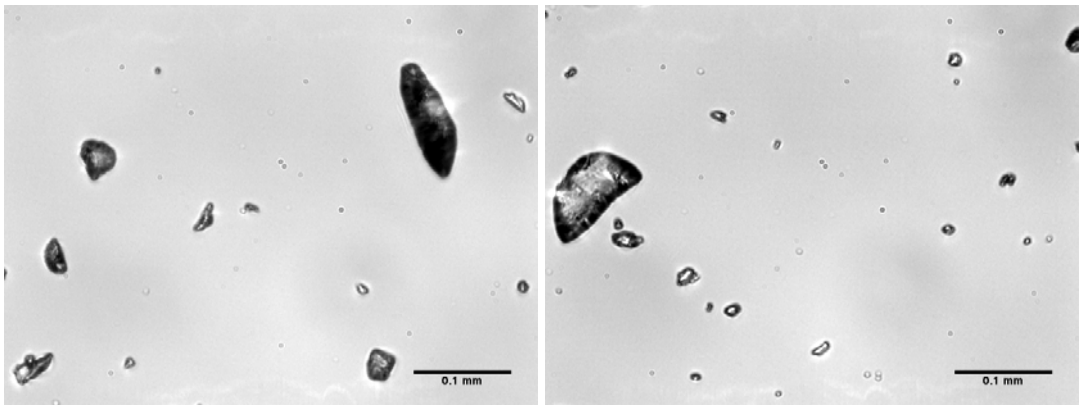

40 minutes 120 minutes

Figure 6-16: Granulated sucrose crystals removed at different times at 6000 rpm in the Silverson inline L4R rotor-stator mixer.

The raw sucrose crystal size reduction profiles with time at 4000, 6000 and 8000 rpm in the Silverson inline L4R mixer are shown in Figure 6-17 and the number of pass the crystals exhibit at specific times is same as Table 6-2. From this figure, it can be found that the crystal size is reduced dramatically at the beginning. After about 6 minutes, the size reduction rate is slowed. Two distinct regimes, mass fracture and attrition regimes, are captured. Compared with granulate sucrose, raw sucrose is much larger, originally. However, the decrease of crystal size with time is much faster

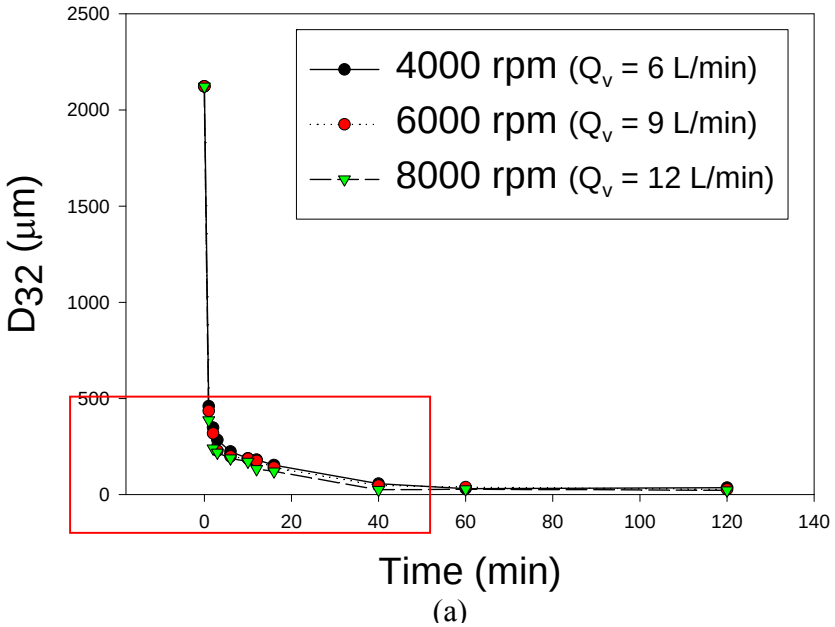

(a)

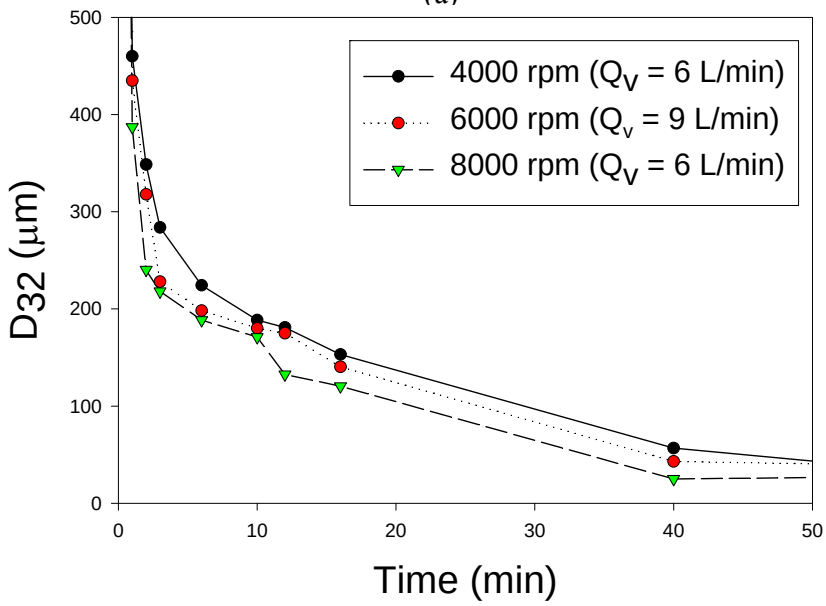

(b)

Figure 6-17: Raw sucrose crystal size reduction with time at 4000, 6000 and 8000 rpm in Silverson inline L4R rotor-stator mixer.
(a) overall figure; (b) zoomed figure of the region circled in (a).

than that of granulated sucrose. In addition, the final crystal size after 2 hours of wet milling is smaller. The reason could be the difference of physical properties between these two sugars.

The PDF of initial raw sucrose is shown in Figure 6-18. And the PDF at different time intervals at 4000, 6000 and 8000 rpm are shown in Figures 6-19, 6-20 and 6-21, respectively. It is found that in the mass fracture region, the number of larger particles decreases from 2 min to 10 min. In the attrition region, the density of small particles increases from 40 min to 120 min.

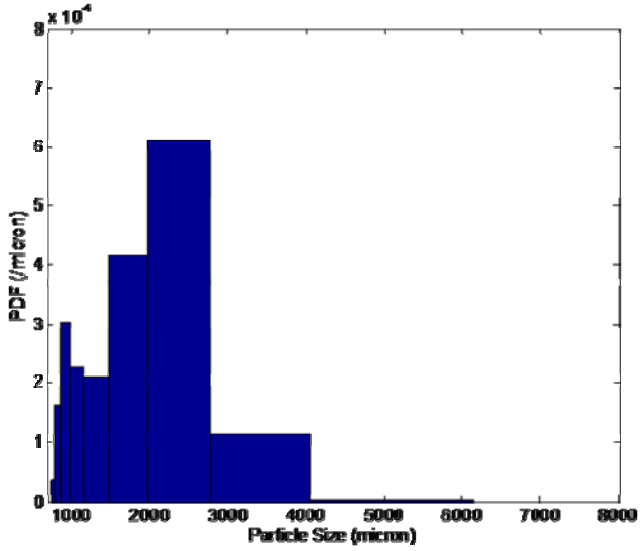

Figure 6-18: The PDF of initial raw sucrose

From Figure 5-15, the power number in the turbulent regime is 2.3. Power can be calculated by equation 4.3.2. SE and power per mass of rotor swept volume, $\dot{\varepsilon}$, are shown in Table 6-3. It is found that SE and $\dot{\varepsilon}$ increase with rotation rate, which could be another reason that smaller particles are found at higher rotation rate.

Table 6-3: SE and $\dot{\varepsilon}$ at different rotation rate (wet milling of sucrose).

$\dot{\varepsilon}$ (J/kg)			SE (J/kg)		
4000 rpm	6000 rpm	8000 rpm	4000 rpm	6000 rpm	8000 rpm
2066	6971	16526	213	462	1403

Wet milling experiments with sucrose at different flow rates

In chapter 5, it is found that when the simulation is performed at constant tip speed, the flow rate of different scale mixers changes significantly. So, will the flow rate affect the wet milling process? To answer this question, wet milling of granulated sucrose experiments were performed at three different flow rates, 6.8 (free pumping), 5.3 and 3.8 L/min, and the rotation rate was kept constant 8000 rpm.

The granulated sucrose samples removed at different time intervals at 5.3 and 3.8 L/min are shown as Figure 6-22,and 6-23 (the sucrose sample at 6.8 L/min are shown in Figure 6-8).

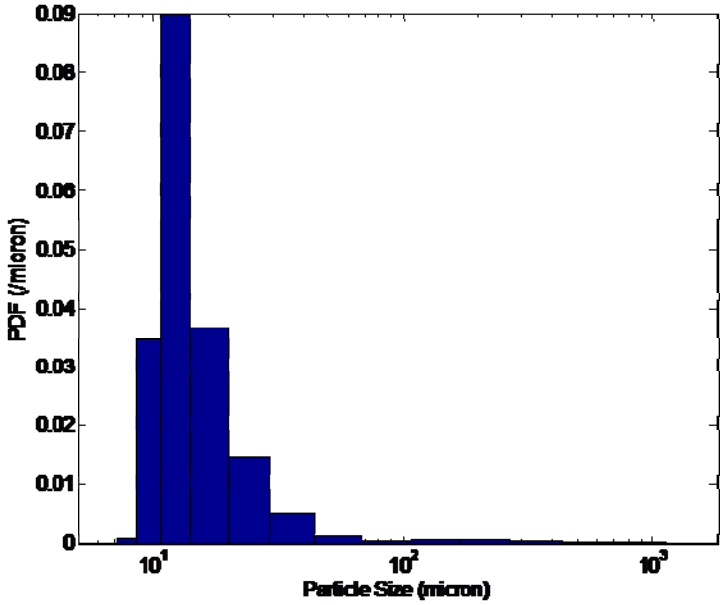

(a) 2 minutes

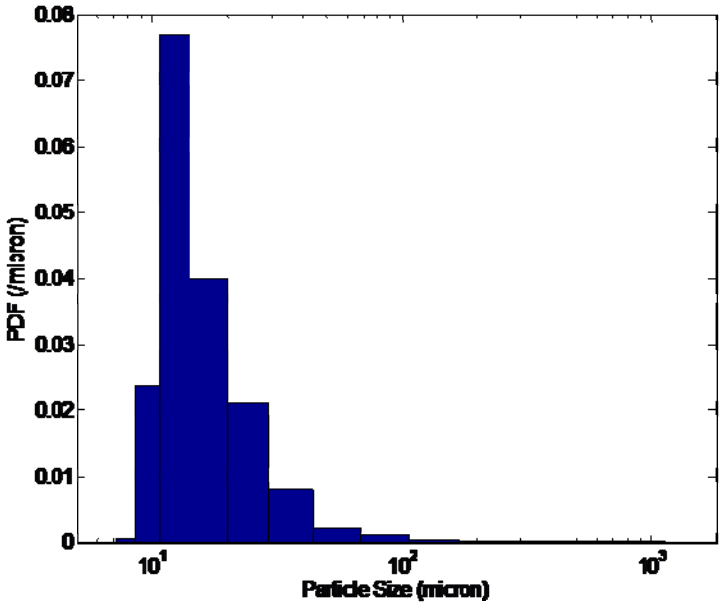

(b) 10 minutes

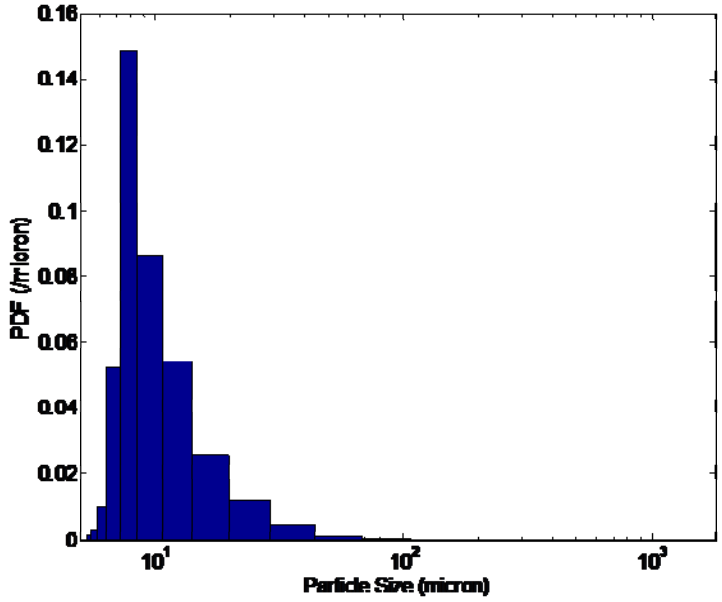

(c) 40 minutes

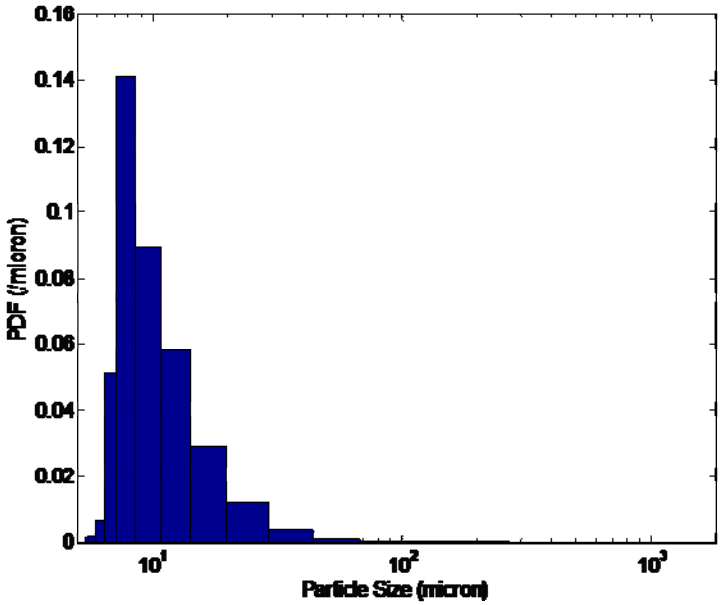

(d) 120 minutes

Figure 6-19: The PDF of raw sucrose at 4000 rpm.

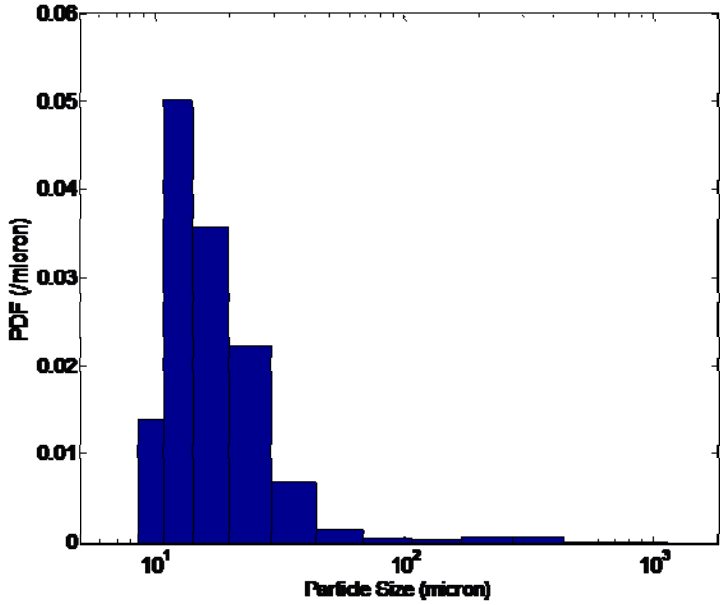

(a) 2 minutes

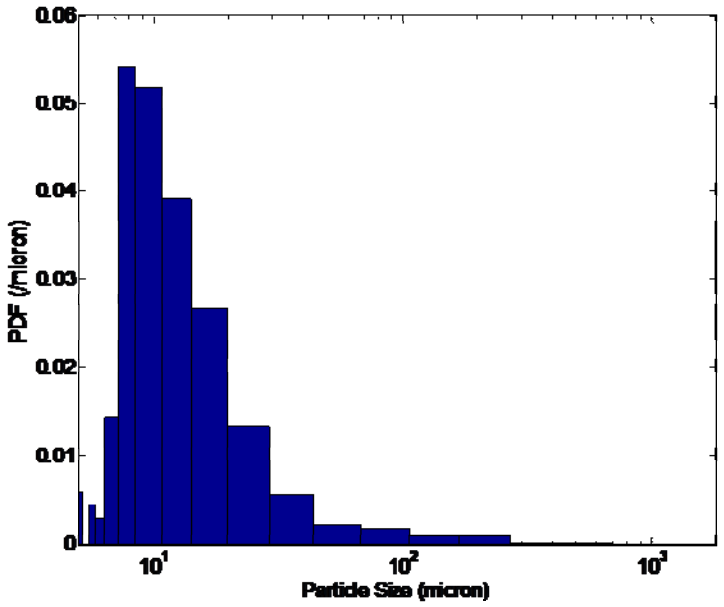

(b) 10 minutes

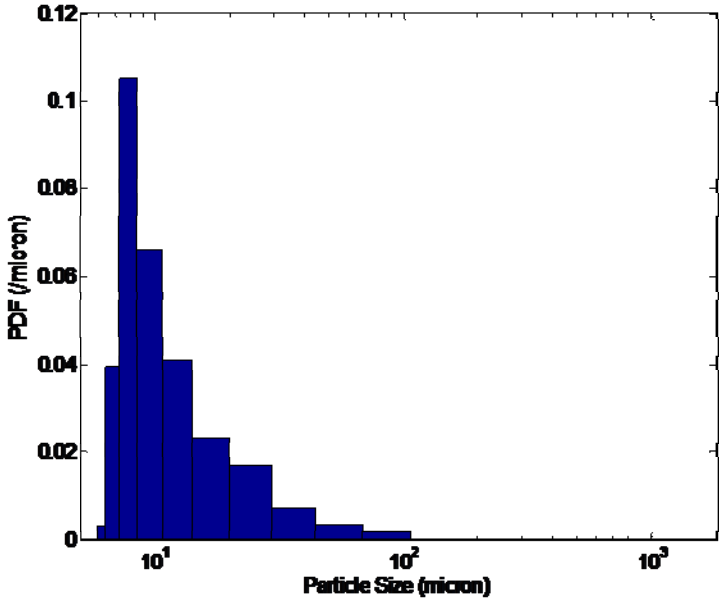

(c) 40 minutes

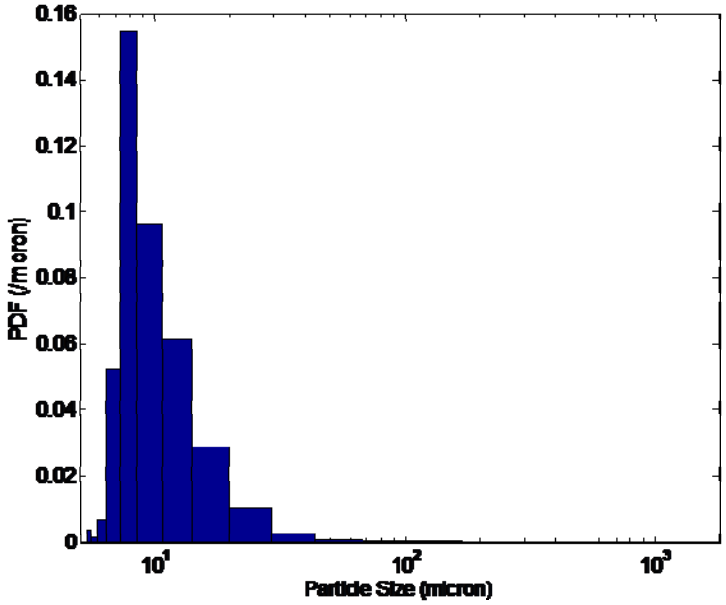

(d) 120 minutes

Figure 6-20: The PDF of raw sucrose at 6000 rpm.

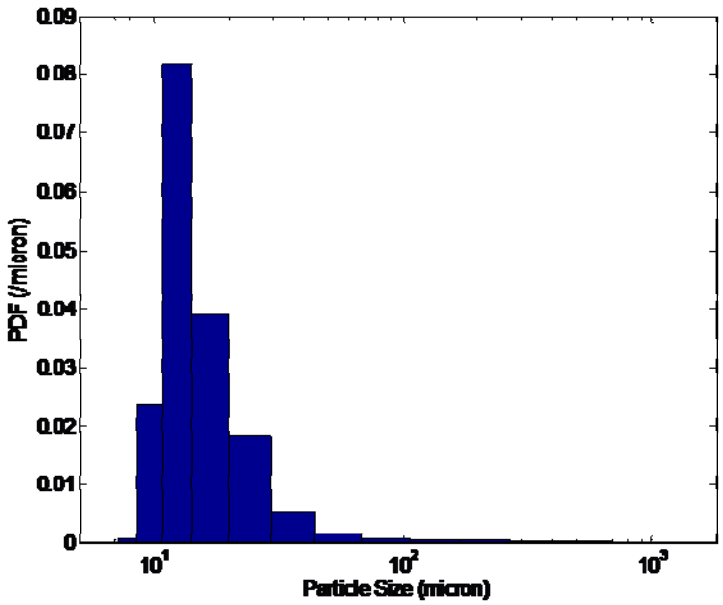

(a) 2 minutes

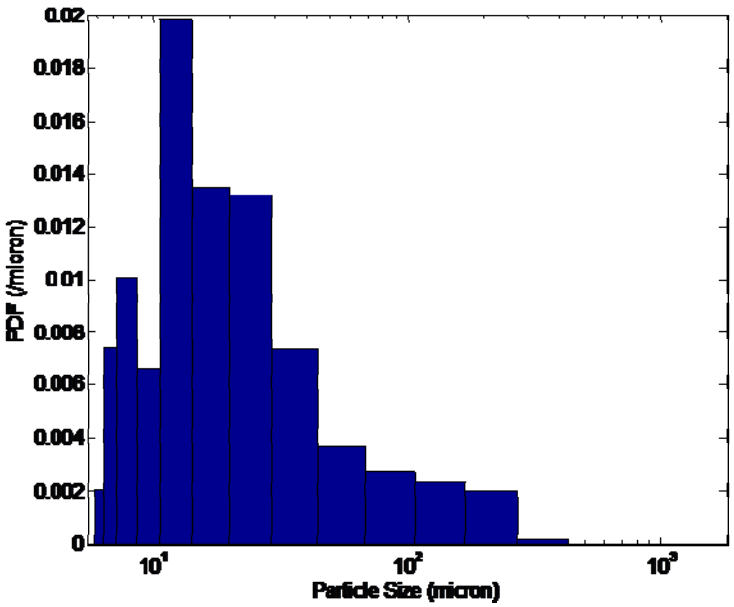

(b) 10 minutes

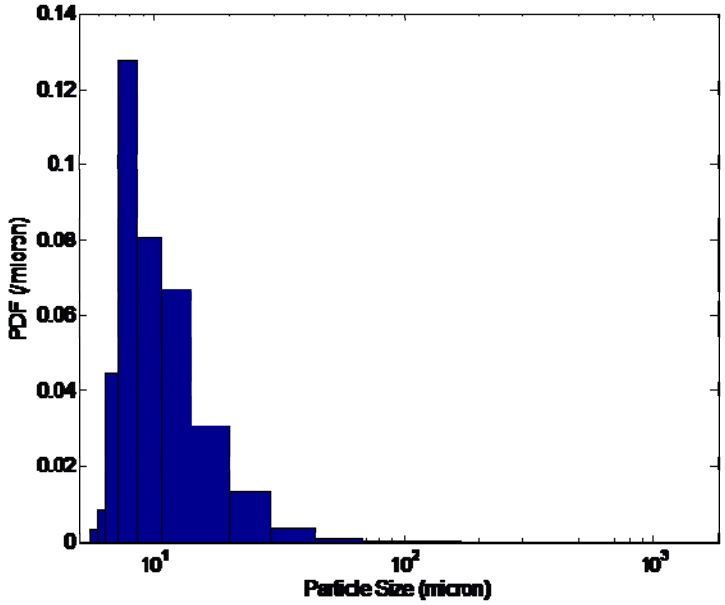

(c) 40 minutes

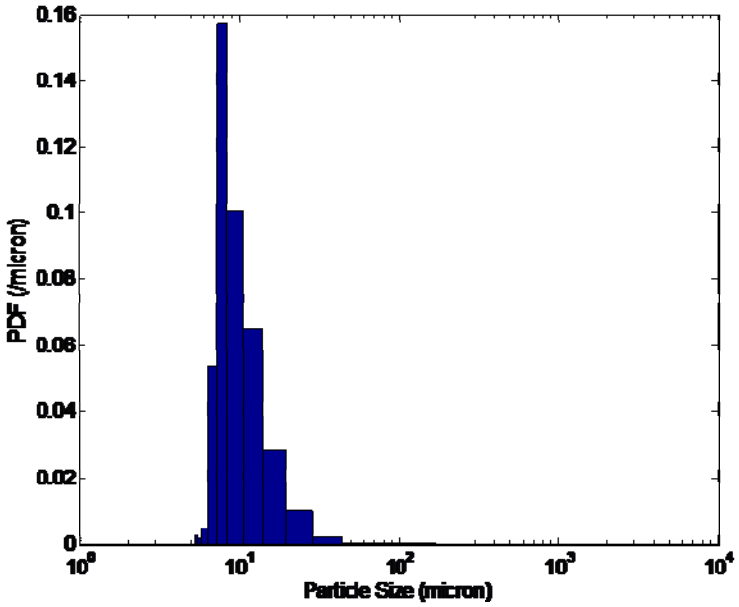

(d) 120 minutes

Figure 6-21: The PDF of raw sucrose at 8000 rpm.

The granulated sucrose crystal size reduction profiles with time at 6.8, 5.3 and 3.8 L/min in Silverson inline L4R mixer are shown in Figure 6-24 and the number of passes the crystals exhibit up to specific times is shown in Table 6-4. It can be found

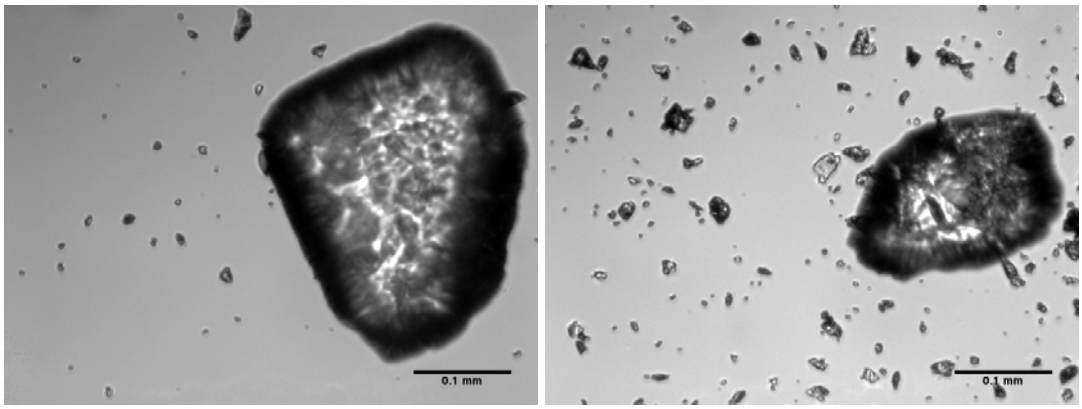

2 minutes 10 minutes

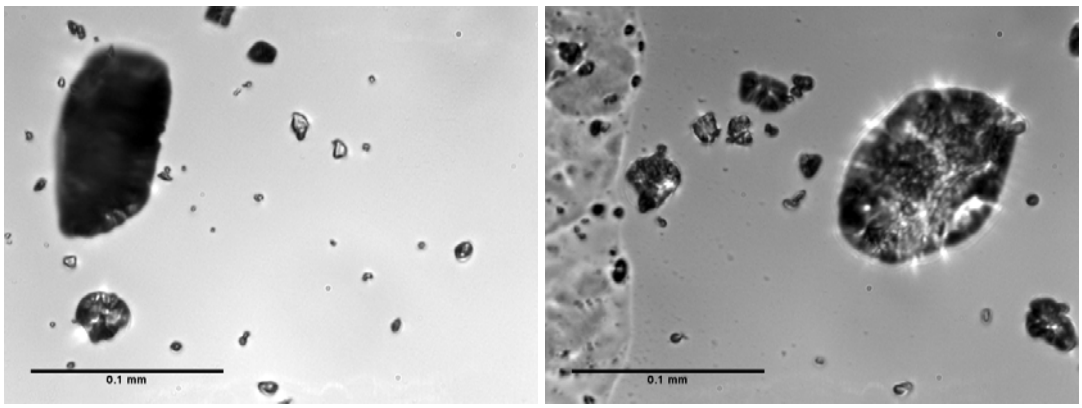

40 minutes 120 minutes

Figure 6-22: Granulated sucrose crystals removed at different times at 5.3 L/min, 8000 rpm in the Silverson inline L4R rotor-stator mixer.

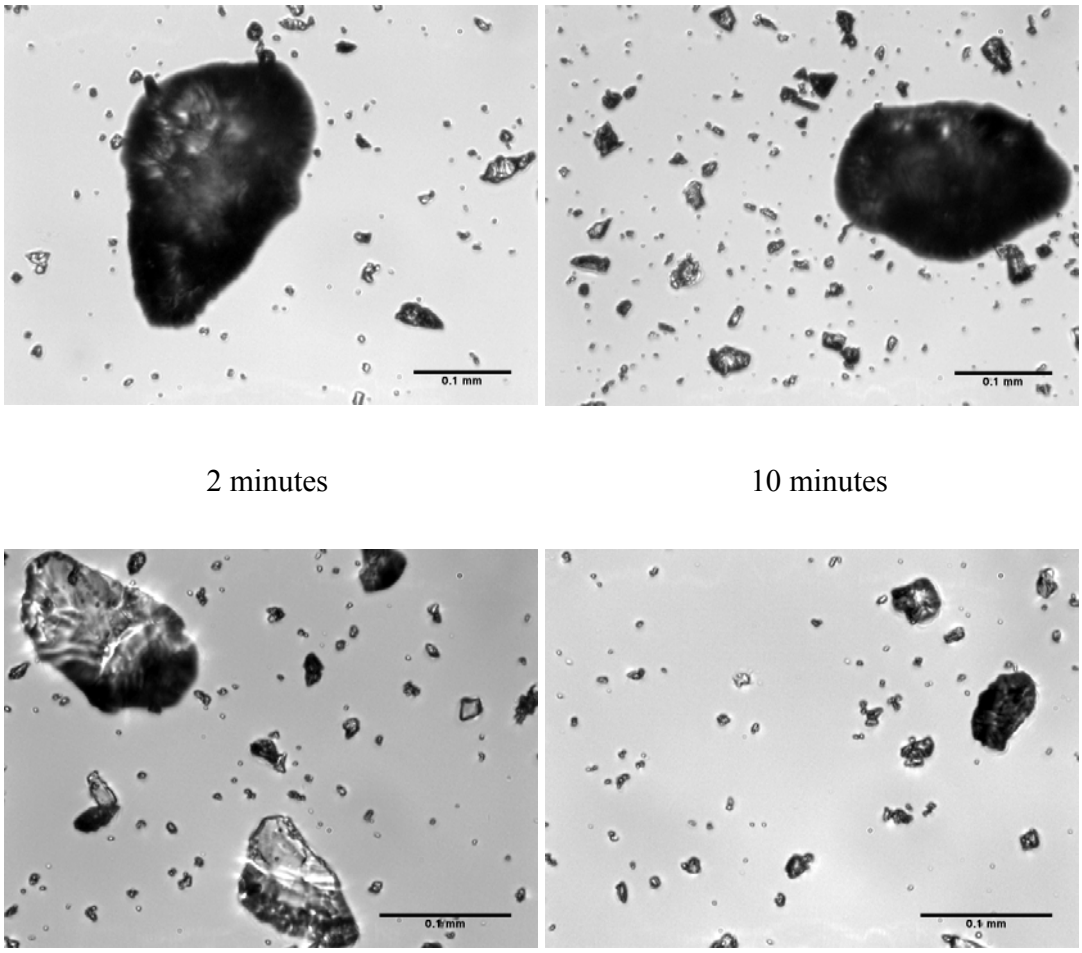

2 minutes

10 minutes

40 minutes

120 minutes

Figure 6-23: Granulated sucrose crystals removed at different times at 3.8 L/min, 8000 rpm in the Silverson inline L4R rotor-stator mixer.

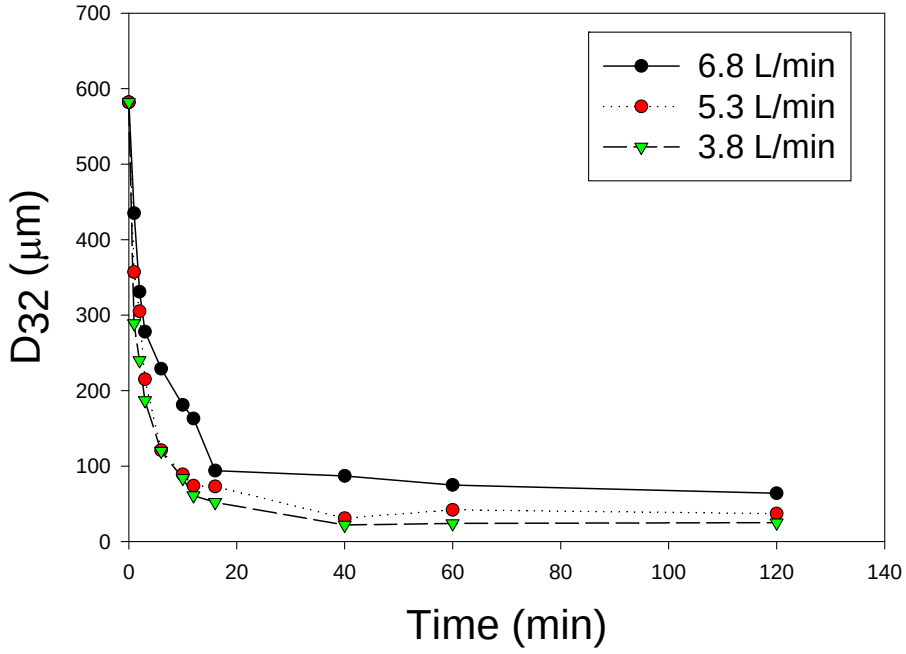

Figure 6-24: Granulated sucrose crystal size reduction with time at 6.8, 5.3 and 3.8 L/min in Silverson inline L4R rotor-stator mixer (8000 rpm).

Table 6-4: Number of passes of sucrose crystals at specific time.

Flow Rate (L/min)	2 min	10 min	40 min	120 min
6.8	7	35	140	420
5.3	5	25	100	300
3.8	4	20	80	240

that with the decrease in flow rate, smaller crystal particles are generated. The reason could be that with smaller flow rate, the particles will exhibit longer residence time in the high shear mixers, which results in smaller particles. Therefore, flow rate does have an effect on the wet milling process.

6.6.3 Wet milling of mannitol

In this section, wet milling of mannitol in ethyl alcohol is discussed. Two kinds of mannitol with different crystal habits, plates and needles, are investigated. The experiments were performed at 4000, 6000 and 8000 rpm and the flow rate was kept constant at 7 L/min.

The initial size of these crystals are shown as Figure 6-25. The plate shape mannitol samples removed at different time intervals at 4000, 6000 and 8000 rpm are shown in Figures 6-26, 6-27 and 6-28.

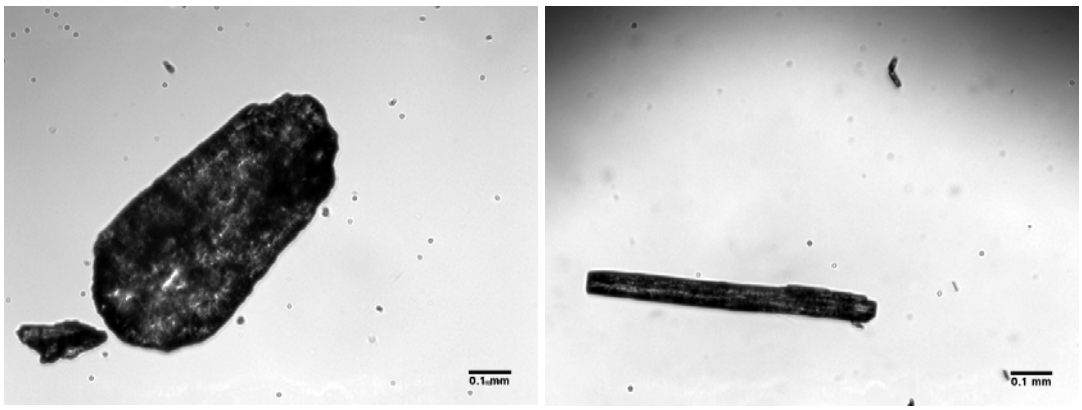

Plate Needle

Figure 6-25: Initial mannitol crystals size before wet milling experiments

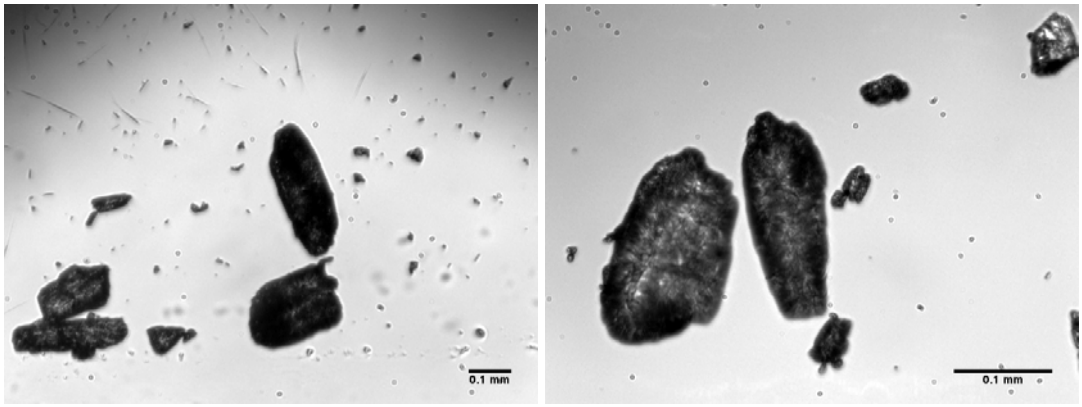

2 minutes 10 minutes

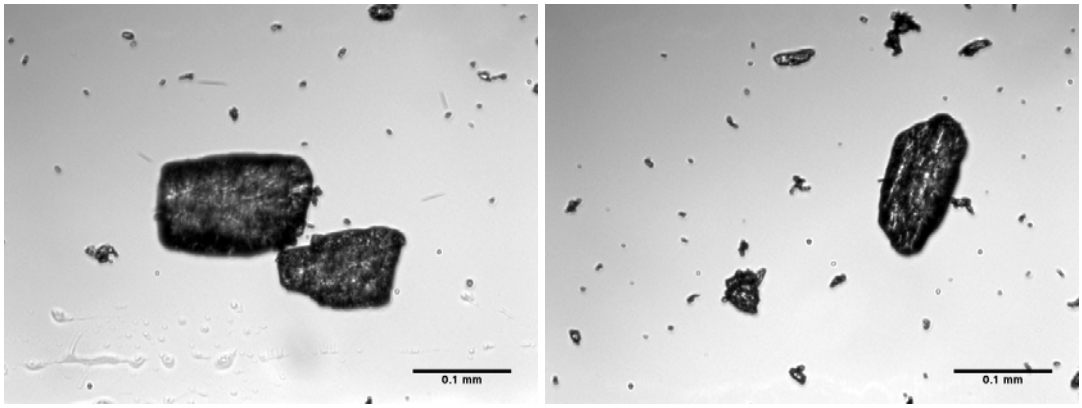

40 minutes 120 minutes

Figure 6-26: Plate shaped mannitol crystals removed at different times at 4000 rpm in the Silverson inline L4R rotor-stator mixer.

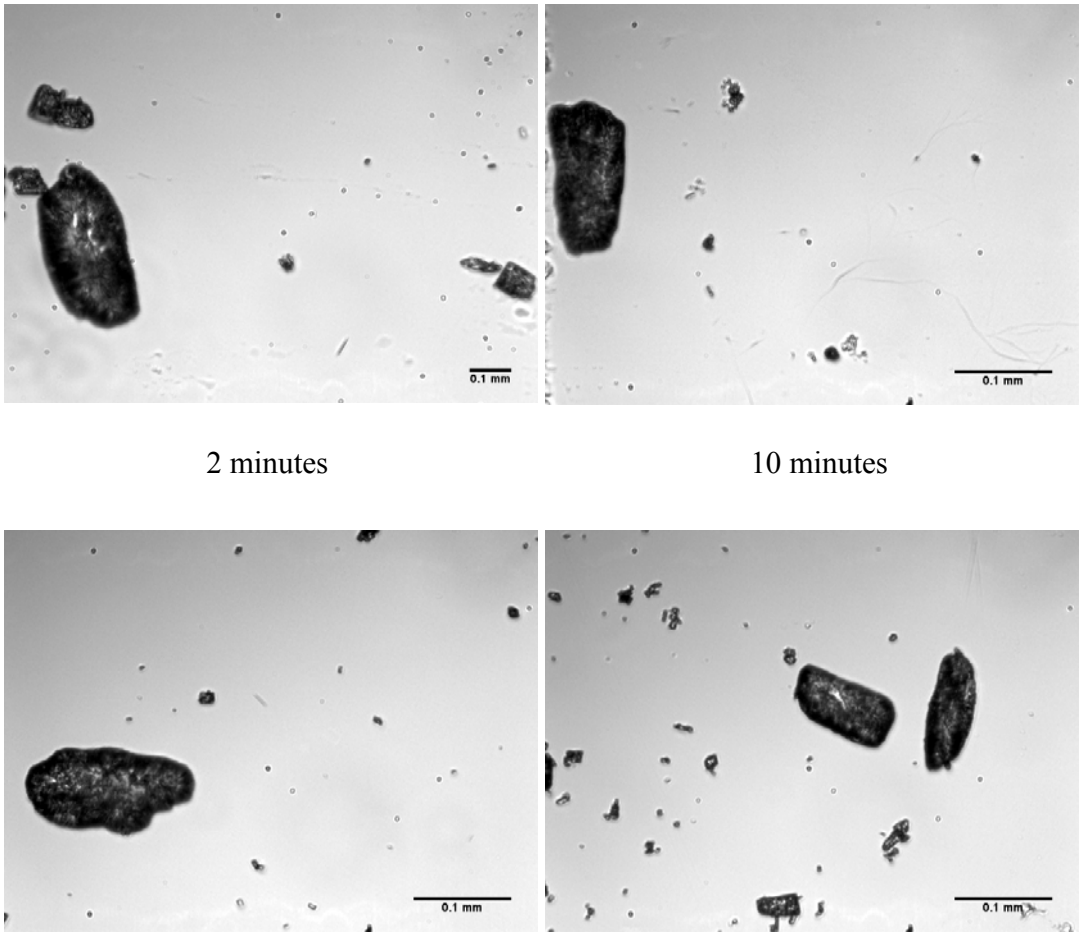

2 minutes 10 minutes

40 minutes 120 minutes

Figure 6-27: Plate shaped mannitol crystals removed at different times at 6000 rpm in the Silverson inline L4R rotor-stator mixer.

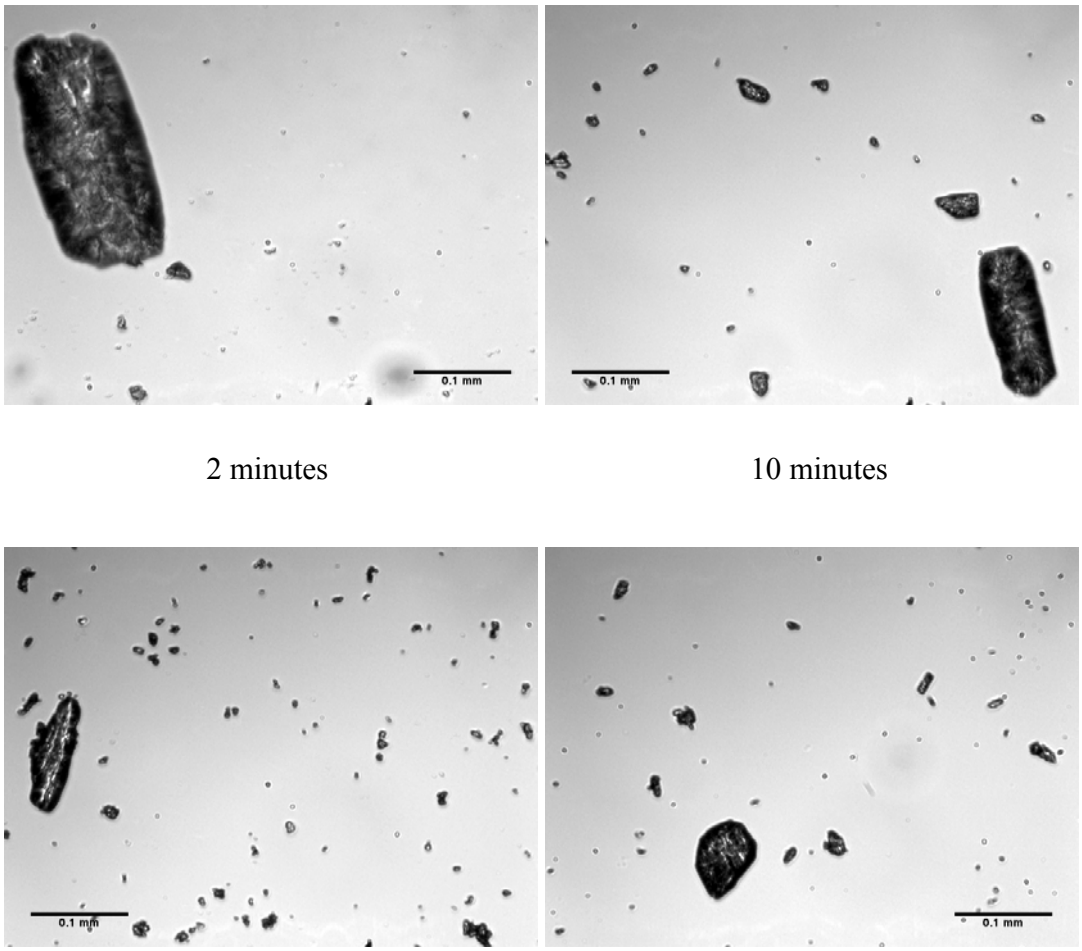

2 minutes 10 minutes

40 minutes 120 minutes

Figure 6-28: Plate shaped mannitol crystals removed at different times at 8000 rpm in the Silverson inline L4R rotor-stator mixer.

Since the 3rd dimension of plate shaped mannitol is significantly different from the width in the mass fracture region, 1/4 of the width is selected as the 3rd dimension. After the crystals have been milled for a sufficiently long time and enter the attrition region, the 3rd dimension could be close to the width. Therefore, the plate shape

mannitol crystal size reduction profiles with time at 4000, 6000 and 8000 rpm in the Silverson inline L4R mixer are shown in Figures 6-29 and 6-30. In Figure 6-29, 1/4 of the width is selected as the 3rd dimension scale while width is used as the 3rd dimension scale in Figure 6-30. At the beginning, the particle size differ significantly when different 3rd dimension scale is selected. The initial size is 283 micron when the width is used as the 3rd dimension scale while it is 178 micron when 1/4 of the width. However after 2 hours milling, the particle sizes are 56, 33 and 24 micron at 4000, 6000 and 8000 rpm respectively while they are 35, 21 and 15 micron at 4000, 6000 and 8000 rpm respectively. Therefore, the difference between the particle size resulting from different 3rd dimension scale is significant in the mass fracture region but relatively small in the attrition region.

From 0 to 16 minutes, the wet milling process is in the mass fracture dominated region and the particle size decrease dramatically; after 16 minutes, the wet milling process enters attrition region where the particle size is reduced slowly. In addition, when the flow rate is kept constant at 7 L/min in the experiments, crystal size decreases with rotation rates and these processes may be controlled by the shear rate only.

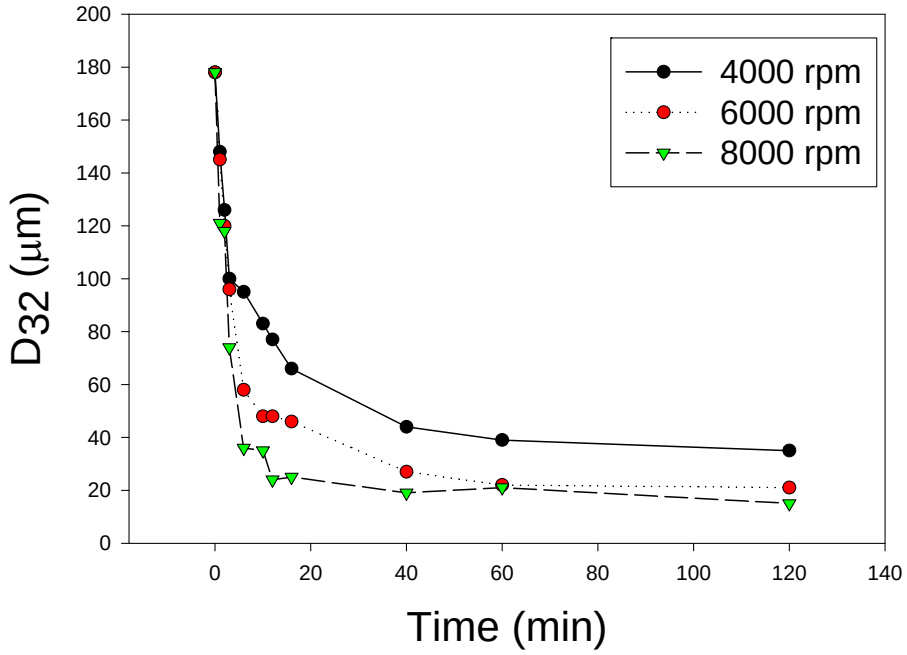

Figure 6-29: Plate shaped mannitol crystal size reduction with time at 4000, 6000 and 8000 rpm in the Silverson inline L4R rotor-stator mixer. 3rd dimension is 1/4 of the width.

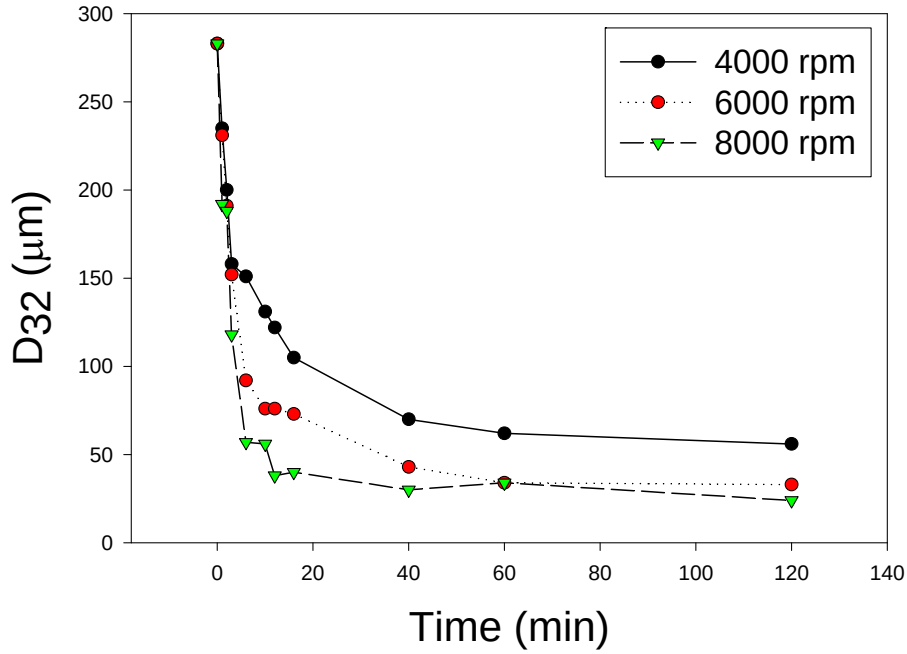

Figure 6-30: Plate shaped mannitol crystal size reduction with time at 4000, 6000 and 8000 rpm in the Silverson inline L4R rotor-stator mixer. 3rd dimension is the width.

The PDF of initial plate shaped mannitol is shown in Figure 6-31 and the PDF at different time intervals at 4000, 6000 and 8000 rpm are shown in Figures 6-32, 6-33 and 6-34, respectively with the width as the 3rd dimension scale. In addition, the PDF of initial plate shaped mannitol is shown in Figure 6-35 and the PDF at different time intervals at 4000, 6000 and 8000 rpm are shown in Figures 6-36, 6-37 and 6-38, respectively with the width as the 3rd dimension scale. It is found that in the mass fracture region, the number larger particles decreases from 2 min to 10 min. And in the attrition region, the density of small particles increases from 40 min to 120 min. When the PDFs with the width as the 3rd dimension scale is compared with that with

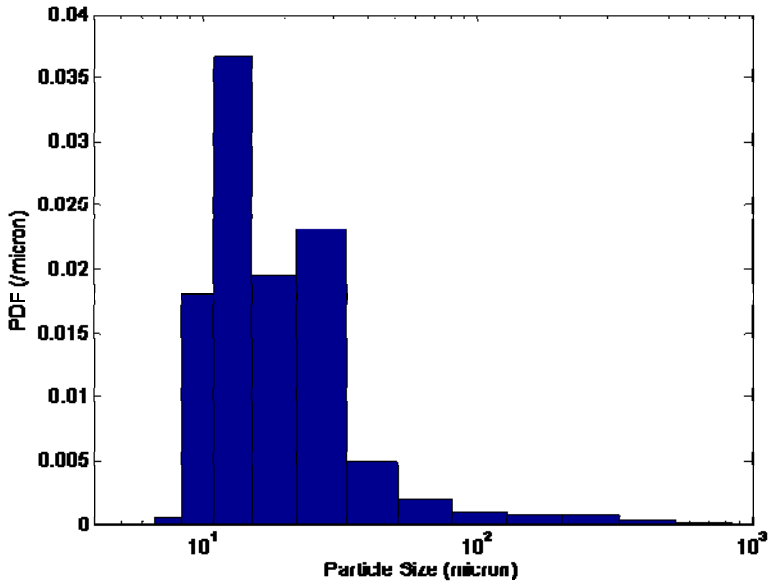

Figure 6-31: The PDF of initial plate shaped mannitol (3rd dimension is the width).

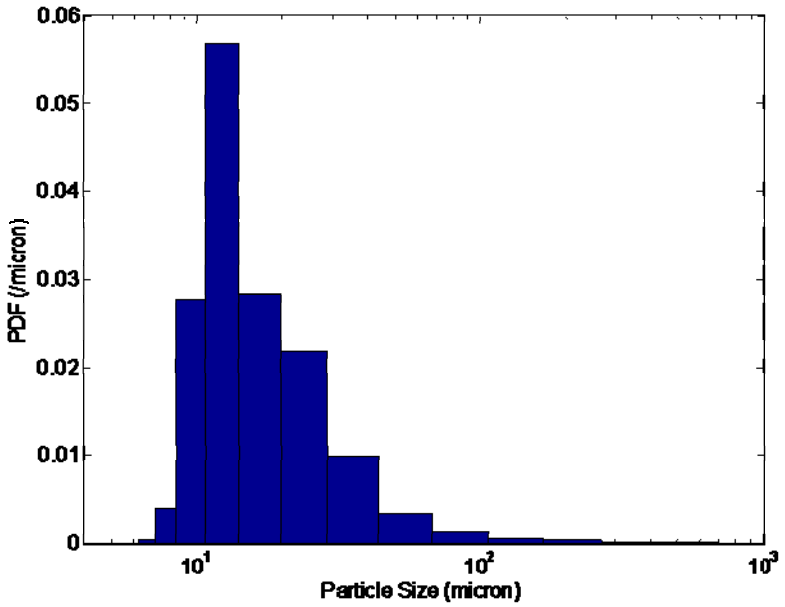

(a) 2 minutes

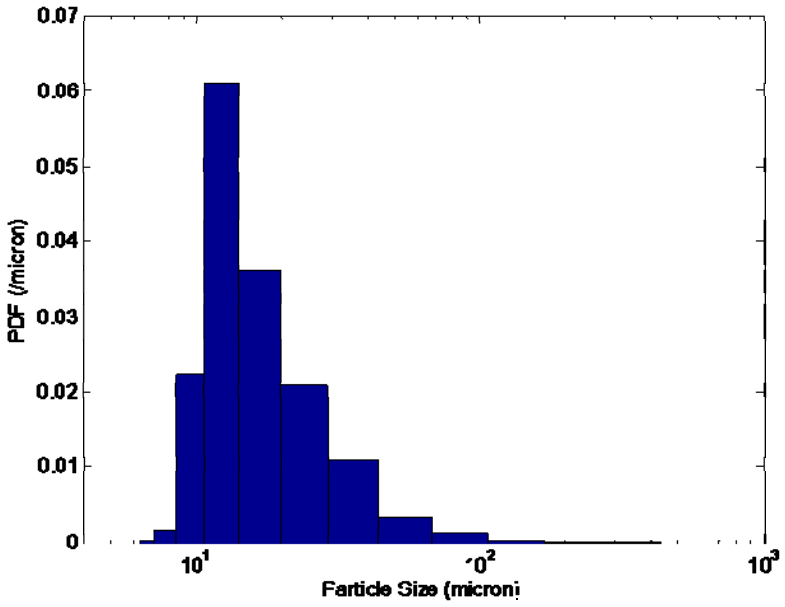

(b) 10 minutes

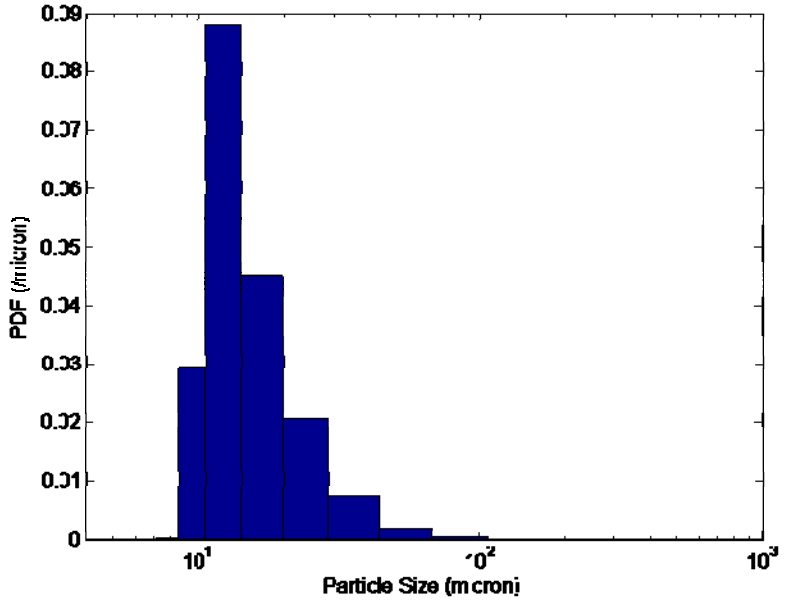

(c) 40 minutes

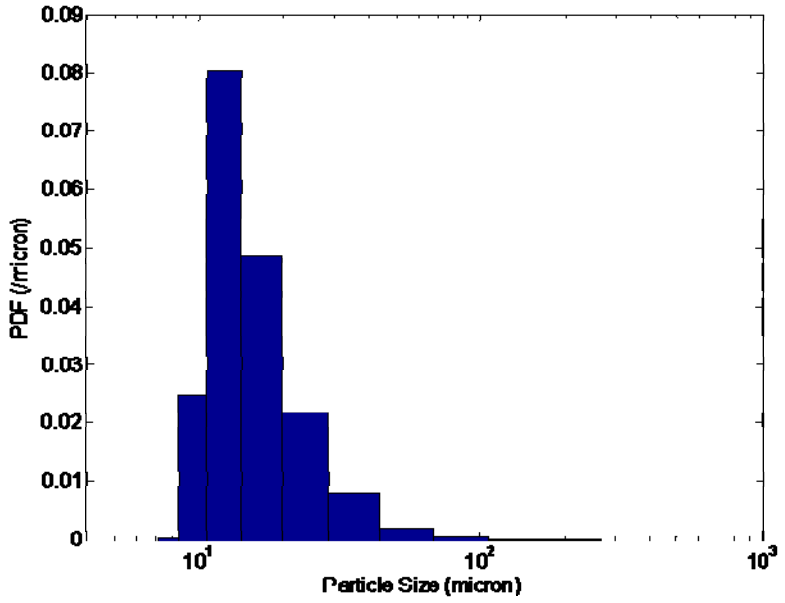

(d) 120 minutes

Figure 6-32: The PDF of plate shaped mannitol at 4000 rpm (3rd dimension is the width).

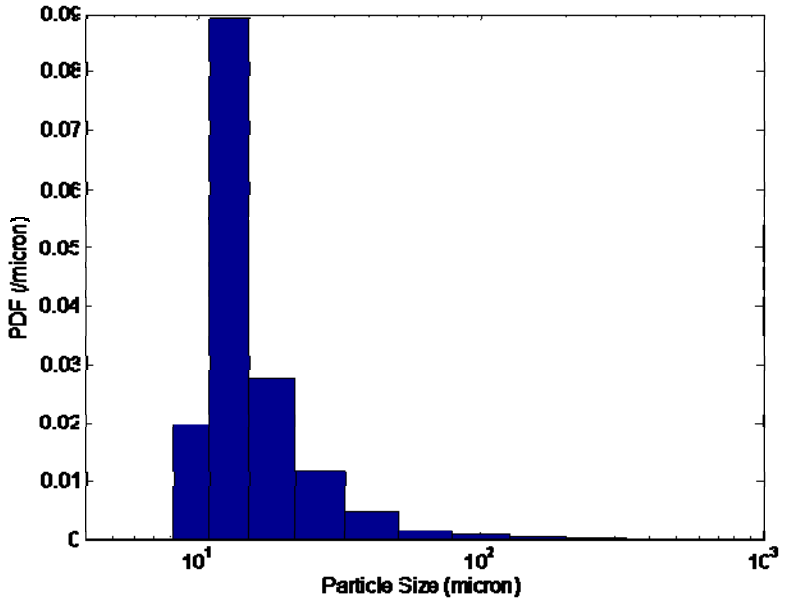

(a) 2 minutes

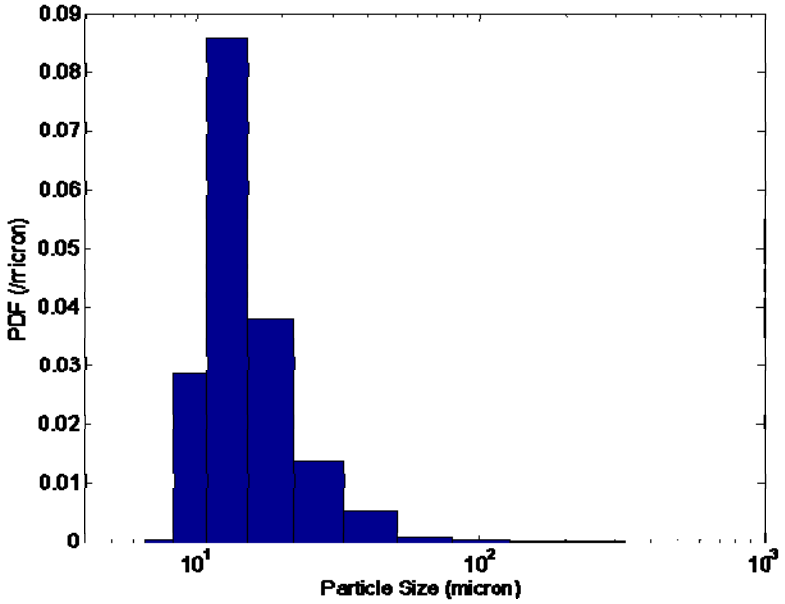

(b) 10 minutes

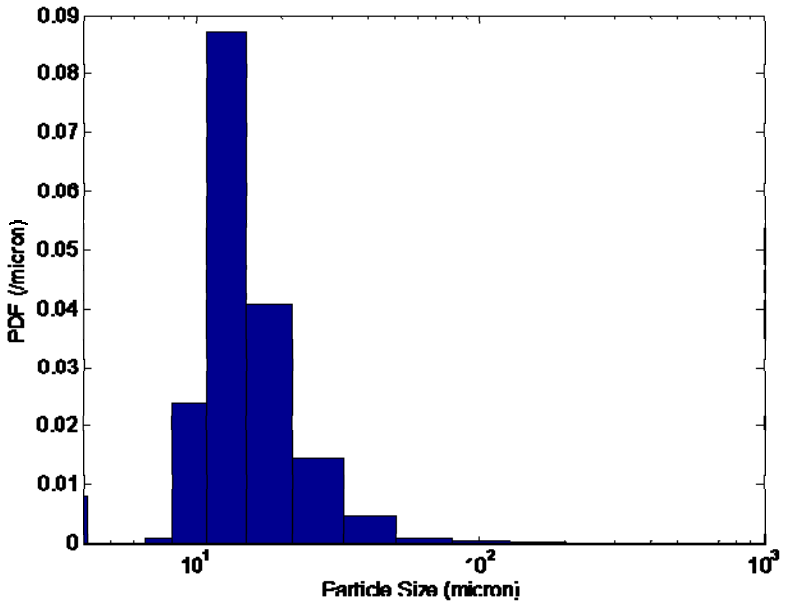

(c) 40 minutes

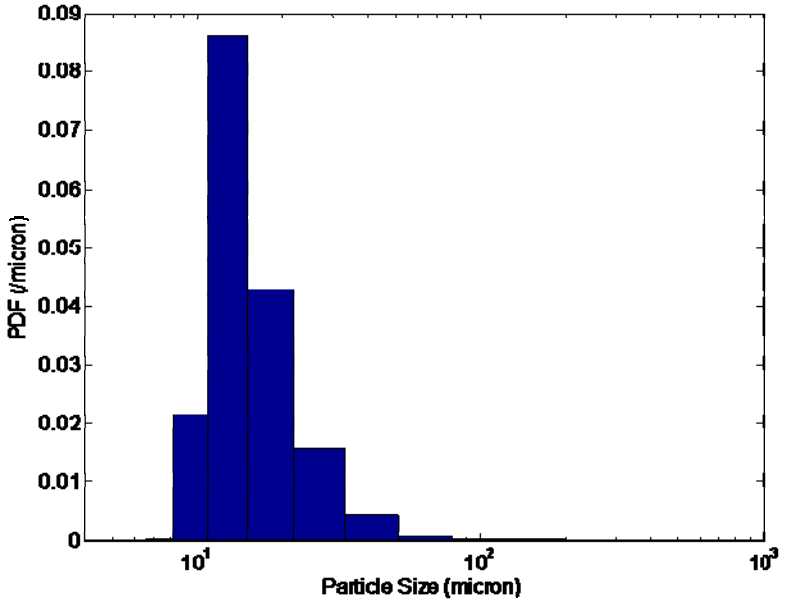

(d) 120 minutes

Figure 6-33: The PDF of plate shaped mannitol at 6000 rpm (3rd dimension is the width).

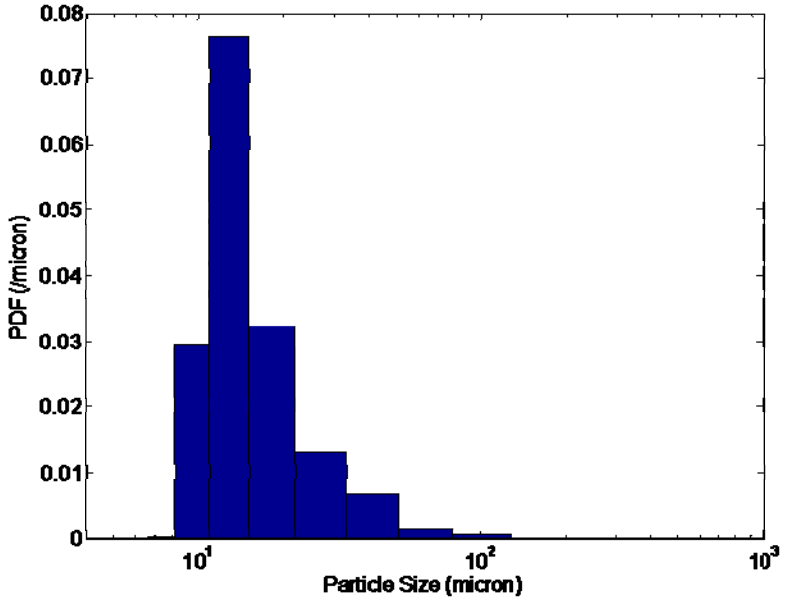

(a) 2 minutes

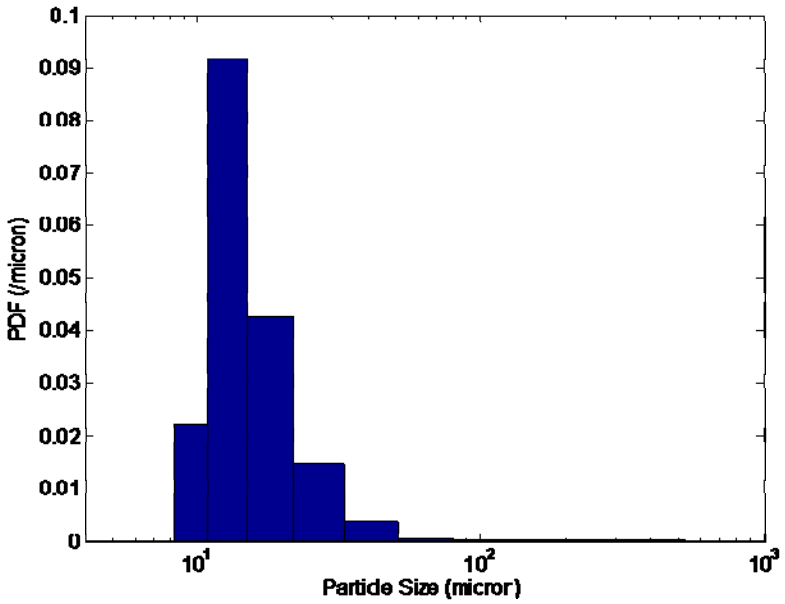

(b) 10 minutes

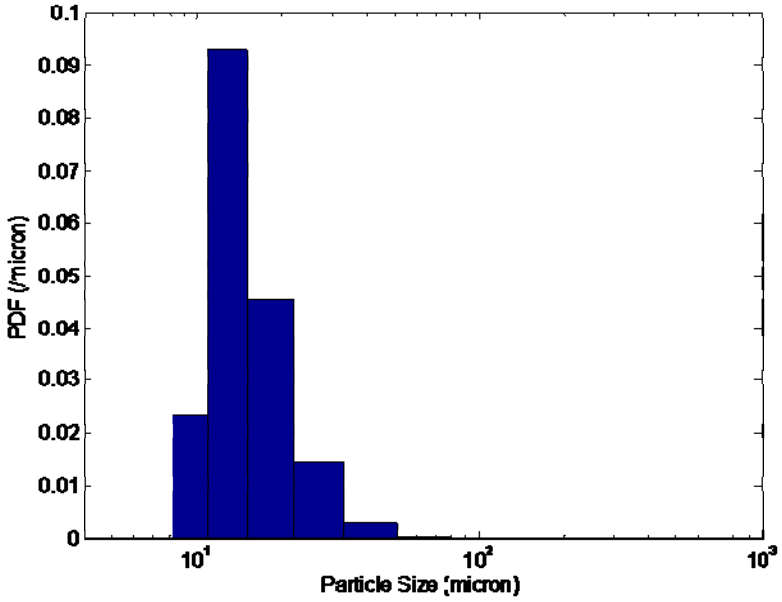

(c) 40 minutes

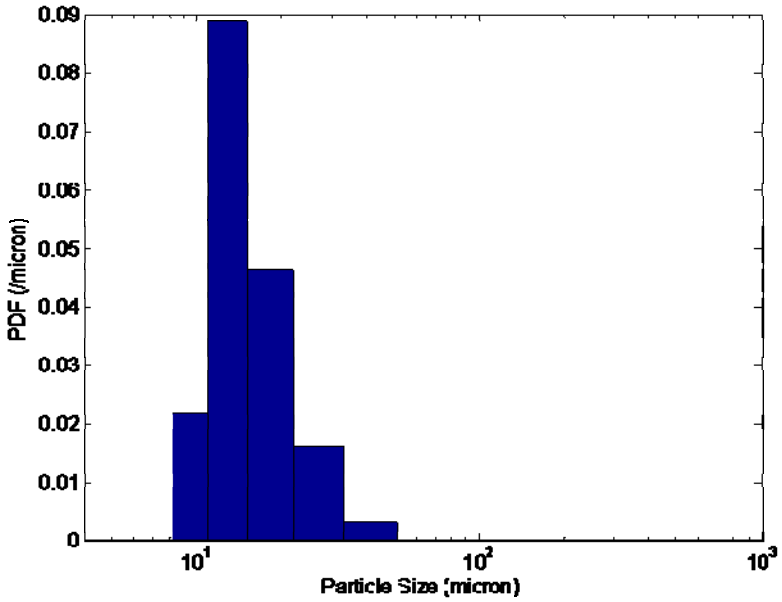

(d) 120 minutes

Figure 6-34: The PDF of plate shaped mannitol at 8000 rpm (3rd dimension is the width).

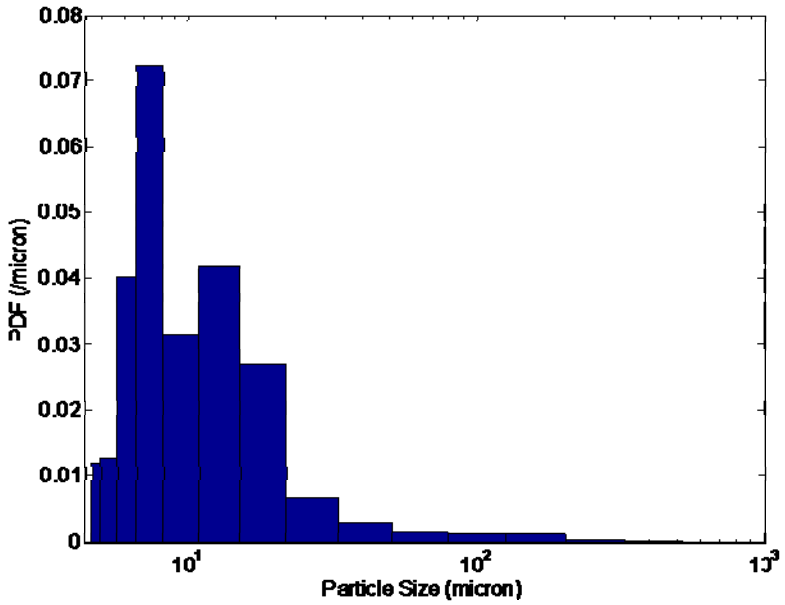

Figure 6-35: The PDF of initial plate shaped mannitol (3rd dimension is 1/4 of the width).

1/4 of the width as the 3rd dimension scale, it is also seen that the number of large particles decrease and the number of small particles increase when smaller 3rd dimension scale is selected.

The needle shaped mannitol samples removed at different time intervals at 4000, 6000 and 8000 rpm are shown as Figures 6-39, 6-40 and 6-41.

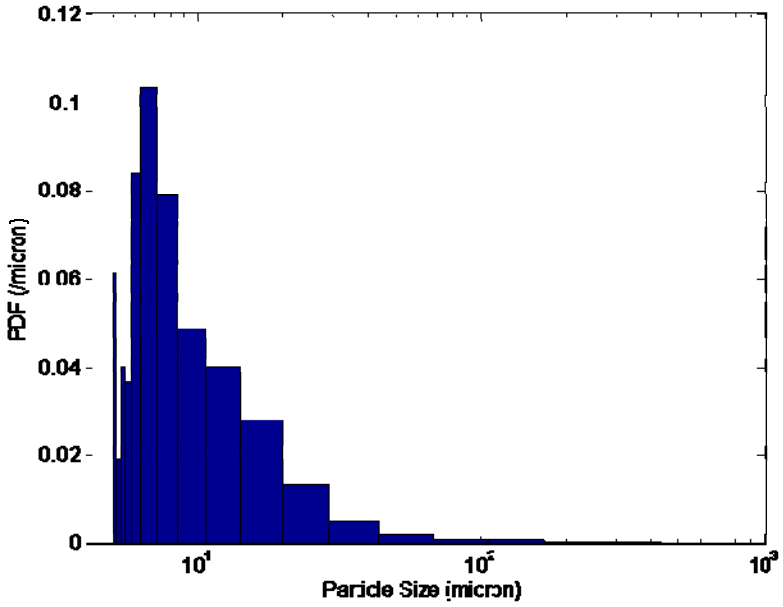

(a) 2 minutes

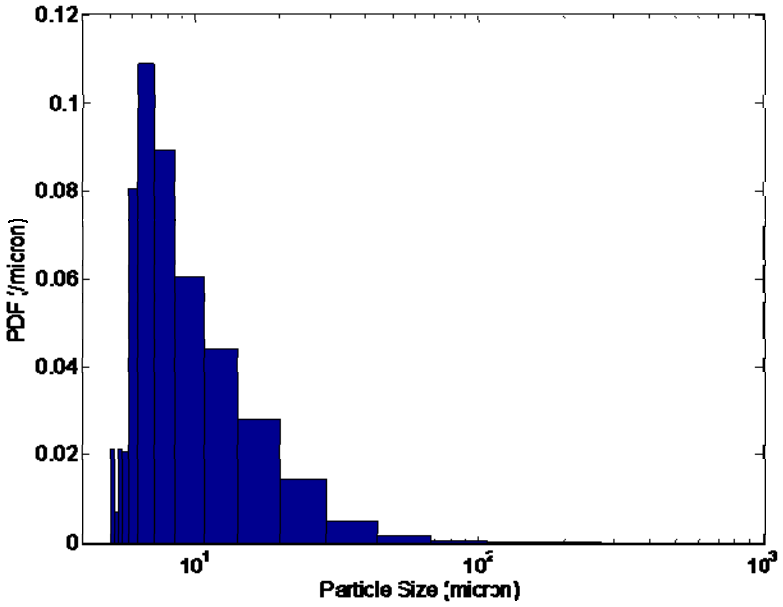

(b) 10 minutes

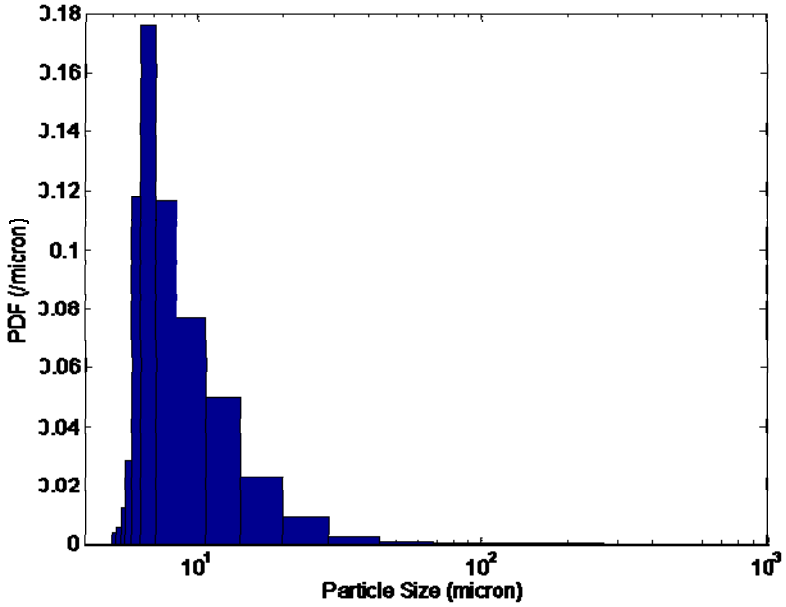

(a) 2 minutes

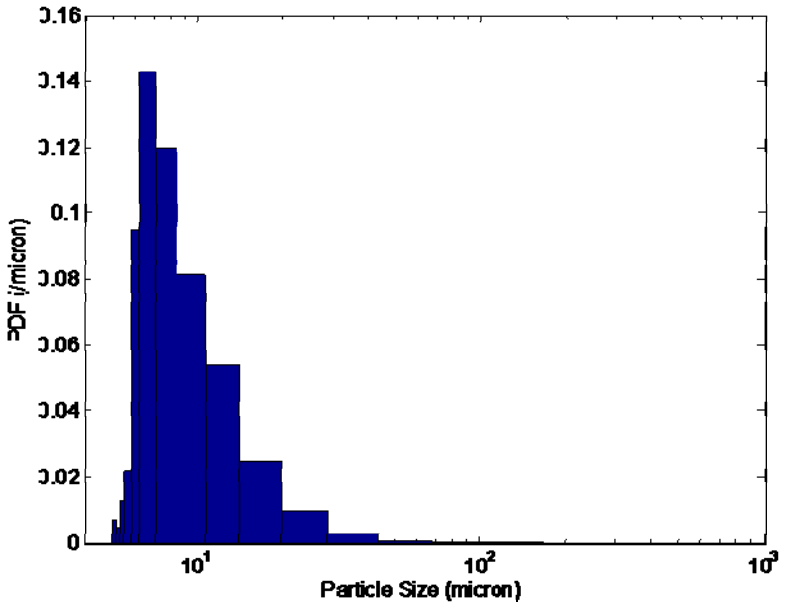

(b) 10 minutes

Figure 6-36: The PDF of plate shaped mannitol at 4000 rpm (3rd dimension is 1/4 of the width).

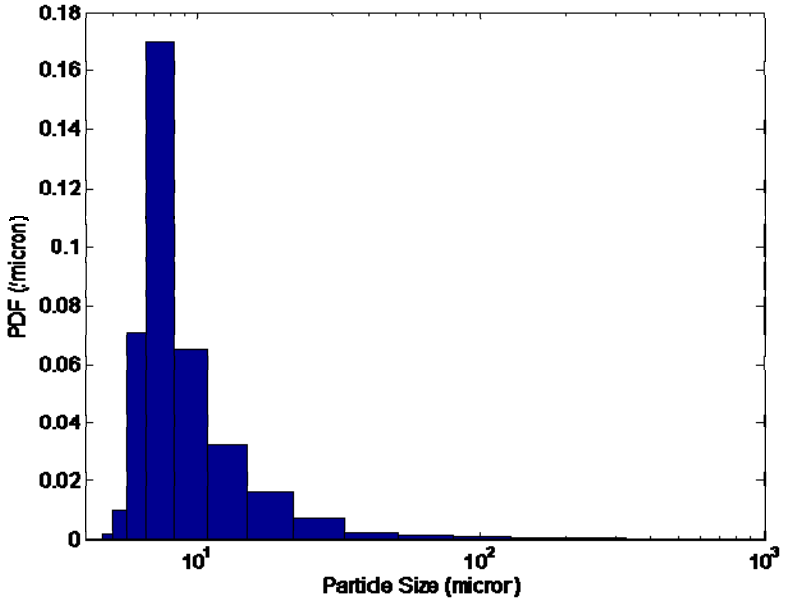

(a) 2 minutes

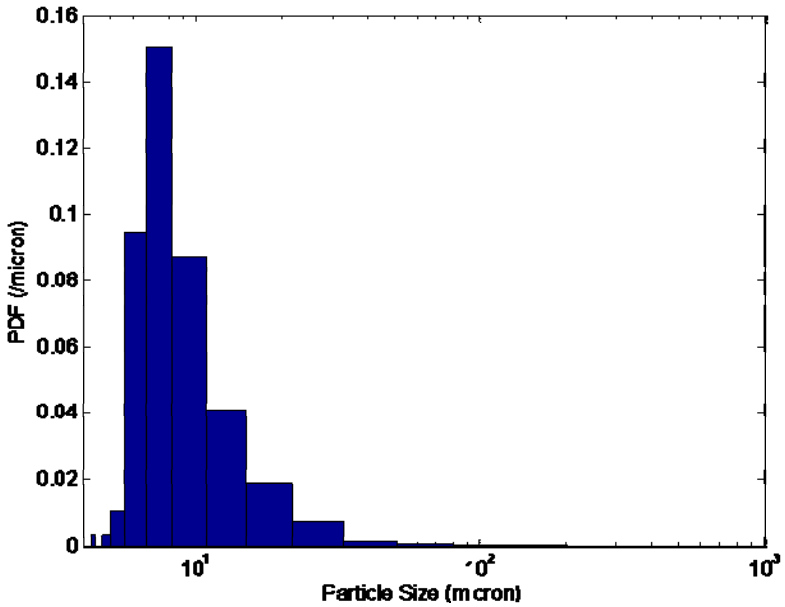

(b) 10 minutes

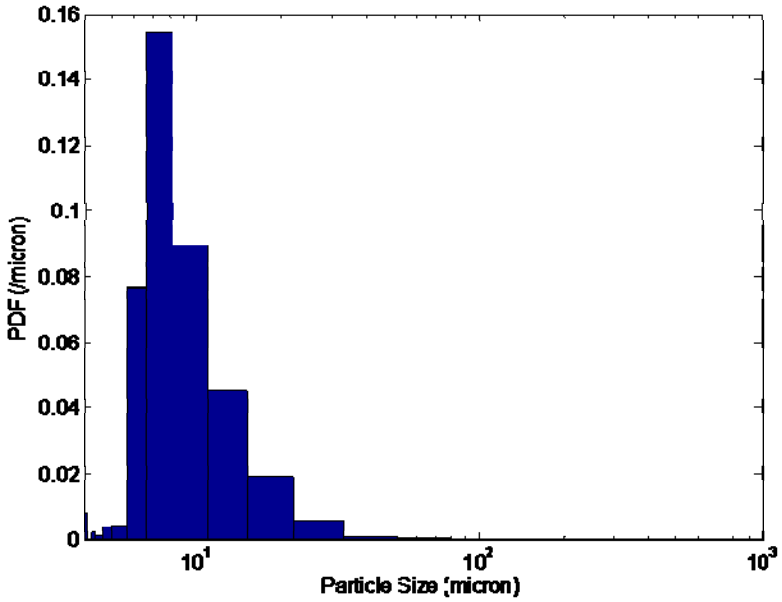

(c) 40 minutes

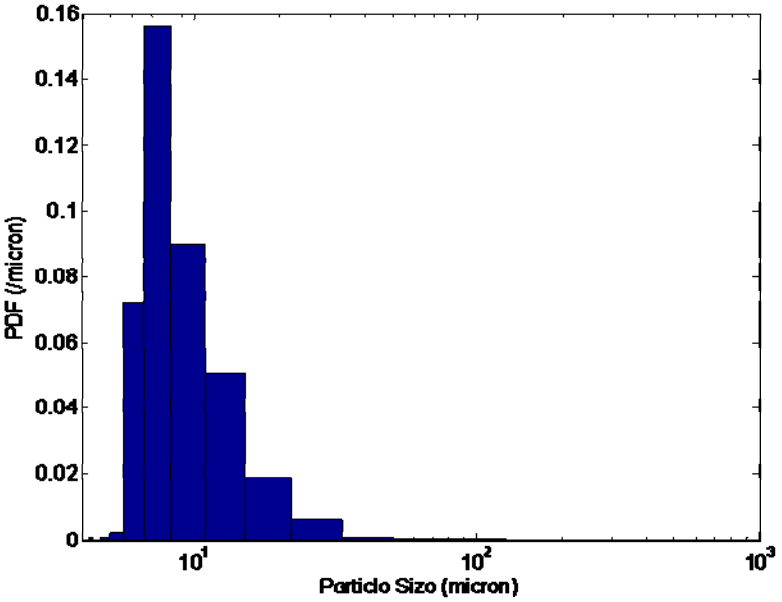

(d) 120 minutes

Figure 6-37: The PDF of plate shaped mannitol at 6000 rpm (3rd dimension is 1/4 of the width).

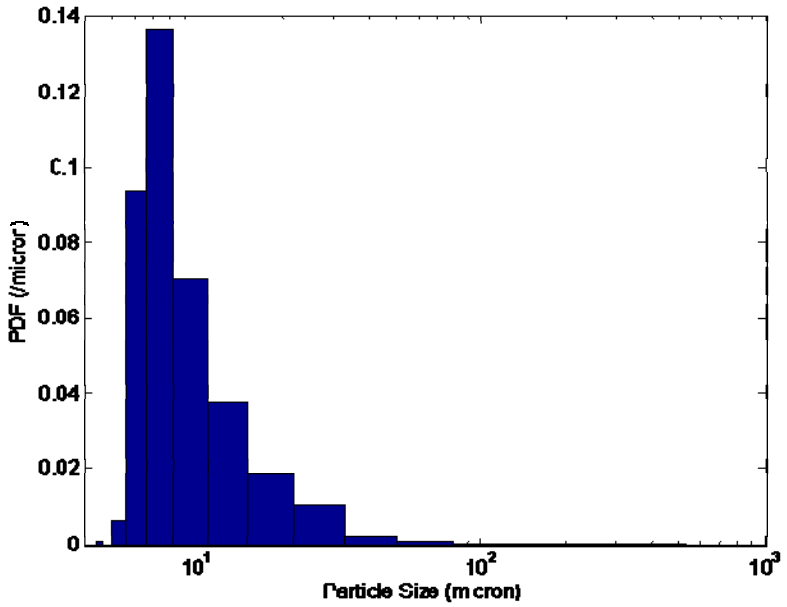

(a) 2 minutes

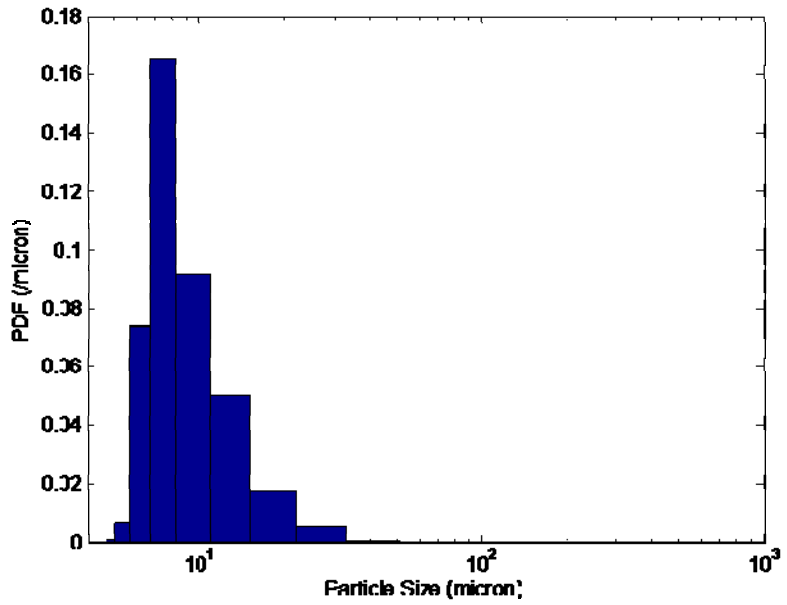

(b) 10 minutes

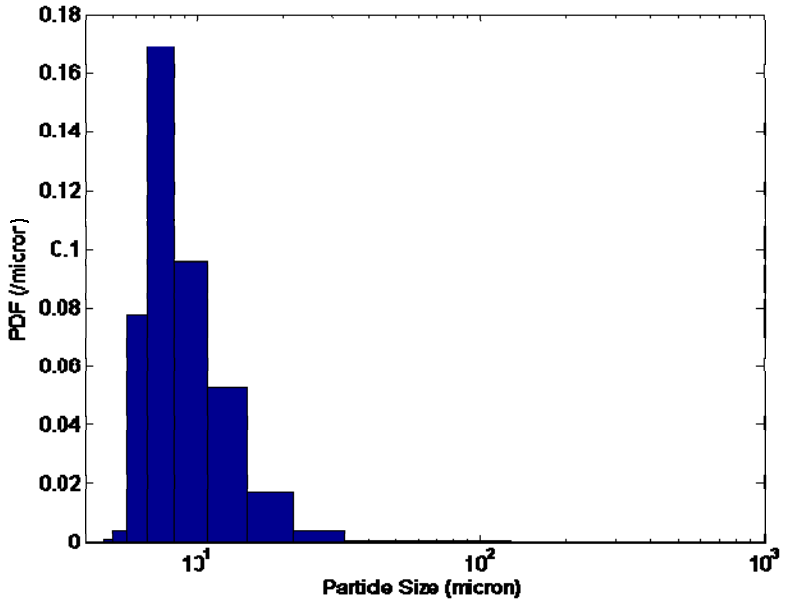

(c) 40 minutes

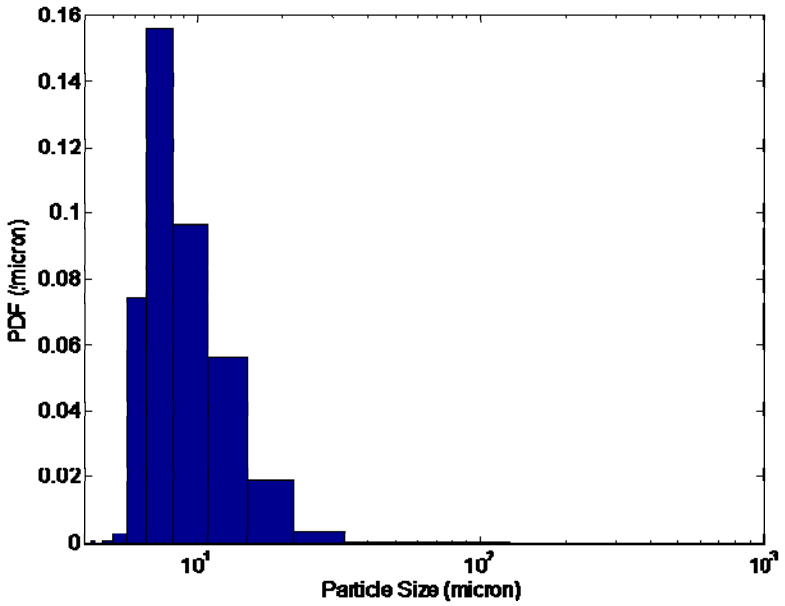

(d) 120 minutes

Figure 6-38: The PDF of plate shaped mannitol at 4000 rpm (3rd dimension is 1/4 of the width).

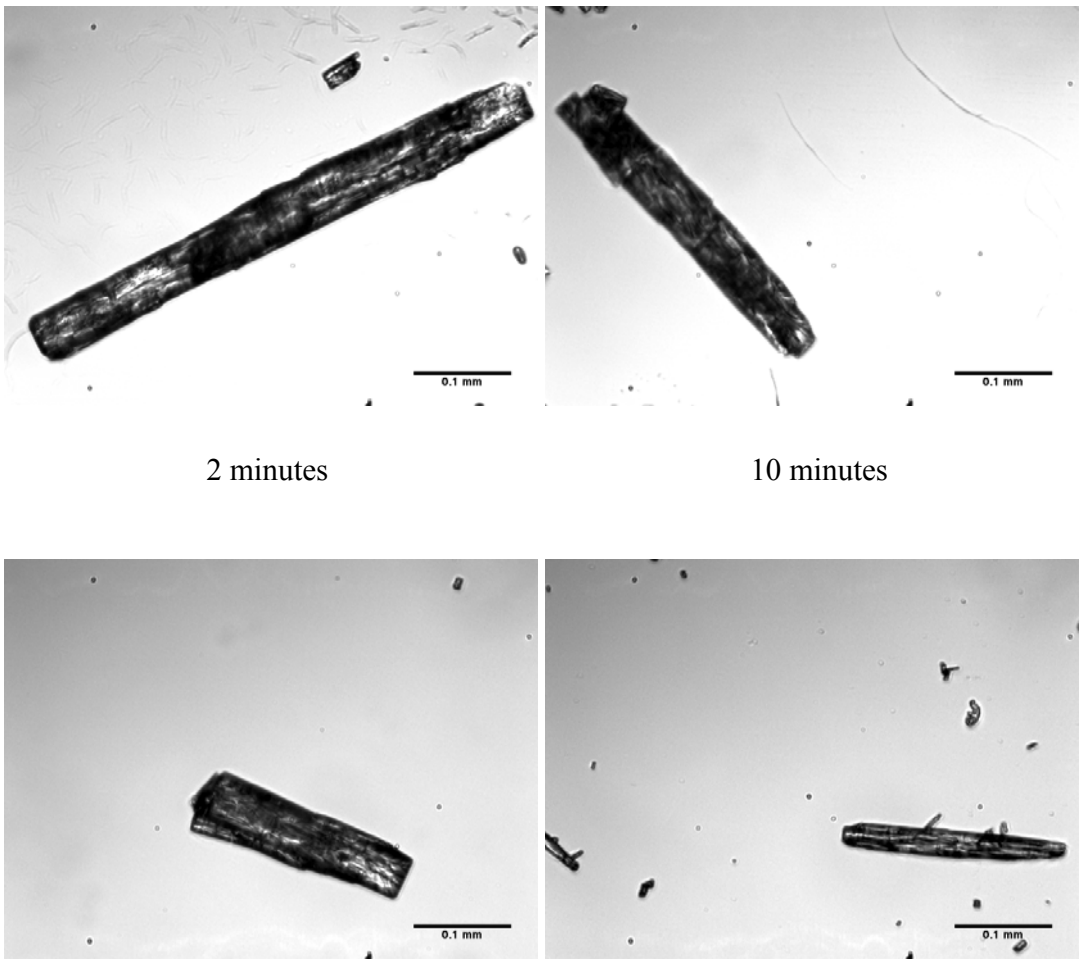

2 minutes 10 minutes

40 minutes 120 minutes

Figure 6-39: Needle shaped mannitol crystals removed at different times at 4000 rpm in the Silverson inline L4R rotor-stator mixer.

The needle shape mannitol crystal size reduction profiles with time at 4000, 6000 and 8000 rpm in the Silverson inline L4R mixer are shown in Figure 6-42. They show similar trends as the plate shaped mannitol crystals.

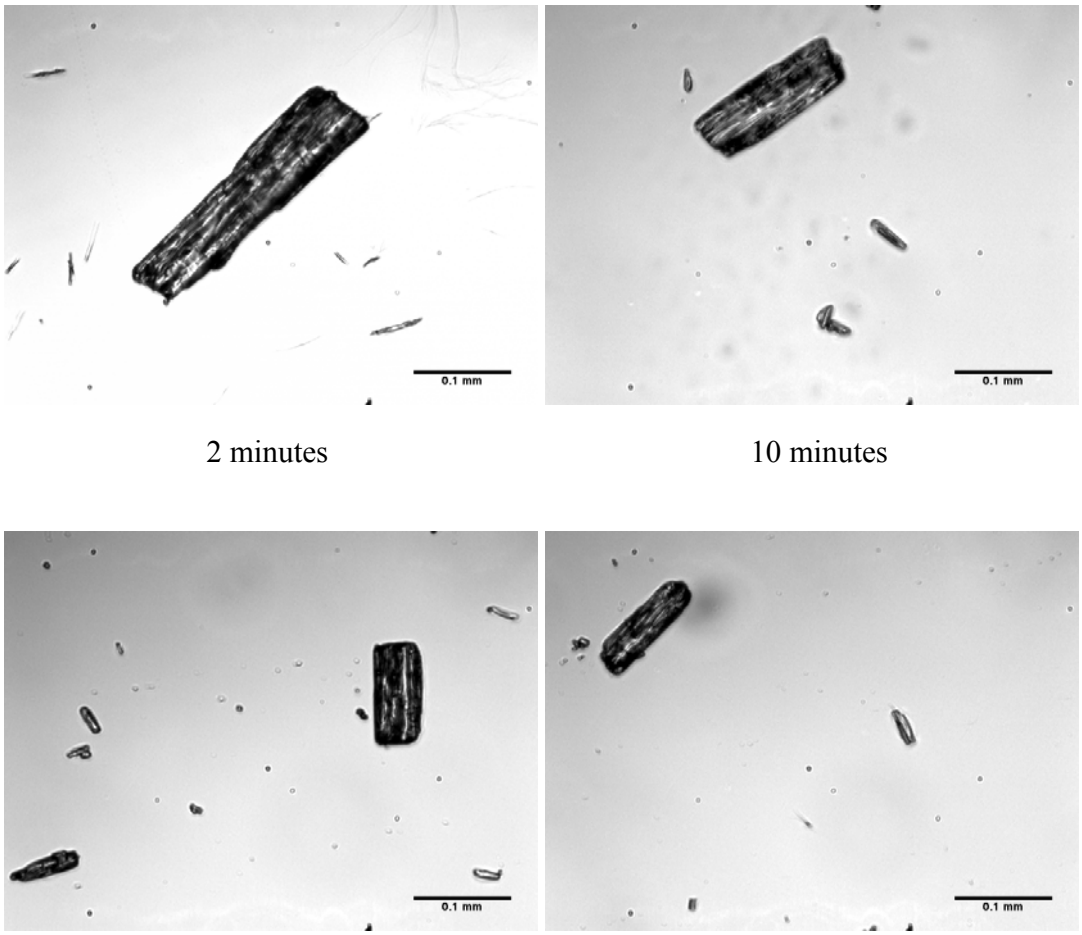

2 minutes 10 minutes

40 minutes 120 minutes

Figure 6-40: Needle shaped mannitol crystals removed at different times at 6000 rpm in the Silverson inline L4R rotor-stator mixer.

The PDF of initial needle shaped mannitol is shown in Figure 6-43. And the PDF at different time intervals at 4000, 6000 and 8000 rpm are shown in Figures 6-44, 6-45 and 6-46, respectively. From these figures, it is found that most of the PDFs exhibit similar trends. The reason for this result could be the mass fracture region of needle shaped mannitol is quite small. After 1 minute, the system transitions into the attrition region.

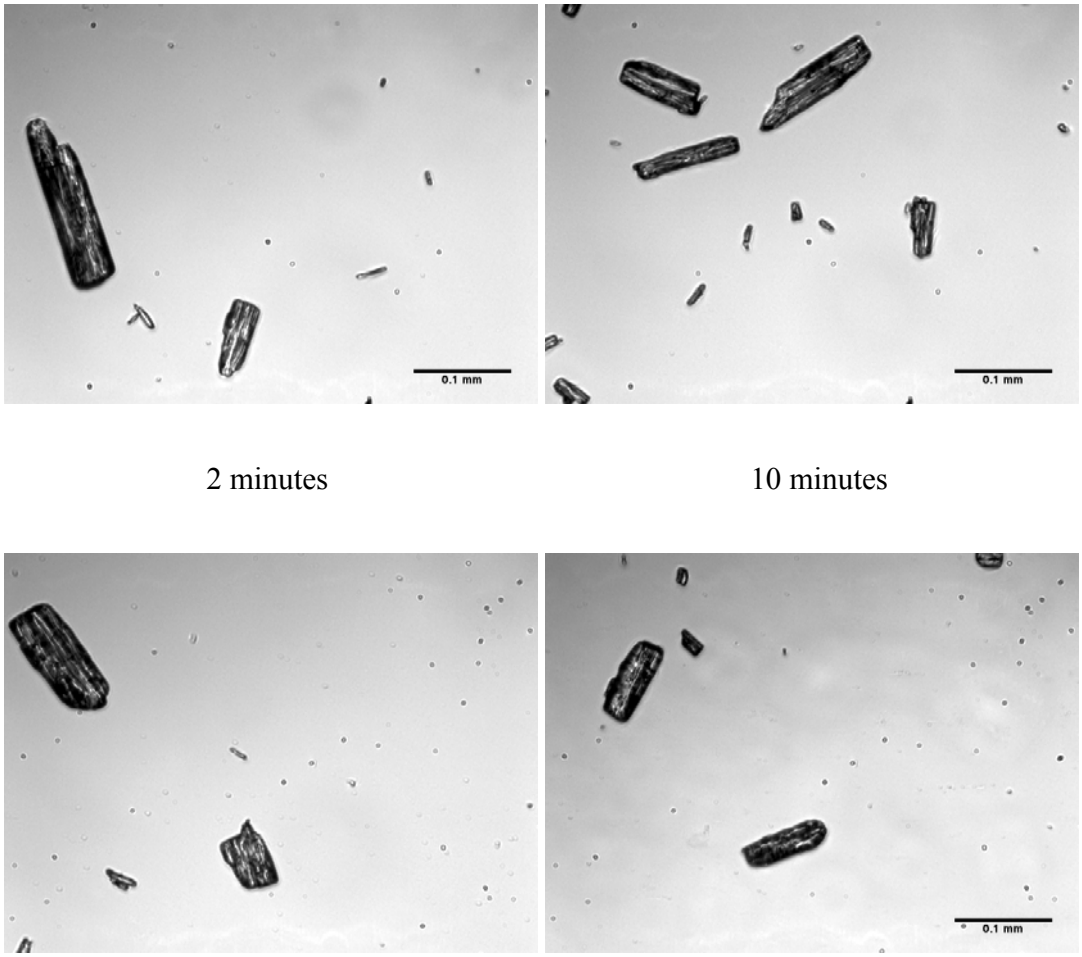

2 minutes 10 minutes

40 minutes 120 minutes

Figure 6-41: Needle shaped mannitol crystals removed at different times at 8000 rpm in the Silverson inline L4R rotor-stator mixer.

SE and power per mass of rotor swept volume, $\dot{\varepsilon}$, are shown in Table 6-4. It is found that SE and $\dot{\varepsilon}$ increase with rotation rate, which results in generation of smaller particles at higher rotation rate.

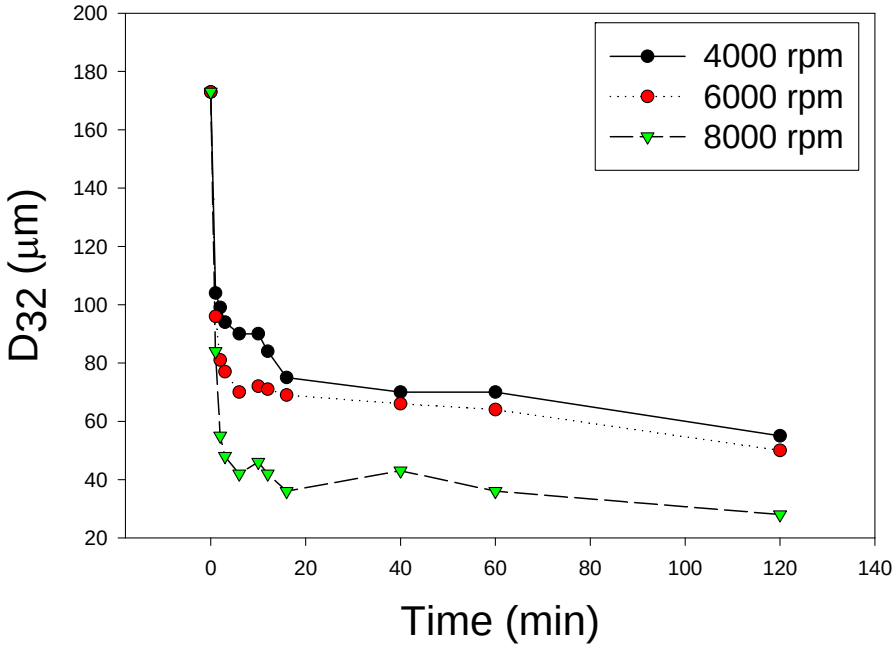

Figure 6-42: Needle shape mannitol crystal size reduction with time at 4000, 6000 and 8000 rpm in Silverson inline L4R rotor-stator mixer.

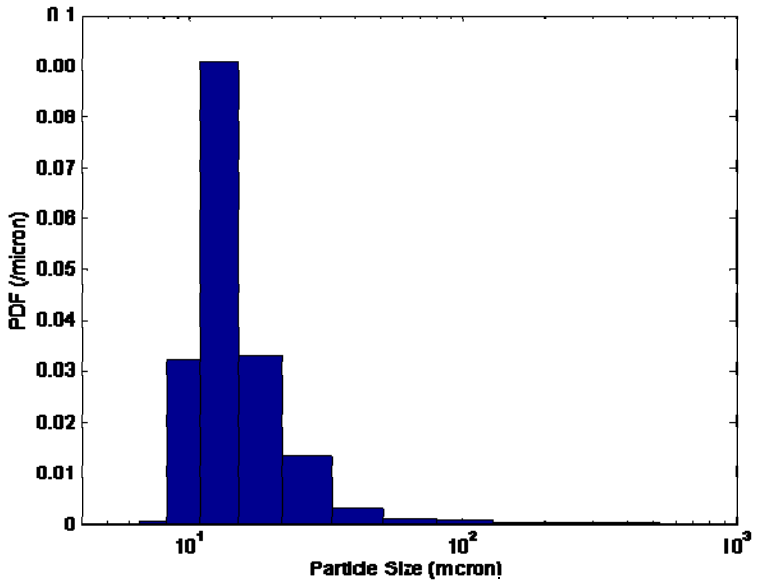

Figure 6-43: The PDF of initial needle shaped mannitol.

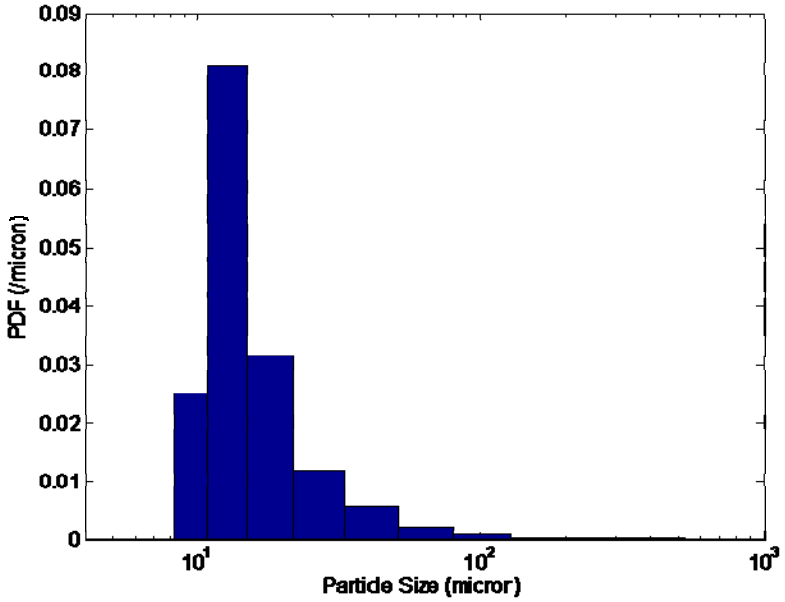

(a) 2 minutes

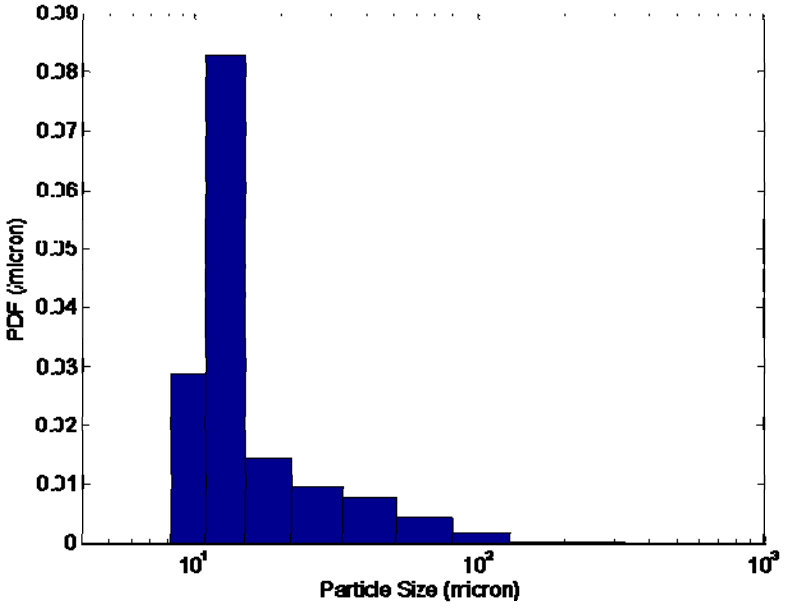

(b) 10 minutes

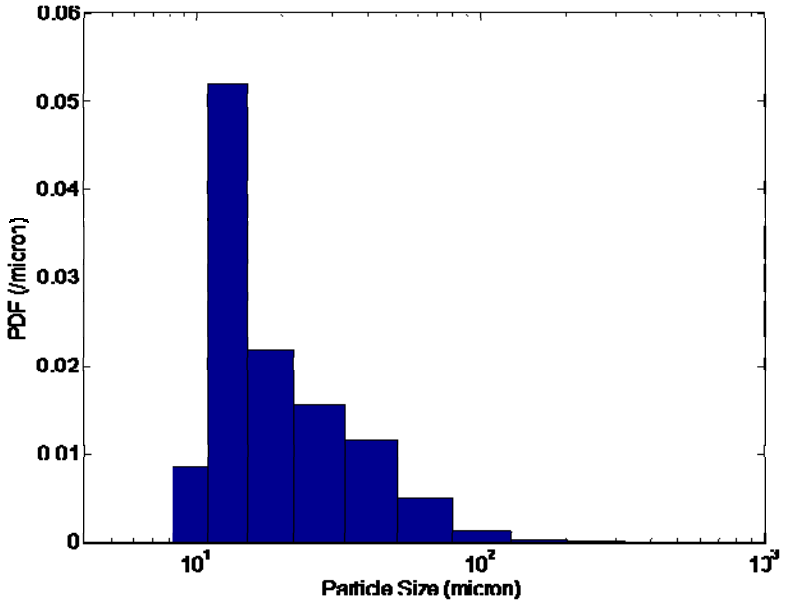

(c) 40 minutes

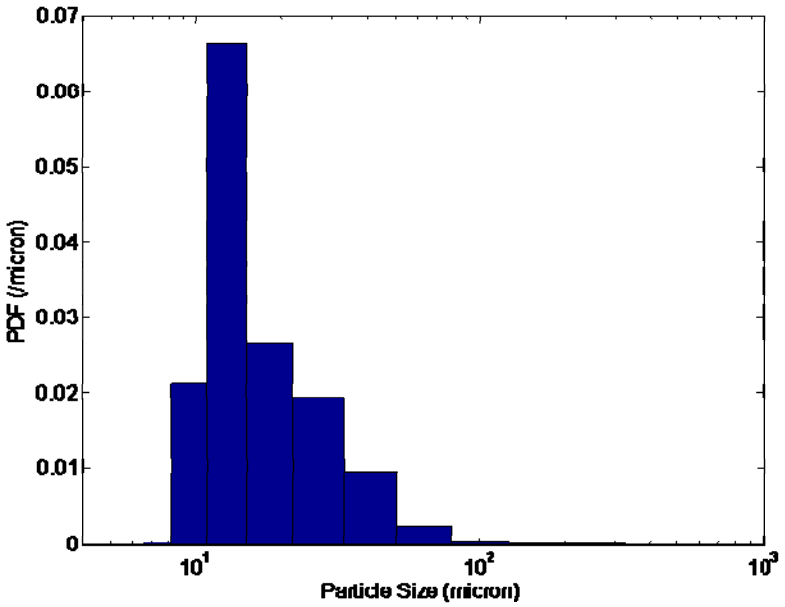

(d) 120 minutes

Figure 6-44: The PDF of needle mannitol at 4000 rpm.

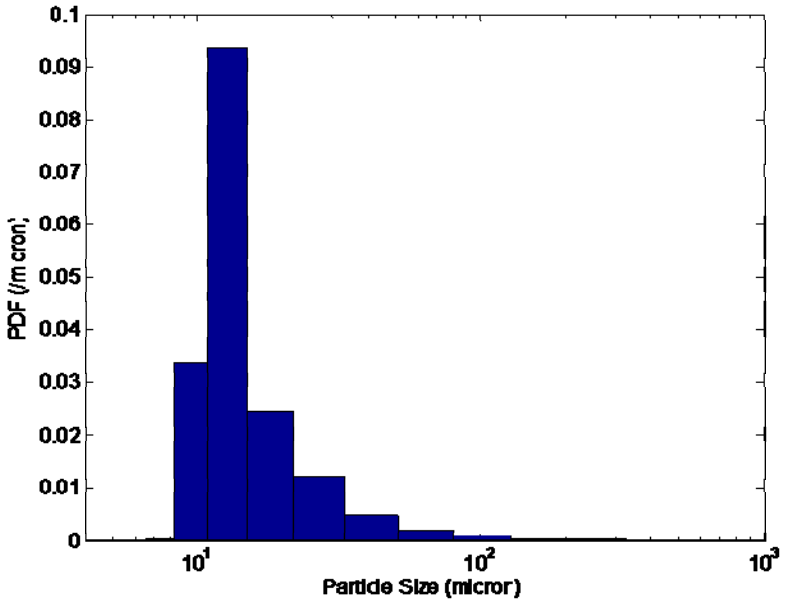

(a) 2 minutes

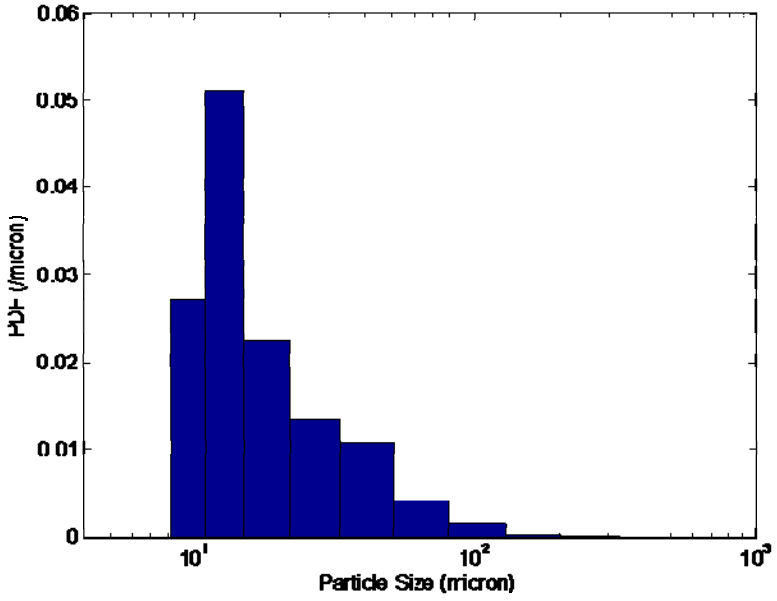

(b) 10 minutes

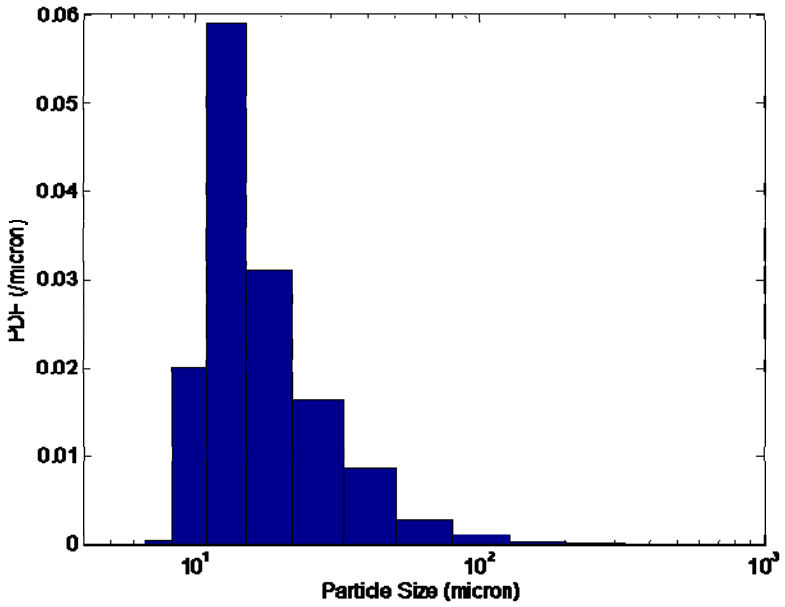

(c) 40 minutes

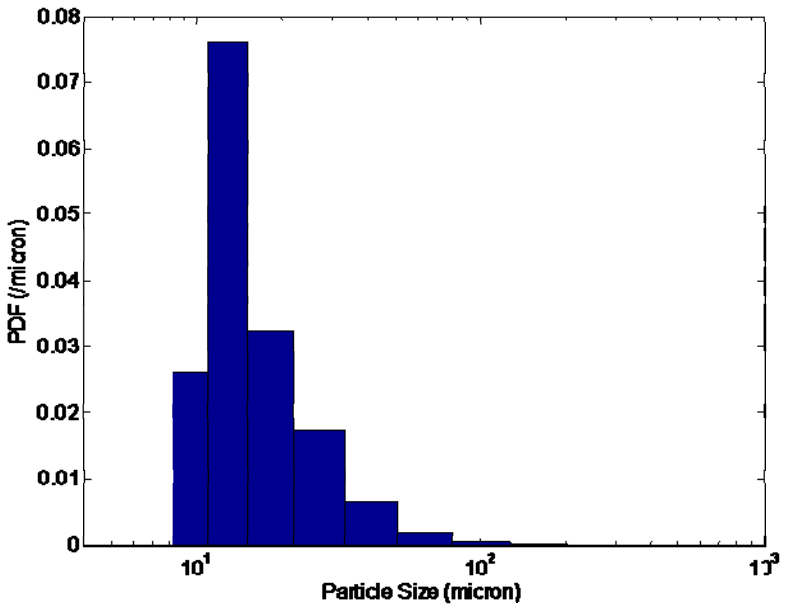

(d) 120 minutes

Figure 6-45: The PDF of needle mannitol at 6000 rpm.

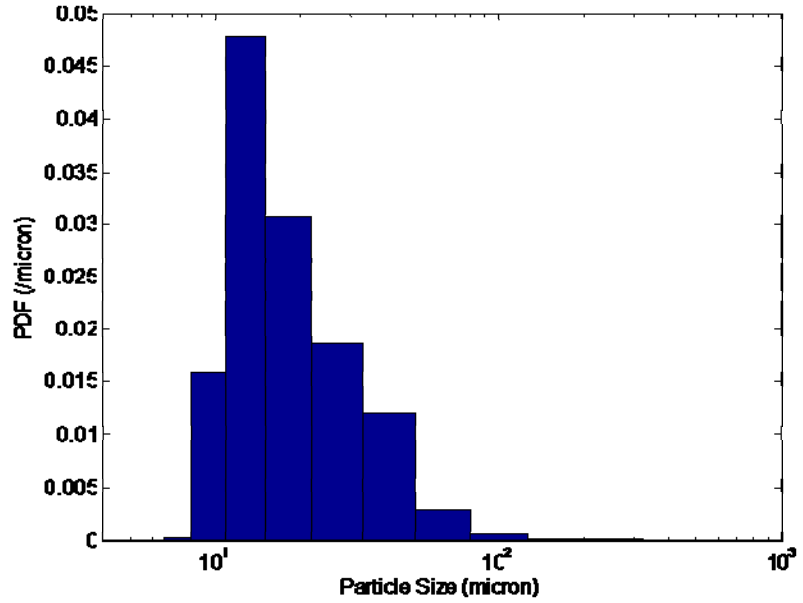

(a) 2 minutes

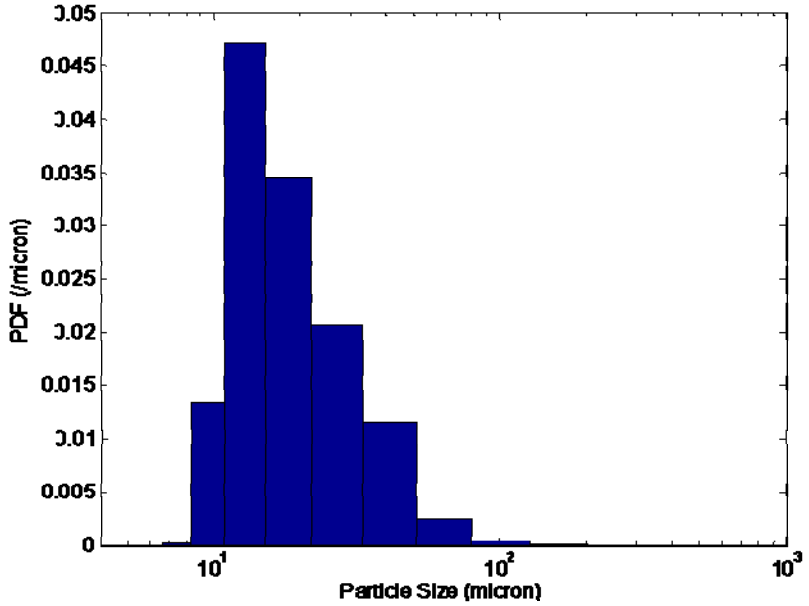

(b) 10 minutes

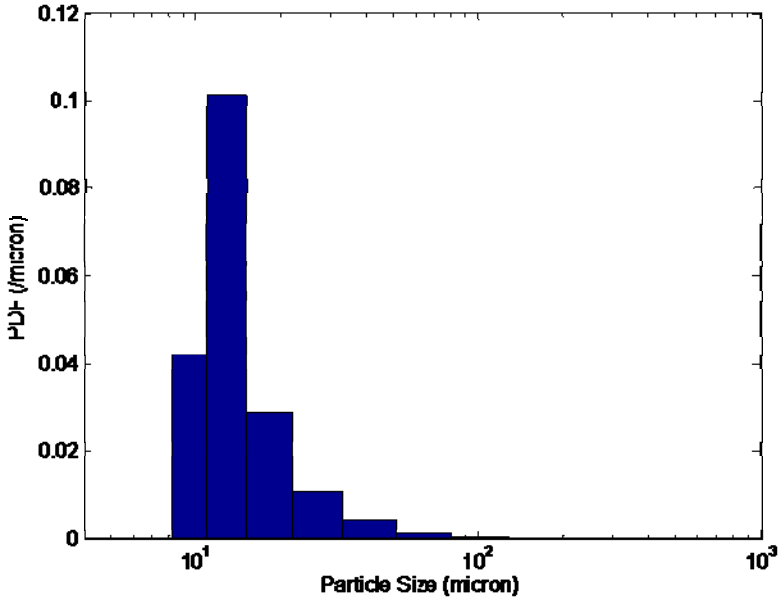

(c) 40 minutes

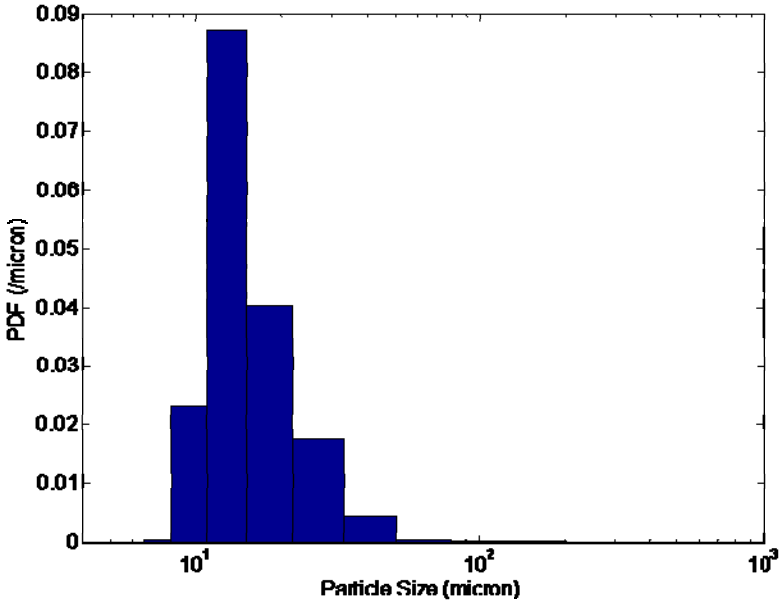

(d) 120 minutes

Figure 6-46: The PDF of needle mannitol at 8000 rpm.

Table 6-5: SE and $\dot{\varepsilon}$ at different rotation rate (wet milling of mannitol).

$\dot{\varepsilon}$ (J/kg)			SE (J/kg)		
4000 rpm	6000 rpm	8000 rpm	4000 rpm	6000 rpm	8000 rpm
2066	6971	16526	175	592	760

6.7 Summary

High shear wet milling is an important process in the chemical engineering industries. However, there are few publications on the performance of high shear wet milling process. To the author's knowledge, only two publications are found[23, 24]. In these papers, very crude experimental data are presented.

This chapter covers the wet milling of crystals in the Silverson inline L4R rotor stator mixer. The purpose of this chapter is to provide the preliminary experimental data at the bench scale and validate some results obtained in the CFD simulation.

Two crystal-antisolvent systems are investigated: sucrose in isopropyl alcohol; and mannitol in ethyl alcohol. The experiments were performed at 4000, 6000 and 8000 rpm. Both free pumping and controlled flow rate conditions were considered. Two distinct regions representing different wet milling mechanisms, a mass fracture region and an attrition region, are found in all experiments. In the mass fracture region, crystal size decreases significantly with time while the size reduction in the attrition region is comparatively slow. For the free pumping case, it is found that the crystal size decreases with rotation rate. The same conclusion is also drawn when the flow rate is kept constant. Moreover, in the CFD simulation in Chapter 5, it was found that

in different scale Silverson inline mixers, the flow rate significantly differs for free pumping. To investigate whether the flow rate plays an important role in wet milling experiments, wet milling of granulated sucrose with constant rotor tip speed (at 8000 rpm) were performed at 6.8, 5.3 and 3.8 L/min inlet flow rates. It was found that the crystal size increases with increasing flow rate. The reason could be that at smaller flow rates, the particles exhibit longer residence time which leads to smaller particles. In addition, the flow rate of Silverson inline L4R mixer was measured at the free pumping condition and compares favorably with the L4R simulation results of chapter 5. From the experiments, it is found that the flow rate plays an important role in the high shear wet milling process. Therefore, during the scale up of a high shear wet mill, the flow rate per stator slot has to be kept constant in addition to the nominal shear rate (tip speed).

Chapter 7: Summary, Conclusions and Recommendations

This chapter presents the summary and conclusions from this research as well as recommendations for future work. There are many conclusions drawn from this research. However, the most important conclusion is that CFD can be applied to aid the scale up process and provide insight into the fundamental physics of flow occurring in rotor-stator mixers.

7.1 Summary of RANS simulation of Silverson L4R batch rotor-stator mixer

The flow in a Silverson L4R batch rotor-stator mixer was modeled by commercial CFD software Fluent. Mesh independence tests were performed to determine the mesh density for the simulation. During the simulation, it is found it will take quite a long computational time to get a converged flow field based on current computational resources by the sliding mesh method. To obtain the converged flow field in reasonable time, a hybrid technique was developed. Macroscopic properties are predicted by the hybrid simulation. Mean velocity field, turbulent fields and deformation rate fields are also investigated at 4000 and 6000 rpm. Tracer particles were introduced into the converged flow field at 4000 and 6000 rpm and the trajectories were predicted by our in-house fast particle tracking model. PIV experiments were performed to validate the flow patterns at 4000 rpm.

7.1.1 Conclusions

- This research demonstrated the feasibility to perform practical CFD simulations in Silverson L4R batch rotor-stator mixers using the widely available commercial CFD code Fluent.
- Mesh independence tests were conducted and a 4.6 million mesh was found to be enough for the simulation.
- Sliding mesh model was used to account for the strong interaction between the rotor and stator.
- Because of the low pumping capacity of the Silverson L4R batch mixer, it will take unaffordable time to obtain the converged flow field by sliding mesh only. A hybrid technique was developed to get a converged flow field in reasonable time, which uses sliding mesh model where the interaction between the rotor and stator is strong, and uses an MRF model where the interaction is weak.
- Predicted power numbers compare favorably with experiment results.
- Predicted pumping numbers appear to be reasonable.
- The predicted mean flow fields show that in the rotor region, fluid moves in an anti-clockwise direction while in the bulk of the mixer fluid flows in the clockwise direction.
- In each stator slot, a strong jet is generated and fluid close to the stator slot outlet is sucked into the slot due to low pressure behind the blade. As a result, vortices are generated.

- The fluid enters the rotor zone from bottom and top, and then it is pumped out of the stator slots radially. Therefore, there are vortices generated behind the rotor blades.
- There are four jets formed in the bulk of the flow. They are also found by full sliding mesh and steady MRF simulation , which confirm that the 4 mid-plane jets are not an artifact of initial CFD conditions.
- The flow fields at different locations in the mixer suggest that the fluid dynamics in a Silverson L4R batch mixer is very complicated and highly 3 dimensional.
- The high TKE, TDR and high shear regions exist in the rotor swept volume and close to the stator slot openings. Most of the turbulent energy is dissipated in the region close to the mixing head.
- The predicted trajectories of tracer particles by a fast particle tracking code shows the deformation rate history experienced by particles in reasonable time.
- Crude PIV experiments confirm the existence of the mid-plane jets. While somewhat disappointing, the data show qualitative agreement with predictions and demonstrate that calculated pumping capacities are within reason.
- From the results of tracer particle movements in the mixer, it is found that the number of pass through the mixing head varies significantly among the particles. It may suggest that Silverson L4R batch rotor-stator mixer is very difficult to scale up.

7.2 Summary of RANS simulation of Silverson inline rotor-stator mixer at lab, pilot and plant scale

CFD simulation of the flow in Silverson inline L4R (lab scale), 450LS (pilot scale) and 600LS (plant scale) mixers was performed. The mesh for these three mixers was prepared by an automated mesh generation technique by Harpoon, in conjunction with Gambit and Tgrid (Fluent). Currently, constant nominal shear rate is used as the scale up criteria for high shear mixers. Therefore, the rotation rates of Silverson L4R, 450LS and 600LS were set as 8000, 2100 and 1575 rpm respectively, so that the tip speed is the same, 12.6 m/s, for the 3 mixers. Since the gap width is constant, the nominal shear rate is also the same. In addition, the simulation of Silverson inline L4R mixer was also performed at 4000 rpm to investigate the rotation rate effect. Macroscopic properties are predicted and compared with experimental results for power draw and flow rate data. Mean velocity field, turbulent field and deformation field of the 3 different scale mixers are also investigated and compared.

7.2.1 Conclusions

- An automated mesh generation technique was developed by use of Harpoon, Gambit and Tgrid, which creates a three dimensional hex dominant mesh with acceptable quality and enables the user to build satisfactory mesh for complicated geometries in reasonable time.
- Sliding mesh model has the capability to predict the complex flow in Silverson inline high shear mixers.

- Predicted power numbers and flow numbers of Silverson inline L4R mixer compares favorably with experiment results. Those of Silverson inline 450LS and 6000LS mixers appear to be reasonable.
- The predicted mean flow fields show that in the rotor region fluid moves in clockwise direction while outside the stator head fluid flows in anti-clockwise direction.
- The fluid enters the rotor from the bottom and top, and is pumped rapidly out of the stator from the side. Therefore vortices between the rotor blades are generated in the vertical plane.
- A strong jet generated in each stator slot is always close to the downstream edge of the stator slot. Outside the stator slots, some fluid is driven to enter the openings and then go into the rotor zone. Therefore, a vortex is generated in each stator slot.
- Normalized mean flow fields of Silverson inline L4R mixer at 4000 and 8000 rpm are quite similar to each other.
- High TKE, TDR and shear regions exist in the rotor swept volume and close to the stator slot openings. The majority of the turbulent energy is dissipated in the mixing head region.
- The mean velocity field, turbulent field and deformation filed of Silverson inline 450LS and 600LS mixers are quite similar. However, they are significantly different from the Silverson inline L4R bench scale mixer. This makes it difficult to scale up from the laboratory to the pilot scale.

- Considering tip speed alone may be ok to scale up from pilot scale to plant scale. But it could lead to a significant discrepancy to scale up from lab scale to pilot scale.
- Beside constant nominal shear rate, scale up of high shear mixers may require an equal flow rate per slot and power per slot, as well.

7.3 Summary of wet milling of crystals in Silverson L4R inline rotor-stator mixer

Wet milling experiments were conducted at 4000, 6000 and 8000 rpm to provide the experimental data in the bench scale Silverson inline L4R rotor-stator mixer. Two crystal-solvent systems were investigated: sucrose and isopropyl alcohol; mannitol and ethyl alcohol. Video microscopy was used to record the crystal sample removed at different times. After that, these images were analyzed by an automatic particle size analysis program developed in ImageJ. The effects of rotation rate and flow rate on the wet milling process were investigated. In addition, the flow rate at different rotation rate was measured and compared with simulation results.

7.3.1 Conclusions

- Silverson inline L4R rotor-stator mixer is a reasonable wet milling apparatus, which can reduce the crystal size significantly in a short time.
- Two distinct regions, mass fracture region and attrition region, representing different wet milling mechanisms, are found in all experiments.
- The crystal size decreases with rotation rate at free pumping conditions.

- The crystal size decreases with rotation rate when the flow rate is kept constant.
- The flow rate has a significant effect on the wet milling performance. When the rotation rate is kept constant, the crystal size increases with flow rate.
- To obtain consistent results in a different scale high shear mixer, the criteria may be that both the nominal shear rate and flow rate per slot have to be kept constant.

7.4 Recommendations

- In this research, all the flows are turbulent. However, laminar flow at low Reynolds number in high shear mixers is also very important. Therefore, CFD simulation of laminar flow in high shear mixers will help in understanding the fundamental physics of high shear phenomena.
- The turbulent flow in high shear mixers is very complicated. Especially close to the mixing head, the flow may not be completely isotropic. Hence Reynolds Stress Model and LES will help to explain the turbulent field.
- The PIV experiments in this research are very crude. An accurate PIV experiment will contribute to understanding the performance of Silverson mixers.
- In this work, the wet milling experiments are performed at bench scale only. Experiments at larger scale high shear mixers would validate the conclusion drawn in this research and provide insight into the scale up mechanism of Silverson inline rotor-stator mixers.

- The computational expense of particle tracking is significant, since tracking must be carried out for tens of thousands of rotor revolutions. The fast particle tracking code needs to be parallelized to reasonably accomplish this task.

Glossary

$\vec{A}$ surface area vector

$\vec{A}_f$ area of face *f*, m^2

C_D drag coefficient

$C_{1\varepsilon}$ constant in *k*-ε closer equation

$C_{2\varepsilon}$ constant in *k*-ε closer equation

C_μ constant in *k*-ε closer equation

D diameter of the rotor, m

d_p particle diameter, m

$\vec{g}$ gravitational acceleration, m/s^2

k turbulent kinetic energy, m^2/s^2

k_P turbulent kinetic energy at point *P*

N number of faces enclosing the controlling volume

N rotation rate, rps

N_P power number

N_ϕ pumping number

n unit vector norm to the wall

P instantaneous pressure, Pa

P power, W

$\overline{P}$ mean pressure, Pa

p	pressure, Pa
Q_v	pumping capacity, m^3/s
Re	Reynolds number
S_{freq}	shear frequency
S_ϕ	source of ϕ per unit volume, $/m^3$
$\overline{\overline{S}}$	rate-of-strain tensor, /s
T	torque, N·m
t	time, s
$\vec{U}$	velocity vector, m/s
U_i	instantaneous fluid velocity in the i^{th} direction, m/s
$\overline{U}_i$	mean fluid velocity in the i^{th} direction, m/s
U^*	dimensionless mean velocity
V	cell volume, m^3
V_f	fluid velocity, m/s
V_{tip}	rotor tip speed, m/s
$\vec{v}$	fluid velocity vector, m/s
$\overline{X}_p$	particle coordinate, m
x_i	component of the position vector in the i^{th} direction
y^*	dimensionless distance from the wall
y_P	the distance from point P to the wall

Greek Symbols

δ_{gap} gap size between the rotor blade and stator wall, m

$\overline{\overline{\delta}}$ unit tensor, /s

ε turbulent dissipation rate of energy, m^2/s^3

Γ_ϕ diffusion coefficient of ϕ, m^2/s

ϕ scalar quantity

ϕ_f convective quantity through face *f*

$\dot{\gamma}$ nominal shear rate, /s

ρ density of fluid, kg/m^3

ρ_p particle density, , kg/m^3

σ_k constant in *k*-ε closer equation

σ_ε constant in *k*-ε closer equation

μ_t turbulent viscosity, kg/m·s

τ_w shear stress on the wall

$\overline{\overline{\tau}}$ stress sensor, $kg/m \cdot s^2$

ω angular velocity, rad/s

REFERENCES

[1] Calabrese, R. V., 2001, Research needs and opportunities in fluid mixing technology. Chemical Engineering Research & Design 79 no. A2: 111-112.

[2] Paul, E.L., Atiemo-Obeng, V.A., and Kresta, S.M., 2004, Handbook of Industrial Mixing: Science and Practice, John Wiley & Sons.

[3] Karbstein, H. and Schubert, H., 1995. Development in continuous mechanical production of oil-in-water macro emulsions, Chem. Eng. Process., 34: 205 – 211.

[4] Davies, J. T., 1985. Drop size distribution related to energy dissipation rates, Chem. Eng. Sci., 40: 839 – 842.

[5] Grace, H. P., 1984. Dispersion phenomena in high viscosity immiscible fluid systems and application of static mixers as dispersion devices in such systems, Chem. Eng. Commun., 14: 225-277.

[6] Myers, K. J., Reeder, M. F., Ryan, D., and Daly, G., 1999. Get fix on high-shear mixing, Chem. Eng. Prog., 95: 33 -42.

[7] Francis, M. K., 1999, The development of a novel probe for the in situ measurement of particle size distributions, and application to the measurement of drop size in rotor-stator mixers, Ph.D. thesis, University of Maryland, College Park, MD, USA.

[8] Phongikaroon, S., 2001, Drop size distribution for liquid-liquid dispersions produced by rotor-stator mixers, Ph.D. thesis, University of Maryland, College Park, MD, USA.

[9] Padron, G. A., 2000. Measurement and comparison of power draw in rotor stator mixer. M.Sc. Thesis, University of Maryland, College Park, MD, USA.

[10] Mortensen, H. H., Rosendahl, L., Calabrese, R. V. and Innings, F., 2011, Characteristics of batch rotor-stator mixer performance elucidated by shaft torque and angle resolved PIV measurement, The Canadian Journal of Chemical Engineering, in press.

[11] LeClair, M. L., 1995, Optimize rotor–stator performance using computational fluid dynamics, Paint Coat. Ind., 1(4), 46–48.

[12] Epee-Bounya, S., 1998, Sliding Mesh Simulation of a Rotor-Stator Device, M.S. Thesis, University of Maryland, College Park, MD.

[13] Kevala, K., 2001, Sliding Mesh Computational Fluid Dynamics Simulation of Wide and Narrow Gap Inline Rotor-Stator Mixer, M.S. Thesis, University of Maryland, College Park, MD.

[14] Pacek, A. W., Baker, M. and Utomo, A. T., 2007, Characterisation of flow pattern in a rotor-stator high shear mixer, Proc. 6th European Congress on Chemical Engineering, R. Gani and K.D. Johansen, eds., Copenhagen, Denmark, Sept.

[15] Utomo, A., Baker, M. and Pacek, A., 2009, The effect of stator geometry on the flow pattern and energy dissipation rate in a rotor–stator mixer, Chem. Eng. Res. Des., 87 (4), 533-542.

[16] Harvey, P. S. and Greaves, M., 1982, Turbulent Flow in an Agitated Vessel Part II: Numerical Solutions and Model Predictions, Trans IChemE, 60, 201-210.

[17] Sheng, J., Meng, H., and Fox, R.O., 1998, Validation of CFD Simulations of a Stirred Tank Using Particle Image Velocimetry Data, Can. J. Chem Eng., 76, 611-625.

[18] Luo, J. Y., Gosman, A. D., Issa, R. I., Middleton, J. C., and Fitzgerald, M. K., 1993, Full Flow Field Computaition of Mixing in Baffeled Stirred Vessels, Trans IchemE, 71 Part A, 342-44.

[19] Ng, K., N. J. Fentman, K. C. Lee, and M. Yianneskis, 1998, Assessment of Sliding Mesh CFD Predictions and LDA Measurements of the Flow in a Tank Stirred by a Rushton Impeller, Trans. Inst. Chem. Eng., 76, 737-747.

[20] Wei, H., Zhou, W., and Garside, J., 2001, Computational fluid dynamics modeling of the precipitation process in a semibatch crystallizer, Ind. Eng. Chem. Res., 40, 5255-5261.

[21] Derksen, J. J. and H. E. A. Van den Akker, 1999, Large Eddy Simulations on the Flow Driven by a Rushton Turbine, AIChE J., 45, 209-221.

[22] Murthy, B. N. and Joshi, J. B., 2008, Assessment of standard k-e, RSM and LES turbulence models in a baffled stirred vessel agitated by various impeller design, Chem. Eng. Sci., accepted for publication.

[23] Lee, I., Variankaval, N., Lindermann, C., and Starbuck, C., 2004, Rotor-stator Milling of APIs Empirical Scale-up Parameters and Theoretical Relationships Between the Morphology and Breakage of Crystals, American Pharmaceutical Review.

[24] Kamahara, T., Takasuga, M., Tung, H. H., Hanaki, K., Fukunaka, T., Izzo, B., Nakada, J., Yabuki, Y. and Kata, Y., 2007, Generation of Fine Pharmaceutical Particles via Controlled Secondary Nucleation under High Shear Environment during Crystallization – Process Development and Scale-up, Organic Process Research & Development, 11, 699-703.

[25] Hinze, J. O., Hinze. Turbulence. McGraw-Hill Publishing Co., New York, 1975.

[26] Jaworski, Z, Wyszynski, M L, Moore, I P T, Nienow, A W., 1997, Sliding mesh computational fluid dynamics—a predictive tool in stirred tank design. Proceedings of the Institution of Mechanical Engineers, 211 (3), 149-156.

[27] Stoots, C. M., Calabrese, R.V., 1995, Mean Velocity Field Relative to a Rushton Turbine Blade. AIChE Journal., 41 (1), 1–11.

[28] Yianneskis, M., Popiolek, Z. and Whitelaw J. H., 1987, An experimental study of the steady and unsteady flow characteristics of stirred reactors. J. Fluid Mech. 175, 537-555.

[29] Yianneskis, M. and NG, K., 2000, Observations on the distribution of energy dissipation in stirred vessel. Trans IChemE, 78, 334-341.

[30] Aubin, J., Sauze, N. Le, Bertrand, J., etc., 2004, PIV measurement of flow in an aerated tank stirred by a down and up pumping axial flow impeller. Experimental Thermal and Fluid Science 28, 447-456.

[31] Wu, Shenchun, 2009, A PIV study of co-ratating disks flow in a fixed cylindrical enclosure. Experimental Thermal and Fluid Science 33, 875-882.

[32] Li, X., Du, Z., Huang, X., Yuan, W. and Ying, H., 2010, Solubility of Sucralose in Different Solvents from (283.15 to 333.15) K. J. Chem. Eng. Data, 55, 2600–2602.

[33] Bouchard, A., Hofland, G. W. and Witkamp, G., 2007, Properties of Sugar, Polyol, and Polysaccharide Water-Ethanol Solutions. J. Chem. Eng. Data, 52, 1838-1842.

[34] Sucrose, International Chemical Safety Card 1507, Geneva: International Programme on Chemical Safety, November 2003.

[35] Yaws, C.L. (1999). Chemical Properties Handbook. McGraw-Hill.